



HAL
open science

Development of a smart coating based on hollow nanoparticles for corrosion detection and protection

Pierre Loison

► **To cite this version:**

Pierre Loison. Development of a smart coating based on hollow nanoparticles for corrosion detection and protection. Materials. Université de La Rochelle, 2019. English. NNT : 2019LAROS009 . tel-02475624

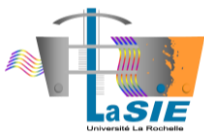
HAL Id: tel-02475624

<https://theses.hal.science/tel-02475624>

Submitted on 12 Feb 2020

HAL is a multi-disciplinary open access archive for the deposit and dissemination of scientific research documents, whether they are published or not. The documents may come from teaching and research institutions in France or abroad, or from public or private research centers.

L'archive ouverte pluridisciplinaire **HAL**, est destinée au dépôt et à la diffusion de documents scientifiques de niveau recherche, publiés ou non, émanant des établissements d'enseignement et de recherche français ou étrangers, des laboratoires publics ou privés.



ÉCOLE DOCTORALE n°618 « EUCLIDE »

Laboratoire des Sciences de l'Ingénieur pour l'Environnement (UMR 7356 CNRS)

Développement d'un revêtement intelligent pour la détection et la protection contre la corrosion

THÈSE

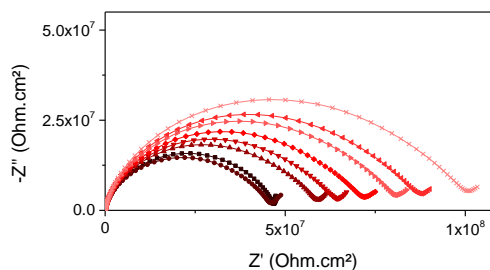
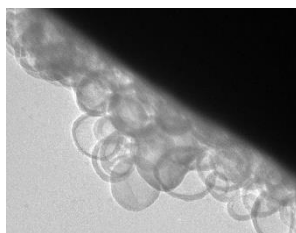
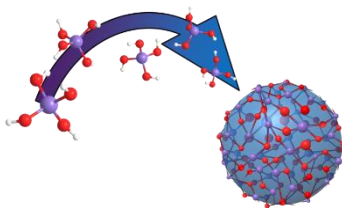
présentée par :

Pierre LOISON

Soutenue publiquement le 12 Avril 2019

pour l'obtention du grade de Docteur de l'Université de La Rochelle

Discipline : Génie des Matériaux



Composition du jury

Pr. Flavio DEFLORIAN	Université de Trente, Italie	<i>Rapporteur</i>
Pr. Mikhail ZHELUDKEVICH	Université de Kiel, Allemagne	<i>Rapporteur</i>
Pr. François-Xavier PERRIN	Université de Toulon, France	<i>Examineur (Président)</i>
Dr. Ing. Elisa CAMPAZZI	Airbus Helicopters, Paris-Le Bourget, France	<i>Examineur</i>
Dr. Ing. Santiago GARCIA	Université technologique de Delft, Pays-Bas	<i>Examineur</i>
Dr. Ing. Vincent DEBOUT	ArianeGroup, Saint-Médard-en-Jalles, France	<i>Invité</i>
Pr. Juan CREUS	Université de La Rochelle, France	<i>Directeur de thèse</i>
Pr. Sébastien TOUZAIN	Université de La Rochelle, France	<i>Directeur de thèse</i>



ÉCOLE DOCTORALE n°618 « EUCLIDE »

Laboratoire des Sciences de l'Ingénieur pour l'Environnement (UMR 7356 CNRS)

Development of a smart coating based on hollow nanoparticles for corrosion detection and protection

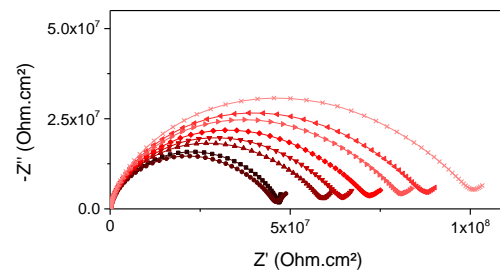
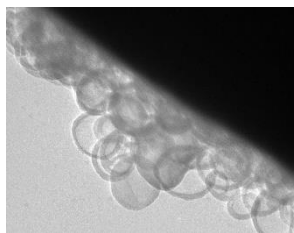
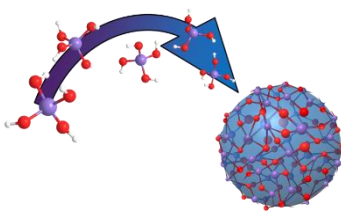
by

Pierre LOISON

Doctoral thesis, defended on the 12th of April, 2019

For the Degree of Doctor of Philosophy

in Materials Science



Composition of the jury

Pr. Flavio DEFLORIAN	University of Trento, Italy	<i>Reviewer</i>
Pr. Mikhail ZHELUDKEVICH	University of Kiel, Germany	<i>Reviewer</i>
Pr. François-Xavier PERRIN	University of Toulon, France	<i>Examiner (President)</i>
Dr. Eng. Elisa CAMPAZZI	Airbus Helicopters, Paris-Le Bourget, France	<i>Examiner</i>
Dr. Eng. Santiago GARCIA	Delft University of Technology, Pays-Bas	<i>Examiner</i>
Dr. Eng. Vincent DEBOUT	ArianeGroup, Saint-Médard-en-Jalles, France	<i>Invited</i>
Pr. Juan CREUS	University of La Rochelle, France	<i>PhD adviser</i>
Pr. Sébastien TOUZAIN	University of La Rochelle, France	<i>PhD adviser</i>

A ceux qui m'ont amené jusqu'ici

Et un peu à moi aussi...

*« La science est surtout une prise de conscience de plus en plus complète
de ce qui peut et doit être découvert. »*

Boris Vian

#LaChimieCestDeLaMagie

Remerciements / Acknowledgement

Avant-propos / Foreword

I guess everyone would be more at ease to say thank you in its mother tongue, or at least I would so I will. However I would like many people to really understand my words and therefore and will have to juggle a bit. To whom feels concerned but does not understand: sorry, but blame Google.

On se dit qu'on aura l'occasion plus tard, et finalement nous y voilà. Puisque l'occasion de dire merci se présente enfin, je tâcherai d'y mettre les formes et d'oublier aussi peu de personnes que possible. Il ne s'agit de toute façon pas d'un classement, et j'essaierai d'éviter de faire un inventaire à la Prévert ;)

Avant toute chose, je tiens à remercier MM. **Karim Aït-Mokhtar** et **Xavier Feugas**, directeur de l'Ecole Doctorale « Euclide » et du LaSIE respectivement pour l'accueil qui m'a été fait et pour le déroulement de ces quelques années, ainsi que pour leur disponibilité malgré tout.

Je remercie aussi sincèrement MM. **Yann Mignot** et **Bruno Rameau**, pour m'avoir fait confiance lorsque Airbus Defence & Space a lancé ce beau projet, ainsi que pour les échanges toujours agréables que nous avons eus même à travers les différentes réorganisation. Un grand merci également à M. **Vincent Debout** qui a su prendre le train en marche avec brio, et pour toute l'aide qu'il a pu m'apporter !

Une thèse ne peut pas aboutir sans des superviseurs attentifs, et je remercie donc naturellement les deux personnes qui m'ont encadré et formé au LaSIE. **Juan Creus** tout d'abord, qui entre ses mille responsabilités a toujours pu trouver du temps pour discuter, voir où j'allais et réussir à me faire voir que même si tout ne marche pas il y a toujours du positif à tirer d'une expérience. **Sébastien Touzain** ensuite, mon chef : tu as réussi à me convertir à l'impédance alors que ce n'était pas acquis, et surtout j'ai toujours apprécié ta franchise et ta façon directe de parler et défendre ton point de vue sans sous-entendu !

Jury members

To all the members of my jury also, I would like to express my gratitude.

First to Pr. **Flavio Deflorian**, for his attention when reading my manuscript, his kind comments and for the effort he made to be part of my defence despite air traffic issues. I hope we will have the occasion to meet in person next time.

Then to Pr. **Mikhail Zheludkevich**, especially for the very interesting discussion we had and for the dispensed advice. It truly was an honor to have someone with such experience about similar systems in my jury.

Merci au Pr. **François-Xavier Perrin** d'avoir fait partie de ce jury et pour les discussions qu'il a pu apporter, notamment par son point de vue de chimiste qui a apporté un intérêt certain au débat.

Un très grand Merci à Mme **Elisa Campazzi**, pour avoir mis en évidence les différences qui existent entre un travail, même appliqué, de laboratoire et la réalité industrielle. Nos discussions m'ont éclairé davantage sur la marche à suivre et le chemin restant à parcourir pour pouvoir appliquer notre système. Merci également pour toute l'aide, dans ma thèse comme en dehors, que tu as pu m'apporter et m'apporte aujourd'hui encore.

Finally yet importantly, I am sincerely grateful to Ass. Prof. **Santiago García**, thanks to whom I was able to stay in TU Delft, what was one of my best experiences as a PhD student. Thank you also for supervising me during these 3 months and for your highlighting comments, as well as for challenging me during my defence, always in a kind manner. I hope we will have the opportunity to work together and talk again (At least we could organize a Skype meeting).

Un merci tout particulier va évidemment à M. **Loïc Exbrayat** pour ses travaux préliminaires et pour son investissement sans faille jusqu'au bout. *“La victoire n'en sera que plus belle“* c'est ça ?

Evidemment, un encadrement et un solide soutien sur le projet ne serait pas suffisants pour mener à bien ces quelques années. Si je devais remercier chacun à la hauteur de ce qu'il m'a apporté, cette section constituerait la majeure partie de ce manuscrit. Je tenais tout de même à écrire les noms de ceux qui m'ont accompagné, soutenu, suivi ou précédé donc que celui qui cherche des capsules tourne quelques pages de plus ! Et d'avance pardon à ceux que je n'ai pas cités dans ma précipitation mais à qui je penserai plus tard.

LaSIE's passing people

Je tiens à remercier tout d'abord mes compagnons d'armes, en commençant par les générations précédentes que j'ai pu croiser et qui m'ont accueilli au sein du laboratoire : **Charlotte**, **Yves**, **Esaïe** (et tes pauses geeko-philosophiques dès 8h00), **vava Malek**, **Coco**, le calme **Marmule** (tes surnoms nuls et tes références parfois approximatives, “N'en jetez plus, la cour est pleine ! “, et évidemment ma « compatriote » et son sourire qui a illuminé les couloirs le matins : misaotra anao **Felana** !

Merci également à la génération suivante que je ne peux pas résumer : **Jiaqi** qui m'a montré qu'on survivra de toute façon à base de BK, **Rymette** toujours prête à prendre l'air et à sortir, **mister Lagarde** qui restera le mythe de la thèse faite à 100% en horaires de bureau et son obsession pour

mes cheveux, et l'inévitable **Cbouleo1** (Clairette la pâquerette te sied bien moins bien) : on a commencé par des sushis, fini par des PCC (C pour carotte hein ;), et toute ce qu'il y a entre les deux risque fort de me manquer ;) Tu n'es pas vraiment de chez nous mais tu as quand même bien participé à la belle ambiance du labo quand tu étais là, quindi grazie a te e torni a trovarmi quando vuoi **Virgilio** !

La génération hétéroclite qui a suivi mérite également son lot de mercis. Je pense que jamais la B225 n'a été aussi calme qu'avec nous et pour cela comme pour le reste je veux particulièrement remercier **Guillaume JaimePasLesGens H.**, présent de 7h à 21h pour parler manga, Zelda ou juste rappeler que tu en es à 785 pages et 1652 refs. Merci aussi à **Simon La Puyd'** : on y est l'ami, docteur et en pro D2, quand tu veux pour le prochain karaoké ou Quiz du Famous, et à **Simon Marti'** : on a pas le même bâtiment, ni la même passion mais on s'est quand même bien marrés ! Et que serait cette génération sans mon coloc de bureau ? Alors pour ces heures sur wikipédia pour apprendre (ou facebook pour stalker) et pour nos discussions des plus aux moins sérieuses merci **Pedro**. Après les sous-marins, les avions ? keep going, t'es bientôt aux fusées ;)

Et puisqu'après toutes nos péripéties il faut bien passer le relais, un merci groupé à la next gen pour avoir rendu mon retour et ces derniers mois souvent moins stressants et/ou déprimants ! Merci **Céline** pour tes attentions et ton souci des autres, **Dewdew** (T'as réussi à me supporter, maintenant prends soin de ma caverne d'Ali Baba #B227), **Alice** (Désolé si mon humour passe pas, mais je suis sûr que quelque part tu as ri ;)), **Walid**, toujours agréable, souriant et prêt à rendre le labo agréable, **Kahina**, j'ai pas retenu un seul mot à part « sorcière » mais j'ai essayé promis ! **Yoyoss**, tu es désormais la seule doctorante de la team peinture t'as intérêt à assurer avec le chef, ("buli bula ?!") mais pas de pression hein ;) **Alex** pour ta quiétude et ta connaissance parfaite de Kaamelott (attention c'est flippant parfois !) **Livy** pour ton sourire, pour « « danser » » avec moi à tout moment de la journée et pour être toujours motivé à aller boire un verre ("Alleeyyyyyy") ou faire un volleyy, **Malo**, parce qu'en plus d'être doux et frais t'es bien plus malin et intéressant que tu en as (ou crois en en avoir) l'air au premier abord ;) , **Cytron**, pas là pour te faire des amis mais t'y arrives quand même vachement bien, bon courage pour la suite avec la team kéké (et n'oublie pas que tes premiers pas ici étaient dans la team peinture), **Carooo**, s'il te plaît garde ton énergie, ta joie de vivre et ta capacité à mener 10 choses de front avec succès (par contre pour les éclats de rire vraiment on peut rien faire ?). Et comme un symbolise des prochains, au tout prochain : toi que l'on cherche tous les matins, et bien souvent hélas en vain, toi mon pilier, je ne vais pas utiliser une application native pour te le dire mais merci **Torty**, et surtout ne laisse personne te dire que tu n'es pas magnifique !

Tant pis si la chronologie me manque, je ne sais pas comment vous classer mais un grand merci pour tous les moments passés ensemble **Shadi** ! J'espère que tu auras bientôt ton permis pour revenir par ici (mais que tu ne mangeras pas tous les poissons de l'aquarium oO). Comme l'écrivait un autre Pierre "Aux âmes bien nées, la valeur n'attend point le nombre des années", et donc même

si tu n'es arrivé que tard merci à **Alexis** (faudra vraiment trouver un surnom un jour) pour ces belles discussions impédance, les solutions à tout ou presque et clairement pour m'avoir servi de psy faut bien l'avouer. Je crois qu'avec toi la #TeamPeinture a pris un envol incroyable !

Et enfin, merci aux stagiaires qui ont su s'intégrer et participer à la vie dans et hors du labo, notamment **Clarita** et **Laura** !

LaSIE's people (les autres)

Heureusement la vie dans un laboratoire ne se résume pas à une vie entre doctorants. Et pour les échanges quotidiens et l'ambiance de travail du LaSIE je tiens à remercier sincèrement l'ensemble des enseignants-chercheurs et permanents que j'ai pu croiser, avec un merci tout particulier à **Christelle**, **Bruno**, **Stéphane** et **Cyril**, souvent travailleurs de l'ombre mais qui ont su veiller au bon fonctionnement du laboratoire durant ces 3 années, ainsi qu'à l'équipe de gestionnaires, spécialement **Camille** et **Nadine**, toujours souriantes et efficaces !

A personnes particulières, une attention particulière, alors merci à toi **Stéphanie** pour ton énergie du matin, ta tournée de bonjours (quand tu t'arrêtes.. dire "Oui ! Toi aussi ? " ;)) et ta compassion à mon égard ! Un énorme merci également à **Arnaud** : certes te parler m'a parfois donné l'impression que je ne savais rien mais qu'est-ce que c'était intéressant. Un de mes grands regrets sera de ne pas t'avoir demandé des conseils musicaux plus tôt. Sans toi ma rédaction n'aurait pas été la même, et c'est sur *Phantom of the Opera* que j'écris ces lignes ! Et enfin, même si je sais que ça ne me dispensera pas de lui payer un coup, je tiens à exprimer ma reconnaissance à monsieur le professeur **Fernando** Pedraza, Commandant en chef de la HT team. Professionnellement comme personnellement et humainement, merci pour tout ce que j'ai appris à ton contact, et un merci tout particulier pour ton talent de recrutement ! Et puisque Dupond ne va pas sans Dupont, merci **Gilles** pour ta tranquillité, promis j'apprends à jouer au tarot avant le prochain !

LIENSs

Je tiens à exprimer ma reconnaissance envers le laboratoire LIENSs, et particulièrement MM. **Thierry Maugard** et **Hugo Groult** qui m'ont permis de réaliser des analyses en poussant la porte du laboratoire d'en face, ce qui m'a énormément facilité la tâche. Merci particulièrement à toi Hugo pour nos discussions et ton ouverture d'esprit et scientifique ! Merci également à toutes les personnes avec qui j'ai pu échangé en mettant un pied dans ce laboratoire avec un merci tout particulier à **Junhi**, je jalouse ton aisance en français et ton sourire colgate mais ta bonne humeur est contagieuse, **Julia**, pour la ronron therapy par Looping (et les réveils par griffure à 3h du mat' associés !), **Amandine** (si tu lis ça j'avouerais peut-être que tu m'as déjà battu au Molky), **Béa** pour ton soutien qui me fera presque oublier que tu n'étais pas là, et **Judith**, pour avoir été à mes côtés dans les pires moments de cette thèse (récupérer un thésard en dernière année juste avant une

opération de la mâchoire, ça s'appelle aimer le challenge), surtout dans les meilleurs qui ont suivi, pour nos projets nippons et parce que toi :)

TU Delft

Working elsewhere was supposed to be an incredible experience, but being part of NovAM has really been above incredible. There is no way I can mention every people I met during my Dutch stay, but I would like to express my gratitude to all the people from **NovAM** I had the chance to meet with in first place Pr. **Sybrand Van der Zwaag** for his warm welcome and for making me feel at home there. Thank you also **Santiago, Atsushi, Johan, Marlies, Mariana, Vincent, Santa-Satya** (I am still using this bottle opener) **Wouter** and your “Lunch time !”), **Wouter** (You probably still have the Atmosfeer card I guess), **Michael** (I swear hugging someone for his birthday is totally acceptable ;)), **Kleo** and your selfies, **Nicolas** (j’espère qu’Atsushi ne te demande plus de parler français devant lui !), **Silvia** (going from the Netherlands to Australia and speaking with no accent, did you finally admit you are not truly Italian?), **Vincenzo** especially for this bad Italy-Sweden but the incredible Italian atmosphere !, **Francesco** (I promise I will continue to like your Insta) **Amber** (Kapsalons are probably my best Dutch food discovery), **Gokhul** and your fancy meals (#Jealousy) and obviously **Shanta**, thank you so much for always sorting everything out so fast and efficiently!

I would also like to especially thank my desk-neighbor **Ren** for his English lesson and open-mindedness (PS: yes I know you have been to Japan). And of course, a huge “Thank you” goes to **Paul**, not only an exceptional researcher but also an amazing person. Your way to always try to understand something as deeply as possible truly inspired me and my work at Delft would have never been the same without you. I know I had a looooot of questions but thank you for answering them all and sincerely Dank u wel!

Friends

Si la majeure partie de la vie d’un doctorant se passe au labo, parvenir à achever ces trois (...) années n’aurait pas été possible sans un soutien inconditionnel de nombreuses personnes plus éloignées géographiquement mais qui ont toujours répondu présent quand j’en ai eu besoin, alors merci énormément à vous **Pierre, Audrey et Théo** (Thaba a été mon meilleur été de doctorant ;)), **Mailys** (besoin d’une traduction ? ;)), **Ericus** (Ericus), **BenJ**, **Bichon, Loveur, Nanabelle, Tommy, La Tych’, Lucie (x), Caro, Jeeeeeen, DinoDino, Josselin & Manu Lagadec** (J’avoue maintenant que je suivais les scores depuis le labo ?). Vous tous avez été là quand j’en ai eu envie ou besoin, alors merci énormément, j’arrive ;)

Je ne tiens pas à transformer ces remerciements en excuses pour le temps que je n’ai pas pris pour chacun, mais je tiens naturellement à remercier ma famille et tout particulièrement ma **Môman Marie-Pierre** et ma sœur **Iris** (oui je sais tu connais ton prénom ;)). Pas toujours facile d’avoir de

mes nouvelles, mais toujours réconfortant pour moi d'en avoir de vous ;) Et je ne serais pas là sans eux alors un grand merci également **Papa**, parrain **Gilles** et tonton **Christophe**.

Euuuuh.... Comme l'impression d'avoir oublié quelque chose . . . Le genre de choses auxquelles on pense longuement, et comme finalement on ne sait pas mettre de mot dessus on ne dit juste rien. Dans le doute que ce puisse être mal pris, j'essaierai tout de même de les trouver. Trois années peuvent paraître longue, et pourtant elles ont filé. Si je dois en partie ceci aux pages qui suivront, une grande part est cependant due à eux deux et je tiens ici à les remercier en quelques lignes pour les nombreuses autres que nous avons écrites ensemble et celles que, j'espère nous écrirons hors du labo. Alors pour la 37^{ème} fois dans ces pages MERCI **Germ'** et **BenBen**, duo de choc d'une équipe hors norme. J'ai souvent eu l'impression que le laboratoire se transformait en énorme coloc une certaine heure passée, et il m'est arrivé d'attendre cette heure pour pouvoir enfin travailler efficacement. Ces trois années sans soirée labo, foutoir, discussions improbables, PG, apéro, femme-cabane, Carrouf, BK, RU, Ciné, île d'Yeu (Lamantine)... n'auraient pas été les mêmes alors **merci**.

List of figures

Chapter I - Bibliographic review

Figure I. 1: Ariane 5 launch vehicle structure, reproduced from ²⁸	11
Figure I. 2: Complexity of AA2024-T3 microstructure, reproduced from ⁴⁸ . Each color represents a different phase. S- θ - and α -phase are mauve, orange and yellow respectively	16
Figure I. 3: Trenching around S-phase particles in AA2024-T3 after 15min exposure to 0.1M NaCl, reproduced from ⁶⁰	18
Figure I. 4: Schematic representation of self-healing and inhibition process for a smart coating ..	23
Figure I. 5: Schematic representation of interfacial polymerization.....	38
Figure I. 6: Example of SEM observations of (a) polyurea ¹⁵¹ , (b) melamino-formaldehyde ⁹⁸ and (c) polyaniline/3-nitrosamine ²³³ capsules formed through interfacial polymerization processes	39
Figure I. 7: Schematic representation of in-situ polymerization.....	41
Figure I. 8: Schematic representation of Layer-by-Layer deposition	42
Figure I. 9: Schematic representation of electrostatic complexation.....	43
Figure I. 10: Schematic representation of solvent evaporation	45
Figure I. 11: Schematic representation of dispersion polymerization	45
Figure I. 12: High-resolution SEM pictures of a fracture area after cryo-fracture of a PU/PUa capsules-loaded epoxy coating, from ²⁶⁹	47
Figure I. 13: Triggered versus switchable release mechanisms	51
Figure I. 14: Summary of the approach chosen in the development of the NC2M system.....	62

Chapter II - Containers formation and characterization

Figure II. 1: Example of correlograms obtained for the analysis of a monodisperse dispersion	85
Figure II. 2: Example of electrophoretic mobility and deduced zeta potential distribution considered as good quality data	87
Figure II. 3: Silica capsules formation using an O/W mini-emulsion process.....	88
Figure II. 4: TEOS polycondensation reaction	89
Figure II. 5: SEM (a & c) and TEM (b & d) observations of the unloaded (a & b) and MBT-loaded (c & d) Si NCs	91
Figure II. 6: TEM observations of silica NCs and zoom in on deformed parts of the silica containers	92
Figure II. 7: FTIR spectrum of silica NCs with and without encapsulated MBT.....	92
Figure II. 8: Size distribution obtained from SEM image analysis	93
Figure II. 9: (a) Capsules' diameter and associated wall thickness from TEM images analysis and (b) the associated calculated free volume	94
Figure II. 10: (a) DLS curves for Si and Si(MBT) NCs), and associated (b)mean sizes and (c) polydispersity indexes	95

Figure II. 11: Correlograms obtained for DLS analyses of (red) Si and (blue) Si(MBT) containers	96
Figure II. 12: Release of MBT from silica NCs in an alkaline medium (pH=10.2)	97
Figure II. 13: Mean size and polydispersity index obtained by DLS for (a) Si and (b) Si(MBT) containers 12h and 20 days after synthesis	98
Figure II. 14: Evolution of the Si NCs hydrodynamic diameter as a function of pH and time	99
Figure II. 15: Zetametry study of the silica capsules, (a) without and (b) with MBT as a payload	100
Figure II. 16: Influence of the sonication amplitude and pulse duration on the Si NCs size and polydispersity index for a total sonication duration of 3min	103
Figure II. 17: Size distribution of mechanically formed suspension for 5 min processing at 3 krpm (a), 7 krpm (b), 10 krpm (c) and 15 krpm (d)	104
Figure II. 18: DLS size distribution (left) and correlation function (right) for a suspension mechanically formed stirring at 7 krpm for 10 min	105
Figure II. 19: ESEM observations of a silica particle suspension obtained through a mechanically formed emulsion	105
Figure II. 20: DLS analysis of a suspension formed using mechanical stirring at 7krpm 5 minutes (a and c) and 15 minutes (b and d)	106
Figure II. 21: Influence of the DTAB concentration (left) and surfactant carbon-chain length (right) on the final suspension's size	108
Figure II. 22: Influence of hexadecane and TEOS amounts on the dispersion's size and polydispersity	109
Figure II. 23: SEM observation of a sample prepared without hexadecane in the dispersed phase	110
Figure II. 24: Influence of the total dispersion's volume and the dispersed phase's relative volume on the final dispersion's size and polydispersity	111
Figure II. 25: Schematic representation of the W/O emulsion and polyurea capsules formation	113
Figure II. 26: Polymerization of DAB with TDI leading to the formation of polyurea shell	113
Figure II. 27: Polyisobutylene succinimide pentamine structure of Lubrizol® U used for the synthesis of PUa capsules, with n=1-10, according to ³⁶	114
Figure II. 28: DLS correlograms obtained for the emulsions formed with a) Span 80 b) Span 85 c) Span 80+Tween 80 0.15 eq. d) Span 80 + Tween 80 0.87 eq.	117
Figure II. 29: generic structure of PIBSA surfactant molecules	118
Figure II. 30: DLS size distributions of PUa syntheses carried out using PIBSA-based surfactants Lubrizol® 5625 (a and c) and Lubrizol® 5620B (b and d) using 0.067 (a and b) and 0.2 (c and d) equivalent versus TDI	119
Figure II. 31: FTIR spectra of the employed PIBSA-based surfactants and reference Lubrizol® U	120
Figure II. 32: ESEM observations of dispersions of capsules formed with (a and b) 0.067 and (c and d) 0.2 equivalents of L5620B respectively	121

Figure II. 33: Particle size distribution obtained by image analysis on 781 particles from an ESEM observation of particles using 0.2 equivalent of Lubrizol 5620B	122
Figure II. 34: DLS (a) size distribution and (b) associated correlograms.....	123
Figure II. 35: DLS size distribution of the reference PUa capsules, (a) before and (b) after purification by dialysis.....	124
Figure II. 36: Effect of the surfactant concentration and pH of the environment on the capsules' mean size (Only the major peak's mean size is considered)	125
Figure II. 37: ESEM observations of PUa capsules after dialysis and transfer in water using 0.5% SDS.....	126

Chapter III - Obtaining homogeneous composite coatings

Figure III. 1: Optical microscopic observation of the uncoated steel Qpanels' surface	137
Figure III. 2: AA2024-T3 samples used for coating application	138
Figure III. 3: (left) AA2024-T3 samples preparation and (right) spraying set-up.....	140
Figure III.4: (a) Dry thicknesses of the pure and 20% diluted epoxy coatings depending on the applied formulation's wet thickness and (b) corresponding relative dry/wet ratio.....	143
Figure III. 5: Microscopy observations of (a,b) pure and (c,d,e,f) diluted epoxy coatings applied by bar coating on top of steel Qpanels with (a,b,c,d) 120 μm and (e,f) 200 μm wet thickness.....	144
Figure III. 6: Observation of a 200 μm wet epoxy sample cross-section.....	145
Figure III. 7: Appearance of epoxy coatings formed and cured at 60°C after (a) 2h and (b) 12h solvent evaporation at RT (bar coating, 120 μm wet)	145
Figure III. 8: Appearance of epoxy coatings for three mixing techniques, applied by bar coating with a 120 μm wet thickness.....	146
Figure III. 9: Appearance of coatings formed from a formulation stirred with (a & b) an Ultra-turrax or (c & d) a stirrer with blades after a 45 min degassing in a mounting-machine	148
Figure III. 10: Appearance of epoxy coatings made from a formulation degassed using (a & b) 60s and (c & d) 90s of sonication.....	149
Figure III. 11: Observations of epoxy films loaded with silica NCs after Ultra-Turrax dispersion and vacuum degassing. Grains are visible in the epoxy layer.	150
Figure III. 12: Effect of the order of addition of the silica NCs suspension with addition of the suspension (S) first to (a & b) Base (B) and (c & d) Hardener (H).....	151
Figure III. 13: Presence of defects in the silica NCs-loaded epoxy coating after US degassing	151
Figure III. 14: Observations of neat PU coatings applied by bar coating with a (a) 60 μm and (b) 120 μm wet thickness degassed (a & b) in a desiccator or (c) by sonication.....	153
Figure III. 15: (a) Thickness of pure PU layers after curing and (b) corresponding volume solid, for 60 and 120 μm wet thickness	153

Figure III. 16: Observations of defects in PU coatings loaded with Si NCs, the suspension being added (a) to the blend of base and hardener and (b) first in the base before addition of the hardener	154
Figure III. 17: Observations of clusters in a PU-Si coating and spots analyzed by μ -XRF	154
Figure III. 18: (a) Appearance and (b) cross-section of a PU-Si coating, after US processing of the formulation.....	155
Figure III. 19: Appearance of AA samples after (a & b) 4s and (c) 6s-spraying of a 10/5/4 (B/H/W) PU formulation.....	156
Figure III. 20: (a) Thickness of PU coatings sprayed on AA2024-T3 samples depending on the spraying time and formulation and (b) influence of the pressure applied	156
Figure III. 21: PU-Si coatings on AA substrate obtained with (a & b) 0.7 mm and (c & d) 1.02 mm nozzle openings	157
Figure III. 22: Thickness of sprayed PU, PU-Si and PU-Si(MBT) coatings on top of AA2024-T3 substrates.....	157
Figure III. 23: FTIR spectra of the neat PU and Si-loaded PU coatings	160
Figure III. 24: μ -XRF analysis of the cured Si-loaded PU resin	161
Figure III. 25: μ -XRF assessment of the silicon capsules distribution in a PU-Si coating made on top of a steel substrate.	162
Figure III. 26: Observation of a PU-Si sample analyzed by μ -XRF.....	163
Figure III. 27: SEM observations of the surface of a sprayed PU-Si coating (a,b) before and (c) after removal of 150 nm of coating by Ar-sputtering	164
Figure III. 28: Depth profile of a PU-Si coating	165
Figure III. 29: TOF-SIMS surface mapping of a PU-Si coating sprayed on AA2024-T3 after Ar-sputtering.....	166

Chapter IV - Corrosion protection and performances of PU coatings

Figure IV. 1: Scheme of a S355 steel sample prepared for inhibitor testing.....	175
Figure IV. 2: (a) bottom view, (b) face cross section, and (c) top view of the electrochemical cell used for EIS measurements	176
Figure IV. 3: Evolution of S355's OCP in 0.05M NaCl with and without 2-MBT	179
Figure IV. 4: Evolution with time of EIS spectra with (a,b) Nyquist plots, (c,d) moduli and (e,f) phase angle for the bare S355 substrate in (a,c,e,) absence and (b,d,f) presence of 25 ppm of MBT. Spectra are taken with 10 pts/decade, the 0.1 Hz measurement is circled in the Nyquist plots	181
Figure IV. 5: OCP and R_p (measured by LPR) of S355 steel immersed in 0.05M NaCl with different amounts of sodium molybdate.....	182
Figure IV. 6: EIS spectra of S355 immersed in 0.05M NaCl (a) without inhibitor and with (b) 150 ppm and (c) 1000 ppm of Na_2MoO_4 . Spectra contain 10 pts/decade; the measurement taken at 0.1Hz is circled.....	183

Figure IV. 7: (a) EEC used to fit the EIS spectra and (b) calculated R_p for S355 immersed in 0.05M NaCl without different amounts of Na_2MoO_4 corrosion inhibitor	184
Figure IV. 8: OCP of AA2024-T3 in 0.05M NaCl without and with 25 ppm of MBT	185
Figure IV. 9: Evolution of EIS spectra for bare AA2024-T3 immersed in (a,c,e) 0.05M NaCl and (b,d,f) 0.05M NaCl with 25 ppm of MBT. Spectra contain 8pts/decade, circled points correspond to measurements taken at (a) 0.1Hz and (b) 1Hz.....	186
Figure IV. 10: Evolution of the charge transfer resistance of bare AA2024-T3 in 0.05M NaCl without and with 25 ppm of MBT, calculated from the EIS spectra fit.....	187
Figure IV. 11: OCP of bare AA2024-T3 immersed in a 0.05M NaCl electrolyte without and with 110 ppm of $\text{Ce}(\text{dbp})_3$	188
Figure IV. 12: Evolution of the impedance of AA2024-T3 in 0.05M NaCl + 110ppm $\text{Ce}(\text{dbp})_3$ over immersion time. 8pts/decade are measured, measurements taken at 0.1Hz are circled.	189
Figure IV. 13: Evolution of the charge transfer resistance R_{ct} for AA2024-T3 immersed in 0.05M NaCl + 110ppm of $\text{Ce}(\text{dbp})_3$, calculated from EIS data.	189
Figure IV. 14: Appearance of AA2024-T3 substrate's surface, immersed in 0.05M NaCl, NaCl with 25 ppm of MBT and NaCl with 25 ppm of $\text{Ce}(\text{dbp})_3$ after 0, 24 and 38h of immersion. Scale bars represent 4 mm	190
Figure IV. 15: Evolution of steel's OCP immersed in 0.05M NaCl with and without addition of 10% Si NCs suspension.....	192
Figure IV. 16: Nyquist and Bode diagrams of a steel Qpanel immersed in an electrolyte containing 10 vol.% silica capsules suspension, measured using 8 pts/decade. Measurements taken at 0.1 Hz are circled	193
Figure IV. 17: Observations of a steel Qpanel (a) before, (b) after immersion in an electrolyte containing silica nanocontainers, and (c) after drying.....	194
Figure IV. 18: Evolution of AA2024-T3's OCP in presence of 10 vol.% of "empty" (Si) or MBT-loaded (Si(MBT)) silica nanocontainers dispersion	195
Figure IV. 19: (a,b) Nyquist and (c,d,e,f) Bode diagrams of AA2024-T3 immersed in 0.05M NaCl with 10 vol.% of (a,c,e) Si or (b,d,f) Si(MBT); Spectra acquired with 8pts/decade. Measurements taken at 0.1 Hz are circled	196
Figure IV. 20: EDS analysis of the silica layer deposited on AA2024-T3 after 24h immersion in 0.05M NaCl + 10 vol.% of Si(MBT) suspension	197
Figure IV. 21: Nyquist diagrams of steel Qpanels coated with (a) PU, (b) PU-Si and (c) PU-Si(MBT) systems. 12 pts/decade have been recorded, the circled values are taken at (a) 0.1 Hz and (b,c,) 1 Hz	200
Figure IV. 22: Bode diagrams obtained for steel Qpanels coated with (a) PU, (b) PU-Si and (c) PU-Si(MBT) systems.....	202
Figure IV. 23: Equivalent circuits used for the impedance plots of coated substrates with (a) 2 time constants (b) 2 time constants and diffusion (c) 3 time constants and diffusion	203

Figure IV. 24: Evolution of (a) the coating's resistance and (b) the charge transfer resistance for PU, PU-Si and PU-Si(MBT) systems, calculated from the adequate electrical equivalents circuits	203
Figure IV. 25: Apparent water uptake of unloaded and Si NCs-loaded PU coatings applied by bar coating on top of steel Qpanels	204
Figure IV. 26: Artificial defects made in PU coatings before opto-EIS measurements	205
Figure IV. 27: Observation of the exposed area during EIS analysis	206
Figure IV. 28: EIS results from opto-EIS analysis for PU coatings.....	207
Figure IV. 29: Nyquist and Bode plots for sprayed PU coatings applied on top of AA2024-T3. Spectra have been obtained with 12 pts/decade. The circled value on the Nyquist plot is the 1 Hz measurement.....	209
Figure IV. 30: Nyquist and Bode plots for sprayed PU coating loaded with silica nanocapsules, applied on top of AA2024-T3. Spectra have been obtained with 12 pts/decade. The circled value on the Nyquist plot is each time the 10 Hz measurement.....	210
Figure IV. 31: Nyquist and Bode plots for sprayed PU coating loaded with Si(MBT) nanocapsules, applied on top of AA2024-T3. 12 pts/decade were taken. The circled value on the Nyquist plot is each time the 1 Hz measurement.....	212
Figure IV. 32: Evolution of the low frequencies modulus for PU, PU-Si and PU-Si(MBT) coatings over immersion in 0.05M NaCl	213
Figure IV. 33: Appearance of (a) Si NCs-loaded PU coating after immersion, and AA's surface after removal of the (b) PU-Si and (c) PU-Si(MBT) coating. Scratches in picture c were made during the coating removal. Contrasts have been enhanced in order to reveal defects	214
Figure IV. 34: Apparent water uptake calculated using Brasher-Kingsbury equation for PU, PU-Si and PU-Si(MBT) systems	214
Figure IV. 35: Degradation mechanism of the (a,b,c) PU-Si and (d,e,f) PU-Si(MBT) developed coatings.....	215

Appendices

Figure 1: UV-vis spectra of the MBT solutions prepared in (a) pure water and (c) 20 mM NaOH and (b & d) respective calibration curves	230
---	-----

List of tables

Chapter I - Bibliographic review

Table I. 1: Composition of the main parts of Ariane 5 ²⁸	12
Table I. 2: Maximum content of alloying elements in S355 steel in wt.%	13
Table I. 3: Aluminum alloys series and alloying elements ³⁵	14
Table I. 4: Heat treatments used in aerospace for Aluminum alloys ³⁶	15
Table I. 5: Chemical composition limits (in wt.%) ⁴⁶	15
Table I. 6: OCPs for various intermetallic compositions in 0.1M NaCl, reproduced from ⁶¹	18
Table I. 7: Literature review on the nature and size of capsules formed by interfacial polymerization	40
Table I. 8: Example of diffusion-governed release processes from the literature.....	49
Table I. 9: Bibliographic review of containers handling techniques used	52
Table I. 10: Worth considering dispersion processes from the literature.....	57

Chapter II - Containers formation and characterization

Table II. 1: Characteristic vibration frequencies in FTIR spectra of Si and Si(MBT) NCs	93
Table II. 2: List of the surfactants used to stabilize W/O emulsions and their properties	115
Table II. 3: Quantity of surfactants tried in order to form PUa capsules using Span [®] 80 and Tween [®] 80	116
Table II. 4: Comparison of FTIR spectra for the PIBSA and Lubrizol [®] surfactants	120

Chapter III - Obtaining homogeneous composite coatings

Table III. 1: Composition of S355 and the used steel Qpanels in wt.%	136
Table III. 2: Roughness parameters of degreased uncovered steel Qpanels, in μm	137
Table III. 3: Composition of the used AA2024-T3 determined by $\mu\text{-XRF}$	137
Table III. 4: Size and qualitative assessment of the number of defects present in epoxy coatings depending on the mixing technique, from microscope observations	147
Table III. 5: Elemental composition of the previously determined spots, determined by $\mu\text{-XRF}$ (in wt.%)	154
Table III. 6: Thickness and composition of PU coatings determined by $\mu\text{-XRF}$ in the absence (PU) and presence of Si NCs, without (PU-Si) and with a payload (PU-Si(MBT) respectively), in wt%	162
Table III. 7: Elemental composition (in wt.%) of a PU-Si covered AA2024-T3 sample, from $\mu\text{-XRF}$ measurements	163
Table III. 8: Elemental composition (in wt.%) measured by $\mu\text{-XRF}$ of a 80 μm PU-Si layer sprayed on top of an A2024-T3 substrate	164

Chapter IV - Corrosion protection and performances of PU coatings

Table IV. 1: Electrochemical setups used and their purpose177

Appendices

Table 1: UV-vis calibration data for MBT in the range 0-30 ppm 231

Table 2: List of the chemicals used for the preparation of silica capsules 231

Table 3: List of the chemicals used for the preparation of PUa microcapsules..... 232

Table 4: Summary of the emulsion process optimization experiments carried out..... 233

List of abbreviations

AA	Aluminum Alloy
ATR	Attenuated Total Reflectance
DAB	1,4-diaminobutane
DLS	Dynamic Light Scattering
DTAB	Dodecyltrimethylammonium bromide
EEC	Electrical Equivalent Circuit
EIS	Electrochemical Impedance Spectroscopy
FTIR	Fourier-Transform Infrared
HF	High Frequency
HLB	Hydrophilic Lipophilic Balance
IEP	Isoelectric Point
IM	Intermetallic
LbL	Layer-by-Layer
LF	Low Frequency
LPR	Linear Polarization Resistance
MBT	2-mercaptobenzothiazole
NC	Nanocontainer
O/W	Oil-in-Water
OCP	Open Circuit Potential
PdI	Polydispersity index
PU	Polyurethane
PUa	Polyurea
PZC	Point of Zero Charge
RMS	Root Mean Square
SCE	Saturated Calomel Electrode
SDS	Sodium Dodecyl Sulfate
TDI	2,4-toluene diisocyanate
ToF-SIMS	Time of Flight - Secondary Ion Mass Spectrometry
W/O	Water-in-Oil
WE	Working Electrode

Table of contents

INTRODUCTION.....	1
CHAPTER I - Bibliographic review.....	5
State of the art: introduction.....	8
I.1. Aerospace and corrosion	9
I.1.1. Aerospace materials and their current use	10
I.1.1.1. Generalities	10
I.1.1.2. Steel	12
I.1.1.3. Aluminum alloys (AA).....	13
I.1.2. Corrosion of materials	16
I.1.2.1. Corrosion	16
I.1.2.2. Structural steel	17
I.1.2.3. AA2024-T3 aluminum alloy.....	17
I.1.3. Actual corrosion protection for aerospace	19
I.1.3.1. Metallic protective coatings ⁶⁶	19
I.1.3.2. Anodizing and Conversion coatings ^{68,69}	20
I.1.3.3. Sol-gel coatings	21
I.1.3.4. Organic coatings	21
I.2. Inhibition of corrosion processes.....	23
I.2.1. Inhibition or self-healing?.....	23
I.2.2. Corrosion inhibitors and their mechanisms.....	24
I.2.2.1. Cathodic inhibitors	25
I.2.2.2. Anodic inhibitors	25
I.2.2.3. Mixed-type inhibitor	26
I.2.3. Corrosion protection for NC2M	27
I.3. Corrosion detection and monitoring.....	29
I.3.1. Methods currently used.....	29
I.3.2. Direct monitoring techniques.....	30
I.3.3. Indirect monitoring techniques.....	31
I.3.4. Coating monitoring	32

I.4. Encapsulation through a colloidal process and smart coating design.....	35
I.4.1. Colloids' stability.....	35
I.4.2. Particles formation and nature.....	37
I.4.2.1. Interfacial reactions.....	37
I.4.2.2. Particles precipitation.....	43
I.4.3. Opening and content release.....	46
I.4.3.1. Release upon fracture.....	46
I.4.3.2. Controlled release.....	48
I.4.4. Integration of containers in a host matrix.....	51
I.4.4.1. Containers handling.....	51
I.4.4.2. Impact of the addition in a host matrix.....	53
I.4.4.3. Incorporation process.....	55
I.5. Summary and experimental approach.....	59
References.....	64
CHAPTER II - Containers formation and characterization.....	77
Containers for the NC2M: introduction.....	80
II.1. Equipment used.....	81
II.1.1. Synthesis of the nanocapsules.....	81
II.1.1.1. Sonication system.....	81
II.1.1.2. Stirring.....	81
II.1.2. Characterization.....	81
II.1.2.1. Dynamic Light Scattering (DLS).....	81
II.1.2.2. Zetametry.....	85
II.1.2.3. Spectroscopy techniques.....	87
II.1.2.4. Microscopy.....	87
II.2. Hydrophobic-core silica containers.....	88
II.2.1. Capsules formation.....	88
II.2.1.1. Materials.....	88
II.2.1.2. Formation procedure.....	88
II.2.2. Characterization of the suspension.....	89
II.2.2.1. Assessment of the capsules formation.....	90

II.2.2.2. Size measurement	93
II.2.2.3. Encapsulation efficiency and release.....	96
II.2.2.4. Stability.....	97
II.2.3. Size optimization.....	101
II.2.3.1. Sonication	102
II.2.3.2. Mechanical stirring	103
II.2.3.3. Composition	107
II.2.3.4. Summary	111
II.3. Hydrophilic-core polyurea containers.....	112
II.3.1. Capsules formation	112
II.3.1.1. Materials.....	112
II.3.1.2. Standard procedure.....	112
II.3.1.3. Importance of the surfactant	113
II.3.1.4. Suspension purification and transfer in water	114
II.3.2. Characterization of the PUa capsules	115
II.3.2.1. Surfactants	115
II.3.2.2. Addition of ethanol in the dispersed phase.....	122
II.3.2.3. Transfer of the suspension in water	123
II.3.2.4. Conclusions on the synthesis of PUa containers	126
Conclusions on the containers formation and characterization	127
References	128
CHAPTER III - Obtaining homogeneous coatings loaded with silica nanocontainers	131
Introduction	134
III.1. Materials and methods.....	135
III.1.1. Materials	135
III.1.1.1. Resins.....	135
III.1.1.2. Substrates.....	136
III.1.2. Capsules incorporation.....	138
III.1.2.1. Approach.....	138
III.1.2.2. Formulation preparation.....	138

III.1.3. Coating application	139
III.1.3.1. Bar coating onto steel panels	139
III.1.3.2. Spraying onto AA panels	139
III.1.4. Coating characterization	140
III.1.4.1. Fourier-transform infrared (FTIR) spectroscopy	140
III.1.4.2. Microscopic observations	140
III.1.4.3. Thickness measurement	141
III.1.4.4. Micro-X-ray fluorescence (μ -XRF)	141
III.1.4.5. ToF-SIMS	141
III.2. Film formation and optimization	142
III.2.1. Epoxy coating	142
III.2.1.1. Addition of water to the epoxy formulation	142
III.2.1.2. Addition of silica nanocontainers	149
III.2.1.3. Conclusion on the use of epoxy	152
III.2.2. Polyurethane coating	152
III.2.2.1. Low carbon steel: bar-coating	152
III.2.2.2. AA2024-T3 Aluminum alloy: Spray	155
III.3. Polyurethane coatings analysis	158
III.3.1. Amount of added capsules and inhibitor	158
III.3.2. Evaluation of the silica-loaded coatings	159
III.3.2.1. FTIR	159
III.3.2.2. μ -XRF	160
III.3.2.3. SEM observations	164
III.3.2.4. Time-of-Flight Secondary Ion Mass Spectrometry (ToF-SIMS)	165
Conclusions and outlook	167
References	169
CHAPTER IV - Corrosion protection and performances of capsules-loaded polyurethane coatings	171
Introduction	174
IV.1. Materials and methods	174
IV.1.1. Materials	174

IV.1.1.1. Chemicals.....	174
IV.1.1.2. Metal samples	174
IV.1.2. Electrochemical measurements	175
IV.1.2.1. Set-ups.....	175
IV.1.2.2. Procedures and data analysis	177
IV.2. Considered inhibitors	179
IV.2.1. Protection of structural steel	179
IV.2.1.1. MBT	179
IV.2.1.2. Sodium molybdate (Na ₂ MoO ₄).....	181
IV.2.2. Protection of AA2024-T3	184
IV.2.2.1. MBT.....	184
IV.2.2.2. Cerium dibutylphosphate Ce(dbp) ₃	187
IV.2.2.3. Conclusions on the inhibitors to use	190
IV.3. Interactions of the silica capsules with the metallic substrates.....	192
IV.3.1. Effect on the corrosion behavior of steel	192
IV.3.2. Effect on the corrosion behavior of AA2024-T3.....	194
IV.4. Inhibition properties of the coatings	199
IV.4.1. On steel	199
IV.4.1.1. Intact coatings.....	199
IV.4.1.2. Artificially damaged coatings	205
IV.4.2. On AA2024-T3.....	208
IV.4.2.1. Reference polyurethane coating (PU).....	208
IV.4.2.2. PU coating loaded with “empty” Si NCs (PU-Si)	209
IV.4.2.3. PU coating loaded with MBT-loaded Si NCs (PU-Si(MBT))	211
IV.4.2.4. Comparison of the performances of the three systems	212
IV.5. Conclusion on the system’s performances	216
References	217
General conclusions and Outlook.....	221
Conclusions	222
Container synthesis.....	222
Incorporation of the capsules and coating formation	223

Coatings characterization	223
Conclusion for the NC2M project	224
Suggestions for improvement	224
Development of nanocapsules.....	225
Process optimization	225
Composition of the emulsion.....	225
Characterization	226
Encapsulation of water-soluble molecules	226
Coating enhancement	226
References	228
Appendices	229
Appendix 1: UV-vis calibration data for MBT.....	230
Appendix 2: List of chemicals used	231
Appendix 3: Summary of the process optimization attempts for silica nanocontainers	232

INTRODUCTION

Introduction

For a few decades now, corrosion has been a major topic for scientific research due to the crucial issue it has become, because of the maintenance and fixing costs it engenders. Many studies have been and are still conducted in order to understand the various forms of corrosion, as well as their mechanisms in different environments and conditions. All these researches are fundamental, in order to ultimately find a way to preserve the metallic structures' integrity while they are sometimes employed in aggressive environments. Fighting a natural phenomenon such as corrosion is definitely one, if not the most, important challenge that industry has to face today. An efficient way has been found and used since the early 20th century, involving hexavalent chromium in conversion coatings. However, chromates have to be banned because of their carcinogenicity and, to date, no alternative could match the efficiency of chromates for corrosion protection purposes.

As one can imagine, all metal-consuming industries are impacted, and amongst them aerospace, and so ArianeGroup, is. ArianeGroup is indeed a world leader in civil and military launch systems. Its activities go from the design and development to the production of several products, amongst which have to be cited Ariane 5, the most reliable launch vehicle with 98 successful launches to date (February 5, 2019), and the M51 ballistic missile. The current activities of ArianeGroup focus on the development of a new generation of rockets, Ariane 6, whose 1st launch should occur in 2020. However, the development and use of launch systems require using a very high quantity of metals and alloys of various types, whether for the launchpad's structures or for specific pieces. This involves important maintenance costs that could be reduced using an efficient monitoring and protecting technology. This is why the New Corrosion Monitoring Material (NC2M) project was set up.

In order to enhance the current anticorrosive coatings and means already used, the idea of this project is to develop a protective coating that could autonomously detect corrosion at its first stage and slow down corrosion processes long enough for the user to be alerted. The targeted technology to achieve both detection and protection is the encapsulation of corrosion sensors and inhibitors in nanocontainers, able to release their payload as soon as the corrosion processes start. The designed capsules would then be fully integrated in a high-performance matrix.

The NC2M project is based on a consortium formed in January 2015 between 4 partners:

- ArianeGroup (AG) (Saint-Médard-en-Jalles, France), formerly known as Airbus Safran Launchers, the ordering and funding institution, is in charge of the coordination and the definition of the technical specification;
- The Laboratoire des Sciences de l'Ingénieur pour l'Environnement (LaSIE UMR 7356 CNRS) (La Rochelle, France), whose expertise concerns corrosion phenomena, metals protection in corrosive environments and organic coatings;
- Max Planck Institute (MPI) (Mainz and Düsseldorf, Germany), who has a recognized knowledge concerning encapsulation and the development of smart

Introduction

containers, as well as on the building of functionalized systems and their characterization;

- Airbus Group Innovations (AGI) (Suresnes, France), a technical expert about surface treatments and new protection technologies, is in charge of technical validation for the developed technology.

This collaboration started with a postdoctoral researcher, Loïc Exbrayat, who worked for 18 months at Max Planck Institutes in order to develop the used nanocontainers and establish a proof of concept for the NC2M technology. In a second time, he worked for 6 months at the LaSIE and was in charge of the technology transfer, what has been the starting point of the presented PhD project. As will be further discussed in the experimental sections, two types of nanocontainers have been developed, either organic (polyurea) or inorganic (silica) ones. The two functionalities that the NC2M coating must bring have been studied. First, with the encapsulation of either a mix of coloring agents (phenolphthalein / thymolphthalein) or a fluorescing molecule (FD1), the sensitivity toward corrosion has been demonstrated. The use of FD1 combined to silica capsules for corrosion detection has in addition led to a patent (FR 17403538). Then, corrosion inhibitors (cerium nitrate or sodium molybdate) have been used. Loïc Exbrayat's work allowed the detection of a color change associated with corrosion products and a decrease in the coating delamination around defects. Moreover, filiform corrosion experiments showed that it was possible to track the corrosion active head using FD1 and that corrosion was stopped by inhibitor-loaded particles. However, only feasibility was proven since the capsules were placed directly onto the substrate, with a model polymer on top.

The next step of this project is naturally to develop a viable system, embedding the capsules in a chosen matrix. The reported work summarizes the 3-year PhD project started in January 2016 that is the direct follow-up of Loïc Exbrayat's Postdoctoral project. Using the previously mentioned encapsulation systems as a starting point, AG, the LaSIE and AGI pursued the NC2M project. The aim of this PhD project is then to characterize more thoroughly the formed particles and study their incorporation within a polymer matrix.

The first part of this thesis typescript is a state of the art review that starts with the materials used for aerospace applications, the issue that corrosion constitutes and the existing technologies for their protection and inspection. A great attention is then paid to the last progress concerning smart coatings and especially corrosion monitoring and inhibiting coatings. This includes the technology developed and focused on encapsulation and processes similar to the ones we used. Then, since the organization structure changed, the first objective of this PhD project has been to adapt the developed protocols to the available materials and equipment.

The second chapter of the report will concern the formation of the containers we will use for our smart coating and the complete characterization needed to understand how they work and what we can expect from them.

Introduction

The third chapter then naturally focuses on the incorporation of the chosen containers into an organic matrix. The procedure we developed will be explained and discussed before assessing the coating homogeneity.

The determination of the coatings properties, mainly assessed using electrochemical impedance spectroscopy (EIS) will be dealt with in the fourth part of this thesis.

A last section is dedicated to a summary of the main results with regards to the development of the NC2M system. Outlook and suggestions for further improvement of the system are then proposed.

CHAPTER I

—

Bibliographic review

Chapter I - Table of contents

State of the art: introduction.....	8
I.1. Aerospace and corrosion	9
I.1.1. Aerospace materials and their current use.....	10
I.1.1.1. Generalities	10
I.1.1.2. Steel.....	12
I.1.1.3. Aluminum alloys (AA).....	13
I.1.2. Corrosion of materials	16
I.1.2.1. Corrosion	16
I.1.2.2. Structural steel.....	17
I.1.2.3. AA2024-T3 aluminum alloy.....	17
I.1.3. Actual corrosion protection for aerospace	19
I.1.3.1. Metallic protective coatings ⁶⁶	19
I.1.3.2. Anodizing and Conversion coatings ^{68,69}	20
I.1.3.3. Sol-gel coatings	21
I.1.3.4. Organic coatings	21
I.2. Inhibition of corrosion processes.....	23
I.2.1. Inhibition or self-healing?.....	23
I.2.2. Corrosion inhibitors and their mechanisms.....	24
I.2.2.1. Cathodic inhibitors	25
I.2.2.2. Anodic inhibitors.....	25
I.2.2.3. Mixed-type inhibitor	26
I.2.3. Corrosion protection for NC2M	27
I.3. Corrosion detection and monitoring.....	29
I.3.1. Methods currently used.....	29
I.3.2. Direct monitoring techniques.....	30
I.3.3. Indirect monitoring techniques.....	31
I.3.4. Coating monitoring	32
I.4. Encapsulation through a colloidal process and smart coating design.....	35

Chapter I - Bibliographic review

I.4.1. Colloids' stability.....	35
I.4.2. Particles formation and nature.....	37
I.4.2.1. Interfacial reactions	37
I.4.2.2. Particles precipitation	43
I.4.3. Opening and content release	46
I.4.3.1. Release upon fracture	46
I.4.3.2. Controlled release.....	48
I.4.4. Integration of containers in a host matrix.....	51
I.4.4.1. Containers handling	51
I.4.4.2. Impact of the addition in a host matrix	53
I.4.4.3. Incorporation process	55
I.5. Summary and experimental approach.....	59
References	64

State of the art: introduction

Developing a new and innovative coating for corrosion protection, respecting general technical specifications, is often tricky due to the numerous possible pathways and very high interest of many industries. Continuous progress and research for efficient and cost-effective solutions to a world-affecting problem make the field of smart coatings both incredibly exciting and competitive.

Since corrosion of metals will lead to their progressive dissolution and important losses of their physical properties, numerous applications are threaten by its development. Accurately calculate the cost of corrosion is nearly impossible since all industries are impacted. Moreover, as explained already in 1949 by Uhlig, induced costs include direct and indirect costs¹. It means that must be taken into account: change of hazardous metallic structures, plants shutdowns, maintenance, loss of stored or transported products, contamination, elimination of damaged products, development of new technologies and costs of preventive treatments. Different calculation methods are then used and studies are carried out in several countries, most of the available data being quite old^{2,3} but all of them warning about the gigantic saving that have to be done. One of the most cited and relevant study concerning the US economy was conducted by Battelle Columbus Laboratories and the National Institute of Standards and Technology (NIST) in 1975 and updated 20 years later. Results highlight that, due to an increasing use of metals and ageing equipment, corrosion costs are tremendously going up. A survey from the National Association of Corrosion Engineers (NACE) even evaluate that direct corrosion was wasting 3.1% of the U.S. Gross Domestic Product (GDP) in 1998⁴. However, this could be limited since more than a third of this cost would be avoided if more efficient protective systems were used. That is why we assume that, today, corrosion costs represent 3.5 to 5% of the world GDP and that with the current technologies it could be decreased by 30%⁵⁻⁷. A last important thing to mention is that the environmental impact of corrosion remains delicate to assess, and even though new standards and regulations tend to restrain the use of toxic chemicals, their replacement will take years and will require precautions⁸.

In this first chapter, we will first place the NC2M project in a precise industrial context before attaching importance to describe and highlight the staggering diversity of corrosion protection, monitoring and encapsulation method that are currently investigated in order to prevent corrosion.

I.1. Aerospace and corrosion

Aerospace is no exception to the mentioned impact, and is rather one of the most critical fields. Corrosion is indeed a phenomenon naturally occurring, but service conditions of a metal will highly influence its susceptibility to corrosion and aerospace activities always involve aggressive environments. In 1989 the first *Aerospace Corrosion Control Symposium* took place, highlighting the problem of corrosion detection and control in aerospace⁹. One of the reasons why aerospace structures are easily corroded is that launch pads are located near the equator for energy savings and close to the coast in order for the space debris (including launchers lower stages) not to fall on inhabited areas. This implies very severe climatic conditions for materials. For example the French and European spaceport, where Ariane rockets for example are launched, is located in French Guiana. Chloride concentration has been measured in precipitation and reached 60mg/m² per day, based on a 1906 study Dunn cites in his book¹⁰. The same problem is observed at the American Kennedy Space Center (KSC) in Florida that has been assessed as the most corrosive environment in the US¹¹.

These naturally corrosive atmospheres are even worsen due to the aerospace activities. Even if new propellants allowing exhaustion of less aggressive and toxic compounds are developed¹², solid rocket boosters at the KSC released 70 tons of hydrochloric acid per launch in 2010¹¹, what is quite similar to Ariane 5 boosters that exhaust approximately 12% of HCl and 16% of water¹³. This acid release contributes to the aggressiveness of the environment for the metallic pieces, during storage, transportation, tests and service^{10,14,15}. Use of other chemicals such as cleaning solvents or hydraulic fluids can also increase the aerospace environment corrosivity and favor localized corrosion like for example stress-corrosion cracking¹⁴.

Due to these factors, combined to extreme temperatures during launches, aerospace industry has to find new solutions to ensure the security of facilities and reduce costs, that have been evaluated for instance at 1.6 million dollars in 2001 for the KSC for corrosion control¹¹. This amount is explained by the space center surface area and metal quantity that is used. For example KSC has 3 mobile launcher platforms, each of them being mainly composed of steel and weighting around 3700 tons unloaded (without space shuttle)¹⁶.

Aerospace is a very wide field that comprises all activities dealing with objects moving in the Earth's atmosphere (aeronautics) and in the space environment (astronautics). Therefore, a staggering number of materials with different properties are used depending on their operational conditions and taking into account metals and their alloys, plastics, ceramics and composites, is it impossible to give an exact number although it is often evaluated above 100,000¹⁷. Naturally, sensibility to corrosion as well as modes of corrosion are, even slightly, different for each metallic alloy and so providing an exhaustive list does not make any sense. The objective of this section is then to briefly describe the materials used by ArianeGroup and launchers in general before lingering over the

mechanism of corrosion involved for the specific selected alloyed. In a third part we will deal with the protective means employed and developed for metallic structures.

I.1.1. Aerospace materials and their current use

When it comes to an aerospace system, the role and environment of a piece during its use will determine the materials that can be employed for its design. For example, aircraft are mainly made of aluminum and composites in order to reduce their weight, while specific pieces that must support re-entry in the atmosphere are generally made of carbon-carbon composites¹⁷. Price is obviously another criterion of high importance for the choice of materials.

As explained before, aerospace includes but is not limited to aeronautics. However, most of the books and articles dealing with this topic generally focus on aircraft (what is not ArianeGroup core business). If requirements for aircraft and launchers can be close, no exact relevant figure has been found for ArianeGroup needs and so we will describe materials used in general before focusing on our concern: aluminum alloys and structural steel.

I.1.1.1. Generalities

The first thing to consider when sending an object in the air being generally its weight, magnesium has quickly been envisaged since it is one of the lightest metals with a good physical resistance. However, although having been intensively used in the 1940's, it has slowly been replaced because of its high susceptibility to corrosion, cost and lower physical properties than other alloys^{18,19}. If magnesium is not used for structural parts today, new alloys are developed and some authors believe that it will play a role in the future for aerospace materials²⁰.

Titanium alloys have also been widely studied and are currently used for structures that require excellent structural properties such as fatigue strength, keeping a low weight compared to steel and an excellent corrosion resistance²¹. The most employed alloying element is aluminum, that is highly soluble in titanium and both strengthens the alloy and reduces its weight. Molybdenum is also used to enhance the high temperature resistance of the alloy²². The price of titanium alloys however remains a limit to its use in very important quantities.

The presented materials could theoretically be suitable for most of the parts of aerospace structures. However, they show limits in corrosion or erosion resistance when exposed for long duration at high temperatures, what happens in combustion chambers or afterburner for example. For these purposes, a specific class of alloys has been developed and are referred to as "superalloys". These alloys are usually nickel-based or cobalt-based and contain many alloying elements in high quantities (up to 40%)²³.

Enabling excellent mechanical properties and lightness, structural composite materials are also more and more used. Thanks to the large choice of matrices (polymeric, ceramic or metallic),

reinforcements (carbon, glass, type of preform..) and architectures (laminated, sandwich, braided...), they indeed offer an extremely wide range of properties and thus applications²⁴. High performance composites are for now expensive materials and sometimes difficult to implement, for large parts for example. If the development of composite materials brings many challenges, they are nonetheless more and more employed, especially in the aerospace industry. For example *ca.* 3 wt.% of Ariane 3 launcher's structure was made composite²⁵ materials while this value reaches around 7 wt.% and 16 wt.% for Ariane 4 and 5 respectively²⁶. This is moreover expected to keep increasing in the future²⁷. Since our study focuses on the protection of metallic materials, composites are not further detailed here as structural materials.

To these high-performance materials have to be added the probably best-known ones. Materials developments gather numerous research projects and industrial interest, so a quick and important evolution is observed, however aluminum and steel remain the most generally used metals for rockets and structures design respectively. An illustrating example, although slightly different from our application, is presented in Table I. 1 and Figure I. 1 which show the structure of Ariane 5 launcher and the composition of the main parts²⁸.

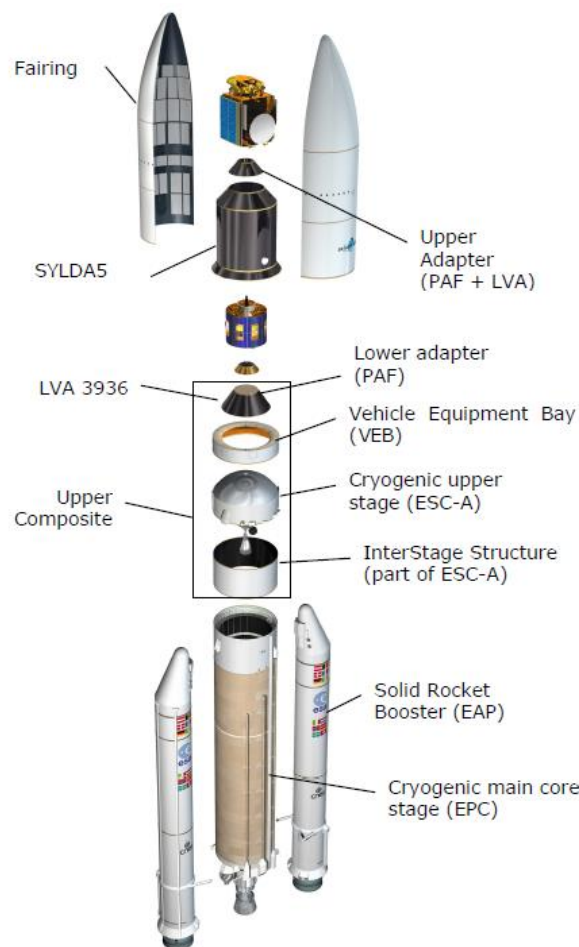


Figure I. 1: Ariane 5 launch vehicle structure, reproduced from ²⁸

Table I. 1: Composition of the main parts of Ariane 5²⁸

Component	Size (m)	Mass (kg)	Structure
Payload Fairing	Ø 5.4 x 17	2 675	Carbon-fiber reinforced plastic Aluminum honeycomb core
Cryogenic upper stage	Ø 5.4 x 4.71	4 540	Aluminum alloy tank
Cryogenic main core stage	Ø 5.4 x 23.8	14 700 (dry)	Aluminum alloy tank
Solid rocket booster	Ø 3.05 x 31.6	38 000 each	Stainless steel case

Aluminum alloys and steel are clearly used in high quantities since the cryogenic stages and boosters represent around 20% and 70% of the empty launcher weight respectively.

I.1.1.2. Steel

Compared to the other metals and alloys, steel has generally a very high strength but is several times heavier than aluminum or titanium. Low-alloy steel remains highly interesting for applications requiring strong pieces and not limited by density such as large ground structures, what is in our scope. The steels used and developed for many decades present various compositions and microstructures²⁹. We will here deal with structural steel and focus on the grade used and defined in the framework of the NC2M project.

Amongst steel alloys, structural steels are defined as low-carbon steels by the American Iron and Steel Institute (AISI) since they have a carbon content below 0.30%, ensuring a high enough ductility, but greater than 0.15% in order to keep a high strength. Within this category are quenched and tempered alloys, high-strength-low-alloys (HSLA) which show the higher strength due to alloying elements, and carbon-manganese steels that are the least expensive and most widely used structural steels.

To the iron and carbon present in steel are added alloying elements. This is mainly done in order to adjust the strength and ductility of the alloy, using manganese, molybdenum or vanadium for example that are mandatory to enable hot rolling. Other important alloying elements can be employed to remove oxygen for instance using deoxidizers such as aluminum or silicon, or to bring corrosion resistance to the steel as seen with the addition of chromium, nickel, copper or molybdenum. In addition to the desired elements, phosphorus and most of all sulphur are often present in structural steel but are undesirable elements since they can form inclusions that reduce the alloy strength³⁰.

Concerning the microstructure, annealed low alloyed steels are generally composed of pearlite and ferrite^{31,32}. An example of structural steel used by ArianeGroup is S355, named according to the European hot-rolled structural steel standard (EN 10025:2004). In “S355”, S stands for “Structural steel” and 355 is the maximum yield strength of the metal, in MPa and for thicknesses up to 16mm.

The composition of S355 defined by the same standard is recorded in Table I. 2. S355 is a low alloyed steel whose main addition element is manganese. The amounts of sulfur and phosphorus suggest the presence of inclusions that are not considered in our study.

Table I. 2: Maximum content of alloying elements in S355 steel in wt.%

Grade	C	Mn	P	S	Si
S355	0.23	1.60	0.05	0.05	0.05

However, it has to be noticed that these values are only maximum contents and so “S355” designates a series of steel alloys.

I.1.1.3. Aluminum alloys (AA)

The price and weight of many metals are a limitation to their extensive use. Being light and affordable, aluminum is therefore highly employed for aerospace structures. Its physical properties also make it suitable for processing and so pieces with complex geometries can be built.

i. Composition

Pure aluminum shows a quite good resistance to corrosion since a protective oxide layer naturally forms at the metal surface in oxidizing environments, preventing further development of corrosion. However, its physical properties (*e.g.* tensile strength, processing...) are too low for applications requiring high performance materials. For this, alloying elements are added to aluminum and the so-formed alloys go through a heat treatment in order to confer its final properties to the alloy^{33,34}. A nomenclature defined by the American Aluminum Association is used³⁵: the International Alloy Designation System (IADS). It consists in 4 digits, the first one being the AA series that corresponds to the major alloying element (or pure aluminum for the 1000 series) as recorded in Table I. 3. The last 2 digits are the alloy number in its series (or Al purity for the 1000 series). When an amelioration is performed on an alloy, the second digit is incremented (*e.g.* AA2124 is a second version of the AA2024).

Table I. 3: Aluminum alloys series and alloying elements³⁵

Serie	Alloying element	Application
1xxx	99.00+% Aluminum	Aluminum foils, chemical tanks
2xxx	Copper	Aerospace, military vehicles, rocket fins
3xxx	Manganese	Cooking utensils, radiators, heat exchangers
4xxx	Silicon	Filler wires for fusion welding and brazing
5xxx	Magnesium	Trucks, trains, buildings, cryogenic tanks
6xxx	Magnesium and silicon (Mg_2Si)	Automotive, bicycle frames, extruded structural pieces
7xxx	Zinc	Aerospace, armored vehicles, bicycle frames
8xxx	Other elements	

Amongst the eight existing series, four are referenced for aerospace applications thanks to their properties:

- 2xxx: Addition of copper, often associated with magnesium, leads to AAs with high strength due to precipitation hardening. Solubility of copper and magnesium in the aluminum matrix makes this kind of alloys heat-treatable, with a low ductility and corrosion resistance compared to other alloys.
- 6xxx: If addition of silicon lowers the alloy melting point, its combination with magnesium enables the formation of magnesium silicide (Mg_2Si) and so the formation of a heat-treatable alloy that can be easily (thus not expensively) extruded.
- 7xxx: Zinc is known to increase the alloy's strength. More specifically alloys containing also copper and magnesium, generally together with other elements such as chromium and manganese give the highest strength heat-treatable alloys through precipitation hardening.
- 8xxx: In this series, Al-Li alloys show a high Young's modulus and precipitation hardening. Use of the light lithium element leads to alloys possessing a desired low density, mainly for aeronautics applications.

ii. Heat treatment (heat-treatable AA)

In order to obtain the desired properties out of a specific alloy, heat treatment plays a considerable role on the AA's microstructure and hence on its final properties. The American National Standard ANSI H 35.1 specifies the temper designation system³⁶, consisting in adding to an alloy designation "Txx", with xx between 1 and 10. Aerospace aluminum heat-treatable alloys usually endure one of the thermal processes recorded in Table I. 4. Natural ageing is carried out at room temperature after

quenching while artificial ageing consists in heating the alloy in precise conditions (temperature and time) to reach stability.

Table I. 4: Heat treatments used in aerospace for Aluminum alloys³⁶

Temper designation	Solution heat treated	Cold worked	Ageing	Example	Ref
T3	Yes	Yes	Naturally	2024-T3	37-40
T4	Yes	No	Naturally	2024-T4	41
T6	Yes	No	Artificially	2014-T6,	41
				7075-T6	42
				6061-T6	43
T7	Yes	No	Artificially overaged*	7075-T7	44
T8	Yes	Yes	Artificially	2139-T8	45

* Overageing leads to better corrosion resistance despite lower strength alloys.

iii. AA2024-T3

Amongst all the available alloys, AA2024 is widely used, but its purification and fabrication are costly and are hardly affordable for other fields than aerospace. Its composition limits as defined by the Aluminum Association are recorded in Table I. 5.

Thanks to its high ductility, fatigue crack propagation resistance and fracture toughness, the T3-tempered version of AA2024 have been one (if not the most) popular for decades and shows good properties due to lack of coarse grain boundary phases and absence of precipitate-free zones.

Table I. 5: Chemical composition limits (in wt.%)⁴⁶

N°	Cu	Mg	Si	Fe	Mn	Zn	Ti	Cr	Others	
									Each	Total
2024	3.8 - 4.9	1.2 - 1.8	0.50	0.50	0.3 - 0.9	0.25	0.15	0.10	0.05	0.15

Due to the high content of copper in the 2xxx series AA, they are particularly sensitive to corrosion. Therefore, despite an extensive industrial use, a lot of effort is accorded to the development of protective solutions.

AA2024 possesses a complicated microstructure composed of several phases with different compositions. This was, for instance, evidenced by Boag *et al.*⁴⁸ who used EDS to determine the composition of AA2024-T3's various phases, as reproduced in Figure I. 2. Each color of the figure represents a different composition. Moreover, as highlighted by Hughes and colleagues⁴⁷,

improvements in AA2024-T3 purification led to changes in composition while comparing old and recent studies.

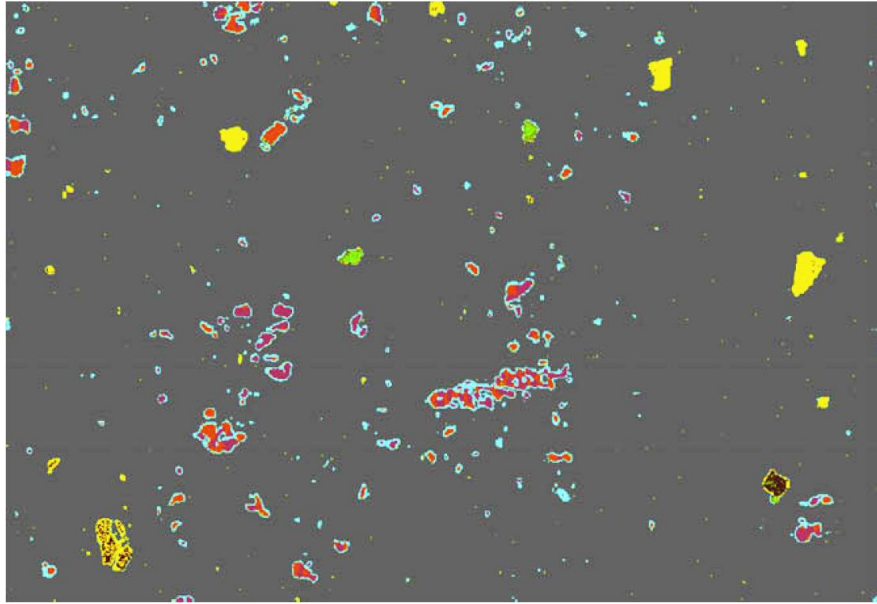


Figure I. 2: Complexity of AA2024-T3 microstructure, reproduced from ⁴⁸. Each color represents a different phase. S- θ - and α -phase are mauve, orange and yellow respectively

We can however easily distinguish three main compositions with different corrosion behaviors for AA2024-T3 intermetallic (IM) particles: Al_2CuMg (S-phase), Al_2Cu (θ -phase) and Al-Cu-Fe-Mn-(Si) (α -phase)⁴⁸⁻⁵¹. The exact composition of the coarse intermetallics is variable⁵². It is reported in literature that the S-phase intermetallics are mainly responsible for the AA's strength⁵³. These IM particles are all the more important that they are very numerous. Boag and coworkers⁴⁸ for instance estimated 271 000 particles. cm^{-2} covering 2.83% of the total surface area. Luo, in his PhD thesis, studied their relative importance and determined that S-, θ - and α -phase were accounting for 48.72%, 15.38% and 35.90% of the IM particles number respectively⁵¹. Concerning their size, S and θ -phase IMs are round particles that are found as either single particles or clusters, while the α -phase IMs are bigger with an angular shape.

I.1.2. Corrosion of materials

I.1.2.1. Corrosion

Corrosion is a natural phenomenon concerning most of the metals in an oxidizing environment, such as air, and leading to their degradation. This degradation, resulting from the physicochemical, and mainly electrochemical, interactions of the metal with its environment, can be rapid and severe depending on the metal's conditions of use. It is worsened by several factors (temperature, presence of aggressive species, mechanical stress, medium's conductivity...). It is important to keep in mind that several forms of corrosion exist (uniform, pitting, crevice, intergranular, filiform, stress corrosion cracking, fatigue...) and occur depending on the metallic substrate's nature and

environment^{54,55}. During corrosion processes, two types of reactions occur at the metal's surface. While dissolution of the metal occurs at the anodic sites, generating electrons in the metal and releasing metallic ions in the surrounding electrolyte, other reactions guarantee the electroneutrality on cathodic sites. These reduction reactions are in general mainly due to oxygen reduction but can also be due to hydrogen or metal ions reduction (and eventually redeposition).

These reactions have been described and studied accurately, in general and for specific metals, for decades^{5,6,54-58}. Corrosion thus corresponds to a stationary state between reactions occurring at cathodic and anodic sites and requires a charge transfer as well as an ionic path between both areas to initiate and continue. This is naturally achieved for immersed metals but in atmospheric conditions specific climatic parameters linked to temperature and relative humidity are involved. Although the forms of corrosion and involved mechanisms are numerous, we will focus and only deal with corrosion initiation for the targeted materials: structural steel and AA2024-T3.

I.1.2.2. Structural steel

Uniform corrosion is the major degradation mode observed in atmospheric or immersion conditions for structural steels. It is quite easily identifiable and is thus not considered as dangerous. When a protective insulating coating is applied on a steel structure, appearance of a defect in the coating triggers corrosion and it is admitted that the total surface is evenly attacked⁵⁸. Therefore, development of iron oxides as corrosion products is seen on the whole exposed surface area. In the case of steel, the anodic and cathodic occurring reactions are the iron metal dissolution and oxygen reduction respectively^{58,59}.

I.1.2.3. AA2024-T3 aluminum alloy

Although pure aluminum is naturally passivable the complexity of their structure makes AAs, and especially AA2024-T3, susceptible to pitting corrosion. This is due to differences in the reactivity of each phase. In presence of chloride anions and during the pitting corrosion, a selective dissolution of less noble elements within the S-phase IMs occurs. Boag *et al.*^{47,60} attribute this dealloying of Al₂CuMg particles to their lower OCP versus the aluminum solid solution. That is corroborated by local measurements they performed on macroscopic IM compounds, as shown in Table I. 6. Dealloying leads to copper-enriched porous particles as studied and accurately described by Hashimoto and coworkers⁴⁹. The proposed mechanism is moreover assessed by the observation of aluminum oxide formed on top of dealloyed IM particles. In a second step, Cu-enriched particles switch from an anodic to a cathodic behavior due to their ennoblement leading to the dissolution of the surrounding less noble aluminum matrix. This manifests through the formation of trenches around the S-phase remnants as evidenced in Figure I. 3, reproduced from Boag and col⁶⁰.

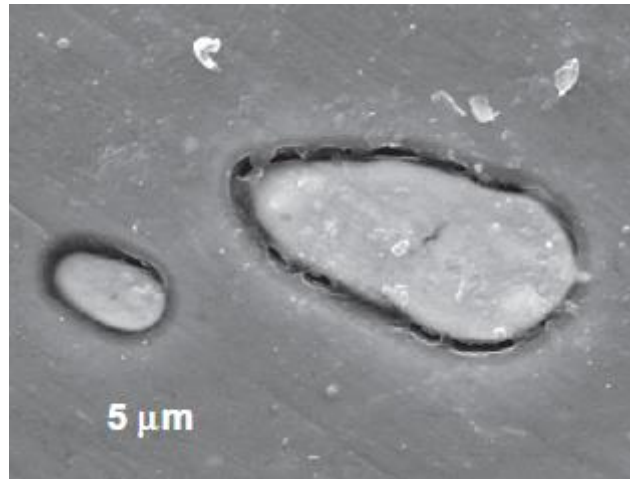


Figure I. 3: Trenching around S-phase particles in AA2024-T3 after 15min exposure to 0.1M NaCl, reproduced from ⁶⁰

θ -phase, when reported, has a nobler potential than the aluminum matrix, what provokes the same trenching phenomenon. Dealloying of the θ -phase particles has also been evidenced when S-phases particles are embedded in the θ -phase IM⁵⁰. This leads to formation of porous copper-enriched particles and corrosion initiation around them. In the following stages of corrosion on AA2024-T3, other types of IM particles are subjected to trenching⁶⁰.

In the case of AA2024-T3, many surface reactions then occur and pitting corrosion is observed. Due to this local characteristic, the corrosion of AA2024-T3 is therefore highly dependent on the metallic surface preparation. Grinding or polishing for example leads to important differences in the surface microstructure⁴⁷. A great care has then to be payed to these treatments.

Table I. 6: OCPs for various intermetallic compositions in 0.1M NaCl, reproduced from ⁶¹

Compounds	OCP (mV vs SCE)
Al ₂ CuMg	-830
Al ₇ cu ₂ Fe	-640
Al ₆ (Fe _{0.5} ,Mn _{0.5})	-609
AA2024-T3	-555
Al ₂ Cu	-484
Al ₃ Fe	-406

To summarize, the two metallic alloys we will study, aside from being used for different applications, have a very different behavior in corrosive environments. This implies probable variation in the involved protection mechanisms.

I.1.3. Actual corrosion protection for aerospace

When it comes to prevent corrosion, various strategies can be set up trying to hinder electronic and ionic exchanges or to displace them. One of the most applied technology used in industries since the 1930's is cathodic protection that consists in stopping the electron leak from the anodic sites to protect. This is achieved either by imposing a current in order to change the natural anode into a cathode (impressed current cathodic protection), or using a sacrificial anode whose oxidation is thermodynamically favored (galvanic cathodic protection). However, classic cathodic protection requires the protected piece to be surrounded by an electrolyte so this is mainly used in soil or marine environment.

Another strategy is then preferred in the aerospace industry and consists in stopping surface reactions (dissolution, adsorption..), isolating the metallic surface from the corrosive environment. This is achieved applying a coating on top of the metal to protect, and/or using inhibitors, chemicals able to slow down reactions occurring either at one of the two or at both reacting areas. Inhibitors are used for the NC2M, and will thus be properly detailed later. Concerning protective coatings, many are currently developed⁶² or already in use. They can be either metallic (chromium, nickel, zinc...), inorganic (sol-gel, conversion or anodizing) or organic (paints) and could be combined with inhibitors. Their role is to protect metallic structures thanks to an enhanced barrier properties, which means they need to be free of open defects. Moreover, the choice of the suitable coating depends on the nature of the substrate as well as on the operating conditions^{5,6,55-58,63,64}. Due to the wide range of usable coatings and existing pretreatments, AAs are naturally the most used and described substrates⁶⁵.

I.1.3.1. Metallic protective coatings⁶⁶

Various application techniques (thermal or cold spray, electrodeposition, chemical or mechanical bonding) and metal nature are used. In the aerospace industry, galvanization and electroplating are the most used.

A zinc-based layer, generally deposited by hot dip galvanizing can protect steel parts. This strategy is another type of galvanic protection since zinc is less noble than iron. A damage in the outer zinc-rich layer therefore leads to preferential corrosion of the zinc, thus preserving the steel substrate's integrity.

Formation of a metallic coating can also be done by electroplating, forming an electrical circuit in which the metal to protect is the cathode. This enables the deposition of chrome or nickel for example for corrosion protection, or even zinc and its alloys (what prevents the heating induced by hot-dip galvanization). Steel or aluminum can be protected by this process, forming zinc-nickel sacrificial coatings or cadmium coatings (although cadmium's toxicity makes its use restricted).

Combination of metallic coatings with other technologies such as incorporation of inhibitors could also be a way to improve metallic coatings. This was proposed for example by Presuel-Moreno and col.⁶⁷. Using an aluminum-cobalt-cerium coating, they evidenced corrosion protection brought by a sacrificial barrier coating loaded with soluble inhibitors.

I.1.3.2. Anodizing and Conversion coatings^{68,69}

Probably the most used in industries and especially in aerospace, a conversion coating is made by oxidation of a metal and formation of an oxide layer whose composition depends on the bath and acid used.

The most usual way to form a conversion coating is by anodization, meaning that the formation of the oxide is governed by an applied potential in order to control the metal dissolution. Potential values range from 0 to 200 V, keeping a low amperage and depending on the bath composition, temperature and desired thickness. Anodization leads to the formation of a non-conductive coating composed of an inner dense and compact layer and an outer thicker porous layer. Further immersion treatments allow to functionalize the porous structure, incorporating corrosion inhibitors, followed by a sealing step in boiled water for instance⁷⁰. Anodized layers therefore improve corrosion resistance as well as adhesion of a top layer. Although being the most efficient ones, baths containing chromates are now restricted in the aerospace industry because of chromates toxicity and should soon be banished for good. Therefore, many alternatives have been investigated. The main anodization techniques found today in the aerospace field are:

- Chromic Acid anodizing (CAA): a thin coating (2 to 5 μm^{68}) with enhanced corrosion protection but to be replaced;
- Sulfuric Acid anodizing (SAA): a transparent coating with incorporated sulfates;
- Phosphoric acid anodizing (PAA): an alternative to CAA;
- Sulpho-tartaric anodizing (STAA): an alternative to CAA developed by Airbus;
- Boric-sulfuric acid anodizing (BSAA): an alternative to CAA developed by Boeing, but limited by the high toxicity of boric acid.

Anodizing however possesses limitations since it is only usable for passivable metals such as aluminum, magnesium or titanium alloys, and leads to a decrease in the metal thickness and so in the substrate's fatigue limit.

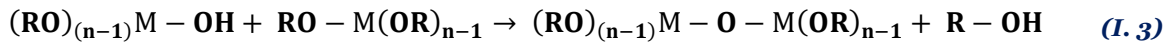
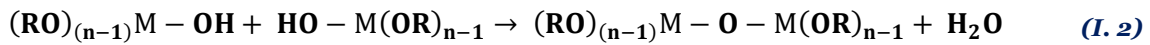
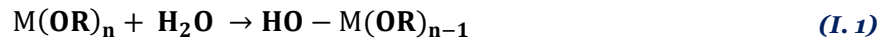
For both passivable and non-passivable metallic materials, a chemical conversion coating can be applied, soaking the substrate to protect in the appropriate solution in order to form chromate or phosphate coatings. These conversion coatings are very thin compared to anodizing layers, with thicknesses below 0.5 μm^{71} .

Chromate conversion coatings are formed on zinc, magnesium or aluminum alloys, potentially on top of an anodized layer in order to bring corrosion resistance. Thanks to their efficiency, chromate

conversion coatings based on hexavalent chromium have been widely used but are now banned because of their toxicity. However, some domains such as aerospace got a temporary dispensation. Potential alternatives to hexavalent chromium include the use of trivalent chromium that does not present the same toxicity⁷². Phosphate conversion coatings are also used for non-passivable metals such as carbon steel. By immersing the steel part in a phosphoric acidic solution, an insoluble complex layer is formed between ferrous and phosphate ions.

I.1.3.3. Sol-gel coatings

Sol-gel is a coating technology that recently aroused extreme interest since it allows to form resistant thin-films through a non-toxic mild process that could easily be set up at an industrial scale. Formation of a sol-gel layer starts with a colloidal suspension of a metal or silicon alkoxide precursor that is deposited on top of the metal to protect. With no heating required (but sometimes used to tune the coating morphology), the precursor then undergoes hydrolysis followed by polycondensation, as shown in equation (I. 1) to (I. 3). Hydrolysis can be partial or total depending on the quantity of water, potential catalyst etc... This leads to the formation of an inorganic or hybrid organic-inorganic polymer network.



Besides their green process, sol-gels are also perfectly adapted to aluminum alloys since hydroxyl groups, present on the AA's surface, can bond with the sol-gel layer, hence increasing the coating's adhesion. Moreover, hydrophobicity of a sol-gel layer makes it very useful for corrosion protection. If the principle of formation is quite simple, the variety of available and developed precursors and processes enables a staggering number of shapes from film to fibers, and applications, especially in aerospace. Concerning their nature, silica is the most used specie but aluminum, zirconia, cerium or titanium alkoxides are also reported⁷³⁻⁷⁵.

For the NC2M, it is very interesting to see the similarity between these reactions and the capsules formation that we will discuss later on. Moreover, despite being already in application (and source of many patents⁷⁶⁻⁷⁸), it seems that sol-gels did not reach their maximal potential yet and thus are currently the center of many research projects for corrosion protection in aerospace.

I.1.3.4. Organic coatings

Organic coatings are widely used, sometimes in combination with previously discussed coating technologies since a pretreatment of the metal highly enhances the primer's adhesion. As paint and

varnishes, thermosetting polymer coatings used in the aerospace are generally multi-layer systems in which have to be distinguished the primer, in contact with the metallic substrate, and top coats that are applied on top. Topcoats are used in order to bring an esthetic finishing, and protection from external perturbations (shocks, UV, thermal protection, impermeability...) ^{79,80}, the most used being polyurethanes.

The role of the primer, on the other hand, is to bring corrosion resistance and a good adhesion of the topcoat. Commercially available primers are mainly bi-component epoxies ^{81,82} and polyurethanes, and have been loaded for a long time with chromates (*e.g.* strontium chromate) as corrosion inhibitors. They are therefore undergoing an important evolution, what led to the design of new coatings, bringing great barrier properties and an efficient active protection against corrosion. Primers are mainly applied by spraying and common thicknesses in aerospace applications are around 25 μm ⁸³.

NC2M in this context

Aerospace applications require high-performance materials with different properties, from metal to composites. Amongst all the metallic alloys used, aluminum alloys and structural steel are of high interest for ArianeGroup, explaining why our study will focus on them and more specifically on AA2024-T3 and structural steel.

Concerning chromate-free protection, first alternatives have been based on optimization of new conversion coatings and more sophisticated techniques ⁸⁴. An alternative pathway however focuses on sol-gel layers and development of multifunctional organic coatings, the so-called smart coatings. The NC2M completely falls under this category since our project tends to optimize an organic coating by bringing new functionalities to an existing organic matrix. We therefore need to accurately define both corrosion inhibition and corrosion monitoring, and to understand the existing strategies.

I.2. Inhibition of corrosion processes

I.2.1. Inhibition or self-healing?

When speaking about corrosion protection, especially using smart coatings, two close phenomena have to be distinguished: inhibition and self-healing. While IUPAC defines an inhibitor as “a substance that diminishes the rate of a chemical reaction”⁸⁵, finding a proper definition of self-healing is quite difficult. In order to be clear in this work, we speak of inhibition when a compound is able to protect a metallic substrate from corrosion (whatever its mode of action), while self-healing describes a coating able to recover, totally or partially from a damage. Concerning corrosion protection, self-healing plays a role isolating the metallic substrates from the aggressive environment but does not involve a reaction with the corrosion products or corrosive species. This implies that self-healing, in our sense, does not depend on the substrate’s nature, and that potentially in the absence of substrate the physical self-healing reaction would occur as for supramolecular assemblies in the case of rubbers⁸⁶. Figure I. 4 shows this difference between self-healing for smart coatings: while self-healing reactions are triggered as soon as the coating is damaged and whatever the substrate, inhibition requires the inhibiting compound to be adapted to the metallic substrate to protect. The work carried out at NASA by Calle *et al.* also considers this difference since they plan to use three different agents for inhibition, detection and self-healing⁸⁷.

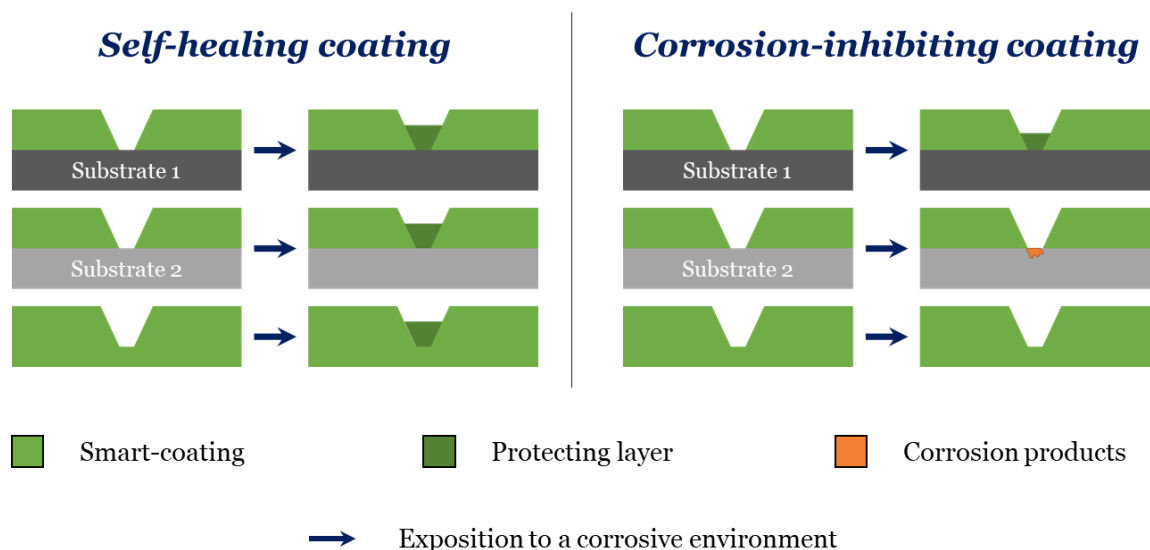


Figure I. 4: Schematic representation of self-healing and inhibition process for a smart coating

Three approaches exist in order to confer self-healing properties to a corrosion-protective coating: using two compounds, a monomer and a catalyst or two monomers that will react in a damage, using a single compound, reacting with either the host matrix, or naturally present elements (moisture, oxygen), or directly bringing functionality to the polymeric matrix. The first fully autonomic self-healing material was described by White *et al.*⁸⁸ in 2001. They encapsulated dicyclopentadiene (DCPD) in urea-formaldehyde microcapsules and incorporated Grubbs’ catalyst in the epoxy

matrix⁸⁸. When a crack is formed and propagates, it likely breaks the microcapsules, thus releasing the healing agent that will fill the entire defect. When the liquid monomer gets in contact with the catalyst dispersed in the matrix, the Ring-Opening Metathesis Polymerization (ROMP) is triggered and allows the composite coating to recover up to 75% of its initial toughness. Use of a living polymerization method enables several healings at the same location. Since this first step in self-healing coatings, several works were published on similar systems^{89,90}, and with several other reactions. We can cite as examples reactions between a liquid epoxy and a hardener⁹¹, a thiol with an isocyanate⁹² or a siloxane and a tin-based catalyst⁹³. The main requirements for this mechanism are the maintained activity of the reactants and their diffusivity into a defect. It is however clear that these systems have a major drawback since use of two components imply that both of them have to be present in a defect or put in contact in order to initiate the reaction.

That is why many studies tend to use only one self-healing agent. The main principle remains the same, except that when delivered into the defect, the healing agent reacts with elements naturally present in the coating. Efficient results have been observed by encapsulating natural linseed or tung oil, that are triglycerides and are oxidized when oxygen is present, leading to a solid layer⁹⁴⁻⁹⁶. Despite their toxicity, diisocyanates have been thoroughly studied, since they are molecules able to form polyurea when reacting with water. Numerous studies use for example isophorone diisocyanate (IPDI)⁹⁷⁻⁹⁹, hexamethylenediisocyanate (HDI)¹⁰⁰⁻¹⁰² or toluene diisocyanate (TDI)¹⁰³ for corrosion protection purposes. A third single-component system consists in using the host matrix on defect sites as a reactant. A very interesting study carried out by Meng *et al.*¹⁰⁴ is a perfect example since they trigger a release of glycidyl methacrylate (GMA), which is a liquid able to diffuse in the used epoxy matrix. This way, GMA provokes a swelling of the matrix, reducing the defect size, and allowing hydrogen and covalent bonding between itself and the two sides of the defect. This is obviously only working for small defects.

A third method consists in functionalizing the polymeric coating itself. This class is quite different from the other two since it usually requires an action from the user such as heating in order to force the polymer to reform bonds^{105,106}.

I.2.2. Corrosion inhibitors and their mechanisms

Inhibition, unlike self-healing, considers the interactions between the inhibiting compound and a metallic substrate. Various molecules can fulfill this role and new inhibitors are continuously developed. They can be classified using different criteria (organic or inorganic, natural or synthetic, passivating or precipitating...). We decided to sort them depending on the corrosion area and process they are affecting, as it could be determinant depending on the capsules used. Inhibitors reducing the rate of cathodic or anodic reactions are called cathodic or anodic inhibitors respectively¹⁰⁷. A third kind of corrosion inhibitors is made of molecules able to act on both cathodic and anodic reactions. They are therefore called mixed-type inhibitors. For all of them, inhibition

efficiency highly depends on the composition of the substrate to protect since intermetallic composition for example plays a role⁴². Therefore, this part only provides information concerning general mechanisms.

I.2.2.1. Cathodic inhibitors

As explained in section I.1.1., several reactions occur at cathodic sites. This type of inhibitors shifts the corrosion potential of the metal toward less noble values by hindering the electron exchange. The main mode of action observed is due to the properties of the product formed by the reaction between the inhibitor and hydroxide ions released at the cathodic site (oxygen reduction): the inhibitor precipitates in alkaline conditions, what leads to the formation of an isolating layer on top of the metal. The precipitate is then a physical barrier, hindering the dioxygen diffusion towards the metal surface.

Amongst cathodic inhibitors, one of the most used and described for steel and iron is zinc ion (in the form of chloride or sulfate salts) since it adsorbs on negative cathodic sites in acidic pH¹⁰⁸, and forms an insoluble ZnO or Zn(OH)₂ layer in presence of hydroxides produced by reduction reactions^{109,110}. Cerium III and cobalt ions can also precipitate and therefore act as cathodic inhibitors, as seen for AA2024-T3¹¹¹. It is important to note that the inhibiting efficiency depends on the salt used. For example Ce^{III} precipitates on cathodic sites and have shown great potential¹¹², whereas Ce^{IV} compounds provide poor inhibition when used alone^{113,114}.

Recently, intensive research focuses on other rare earth salts as cathodic inhibitors. For example, lanthanum has been proved to be an efficient cathodic inhibitor forming lanthanum oxide and/or hydroxide (La₂O₃ / La(OH)₃) precipitate at the cathodic sites¹¹⁵. Praseodymium and neodymium have also showed interesting properties, even if below cerium efficiency¹¹⁶.

Another type of cathodic inhibitor acts by what is called cathodic poisoning, meaning they hinder the protons reduction. This is the mode of action of antimony, bismuth or arsenic-based compounds¹¹⁷. However, since they are mostly very toxic compounds, less attention is accorded to them.

The main advantage of cathodic inhibitor is that even at low concentration they are able to reduce the cathodic surface area and then reduce the cathodic reactions rate, thus reducing the corrosion rate¹¹¹. They are however less efficient than anodic inhibitors and usually employed in combination with them.

I.2.2.2. Anodic inhibitors

Anodic protection occurs when the inhibitor is able to passivate the metal surface for example by reacting with the metallic ions formed. The anodic sites' surface will then decrease until the corrosion is stopped, meaning that a sufficient quantity of inhibitor has been released. An anodic

shift in the metal potential can be measured. Oxidizing and non-oxidizing anionic inhibitors are sometimes distinguished, the first being able to protect a metal in the absence of oxygen while the second kind requires oxygen⁵⁸.

Amongst oxidizing compounds, chromates are the most well-known since their efficiency has no match and they still serve as a reference. Hexavalent and trivalent compounds can be used, Cr^{VI} being more efficient and toxic at the same time¹¹⁸. Even today, chromates are still studied since their mechanisms are not fully understood. It is however commonly admitted that their incomparable properties are due to reduction of Cr^{VI} to Cr^{III}, forming a protective layer, and to a very high mobility. Formation of Al^{III}-Cr^{III} mixed oxides has also been reported^{58,119-122}. Nitrite (usually used as sodium nitrite NaNO₂) is a similar passivating inhibitor working in the absence of oxygen, despite a lower inhibition efficiency^{5,122-124}. Although being used in food preservation, nitrites is now suspected to be a carcinogenic compound.

Non-oxidizing passivating inhibitors are the subjects of an increasing number of studies, because of their non-toxic characteristic. Amongst them the most used are molybdate anion MoO₄²⁻, which has been proved to inhibit corrosion on AA2024 and mild steel^{125,126}, but also tungstate (which has the same structure as molybdate)¹²⁷⁻¹²⁹, silicate^{127,130} and phosphate^{122,123,131}. If their modes of action are still subject to discussions, it seems that molybdate inhibiting properties are due to redox reactions. First reduced and adsorbed on top of metallic substrates, molybdate forms an insoluble physical barrier, and competes with oxygen reduction reactions¹³². According to a mechanism proposed by Lopez-Garrity *et al.*¹²⁶, molybdate is then oxidized in the presence of oxygen, forming molybdenum oxides and leading to a local pH increase. This promotes the polymerization of molybdates species forming a protective layer. A different mechanism is evidenced for silicate that forms aluminosilicate protective layers on anodic sites. It has also been shown that this layer can be quite porous and hence less effective in alkaline media¹³⁰.

Contrary to cathodic inhibitors, a risk with this kind of compounds is that a too low concentration will lead to higher anodic current densities. Indeed, the anodic surface being only partially covered, it favors pitting corrosion, harder to detect and to heal than uniform corrosion. For this reason, a critical concentration has to be reached and maintained to totally block the corrosion process. Below this concentration, presence of an anodic inhibitor can exacerbate corrosion activity. To prevent this, anodic inhibitors are often combined with cathodic ones, or replaced by mixed inhibitors.

I.2.2.3. Mixed-type inhibitor

These compounds are mainly organic molecules and can be either natural or synthetic, enabling an almost infinite number of possibilities. Mixed-type inhibitors protect a substrate by adsorbing on the whole exposed surface, by chemisorption or physisorption, meaning the metal's nature is more or less importance. They hence form a protective layer, isolating the metal from the aggressive environment and hindering oxygen diffusion and reduction. Organic inhibitors are molecules

containing heteroatoms, mainly nitrogen (N), oxygen (O), sulfur (S) or phosphorus (P), and/or conjugated systems that enhance adsorption¹³³. As for anodic inhibitors, a certain quantity of an organic inhibitor has to be present at the metal / electrolyte interface in order to confer protection. Below this threshold value, worsening effect could occur.

An exhaustive list cannot be made. It is however very interesting to notice that many natural molecules can fulfill the mentioned characteristic and therefore act as inhibitors. Literature offers lots of studies concerning specific natural molecules and especially plant extracts¹³⁴⁻¹³⁸. Amongst them chitosan shows very promising result for steel protection and potentially aluminium¹³⁹⁻¹⁴¹. Chitosan is a polysaccharide obtained from the exoskeleton of crustaceans and had to be mentioned since its encapsulation properties are also intensively studied.

Amongst other organic inhibitors that can be found in the literature are various amines^{142,143}, thiols¹⁴⁴ and heterocycles^{133,144} such as pyridine and its derivative (8-hydroxyquinoline¹⁴⁵⁻¹⁴⁸...), benzotriazole and its derivatives, and benzothiazole and its derivatives such as 2-mercaptobenzothiazole (MBT) that may be the most used for aluminum alloys^{147,149-154}.

Another approach, instead of using adsorbing molecules, is to form mixed-type inhibitors by adding an organic moiety to precipitating elements and therefore synthesize and “artificial” mixed-type inhibitor. If this category does not constitute a major part of current research, very promising results have been obtained for example with cerium dibutylphosphate¹¹⁵ and lanthanum diphenylphosphate¹¹⁵. Optimization concerning the complexes solubility or integration in a protection system for example should however be carried out. The same system can be achieved using a cathodic inhibitor, such as zinc, combined to an anodic one, either inorganic *e.g.* vanadate¹⁵⁵ or organic¹⁵⁶.

Synergies can also be achieved using multiple corrosion inhibitors¹⁵⁷, and due to the wide variety of existing organic compounds, there is a high probability that chromates alternatives could be found this way. A very interesting recent study carried out by Giuliani and colleagues highlighted for example the synergistic effect of a chitosan film with BTA and MBT incorporated for the protection of copper alloys¹⁵⁸.

I.2.3. Corrosion protection for NC2M

The objective of NC2M project is to bring a solution to corrosion monitoring as well as protection. Therefore, our aim is to confer a high corrosion resistance to the coating without considering its mechanical properties or long term coating integrity in the first instance. In our concept, protection has to be achieved as long as it is needed for the user to detect the corrosion onset. This is why self-healing (as defined above) is not suitable. Moreover self-healing could be an issue for corrosion protection if corrosion is triggered between the metallic substrate and the healed layer. The user could then miss a critical situation. Although combination of self-healing and inhibition is also a

Chapter I - Bibliographic review

possibility, studied notably by Siva *et al.* with the use of linseed oil⁹⁵ together with MBT, we decided to focus on an inhibiting system.

For the choice of corrosion inhibitors, high importance criteria are the innocuousness of the inhibitor and a satisfying efficiency. However, in our system, the encapsulation efficiency remains the main criterion to keep in mind, as it will be discussed.

I.3. Corrosion detection and monitoring

If smart protective coatings present a real interest, hindering corrosion and eventually fixing the coating integrity, they also show limits since the effect is only temporary and depends on the healing agent or inhibitor available quantity. Moreover, inhibitors only slow down and do not stop corrosion as seen before, and are reacting and therefore consumed. A constant supply can be achieved in water systems for example, but in the case of coatings, adding more inhibitors means replacing the coating, partially or totally. The role of inhibition is then to save time once the coating fails to protect the substrate.

The idea of NC2M is to combine an efficient inhibition to corrosion monitoring in order to prevent this failure: the earlier the corrosion can be detected, the more easily the structure integrity is preserved. The NC2M coating objective is thus to enable an early detection of corrosion while controlling its development.

In this part, we will see what forms corrosion monitoring can take in order to design an optimal system. After a review of what industry already proposes, we will describe currently developed and promising technologies for corrosion detection and monitoring. As it will be shown, a common approach consists in evaluating the corrosion state of the metal by direct measurement of physical (and mostly electrical) properties. Another one relies on physical-chemical parameters indirectly linked to corrosion processes, that functional coatings tend to exploit. This second kind of techniques will naturally be described more thoroughly.

I.3.1. Methods currently used

For a long time, industries played on the facilities design and choice of employed materials to prevent corrosion. Service conditions severity are thus determined in order to choose the most adapted alloys. Ageing studies and corrosion rate measurements are then performed on representative coupons placed in similar atmospheres or *in situ*^{56,58,159}. Destructive techniques can then be performed in order to determine how impacted the structures are, such as potentiodynamic-galvanodynamic polarization or mass loss measurement. Although they give useful information on the alloy behavior in corrosive environments, long (and increasing) operational lifespans tend to impose a real-time surveillance for corrosion.

The first concerned industry was oil & gas, since it uses huge amounts of metals for pipelines for instance. They have hence naturally driven the major part of the available research about corrosion monitoring. However, most of the developed techniques require the metal to be placed in a conductive medium (water, soil...), and/or are designed and efficient for pipelines for example such as the field signature method^{159,160}. This particularities are not applicable for aerospace purposes¹⁶¹. Hence, although being perfectly designed for corrosion evaluation and monitoring, even in the case

of under-film corrosion and inhibition evaluation, electrochemical techniques can hardly been setup for our applications (despite being widely used at lab scale).

In many other industries, and especially in aerospace, no particular technique seems to be used as a standard, mainly because no technique is adapted to complex geometries and important structures yet. Common procedures consist in a routine visual inspection, regularly scheduled depending on the structure susceptibility to corrosion. For hardly accessible areas or when needed, borescopes or simple magnifying glasses can be used¹⁶². If a corrosion onset is suspected, then local techniques can eventually be set up for the analysis of smaller areas¹⁶³, although there is no systematically used technique.

Usable NDT can be organized in three categories that are direct or indirect monitoring, and use of coatings. Direct techniques consist in monitoring corrosion by direct measurement or evaluation of the occurring processes while indirect ones quantify a consequence of occurring corrosion.

I.3.2. Direct monitoring techniques

Direct monitoring techniques are in theory the most efficient ones since the very first stages of corrosion are detected, but in practice they imply the development of accurate detection devices and procedures. As we will see, most technologies are intrusive since they require direct access to the metallic substrate, what can barely be set up and hence will not be thoroughly detailed.

The simplest and most direct technique is obviously optical monitoring since corrosion is a surface phenomenon. Observation can therefore allow to confirm corrosion development, although only some types of corrosion are clearly visible and only after a certain time, seldom during the first stages. Optical monitoring moreover requires being able to observe the whole surface, what can be a problem when a coating is used for instance. In order to make optical assessment more accurate, techniques are also developed based on observable changes of the metal's surface, recorded using a camera. Degradation of the surface can then be quantified by image analysis^{164,165}. Enhancement of the optical detection can also be performed using revealing compounds such as liquid penetrant dies. Routine visual inspection, however, has some major drawbacks since it is a time-consuming and not very efficient operation. Moreover, inspection has to be regularly and thoroughly performed, and since some parts are not directly observable, moving or opening panels is often required. This could even lead to enhancing the exposition of the structures and have the opposite effect¹⁶⁶.

Most of the developed techniques generally require a probe or sensor to be placed directly in the corrosive environment, and therefore its use has to be thought from the construction to be placed in the metallic structure. This is why, NC2M aiming at developing a smart coating, these techniques only present a little interest. We can however cite electrochemical corrosion evaluation techniques such as electrical resistance¹⁶⁶⁻¹⁶⁸, linear polarization resistance^{169,170}, electrochemical noise

analysis^{171,172}, harmonic distortion analysis^{173,174} and obviously electrochemical impedance spectroscopy^{175,176}.

Other techniques are currently under investigations and can be used through coatings, but do not seem to be easily applicable to important structures and especially in aerospace. Interesting progress has nonetheless been made using acoustic emission^{177,178}, radiographic monitoring¹⁷⁹⁻¹⁸¹, electromagnetic testing and Eddy current¹⁸²⁻¹⁸⁴.

These techniques show accurate and efficient monitoring, and combination of several methods can easily be achieved¹⁸⁵. However, required access to the metal, impossibility to localize corrosion on the operating structure and impossibility to use on complex geometries are limitation that hinder the use of these techniques.

I.3.3. Indirect monitoring techniques

Indirect monitoring techniques are based on the detection of consequences of corrosion processes. In other words, they use stimuli related to corrosion processes, sometimes on the same principle as corrosion inhibitors.

Similar to direct monitoring, corrosion potential measurement is an intrusive technique that gives an insight on the activity of the metal surface but remains very inaccurate and therefore is not very useful when used alone^{59,170}. Oppositely, infrared thermography has recently shown promising results to detect alterations such as corrosion in a metallic structure and can be used on wide areas and for instance for aircraft monitoring¹⁸⁶. Yang *et al.*¹⁸⁷ even recently detected corrosion under a coating using thermography coupled with electromagnetic induction. Such systems need improvements to be industrially used but are promising.

Numerous indirect techniques adopt a different strategy and consist in monitoring the evolution of one of the corrosion products concentration. These techniques are more widely used in water cooling and processing systems. However, since the same philosophy could be adapted to smart coatings, it is interesting to cite hydrogen flux monitoring¹⁵⁹, dissolved oxygen concentration measurements, conductivity measurements or redox potential measurements¹⁸⁸ that can also be combined¹⁸⁹.

To these corrosion indicators have to be added pH, which is in itself a very easy and useful parameter to monitor. As seen before, cathodic and anodic sites indeed show important variations of pH with alkaline or acidic values on the cathodic or anodic sites respectively. The observed pH values are highly dependent on the considered metal or alloy. A local pH measurement at the metal's surface can therefore help to detect the corrosion's onsets and constitutes an important trend in research on corrosion monitoring. The most promising (and today studied) approach is to use a pH-sensitive compound in order to detect pH changes more easily. Amongst others, recent published studies

combine the use of coumarin and its derivatives, that are fluorescent molecules whose emission under UV radiation depends on the medium pH, with an adapted detection system. The corrosion's onset is therefore detected before corrosion products are visible^{190,191}. Since pH changes are related to the metal aggression, a logic tool is also coloring agents that would indeed be able to reveal corrosion activity. Uzundal and Ugult¹⁹² used phenolphthalein in a very interesting 2-cell system for corrosion detection under a coating. Forcing the reduction of hydrogen on the uncoated side and oxidation on the coated one, they induced the formation of protons (and so the local acidification of the electrolyte) in the defect, hence evidenced.

In the case of metallic structures placed in atmospheric conditions, however, these techniques seem to be hardly applicable since gases concentrations cannot be accurately determined and other measurements need an electrolyte to be performed. Moreover, most of them give information about the general corrosion degree but can hardly accurately locate defects. Then came the idea to combine the forementioned strategies with the use of protecting coatings.

I.3.4. Coating monitoring

The need for monitoring coatings comes from the mentioned issues concerning corrosion localization and potential need of an electrolyte to conduct measurements. Since most of the metal pieces used are protected by coatings, the idea is to confer a new functionality to the coating and so facilitate or enable corrosion detection and monitoring. Suitable systems are made of a host matrix in which a sensor is added and reacts upon corrosion. The developed systems can be classified in different ways depending on the sensor nature, the stimulus used or the response given. Physical trigger will be shortly presented through a few innovative techniques before focusing on pH-triggered detection that is the most studied system and probably the most promising one as well.

The approach sometimes used consists in enhancing the detection enabled by non-intrusive techniques by incorporating a physical sensor at the substrate/coating interface. In their work, Banks *et al.*¹⁹³ used a ferroelectric compounds mixed to a sol-gel slurry in order to embed it by covalent bonds with the substrate at the substrate/coating interface. These spray-on transducers are placed on strategical locations on the structure, and can send an ultrasonic signal when they receive a specific frequency stimulus. Analysis of the ultrasonic signal gives information on the substrate's state of degradation. This is a quite inexpensive system but that requires analysis methods. Another technology that can be embedded at the substrate/metal interface is Bragg Fiber Grating (BFG) that are kind of optical fibers highly sensitive to mechanical stress. Deng and colleagues^{194,195} deposited these fibers on top of steel before an epoxy coating is applied. Under-coating corrosion generates deformations that change the BFG properties. Sending an optical signal in the fiber, corrosion can then be detected. This requires however to have access to the BFG ends as well as signal processing. Most of all, such techniques need a specific deposition step and can hardly be set up on the entire surface to monitor.

A solution recently reported can be to modify the used matrix. In their studies, Dhole and colleagues^{196,197} directly functionalized an alkyd or acrylic paint with phenanthroline derivatives. Phenanthroline has the capacity to form red complexes with ferrous ions, what has been conferred to the modified resin applied on top of mild steel substrates. They hence showed that upon corrosion onset, oxidation of the steel leads to the appearance of red spots, whose number and intensity are related to corrosion progress. Such a coating is very efficient and, combined to visual investigation or optical monitoring system, could show great results. However modifying a resin implies a perfect knowledge of its composition and reactivity, so this has been achieved for specific model synthesized resins, what is very different from commercial filled resins. Modification would then require an important development adapted to every resin used, what seems complicated. Therefore, adding a compound that would not interact with the host matrix would lead to a more versatile technology.

Incorporation of the sensing compounds within the matrix is often achieved. Trinchi et al.¹⁹⁸, for instance, directly incorporated maghemite nanoparticles to an aerospace primer resin. Maghemite nanoparticles are magnetic. When placed in a corrosive environment, maghemite is transformed to another oxide and loses its ferromagnetic properties. The particles then show a variation in their magnetic properties depending on the corrosivity of the environment and can be used to detect corrosion or inhibitor depletion. Monitoring is performed using a coil and measuring the alternating current through the coil, what is easy to carry out. An improvement of the system would be to find a way to get fast analyzes of high surface areas but keeping a good spatial resolution.

The main idea to achieve this is to use an easily processed response from the coating. It is therefore naturally that the major part of studies currently carried out on the topic concerns compounds with a color change or a fluorescence emitted upon corrosion. A US patent has for example been filed in 2011, concerning a paint for the detection of corrosion combined with an adapted monitoring system, proving the economic interest and technological maturity of monitoring coatings¹⁹⁹. In recent literature, pH change or complexes with metallic ions are the main investigated stimuli.

In this field, a paper from 1999 by Zhang and Frankel²⁰⁰ serves as a reference. They added either a coloring agent (phenolphthalein or bromothymol blue) or a fluorescing indicator (7-hydroxycoumarin or coumarin) to an acrylic transparent paint. They then induced corrosion by immersion and observed color changes related to an increase of pH at the cathodic areas. The fundamental parameter for these system is their sensitivity, linked to the nature and concentration of the compound used. Use of pH indicators also makes this system suitable for various substrates. Other studies for instance present the use of molecules that become fluorescing when complexing with metallic ions, what makes it specific for a certain metal or seldom a few of them²⁰¹⁻²⁰⁴. An interesting fluorescing molecule is FD1, since it has two modes of action. Augustyniak *et al.*²⁰⁵ first used FD1 as a corrosion sensor for steel since it is able to form a complex with ferric ions, what enables early detection of steel anodic dissolution when incorporated in a commercially filled epoxy coating. Moreover, they showed in a second study²⁰⁶ that besides the complex formed, FD1 acidic

hydrolysis also triggers fluorescence and so enables the monitoring of cathodic reactions even on top of aluminum alloys. FD1 alone could then reveal both cathodic and anodic sites. Moreover, fluorescence has been detected in clear epoxy model coatings, but also in a commercial filled epoxy resin coated on top of AA2024-T3.

Due to its reliability, local pH variation is a frequently used and efficient parameter to assess the corrosion's onset. Color change and fluorescence are the most used response for a monitoring coating and have shown both a great interest and promising results. Addition of a selected molecule directly to an organic matrix is an easy way to obtain a monitoring coating. However, when using a commercial resin, many pigments and components can interfere and lead to deactivation of the active compound²⁰⁷ or decrease in the coating's barrier properties. Moreover, addition of the sensing molecule often requires its dissolution in an organic solvent (xylene and toluene for 8-HQ²⁰⁴ or toluene for FD1 for example²⁰⁶) that can provoke defects²⁰⁶. In order to prevent this, and protect both the sensing molecule and the host matrix, the most promising strategy is to encapsulate the active agent. Besides, if this is directly noticeable with colored agents, deactivation of the active agent could also occur with corrosion inhibitors²⁰⁸.

A viable monitoring system would then combine an efficient detection of the corrosion development, a potential assessment of the degree of corrosion (pitting can sometimes hide a wide damaged area) and an easy-to-perform analysis such as visual inspection. In order to achieve that, encapsulation of active agents has been proved to work and naturally constitutes the basis of the NC2M.

I.4. Encapsulation through a colloidal process and smart coating design

Encapsulation is widely studied and has applications in many fields such as the food industry, cosmetics, pharmaceuticals and materials science. Due to the different requirements in terms of size, function, compatibility etc... a staggering number of architectures exists and providing an exhaustive list is not useful and almost impossible. Therefore, we here deal with particles formed using colloids for two main reasons: it is a quite simple process that does not require an heavy equipment, and this kind of syntheses can be carried out at lab scale and transferred to industrial scale. Although they are sometimes considered as encapsulation techniques and reported in the literature for similar applications, hollow fibers^{209,210} and Layered Double Hydroxides^{149,211} (LDH) are beyond the scope of this literature review.

In order to be as clear as possible, the terms we use hereafter are based on a IUPAC recommendation from 2012²¹². This means that are called nanoparticles and microparticles particles whose size ranges from 1 to 100 nm and 0.1 to 100 μm respectively. When speaking about spherical particles, “capsules” designs hollow particles with a solid shell and an inner space whereas “spheres” mean there is no distinction between the inner and outer parts of the particle. The terms particles and containers are used without distinction.

Nature of the containers is naturally linked to their reactivity, release and applications, hence dissociating each parameter can be meaningless. In order to structure this part, we will first deal with the containers’ formations, *i.e.* the formation technique, how to achieve loading and the nature of the particle or shell, before looking at the release mechanisms that can be used. Since we want to use containers as reservoirs in a host matrix, we will then identify the similar coatings that exist in order to see how capsules or spheres are incorporated in a polymeric matrix and the consequences of this addition.

I.4.1. Colloids’ stability

Emulsions are formed when two immiscible liquids are mixed, forming two phases, the dispersed phase forming droplets dispersed in the continuous phase. The dispersed phase is made of the liquid with the lower volume fraction, while the droplets’ size is driven by the mixing parameters (stirring or sonication parameters, geometry of the vessel, temperature...), and composition of the medium. It is essential to control the formed emulsion since it defines the containers size and shape.

Would it be during the particle’s formation reaction or once the particles are formed, suspension collapse (agglomeration, aggregation...) has to be prevented. Stability has then to be ensured from the beginning of the synthesis until the containers incorporation in a matrix. This stability is usually achieved either by steric hindrance or by electrostatic repulsion between the containers. For

electrostatic repulsion, pH and ionic strength of the medium are key factors that have to be accurately controlled.

However, stabilization of an emulsion or suspension often requires the use of surfactants. Surfactants are amphiphilic molecule with a hydrophilic polar moiety and a hydrophobic non-polar one. For the emulsions' formation and stabilization, hydrophobicity leads to the adsorption of surfactants on the droplets' surfaces and prevent phase separation and coalescence. A surfactant then has to be soluble in the continuous phase, according to Bancroft's rule²¹³. For solid particles dispersion, surface charges make surfactant molecules electrostatically bond with the particles, increasing the steric hindrance between particles, hence avoiding agglomeration or aggregation.

A good criterion to choose a surfactant is its Hydrophilic Lipophilic Balance (HLB), as defined by Griffin²¹⁴ in 1949. The HLB is a value from 0 to 20 that can easily be calculated from the chemical structure of the surfactant molecule according to (1) and can help predicting the surfactant's behavior. In (1) $M_{\text{hydrophilic}}$ is the molecular weight of the hydrophilic groups in the molecule whilst $M_{\text{surfactant}}$ is the surfactant's molecular weight.

$$\text{HLB} = 20 \times \frac{M_{\text{hydrophilic}}}{M_{\text{surfactant}}} \quad (1)$$

It is then possible to distinguish surfactants with a HLB comprised between 4 and 6, oil soluble and able to form stable W/O emulsions, from those with a HLB between 8 and 16 that can form O/W emulsions²¹⁵. For example, two surfactants used for O/W emulsions are sodium dodecyl sulfate (SDS) and dodecyltrimethylammonium bromide (DTAB), which have HLBs of 8.3 and 9.0 respectively.

The surfactant is a very important component of a colloidal system since its concentration can act on the emulsion's (and then particles') size²¹⁶. A change in the surfactant's nature, number or concentration then leads to very different results²¹⁷. It is also generally admitted that most of the available surfactants are water soluble, what often makes the formation of a W/O emulsion more difficult^{218,219}. Moreover, getting particles as a suspension in an oil phase (organic solvent) can be a problem for several applications, including when adding the suspension in a paint formulation. In order to achieve this, the W/O emulsion is transferred in water after the formation of the particles is complete. However, this often requires the addition of another surfactant.

New surfactants are therefore more and more studied and developed. This includes the synthesis of polymeric surfactants (especially block-polymers), but also the use of natural molecules that possess emulsifying properties. Numerous molecules from bacteria for instance are currently used such as xanthan gum²²⁰ or further investigated. Rhamnolipids can be cited, although the low quantity produced makes them unaffordable for materials science uses for now²²¹.

A strategy to perfectly control an emulsion's size and stability can also be to use several surfactants. In this case, they can be dissolved in the continuous phase²²², or in both phases. Kakaroglou *et al.*¹²⁵ for instance formed a W/O emulsion with Span 80 as a lipophilic surfactant in toluene and Tween 80 as a hydrophilic surfactant.

If surfactants are often only adsorbed on the particles' surface, covalent bond can also be formed. Silica containers, for example, possess silanol groups and a negatively charged surface. Cationic surfactant are naturally used. However, using ammonium cationic surfactants, it has been proved that covalent –Si-O-N- bonds are formed²²³, what allows suspension stability when using an adapted surfactant chain. A last approach consists in using a surfactant that will stabilize an emulsion, and take part in the shell's formation reaction. Such molecules are sometimes referred to as “surfmers” since they act as both a surfactant and a monomer^{222,224}.

Whatever the system used, however, a colloidal system remains metastable and tends to collapse. Therefore, emulsions and suspension are only described as stable according to a certain time scale²²⁵. In our study, a system will be defined as “stable” as soon as the colloid's size is unchanged for enough time to allow its handling and incorporation in a host matrix, meaning days.

I.4.2. Particles formation and nature

Containers formed using colloids can be synthesized in many ways, using either specific chemicals or equipment. Two types of colloids are used for our purpose: emulsion (liq/liq) and suspension (sol/liq). Our aim not being to develop a specific technique such as microfluidic devices²²⁶ or membrane emulsification²²⁷, the considered suspensions are formed by mechanical or magnetic stirring or ultrasonication. We can distinguish two main kinds of reactions that are interfacial reactions and precipitation methods.

I.4.2.1. Interfacial reactions

i. Interfacial polymerization

Interfacial polymerization is one of the most used technologies and is based on the formation of either an Oil-in-Water (O/W) or a Water-in-Oil (W/O) emulsion. Then, for interfacial polymerization to occur, two monomers (or possibly 3 when a surfactant takes part in the polymerization reaction) are used according to Figure I. 5. The first monomer (in green) has to be soluble in the dispersed phase only, unlike the second one that is only soluble in the continuous phase. The only location where the monomers can react is then the surface of the dispersed droplets. Polymerization reaction can sometimes be triggered by temperature or acid/ base catalysis.

Interfacial polymerization leads to the formation of capsules whose reactivity depends on the shell's nature. Composition of the two phases can also act on the shell surface groups. Encapsulation of

molecules is achieved by dissolving it in the dispersed phase prior to polymerization, or by soaking in the case of porous shells.

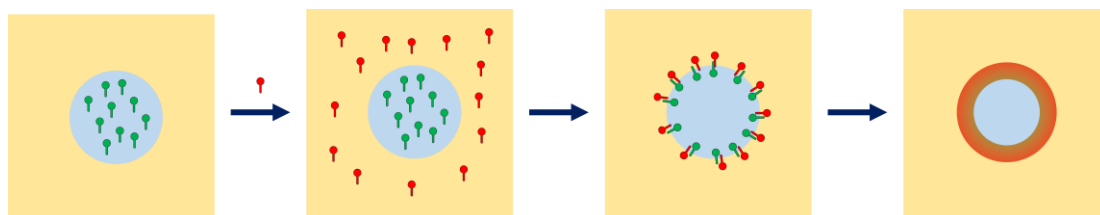


Figure I. 5: Schematic representation of interfacial polymerization

In materials science, interfacial polymerization is often used to form polyurethane (PU) and polyurea (PUa) capsules. Many studies are focused on the encapsulation of self-healing or corrosion protecting agents from an O/W emulsion with a diisocyanate (*e.g.* isophorone diisocyanate (IPDI) or toluene diisocyanate (TDI)) as the hydrophobic monomer and a diamine as the hydrophilic one (such as diethylenetriamine (DETA) or triethylenetetramine (TETA)). In this case, the polycondensation leads to polyurea spherical microcapsules^{218,228,229}. Polyurethane microcapsules can also be obtained using a diol instead of a diamine^{102,230}. These reactions are highly favorable and usually do not need any energy but heating is sometimes reported in order to modify the shell's thickness for example²²⁸.

W/O emulsions, despite being sometimes harder to obtain, have been successfully employed to form polyurethane, polyurea or polythiourea shells. In a very complete study, Crespy *et al.*²³¹ tried several surfactants and monomers in order to form such capsules. If the final dispersion can be unstable, stable capsules have been successfully synthesized. An interesting approach Kakaroglou¹²⁵ recently described consists in using the water from the dispersed phase as a monomer. For this, a diisocyanate is dissolved in the continuous phase and polymerization is triggered by heating the medium to 63°C.

Polyaniline (PANI) is a conductive polymer that is also studied for its encapsulation properties²³²⁻²³⁴. The synthesis of PANI capsules is based on W/O interfacial polymerization as well. The aniline monomer is dissolved in the dispersed oil phase, while a slight difference with other interfacial polymerizations is that the second reactant is an oxidizing compound (*e.g.* a persulfate)²³⁵.

A variant of interfacial polymerization is interfacial complexation. The only change is that no reaction occurs so there is no covalent bond but only electrostatic interactions between the two components that are polyelectrolytes. An example is presented by Plawecka *et al.*¹⁵², who encapsulated MBT in an oil phase using an anionic oil soluble surfactant, namely docusate sodium salt (AOT), and a water-soluble polycations, Poly(diallyldimethylammonium chloride) (pDADMAC).

Concerning the size of these polymeric containers, the influence of the surfactant's nature and concentration have been evidenced, as well as stirring mode and speed. Using sonication, Crespy *et al.*'s²³¹ experiments led to PU, PUa and PTUa particles from 200 to 400 nm, while changing the stirring rate, Huang *et al.*^{102,230} obtained PU microcapsules ranging from 5 to 500 μm . Other studies also reported the formation of microcapsules obtained by magnetic stirring whose size are between 10¹²⁵ and 100 μm ²²⁸. For PANI capsules, reported size are around 500 to 1000 nm^{232,233}. Figure I. 6 is an illustration of the differences in sizes and polydispersity that can be obtained with interfacial polymerization processes. Figure I.6a presents a very polydisperse suspension of PUa capsules while I.6c represent monodisperse PANI particles. Both are in the micron range while I.6b is a picture of ca. 50 - 130 μm polymeric capsules.

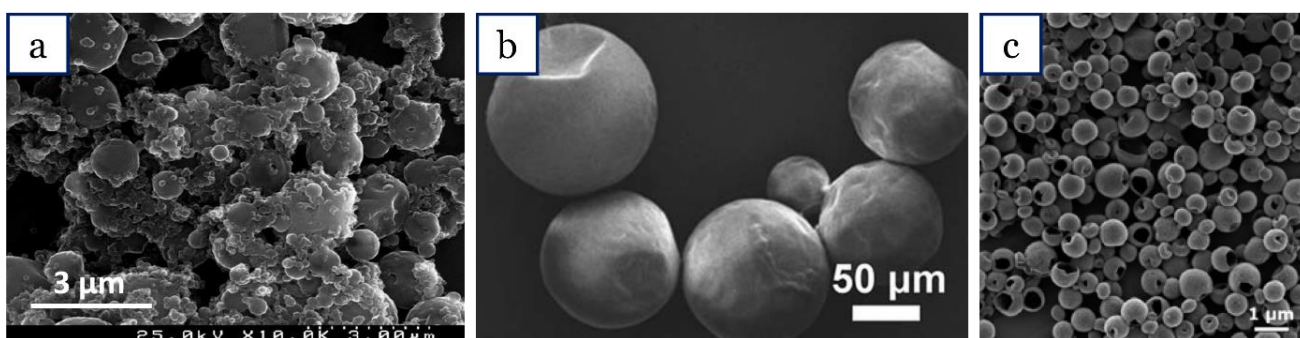


Figure I. 6: Example of SEM observations of (a) polyurea¹⁵¹, (b) melamino-formaldehyde⁹⁸ and (c) polyaniline/3-nitrosamine²³³ capsules formed through interfacial polymerization processes

Various conditions and compositions can therefore enable interfacial polymerization. Relevant examples are reported in Table I. 7. Depending on the emulsion's composition and formation method, the size of the particles ranges from about ten of nanometers to hundred of microns. A perfect control of its formation is hence required. Emulsion are formed either by stirring (magnetic, high-performance homogenizer...) or sonication, the latter usually leading to particles with lower sizes.

Table I. 7: Literature review on the nature and size of capsules formed by interfacial polymerization

Type	Nature	Emulsion formation	Size	Ref.
O/W	PUa	vigorous agitation	100-1000 nm	229
O/W	PUa	stirring	50 μ m	236
O/W	PUa	stirring	60 μ m	237
O/W	PUa	stirring	100 nm - 2 μ m	151
O/W	PU	stirring	40 - 400 μ m	97
O/W	PU MCs	blade propeller	5 - 350 μ m	102,238
O/W	Melamine formaldehyde	vigorous shaking	40 - 117 μ m	98
O/W	Silica	vigorous stirring	100 - 150 nm	207,239
O/W	Silica	sonication	100 - 400 nm	89
O/W	Silica-imidazoline	vigorous stirring	3 ; 5 μ m	240
O/W	Polyaniline	sonication	700 \pm 400 nm	232,233
O/W	Polypyrrole		100 \pm 5 nm	
O/W	PUa/silica hybrid	blade propeller	50 - 300 μ m	241
O/EtOh	SiO ₂ -imidazoline	stirring	50 - 100 nm	242
	PU		200 nm	
W/O	PUa	sonication	100 - 300 nm	231
	Poly(thiourea)		370 - 420 nm	
W/O	PUa	stirring	10 μ m	125
W/O	Urea formaldehyde	sonication	7 - 18 μ m	222
W/O	PANI	sonication	500 nm - 1 μ m	234

As mentioned before, the encapsulated compound is preferentially only soluble in the dispersed phase and placed before the shell is formed. Two representative examples of current research on this topic are encapsulation of phenolphthalein in PUa microcapsules through an O/W process and encapsulation of sodium molybdate in polyurethane microcontainers made from a W/O emulsion¹²⁵. Phenolphthalein and sodium molybdate are indeed respectively hydrophobic and hydrophilic in neutral media, what makes them perfectly suitable for interfacial polymerization encapsulation.

ii. *In-situ* polymerization

For *in-situ* polymerization, the monomers are dissolved in the same phase. This reaction can be carried out from an emulsion or a suspension. Since most of the time the reaction is carried out in the continuous phase, we describe here this version of *in-situ* polymerization, as in Figure I. 7. However, more seldom, polymerization can be achieved in the dispersed phase, using the droplets as reactors, and leading preferentially to microspheres²²². When the reaction is realized in the continuous phase, a monomer is adsorbed (or potentially covalently bonded) on the surface of either liquid droplets or solid particles. A second monomer then reacts with the first one, hence encapsulating the dispersed phase. Therefore, *in-situ* polymerization requires the first monomer to be able to remain on the dispersed phase surface, what is generally achieved by electrostatic interactions of molecules with a charged sphere surface, or using block copolymer surfactants as monomers (for emulsion).

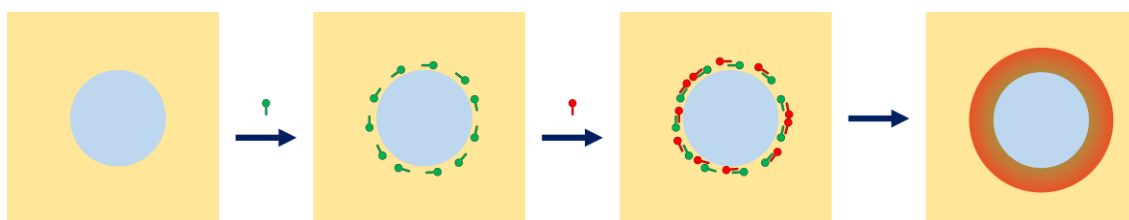


Figure I. 7: Schematic representation of *in-situ* polymerization

Unlike interfacial polymerization, *in-situ* polymerization can be employed to form either spheres or capsules, potentially by removal of the sacrificial core. However this is mainly done using toxic chemicals such as hydrofluoric acid²⁴³ and so we deliberately will not deal with this kind of *in situ* polymerization.

This technique is most of the time referenced for self-healing properties, probably because particles bigger than 10 μm are obtained and that self-healing requires a high quantity of active agent in order to fill a defect. Formaldehyde is a water-soluble reactant often employed for *in-situ* polymerization and the reaction is controlled by pH adjustment and heating. Melamine-formaldehyde¹⁰⁴ and especially urea-formaldehyde^{88,98,244,245} capsules are often referenced.

The sizes observed when *in-situ* polymerization is used are between 10 and 300 μm ^{88,98,104,222,244,245} while the encapsulated agent is generally directly dissolved in the dispersed phase (*e.g.* DCPD or linseed oil). A core material content around 80% can be achieved⁹⁸.

Both interfacial and *in-situ* polymerization can also be combined, as described for example by Jia and colleagues²⁴⁶ who first formed a silica shell around epoxy droplets composing the oil phase, before thickening the capsules' shell. In this example, the encapsulated self-healing agent is the liquid oil dispersed phase.

iii. Layer-by-Layer (LbL) deposition

The first step for LbL assembly, as represented in Figure I. 8, is similar to *in-situ* polymerization except that the molecule used is a polyelectrolyte. This polyanion or polycation, instead of reacting with a second monomer, does not covalently but electrostatically bond with it. First, the polyelectrolyte adsorbs on the dispersed phase (usually a metal or an oxide). A second, oppositely charged polyelectrolyte can then be adsorbed and forms a new layer. This process can be repeated several times in order to increase the size and loading efficiency^{247,248}.

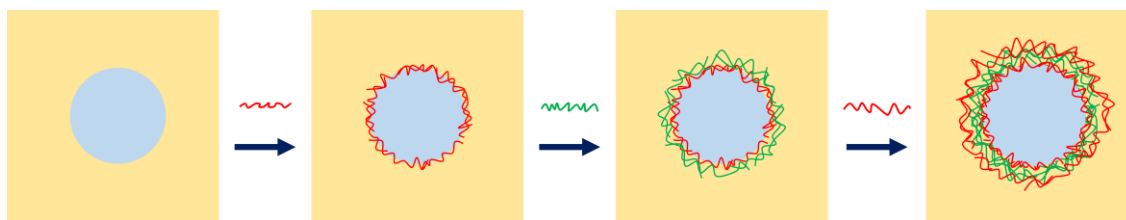


Figure I. 8: Schematic representation of Layer-by-Layer deposition

LbL polyelectrolytes assemblies can be either the only constituent of the container, or be used as a second layer and add a new sensitivity to the encapsulated container. The first approach means that the encapsulated compound is also a charged molecule that can be entrapped between polyelectrolyte layers whereas in the second one the active agent is encapsulated in (or constitute) the core material. The polyelectrolyte then acts as a smart protective layer. It can be combined with several encapsulation methods, what makes it a very versatile and useful technique.

For example Li and colleagues²²⁸ used LbL deposition on the surface of PUa microparticles that they first functionalized. Silica core particles are also several times referenced, whether it be commercial SiO₂ nanoparticles^{143,249}, *in-situ* formed ones²⁴⁷ or hexagonal porous silica containers²⁴⁸. Their negatively charged surface indeed makes them ideal for cation adsorption. Concerning polyelectrolytes, polystyrene sulfonate (PSS) is a common polyanion, while polycations containing amine groups are efficient for LbL processes.

Layer-by-layer systems are mostly developed for biomedical applications since it is an efficient way to obtain biocompatible containers with sizes suiting drug vectorization²⁵⁰. Moreover proteins, carbohydrates and lipids are natural biopolymers with cationic or anionic properties, what enables the formation of non-toxic natural containers^{251,252}. Amongst all the available molecules, chitosan has to be mentioned here again since it is a natural cationic polysaccharide obtained from crustaceans that is more and more studied for its emulsifying and film-forming properties. It is thus an interesting molecule for encapsulation and can be combined with polyanions such as carrageenan²⁵³ or carboxymethyl cellulose. Iwata and colleagues²⁵⁴ for instance formed stable emulsions with chitosan and carboxymethyl cellulose that are adsorbed directly on soybean oil droplets. Encapsulation of an anti-inflammatory drug has also recently been carried out by

Kamburova and colleagues²⁵⁵ by deposition of chitosan and pectin on the surface of the anti-inflammatory nanocrystals, hence using LbL deposition as a coating.

The size of emulsions or containers formed using a LbL deposition process are extremely variable since it depends on the core material and to a lesser extent on the number of adsorbed layers. For example Shchukin²⁴⁷ measured coated particles' size from 70 to 105 nm with 0 to 5 layers of polyelectrolytes, while adsorption on oil droplets may lead to bigger capsules, *e.g.* 25 μm in the case of Iwatas's paper²⁵⁴.

I.4.2.2. Particles precipitation

Particles precipitation methods are described for encapsulation of inhibiting or sensing molecules and find many medical applications. Electrostatic complexation is the most described method and will be described thoroughly.

i. Electrostatic complexation

Using charged molecules, electrostatic complexation does not involve the use of a core particle. Therefore, it can be carried out in a single phase, what allows to prevent the use of organic solvents for example. The formation of these complexes is only driven by electrostatic interactions and steric hindrance and thus is very sensitive to the medium's ionic strength and pH, what could make it tricky to encapsulate ionic salts for example. Figure I. 9 illustrates the principle of electrostatic complex formation. As shown, the ratio between the two polyelectrolytes, as well as their molecular weight are critical factors to get stability. Bridging and agglomeration can indeed happen if there is not enough electrostatic repulsion between the particles²⁵⁶.

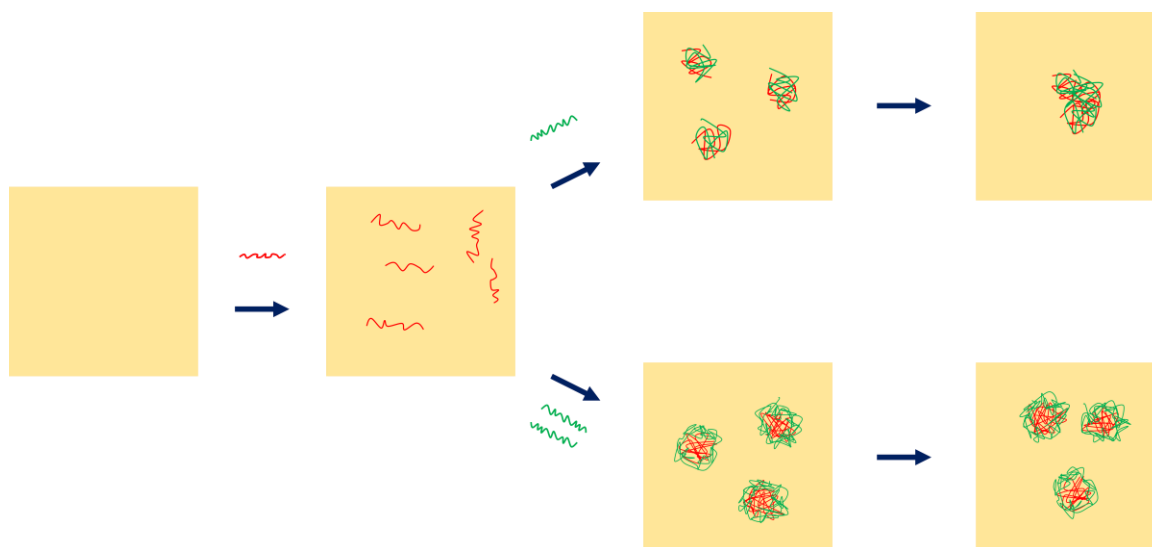


Figure I. 9: Schematic representation of electrostatic complexation

For such complexes, the payload is entrapped between the polyelectrolytes chains, or can be ionically linked to one or the other of the polyelectrolytes. This technique shows very good results in the case of biomolecules.

Amongst the available examples, formation of an insoluble complex formed between a protein and a polysaccharide has been achieved by Kurukji and colleagues²⁵⁷ by mixing sodium caseinate and chitosan in the right pH conditions (*i.e.* below 6). The addition of chitosan to a caseinate solution leads to the formation of a bulk complex that is then dispersed using ultrasonication. They showed that the ratio between the two biomolecules is a very important factor. Indeed, a too low concentration in chitosan leads to a non-uniform coverage and as a consequence the particles formed have a partially negatively and positively charged surface. This then provokes bridging between particles since the electrostatic repulsion between particles is not achieved.

Another method that is often described consists in preparing nano- or micro-beads by first forming a gel that is then coated with an oppositely charged polyelectrolyte. The most used polyelectrolytes for these microbeads are two polysaccharides: alginate and chitosan. This approach consists in first forming a gel between negatively charged alginate and divalent calcium ions. This gel is shaped by mixing and/or ultrasonication before adding the polycation. In this case, the encapsulated molecule is placed in the gel beads by dissolving it in the alginate solution before the formation of the pre-gel, as done with insulin for instance²⁵⁸.

Various sizes can be obtained by formation of electrostatic complexes. For example, Yu *et al.*²⁵⁹ formed complexes between ovalbumin and chitosan, whose sizes range are from 50 to 500 nm depending on the pH and heating conditions. Using different caseinate-chitosan ratios, Kurukji and colleagues²⁵⁷ obtained sizes around 500 nm with 22% to 78% chitosan, lower concentrations leading to agglomeration. Changing the polyanion for albumin, they got particles from 500 to 4000 nm for chitosan ratios between 10 and 78% with no linear relation. By the microbeads preparation methods, Sarmiento²⁶⁰ got microbeads with diameters from 760 to 2200 nm by changing the ratio and pH, while De *et al.*²⁶⁰ reported the formation of alginate-chitosan and poly-L-lysine-alginate beads from 200 to 600 nm. It is therefore possible to get a wide range of diameters playing with the polyelectrolytes' nature, molecular weight and concentrations, pH and temperature. Increasing the concentration in biopolymers usually leads to bigger particles.

ii. Solvent evaporation

The solvent evaporation method is based on the difference of solubility of a compound in different solvents. It consists, as shown in Figure I. 10, in solubilizing a polymer in a good solvent and then forming an emulsion with this solvent as the dispersed phase. By evaporation of the good solvent, the polymer naturally precipitates in the continuous phase.

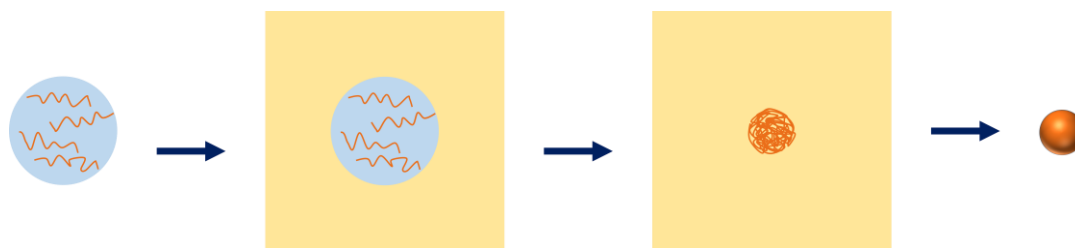


Figure I. 10: Schematic representation of solvent evaporation

A great interest of solvent evaporation is that it can be used to obtain particles from a single polyelectrolyte. For instance, Huang *et al.*²⁶¹ encapsulated resveratrol in a protein shell made of zein. A resveratrol complex, soluble in ethanol, is formed and then ethanol is removed under vacuum. This leads to particles with diameters of 220-230 nm. However, most of the studies use organic (and potentially toxic) solvents as a dispersed phase in water to get polymer particles²⁶².

Dowding *et al.*²⁶³ even used a third solvent, or co-solvent in order to partially remove the volatile compounds before completing the evaporation. They obtained hollow polystyrene capsules with 4-nitroanisole as an encapsulated active ingredient. Their approach requires good solubility parameters for both the polymer and the encapsulated molecule, what makes it not very versatile.

iii. Dispersion polymerization

Like for solvent evaporation, dispersion polymerization is based on soluble monomers that react to form an insoluble encapsulating polymer, as shown in Figure I. 11. The polymer precipitates as the reaction occurs, leading to the particles formation while increasing the polymerization yield²⁶⁴. Polymer precipitation can be used with a wide range of compositions, leading for example to 100 nm-diameter silica nanoparticles²⁶⁵ or biodegradable polymer capsules²⁶⁶.

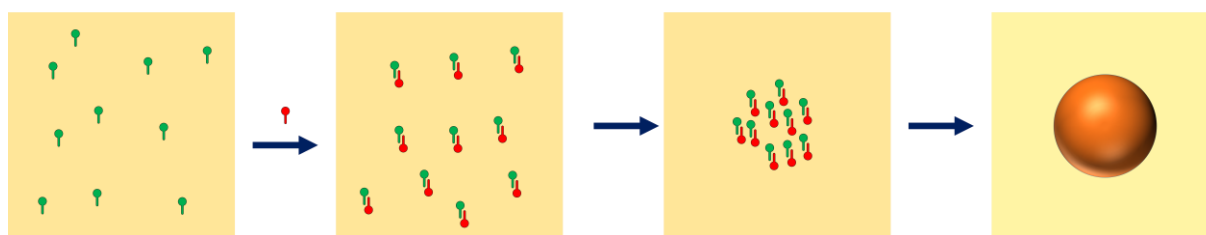


Figure I. 11: Schematic representation of dispersion polymerization

A very important dispersion precipitation reaction is the fabrication of monodisperse silica particles. This process is of great interest since silica spherical particles can be used as a hard template (sacrificial core) for many reactions, the silica surface being negatively charged and having silanol reactive groups. A reference for the synthesis of these particles is the work done by Stöber *et al.*²⁶⁷ in 1968. Using different tetraalkyl silicates and alcohols, they realized the synthesis of silica particles, whose size is controlled by the medium's composition and use of an ultrasound bath. In

presence of water and ammonia as a catalyst, the silicate precursor forms silicic acid that polymerizes and makes silica spherical particles. They reported monodisperse dispersions with sizes between 50 nm and 2 μm .

Nonetheless, no common procedure is used for encapsulation, and therefore the design of a viable system requires the optimization of its composition (monomers, solvents, active agent) as well as process optimization (mixing, heating...). For these reasons, dispersion polymerization was not further considered.

I.4.3. Opening and content release

As seen before, many ways to encapsulate different compounds can be carried out and the choice of an adapted protocol may lie in the compounds' toxicity, availability or solubility. However, once the encapsulation is achieved, the objective remains to release the encapsulated and protected compound when and where it is the most needed.

We may note here that an innovative approach for monitoring has been proposed by Maia and colleagues²³⁹ and not involving any release. In their work, a colored agent (phenolphthalein) is encapsulated as a corrosion-monitoring molecule in silica nanocapsules. The nanocapsules are then used as reservoirs, and instead of leaching phenolphthalein out, hydroxide ions are entering in the capsules in order to trigger the color change. However this kind of system, although being very interesting, will not be further described since it is not compatible with inhibition and we here look for a versatile system for both functions.

For this, several mechanisms can occur depending on the particle's nature. For corrosion protection, three types of release can be of help and will be distinguished. The first is a mechanical breakage of the container that leads to the spreading of its core compound. We will then pay attention to releases triggered by a corrosion-related stimulus before describing smart switchable containers that are promising alternatives for corrosion detection and protection.

I.4.3.1. Release upon fracture

In order to release their content, the capsules need an external stimulus. In most of the cases, a sufficient mechanical stress is able to break the capsules. This release mechanism does not allow a controlled or long-lasting release since the burst of the capsules leads to a total immediate release of the encapsulated compound. Although this type of release can be of great use for some applications, such as self-healing for instance that requires a total filling of the defect^{88,94,104}, corrosion protection often requires a long-lasting supply of inhibiting compounds to maintain protection since the inhibitor can be consumed²⁶⁸.

Raps *et al.*²⁶⁹ have carried out tensile tests on a smart coating made of an epoxy primer containing 5 μm large polyurea capsules filled with a corrosion inhibitor. SEM observations of the fracture,

reproduced in Figure I. 12, evidenced that the rupture of the polymer leads to the rupture of the capsules. A similar study carried out by Blaiszik and colleagues²⁷⁰ compared the rupture of an epoxy matrix loaded with urea formaldehyde capsules for self-healing purpose. They compared 220 nm-diameter and 1.65 μm -diameter capsules using tensile tests and fracture toughness tests. They proved that upon propagation of the fracture, the polymeric capsules are likely to break and therefore release their content. With bigger urea-formaldehyde capsules, ranging from 25 to 45 μm , Thanawala *et al.*⁹⁴ performed corrosion tests on scribed coatings made on mild steel, and also evidenced the release of a self-healing agent upon defects made with a sharp blade.

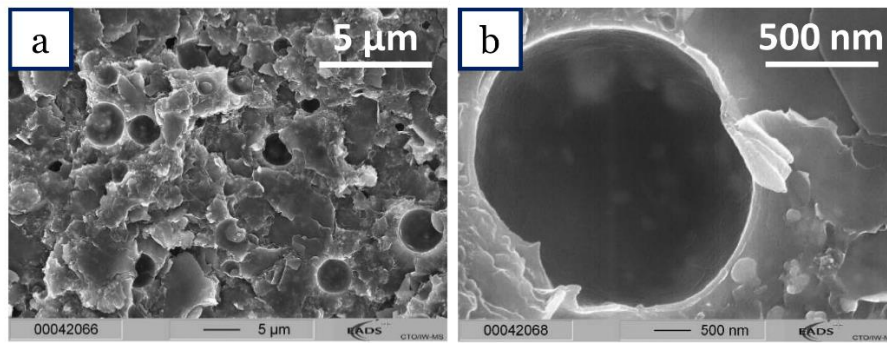


Figure I. 12: High-resolution SEM pictures of a fracture area after cryo-fracture of a PU/PUa capsules-loaded epoxy coating, from ²⁶⁹

However, if this failure mechanism is the most obvious, it shows a few limits. More than its all-or-nothing intrinsic nature, there is a risk that the capsule does not open. Keller and Sottos²⁷¹ performed compression tests with PUa-formaldehyde capsules, filled with DCPD (a healing agent) and with sizes from 60 to 180 μm . The experiment consists in placing a single capsule on a platen and then apply a force on it with a second parallel platen. The applied force is then measured and pictures are taken during the experiment in order to observe the deformation and failure of the capsule's shell. The conclusion of their work is that the failure force is dependent on the size of the capsule and that breaking bigger capsules requires a higher load. However, once normalized to the capsules cross-sectional area it appears that the failure strength (so the pressure required to break the capsule) is higher for smaller particles. In their example, normalized failure strength increases from 0.24 ± 0.04 MPa to 0.8 ± 0.3 MPa when the capsules' size decreases from 187 ± 15 μm to 65 ± 7 μm . The same experiment has been conducted by Zhang and colleagues²⁷² with melamine-formaldehyde capsules and diameters between 4 and 40 μm . They reported the same behavior, and highlighted the proportional relation between the capsules' diameter and the burst force. Finite Element Modeling carried out by Mercadé-Prieto²⁷³ for melamine-formaldehyde capsules also confirmed this.

Mechanical rupture of the capsules' shell therefore leads to a non-controlled release of the encapsulated compounds, meaning premature shortage on a wide area could happen. This explains why such systems were developed for self-healing coatings first, and with polymeric (possibly not

reactive) shells. Despite being useful in the cited cases, the breakage of numerous embedded capsules would be mainly due to the appearance of a macroscopic defect that would require a high quantity of inhibitor to be delivered. A mechanical failure is then desired. However, rupture of small capsules (compared to the defect's size) requires an application of a localized force that is not always likely to happen. Thus, small defects within a polymer matrix do not necessarily provoke the rupture of the capsules' shell. This is why, if mechanical failure is always likely to occur whatever the employed containers, an efficient system cannot only rely on this release mechanism.

I.4.3.2. Controlled release

In the context of corrosion, the release of either the inhibiting or sensing molecules has to be achieved as soon as the corrosion process starts. The release has then to be triggered by a related stimulus. Therefore, we will not pay attention to responsive particles based on stimuli like photodegradation²⁷⁴, enzymatic activity²⁷⁵ or temperature^{276,277} that are sometimes already viable in other domains but not applicable for the aerospace paints we use.

As for inhibitors mode of action, several triggers based on the changes observed in a corrosive medium can be used, the most common being pH change. Various types of nano or microcontainers that could be suitable have therefore already been developed.

i. pH-triggered release

As seen before, corrosion induces local pH variations on cathodic and anodic sites towards alkaline and acidic values respectively. An idea is naturally to use a system releasing its payload in acidic, alkaline or even both conditions, so pH is naturally the most used trigger^{142,218,222,229,248,249,253}. Two approaches exist, based on the reactivity of the container's shell or on the diffusivity of the encapsulated compound, and can be combined. In the second case, control of the release is guaranteed by the compound's solubility while the container acts as a protective reservoir.

The destruction of the containers' shell is used in the case of capsules and involves chemical reactions. A research team at the NASA's Corrosion Technology laboratory developed and patented capsules made of a polymeric shell that breaks down in alkaline media²²⁰. They claim that, using an interfacial polymerization in a W/O emulsion with an ester or thioester as a cross-linker, they obtained pH-sensitive capsules. These containers enabled the release of inhibiting or sensing molecules in an alkaline media. The same principle is reported by Matsuda and col.²²² with PUa-formaldehyde capsules, but with a responsiveness in both acidic and alkaline media. The release mechanism, as they explained, is here driven by the hydrolysis of esters groups in the shell. This reaction being catalyzed by either an acid or a base, the release (of cerium salts in their case) is then triggered by either anodic or cathodic activity respectively.

In order to get a release upon pH changes, another approach employed by Snihirova and col.¹⁴⁸ consists in using solid particles that dissolve in alkaline environments. They used Eudragit particles impregnated with 8HQ as a corrosion inhibitor. Derived from esters of acrylic acids, Eudragit particles are a family of cationic polymers whose properties depend on its exact composition. This is a commercial compound, used in pharmaceuticals for oral delivery. For their application, Snihirova *et al.* employed Eudragit particles that are soluble in acidic media and highlighted the corrosion protection brought by these containers embedded in a host matrix. One of the main advantages of this technique is that the particles can dissolve only partially at the acidic electrolyte/Eudragit interface, which could enable several releases from the same capsule.

Release, and potentially longer release, can be achieved using slow diffusion processes. Some works dealing with this kind of mechanisms are presented in Table I. 8. Instead of breaking down the capsules' shell, pH variations in the environment of the particles trigger the diffusion of the payload towards the external part. This is due to either an increase in the encapsulated compound's solubility within the environment, a change in the shell making it permeable or the combination of both effects.

Table I. 8: Example of diffusion-governed release processes from the literature

Nature	Release mechanism	payload	pH of release evidenced	Ref.
PDVB-graft-P(DVB-co-AA) microspheres	Osmotic swelling due to surface carboxylic acid		pH > 9	264
PUa	Swelling due to hydroxides diffusion	PhPh in alkaline	10 and during corrosion	229
Acrylates/acrylic acid	Preamble shell (diffusion through polymer)	amine salt	12 and during corrosion	142
Silica	mesoporous shell	MBT (acidic m.)	4	278
Silica nanospheres	mesoporous shell	MBT (alkaline m.)	11 and during corrosion	279

Specific polymeric or silica shells can then bring pH-responsiveness to containers, and this whatever their formation process. Moreover, as seen in section I.4.2., LbL deposition is based on electrostatic bonding between cationic and anionic chains. Therefore, it is naturally suitable for the fabrication of pH-responsive particles. A change in pH obviously acts on the charges equilibrium and leads to the disintegration of the polyelectrolytes assembly. This release is thus occurring for pH values either acidic or alkaline enough compared to the LbL suspension's pH, as evidenced by Shi *et al.*²⁴⁸ with the release of 8HQ from porous silica particles embedded in a LbL polyelectrolytes shell.

ii. Use of other stimuli

Another advantage in using polyelectrolytes layers is that such architectures are highly sensitive to the composition of their environment. As evidenced by Liu and col.²⁵³, a LbL capsule made of two polysaccharides (carrageenan and chitosan) is able to release its content depending on the medium's acidity (for either low or high values), but also when the salt content increases. This stimulus could be useful for corrosion protection since a defect in a protective coating leads to a water ingress. This ingress could bring various ionic species to the metal's surface, whereas pH variations can be very limited (in range or due to the precipitation of hydroxides for instance).

The same release mechanism has been evidenced by De and col.²⁶⁰ with chitosan/alginate or poly-L-lysine/alginate complexes. After forming 200 to 600 nm-large insoluble particles, they studied the release of methylene blue in presence of sodium chloride at various concentrations. The microspheres are indeed formed by electrostatic interactions between the carboxylate group of alginate and the ammonium of chitosan or poly-L-lysine²⁸⁰. The presence of sodium ions competes with these interactions and leads to the loss of cohesion in the particles, thus triggering the release of the encapsulated molecule.

Ionic strength is a viable trigger; it is however difficult to assess the changes in ionic strength happening around a corroded area. To the contrary, corrosion involves redox activity that is well observed. A strategy could then be to use redox-responsive containers. In a study performed by Staff and col.²⁸¹, the synthesis of this kind of structures is reported. They built a PMMA shell that contains oxidizable block parts. Upon oxidation, these patches swell and lose their hydrophobicity, hence allowing the release of the hydrophobic encapsulated compound (pyrene). These particles seem to be hardly usable for our application, mainly because the release they got is dependent on the oxidizing compound used. The principle, on the other hand, remains relevant.

iii. Switchable release

An advantage in using redox activity as a trigger is that redox reactions are reversible, what can allow a multiple release (assuming that the payload has not been previously fully released). As illustrated in Figure I. 13, an issue of one-time release for corrosion protection is that a part of the encapsulated inhibitor can be released whereas the metallic dissolution has already been stopped. In the case of a switchable release, on the other hand, the inhibitor is supplied only during corrosion process and an excess can be stored until needed. Polyaniline capsules are, to our knowledge, the most advanced solution for this.

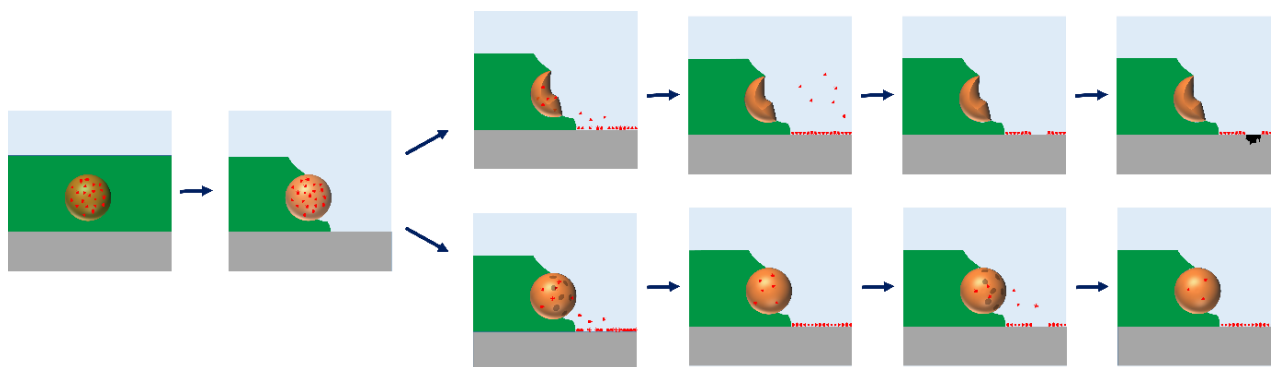


Figure I. 13: Triggered versus switchable release mechanisms

Polyaniline is a conductive polymer that has already been used for corrosion protection thanks to the ennoblement brought to an epoxy resin²⁸². It is therefore sensitive to variations of the electrochemical potential. In the case of PANI capsules, as described by Vimalanandan²³⁴, the shells are reduced when corrosion starts (simulated by increasing the applied potential). A negative charge appears on the polymer's structure and so counter ions (K^+ for instance) are incorporated. This makes the PANI capsules swell and become permeable, letting the inhibitor out. Vimalanandan *et al.* also highlighted the "switchability" of PANI capsules that can be reduced and oxidized several times depending on their environment. This way capsules are not fully broken by the stimulus and the release can be more accurately controlled. Another study carried out by the same research group²³³ showed the same results, and even improved the system allowing a second triggered release. They indeed used the gold particles that decorate the PANI capsules' shell to adsorb thiol-functionalized molecules. Upon a pH increase, the Au-S bond cleaves, releasing the second inhibitor.

Therefore, the release of corrosion sensing or inhibiting molecules from nano- or microcontainers could be performed through different mechanisms, more or less corrosion-related. In any case, breaking down of the containers can happen when a sufficient mechanical stress is applied. For our work, the formation process will be the main determining factor in the container choice.

I.4.4. Integration of containers in a host matrix

I.4.4.1. Containers handling

Prior to their integration in a coating layer, containers often have to be handled, either for washing, loading or simple drying purposes. These steps require having a suspension that can recover its colloidal properties once re-dispersed, *i.e.* no irreversible aggregation occurs. Table I. 9 shows the operations needed in order to incorporate containers in a matrix as found in the literature for corrosion protection purposes (inhibition, detection, self-healing). As one can see, most of the conducted studies involve a drying step and integrate the containers in the form of a powder.

This drying step is not dependent on the containers size since it is observed for particles from 100 nm to several hundreds of microns. However, the nature of the containers is crucial and can

enable or prevent drying. Polymerization can often be tuned in order to increase steric hindrance and/or repulsion and enable a reversible drying. Addition of surfactants to a formed suspension can bring the same effect. However, when the containers formation only relies on electrostatic interactions, drying might be unnecessary but is most of all hardly achieved since the concentration of the suspension can lead to the destabilization of the LbL assembly.

Table I. 9: Bibliographic review of containers handling techniques used

Nature	Size (μm)	Centrifuged	Filtered	Dried	Ref.
Polystyrene	0.4 - 0.45	-	-	-	283
Specific copolymer	3	Y	-	Y	264
Eudragit polymer	35	-	-	Y	148
PU	5 - 350	-	Y	Y	230
PU	30, 50, 100	-	-	Y	102
PUa	0.1 - 1	-	Y	Y	284
	0.1 - 2	-	Y	Y	151
PU-PUa	10	-	Y	Y	125
	0.15	Y	-	Y	95
PUa-formaldehyde	7 - 18	Y	Y	-	222
	10	-	Y	Y	96
	25 - 45	-	Y	Y	94
	100 - 160	-	Y	Y	285
	125	-	Y	Y	244
Silica	220	-	Y	Y	88
	0.1	Y	-	Y	286
	0.1 - 0.15	-	Y	Y	278
	0.1 - 0.4	-	Y	Y	287
	0.1 - 0.15	-	Y	Y	239
Silica nanorods	10 - 100	Y	-	Y	90
	0.5 - 1	Y	-	Y	288
Silica + polyelectrolytes	0.1	Y	-	-	249
	0.5 - 1	-	Y	-	248
Polyelectrolytes	0.1	-	-	-	247
	0.1	-	-	-	150,152

Another very important parameter that is not always mentioned (or measured) in the case of hollow particles is the walls' thickness. It plays a role when particles have to be processed (blended in a resin, dried...) since the mechanical properties of the capsules depend on the shell wall's thickness. A certain thickness has then to be reached in order to ensure the integrity of the containers but this can be detrimental to the capsules' sensitivity (increase of the diffusion time through the shell, need for a higher stress to break). Li *et al.*²¹⁸ for example observed breakage of capsules, and so waste of containers when processed.

Lv and col.²³², in one of their studies, investigated the ability of PANI capsules to resist the application process. They incorporated the containers in a poly(vinyl alcohol) (PVA) matrix before extracting the capsules from the PVA by dissolving the matrix in water. They succeeded this way to prove that the nanocapsules' shape hardly changed after coating and that around 5% of the capsules were collapsed. Although they did not specify how they incorporated the capsules within the PVA, this shows that a non-adapted process can threaten the capsules' integrity and efficiency.

The design of a container should therefore take into account the whole process including the integration in a matrix. A viable dispersion can be obtained and show great properties in its colloidal form but would be unusable if it cannot be handled. A work carried out by Latnikova and col.²⁸⁹ highlighted this fact through the synthesis of polyamide nanocapsules loaded with 2-methylbenzothiazole as a solvent. Due to a low affinity between the solvent and the polymer, the capsules obtained, after washing and drying are very fragile and cannot be handled, even gently, without collapsing.

Depending on the use of the suspension, meaning as a liquid or as a solid, an adequate process has then to be chosen.

I.4.4.2. Impact of the addition in a host matrix

Although the integrity of the containers has to be preserved so no premature leakage or loss of materials could happen, one has to keep in mind that encapsulation is also used in order to protect both the loaded compound and the host matrix. As seen in the first sections, encapsulation enables a local release of an active molecule when needed. However, more than improving the active agent efficiency, it is often mandatory to preserve a molecule's efficiency or activity.

If a direct addition of sensing or inhibiting molecules in a polymeric host matrix seems to be a simple way to form smart coatings, potential interactions prevent it. A coating being a complex multi-component system, the efficiency of a payload can indeed be reduced. In a recent study, Galvão and col.²⁰⁷ for example used phenolphthalein (PhPh), a colored agent, as a pH-sensitive corrosion sensor. The encapsulated PhPh triggered the appearance of pink spots linked to corrosion processes, while PU coatings in which the colored agent had been directly incorporated did not show any color change. This deactivation could be due to chemical reactions between the PhPh molecule

(containing in particular hydroxyl groups) and the paint's monomers, and led to a non-working coating. It also means that the non-encapsulated part of the PhPh is not able to enable detection. The same conclusion can be drawn with a corrosion inhibitor from a study performed by Kakaroglou *et al.*¹²⁵, who used sodium molybdate either encapsulated in PUa-PU capsules or directly added to a PU matrix. They showed that, even though the addition of the inhibitor can delay the development of corrosion, encapsulation of the inhibitor allows to obtain better performances. Another close issue with direct loading of sensing molecules could be the trigger of a false positive, as showed for instance by premature fluorescence of a sensing dye²⁶⁴. This kind of response from the coating is a problem since it would lead to an unnecessary maintenance and hide actual defects.

In addition to maintaining active compounds' activity, encapsulation must not be destructive for the host matrix itself. When the incorporation of containers is achieved, structural changes can indeed occur in the coating layer, what can cause a loss of the barrier properties that any protective coating should bring. Despite observing an effect of the encapsulated inhibitor, Kakaroglou and col.¹²⁵ also evidenced an increase in delamination upon corrosion when polymeric capsules were added to the coating. Raps *et al.*²⁶⁹ studied the adhesion of an epoxy-based primer upon addition of polyurea capsules. They proved that, although PUa and epoxy are highly compatible, when a certain content of capsules is reached, the volume of matrix is not sufficient around the 5 μm capsules, and favorable breaking points are created. The coating adhesion then naturally collapses.

In order to limit the negative impact the containers can have on the hosting matrix, two strategies can be thought of. First, as mentioned before, the natures of the containers and the matrix are very important and a compatibility between them prevents the formation of preferential weakness points. Several studies then use the same chemistry for the two components, incorporating for instance silica containers within sol-gel layers^{247,286,290,291}, or polymeric capsules with groups similar to the matrix one, such as polyurea nanocapsules in a polyurethane matrix, as presented by Maia and col.²²⁹. The idea is that covalent bonds can be formed between the shell surface and the matrix so there is no heterogeneous zone within the coating.

A second approach consists in playing with the containers' size, since smaller containers can be more homogeneously dispersed. Using an inhibitor-loaded polyelectrolyte assembly with diameters around 100 nm, Kopeć and col. achieved a good dispersion within an epoxy matrix, without involving any change in the structure and barrier properties of the layer¹⁵⁰. They hence apparently prevented the loss of mechanical properties that could be induced by the incorporation of the containers²⁹². However, since they added the nanocontainers as a low concentration suspension, the absence of detrimental effect might be mainly due to a low content. Another interesting study published by Matsuda *et al.*²²² shows that a higher protection is conferred when smaller particles are used in the case of microcapsules (from 7 to 18 μm) loaded with cerium nitrate as an inhibitor. On the other hand, Huang and Yang¹⁰² evidenced the need of a sufficient volume of capsules to bring protection. The encapsulation efficiency must then be high enough, and enough containers have to

be dispersed in the coating. A compromise has then to be found in order to use small enough capsules but keeping a sufficient amount of loaded inhibitor.

Encapsulation is thus required to enable (or enhance) an active compound's action. Nonetheless, the integration in a coating system requires precaution in order to maintain both the containers and the matrix's integrity and barrier properties. Development of a proper process has then to be achieved depending on the nature of the different components of the system.

I.4.4.3. Incorporation process

The "right" quantity of containers to add has to be determined for each system and depends on the containers' intrinsic properties (volume, loading and release efficiency, release duration), but is also highly dependent on the payload's efficiency and mode of action. For example self-healing requires a high volume of materials so containers of tens to hundreds of microns are incorporated at a concentration up to 10wt.%^{88,94,102}. In our case, organic inhibitors require a sufficient quantity to form a monolayer of adsorbed molecules on the exposed surface area, while cathodic or anodic inhibitors can be efficient as soon as cathodic or anodic sites are protected respectively. For sensing molecules, the sensitivity will highly depend on the measurement technique employed but fluorescent probes can generally be detected for concentration in the μM range²⁹³. We here want to identify the protocols found in the literature that we could use as a model, only based on the weight percentage of added containers and leading to homogeneous coatings.

This first observation made is that most of the studies naturally focus on the containers formation and coatings' properties and do not present the incorporation as a critical or difficult step so only pieces of information are given. Many studies, however, use commercial formulations to which they add the synthesized capsules, what is our approach as well.

i. Mixing order

In the studies detailing the formulation process of the coating, the order of mixing apparently does not always have a significant role. For many of them, capsules are added to the final formulation. Epoxy is the most used matrix, and incorporation rates are up to 10wt.% usually with respect to the liquid formulation^{90,94,152,264,284}. This absence of addition order is also commonly seen for sol-gels^{151,286}. If no explanation is generally given, the reticulation kinetics inherent to each formulation can however lead to a shorter pot life and application time that a good dispersion requires. This could explain why many authors specify that particles are mixed to the resin until a uniform dispersion is obtained, and only after that the hardener is added^{230,239,248,249}. This is seen for both polymeric and inorganic containers with bi-component (and mainly epoxy) paints.

It is also very important to notice that the addition of capsules as a suspension is quite rare in the literature and the assessment of the dispersion seldom reported. A relevant example is the work

carried out by Kopec and col.¹⁵⁰ who incorporated 100 nm-large polyelectrolyte nanocapsules in a commercial aerospace water-based epoxy primer. The capsules were dispersed in water and then added to the epoxy primer before being applied with a spray gun. The capsules are then the last component to add in their case, what apparently leads to homogeneous coatings.

ii. Dispersion process

Since a formed emulsion will likely become unstable upon addition in another environment as an organic matrix, blending conditions of the suspension in the formulation is a crucial step toward an optimal dispersion. However, very little attention is generally paid to this process. Table I. 10 sums up relevant pieces of information found in the literature concerning the dispersion of containers in an organic matrix. As one can see, the mixing step duration can go from 30 minutes to many hours and dispersion tools are varied, although most of the time only magnetic stirring is sufficient. A final operation sometimes performed consists in degassing the formulation since an important quantity of air could have been injected in the formulation during mixing. Use of a vacuum step is however not frequent and might be mandatory only in the case of an energetic mixing step.

It also very important to notice that very few articles work with the nanocontainers in the state of a suspension without any drying step, and therefore only few information about processes adding a dispersion to an organic matrix have been found.

Table I. 10: Worth considering dispersion processes from the literature

Nature of the containers	State	Dispersion	Duration	Quantity	Vac.	Ref
Silica	Dry	Stirring	~30 min	5 wt.% resin	-	239
Silica	Dry	Ultraspeed dispersion machine 1200rpm	30 min	3%	-	248
Silica capsules	Dry	NS	NS	10 - 20%	Y	90
Silica	Slurry	Magnetic	24h	3%	-	207
Silica nanorods	Dry	Stirring	1h	0.15 wt.% dry	-	288
Silica + polyelectrolytes	Dry	Stirring	10 min	5 wt.%	-	249
TiO ₂ containers	Dry	Pearl-mill	30 min	0.5 to 2 wt.%	-	294
Kaolin	Suspension in solvent	Mechanical	24h	10 – 46 phr	-	295
PU	Dry	NS	NS	10 wt%	Y	102,230
PUa-formaldehyde	Dispersion in solvent	3-blade mechanical stirrer	30 min	3 wt.%	-	94
PUa-formaldehyde	Dry	Attritor	NS	10 vol.% capsules	-	95
PS	Dispersion in water	NS	NS	33.3% solid content	-	283

NS: not specified Vac.: Vacuum applied

ii. Dispersion assessment

After application of a coating, the assessment of the capsules dispersion is then performed, what could be carried out using various detection techniques although microscopic ones are generally favored. However, even though the easiest method is the observation of a coating's cross-section, this can turn out to be tricky depending on the capsules quantity and size. A fracture or cryo-fracture is made and either optical microscopes or SEMs are used to visually assess the dispersion. This method is commonly used for micron-sized particles than can be quickly observed^{90,269,270,296}.

However, if microscopy is a very powerful tool, a clear observation cannot always be performed, especially for nano-sized particles. For example Galvão *et al.*¹²⁵ assumed that a good dispersion was obtained based on rheological measurements, since the presence of aggregates would imply an increase in the formulation's viscosity for 400 nm particles. Otherwise, the detection of the capsules can be made using elementary analysis when detectable elements are present in the particles' shells or payload. For example Kakaroglou¹²⁵ and col. performed a mapping using Raman spectroscopy.

Chapter I - Bibliographic review

Identifying peaks related to the matrix and the inhibitor (sodium molybdate), they were able to assess the homogeneity of the coating. This however requires to first check that there is no premature leakage and so that the detection of the payloads is equivalent to the detection of the containers.

Due to the high variety of processes and natures of both containers and matrices used, we can conclude that no universal application method exist. Depending on the nature of the capsules finally chosen, an important optimization work will then have to be carried out.

I.5. Summary and experimental approach

In this chapter, an overview of the available literature and data concerning the means to detect and prevent corrosion, applicable to the aerospace industry, has been drawn up. We have seen that an important variety of materials are employed and developed in this domain, amongst which structural steel and aluminum alloys represent a consequent amount. The present work therefore focuses on these materials, considering S355 structural steel and AA2024-T3 aluminum alloy. Both of them are susceptible to corrosion, especially in chloride media where steel undergoes uniform corrosion while pitting corrosion is the main form that develops on AA2024.

Corrosion being the source of important costs, the use of an efficient protection is mandatory. To this end, different surface treatments are implemented in the industry, amongst which chromate-based treatments are the most effective. However, because of their toxicity, these options have to be banned, requiring to find efficient alternatives. To this end, a great attention is paid to the development of high-resistance organic coatings containing corrosion-inhibiting molecules. In addition to the protection brought thanks to a barrier effect, the use of inhibitors indeed allows to overcome the corrosion development due to the coating aging or defects. An increasing number of non-toxic inhibitors are hence developed. They can be sorted depending on their mode of action according to their ability to act on the cathodic or anodic sites or on both, passivating the exposed surface. Due to the importance of the research conducted on this topic, we assume that new efficient molecules will continue to be identified.

More than focusing on corrosion protection, very promising approaches tend to multiply the coatings' functionalities, creating a new class of "smart" materials. Although protection is obviously the paramount functionality to implement, preventive detection of a coating failure is also seriously considered. A self-reporting system could save maintenance cost, by simplifying the heavy existing routine procedures. Detecting the corrosion processes is indeed hardly set up in the aerospace industry and is mainly based on visual inspection, hardly reliable for some forms of corrosion, or indirect monitoring techniques. An *in-situ* monitoring of the installation would then be a clear improvement. Using functional coatings, the main approach consists in using the products of corrosion processes to trigger a response. The most obvious stimuli are local pH variations occurring at anodic and cathodic sites and the release of metallic species, while an ideal response have to be easily observable, and so color change and emission of fluorescence are the main options.

Finally, we have seen that in order to integrate either corrosion inhibitors or sensors to an organic matrix, one has to take into account the potential interactions with the matrix. That is why, in order to protect both the matrix and the active compound, encapsulation of the targeted molecule is performed. Moreover, encapsulation can enable an on-demand release by controlling the container's properties. Several methods exist to do so, the most used one being through an emulsion

step, by interfacial polymerization. The payload is then placed in the dispersed phase prior to the shell formation.

The NC2M system specifications were then defined according to the available literature and information. It was decided to use either an epoxy or a polyurethane matrix since they are frequently employed primers in the aerospace industry. Moreover, the use of water-based formulations reduces potential emissions of toxic compounds. Concerning the final formulation application, industrially applicable techniques are considered: brushing and spraying. However, in order to control the homogeneousness and thickness of the experimental coatings, bar coating will be used as a simplified brushing

Concerning the capsules' payload, model molecules are encapsulated at first in order to validate our system. We opted for 2-mercaptobenzothiazole (MBT), a well-known organic film-forming inhibitor for several reasons: thanks to its structure, MBT is easily detectable²⁹⁷ and it is an efficient organic inhibitor for aluminum alloys^{153,298,299}. Moreover, there is an important available literature about the use of MBT and some studies suggest that it could be efficient on mild steel^{279,300}. Since it is soluble in organic solvents and only slightly in water, an O/W is required. It however has to be kept in mind that MBT is suspected to be carcinogenic and that alternatives will have to be considered.

About detection, color change is the most easily detectable response we can get from a coating. For color change however, the clearest results in the literature have been seen for coloring agent such as phenolphthalein and thymolphthalein. Both molecules can be solubilized in water by addition of ethanol and hence encapsulated through W/O emulsions.

Coloring agents using pH variations as a trigger, this was chosen as a stimulus for the capsules opening. In order to be able to encapsulate the desired compounds, both an Oil-in-Water and a Water-in-Oil process therefore have to be used. As highlighted in this chapter, polyurea are well-referenced pH-responsive capsules that could be suitable for encapsulation of hydrophilic molecules. Concerning oil-soluble compounds, silica containers can be formed in a wide range of submicronic particles' sizes with an O/W emulsion. Moreover, they can be pH-responsive. Due to the usual thicknesses of aerospace primer layers, and in order to enable a proper dispersion within the coating, a maximum size of 1 μm was specified for the containers. Use of a sonication-assisted emulsion process was therefore identified to be the most suitable existing technology that could be scaled-up.

Choice of the different components of our system being settled, our approach was as schemed in Figure I. 14:

- Hydrophilic- and hydrophobic-core nanocapsules are synthesized through a W/O and an O/W emulsion-based processes respectively. The formed containers are then characterized in terms of shape, morphology, stability and ability to release their payload in alkaline and/or

Chapter I - Bibliographic review

acidic media. An optimization of the process will be attempted in order to control the size of the containers that is a critical parameter.

- The so-formed nanocapsules will be added to a water-based primer formulation and a protocol will have to be defined to get defect-free coatings. In order to limit the number of parameters to vary, bar-coating is used for steel substrates while spray is applied on AA2024-T3 samples. Once homogeneous coatings are obtained, the capsules dispersion will have to be evaluated.
- Successfully prepared coatings are then tested using electrochemical impedance spectroscopy. The impact of the nanocapsules addition to the polymer matrix as well as ability of the capsules to bring protection to the substrate are studied.

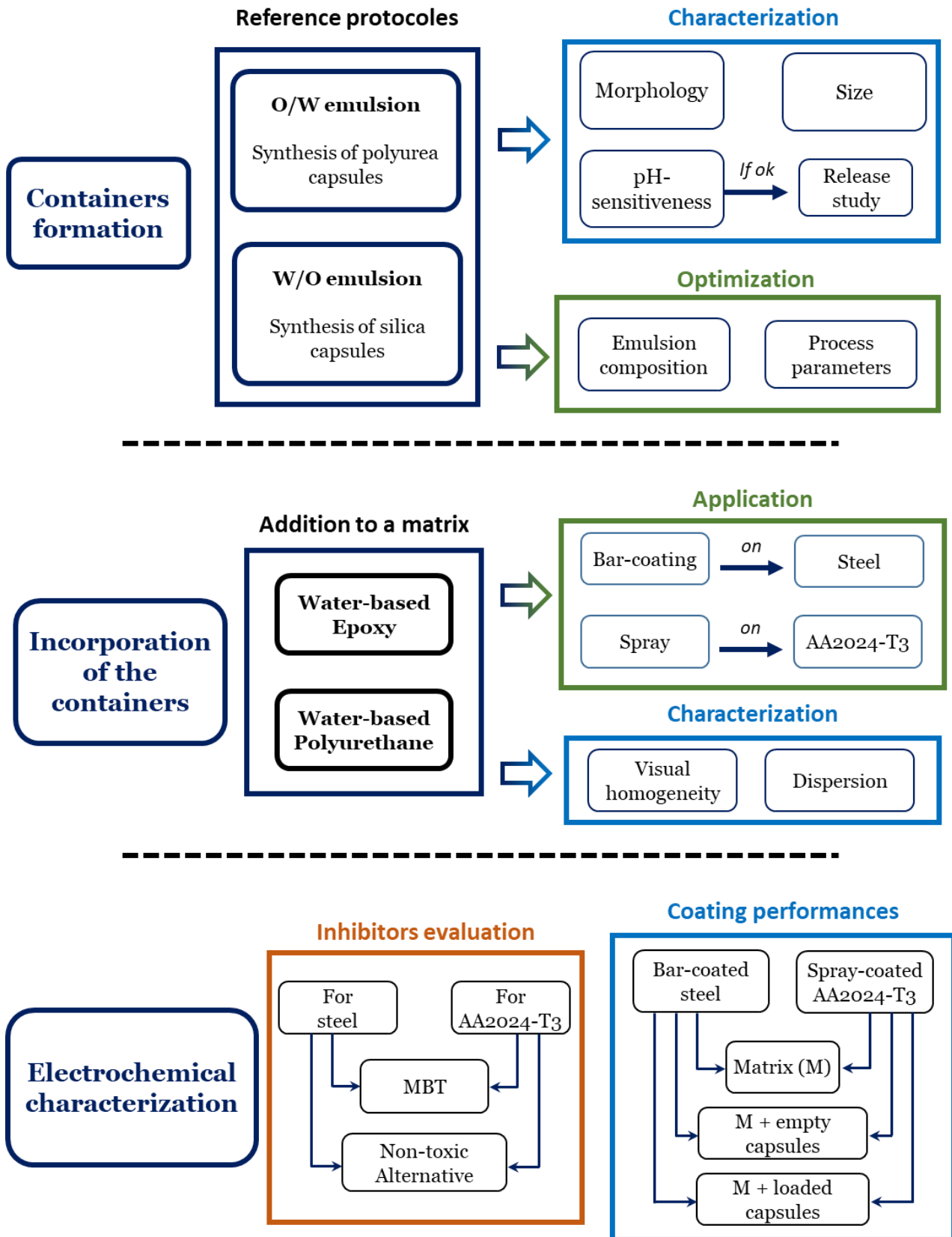


Figure I. 14: Summary of the approach chosen in the development of the NC2M system

If our work tends to be innovative, two recent articles published in 2018 have to be mentioned due to their similarity with the presented work:

- Wang and col.²⁶⁴ designed a polymeric pH-responsive capsule, with a porous shell whose size is around 3 μm . The capsules are loaded with either a fluorescent dye (coumarin) or a corrosion inhibitor for carbon steel (benzotriazole). The microcontainers are then dispersed in an epoxy matrix that showed protection and reporting of the defect upon scratching when immersed in a 3.5% NaCl medium.
- Galvão *et al.*²⁰⁷ reported the encapsulation of phenolphthalein (PhPh) in 300-450 nm-diameter silica capsules. Release of the payload occurs in alkaline media in order to detect corrosion processes on AA2024. They also showed that the incorporation of the silica capsules in a water-base polyurethane matrix improves the coating's hardness and corrosion resistance, probably due to the filler effect of the capsules.

These two studies have the same aim as ours and important progress towards the detection of corrosion has been made. They should therefore be kept in mind for further development and improvement of the NC2M.

References

1. Uhlig, H. H. The Cost of Corrosion to The United States. *Corrosion* **6**, 29–33 (1950).
2. Kruger, J. Cost of Metallic Corrosion. in *Uhlig's corrosion handbook* (eds. Revie, R. W., Uhlig, H. H. & Electrochemical Society) (Wiley, 2011).
3. Bhaskaran, R., Palaniswamy, N. & Rengaswamy, N. S. A review of differing approaches used to estimate the cost of corrosion (and their relevance in the development of modern corrosion prevention and control strategies). 13
4. NACE Internationa. Corrosion Costs and Preventive Strategies in the United States. 12
5. Cicek, V. *Corrosion Engineering and Cathodic Protection Handbook*. (John Wiley & Sons, Inc., 2017).
6. *Corrosion: understanding the basics*. (ASM International, 2000).
7. NACE International. *International Measures of Prevention, Application, and Economics of Corrosion Technologies Study*. (2016).
8. Moulinier, F. Combien coûte la corrosion? *Techniques Sciences Méthodes* 26–38 (2010). doi:10.1051/tsm/201007026
9. Aerospace Corrosion Control. *Aircraft Engineering and Aerospace Technology* **61**, 18–19 (1989).
10. Dunn, B. D. *Materials and processes: for spacecraft and high reliability applications*. (Springer, 2016).
11. Calle, L., Hintze, P., Li, W., Buhrow, J. & Curran, J. Launch Pad Coatings for Smart Corrosion Control. in (American Institute of Aeronautics and Astronautics, 2010). doi:10.2514/6.2010-2017
12. Schoeyer, H. F. R. *et al.* High-performance propellants based on hydrazinium nitroformate. *Journal of Propulsion and Power* **11**, 856–869 (1995).
13. Turner, M. J. L. *Rocket and spacecraft propulsion: principles, practice and new developments*. (Springer [u.a.], 2009).
14. Bussu, G. & Dunn, B. D. ESA Approach to the Prevention of Stress-Corrosion Cracking in Spacecraft Hardware. 7 (2002).
15. Griffith, G. & Goka, T. The Space Environment: Natural and Induced. in *Safety design for space systems* (eds. Musgrave, G. E., Larsen, A. M., Scobba, T. & International Association for the Advancement of Space Safety) (Elsevier, 2009).
16. NASA. Countdown! NASA Launch Vehicles and Facilities. *PMS 018-B (KSC)* (1991).
17. Mouritz, A. P. *Introduction to aerospace materials*. (AIAA, American Inst. of Aeronautics and Astronautics, 2012).
18. Mouritz, A. P. Magnesium alloys for aerospace structures. in *Introduction to aerospace materials* (AIAA, American Inst. of Aeronautics and Astronautics, 2012).
19. Czerwinski, F. Controlling the ignition and flammability of magnesium for aerospace applications. *Corrosion Science* **86**, 1–16 (2014).
20. Luo, A. A. Applications: aerospace, automotive and other structural applications of magnesium. in *Fundamentals of Magnesium Alloy Metallurgy* 266–316 (Elsevier, 2013). doi:10.1533/9780857097293.266
21. Walczak, Mariusz, Gaska, Daniel & Sidor, Joanna. Properties and application titanium and titanium alloys in aerospace systems. in *Modern Techniques in Mechanical Engineering* (ed. Świć, Antoni) 150 (2009).
22. *Advanced Aerospace Materials*. (Springer Berlin Heidelberg, 1992). doi:10.1007/978-3-642-50159-3
23. Zagula-Yavorska, M., Sieniawski, J. & Filip, R. The Influence of the Chemical Composition of Superalloys on the Oxidation Resistance of Aluminide Coating. *Solid State Phenomena* **227**, 365–368 (2015).
24. *Advanced composite materials for aerospace engineering: processing, properties and applications*. (Elsevier/Woodhead Publishing, 2016).
25. Hubert, P. Survey on Ariane 5 design and structural developments. in *36th Structures, Structural Dynamics and Materials Conference* (American Institute of Aeronautics and Astronautics, 1995). doi:10.2514/6.1995-1328
26. Prel, Y. Composite materials on Ariane 5 launcher. *S.A.M.P.E journal* 5 (1999).

Chapter I - Bibliographic review

27. Maria, M., The Faculty of Operation and Economics of Transport The Air Transport Department Univerzita 1, 010 26 Zilina, Slovak Republic, Advanced composite materials of the future in aerospace industry. *INCAS BULLETIN* **5**, 139–150 (2013).
28. Ariane 5 User's Manual. (2016).
29. Bhadeshia, H. K. D. H. & Honeycombe, R. W. K. *Steels: microstructure and properties*. (Elsevier/Butterworth-Heinemann, 2006).
30. Allen, D. J. & Wolstenholme, D. A. Sulphur segregation and intergranular microcracking in ferritic steel weld metal. *Metals Technology* **9**, 266–273 (1982).
31. Bozkurt, F. & Schmidová, E. Fracture Toughness Evaluation of S355 Steel Using Circumferentially Notched Round Bars. *Periodica Polytechnica Transportation Engineering* (2018). doi:10.3311/PPtr.11560
32. Lipinski, T. Corrosion effect of 20 % NaCl solution on basic carbon structural S235JR steel. in (2017). doi:10.22616/ERDev2017.16.N225
33. Rana, R. S., Purohit, R. & Das, S. Reviews on the Influences of Alloying elements on the Microstructure and Mechanical Properties of Aluminum Alloys and Aluminum Alloy Composites. **2**, 7 (2012).
34. Fayomi, O. S. I., Popoola, A. P. I. & Udoeye, N. E. Effect of Alloying Element on the Integrity and Functionality of Aluminium-Based Alloy. in *Aluminium Alloys - Recent Trends in Processing, Characterization, Mechanical Behavior and Applications* (ed. Sivasankaran, S.) (InTech, 2017). doi:10.5772/intechopen.71399
35. Mouritz, A. P. Aluminium alloys for aircraft structures. in *Introduction to aerospace materials* (AIAA, American Inst. of Aeronautics and Astronautics, 2012).
36. Benedyk, J. C. International Temper Designation Systems for Wrought Aluminum Alloys: *Light Metal Age* **6** (2010).
37. Huda, Z. & Zaharinie, T. Kinetics of grain growth in 2024-T3: An aerospace aluminum alloy. *Journal of Alloys and Compounds* **478**, 128–132 (2009).
38. Hughes, A. E., Markley, T. A., Garcia, S. J. & Mol, J. M. C. Comparative study of protection of AA 2024-T3 exposed to rare earth salts solutions. *Corrosion Engineering, Science and Technology* **49**, 674–687 (2014).
39. Lopez-Garrity, O. & Frankel, G. S. Corrosion Inhibition of AA2024-T3 By Sodium Silicate. *Electrochimica Acta* **130**, 9–21 (2014).
40. Recloux, I. *et al.* Active and passive protection of AA2024-T3 by a hybrid inhibitor doped mesoporous sol-gel and top coating system. *Surface and Coatings Technology* **303**, 352–361 (2016).
41. Rambabu, P., Eswara Prasad, N., Kutumbarao, V. V. & Wanhill, R. J. H. Aluminium Alloys for Aerospace Applications. in *Aerospace Materials and Material Technologies* (eds. Prasad, N. E. & Wanhill, R. J. H.) 29–52 (Springer Singapore, 2017). doi:10.1007/978-981-10-2134-3_2
42. Rodič, P. & Milošev, I. Corrosion inhibition of pure aluminium and alloys AA2024-T3 and AA7075-T6 by Cerium (III) and Cerium (IV) Salts. *Journal of The Electrochemical Society* **163**, C85–C93 (2016).
43. Kiyota, S., Valdez, B., Stoytcheva, M., Zlatev, R. & Schorr, M. Electrochemical Study of Corrosion Behavior of Rare Earth Based Chemical Conversion Coating on Aerospace Aluminum Alloy. in 115–123 (2009). doi:10.1149/1.3259803
44. Kumar, P. V., Reddy, G. M. & Rao, K. S. Microstructure, mechanical and corrosion behavior of high strength AA7075 aluminium alloy friction stir welds – Effect of post weld heat treatment. *Defence Technology* **11**, 362–369 (2015).
45. Cheeseman, B., Gooch, W. & Burkins, M. Ballistic Evaluation of Aluminum. 10
46. The Aluminum Association. International Alloy Designations and Chemical Composition Limits for Wrought Aluminum and Wrought Aluminum Alloys. (2009).
47. Hughes, A. E., Parvizi, R. & Forsyth, M. Microstructure and corrosion of AA2024. *Corrosion Reviews* **33**, 1–30 (2015).
48. Boag, A. *et al.* How complex is the microstructure of AA2024-T3? *Corrosion Science* **51**, 1565–1568 (2009).
49. Hashimoto, T. *et al.* Investigation of dealloying of S phase (Al₂CuMg) in AA 2024-T3 aluminium alloy using high resolution 2D and 3D electron imaging. *Corrosion Science* **103**, 157–164 (2016).

Chapter I - Bibliographic review

50. Zhang, X., Hashimoto, T., Lindsay, J. & Zhou, X. Investigation of the de-alloying behaviour of θ -phase (Al₂Cu) in AA2024-T351 aluminium alloy. *Corrosion Science* **108**, 85–93 (2016).
51. Luo, Chen. Role of Microstructure on Corrosion Control of AA2024-T3 Aluminium Alloy. (University of Manchester, 2011).
52. Hughes, A. *et al.* High Strength Al-Alloys: Microstructure, Corrosion and Principles of Protection. in *Recent Trends in Processing and Degradation of Aluminium Alloys* (ed. Ahmad, Z.) (InTech, 2011). doi:10.5772/18766
53. Ralston, K. D., Birbilis, N., Weyland, M. & Hutchinson, C. R. The effect of precipitate size on the yield strength-pitting corrosion correlation in Al–Cu–Mg alloys. *Acta Materialia* **58**, 5941–5948 (2010).
54. Shreir, L. L. *Metal, environment reactions*. (Newnes-Butterworth, 1977).
55. Perez, N. *Electrochemistry and corrosion science*. (Kluwer Academic Publ, 2004).
56. Ahmad, Z. *Principles of corrosion engineering and corrosion control*. (Butterworth-Heinemann [u.a.], 2006).
57. Landolt, D. *Corrosion and surface chemistry of metals*. (EPFL Press, 2007).
58. Roberge, P. R. *Handbook of corrosion engineering*. (McGraw-Hill, 2000).
59. Bardal, E. *Corrosion and protection*. (Springer, 2005).
60. Boag, A., Hughes, A. E., Glenn, A. M., Muster, T. H. & McCulloch, D. Corrosion of AA2024-T3 Part I: Localised corrosion of isolated IM particles. *Corrosion Science* **53**, 17–26 (2011).
61. Boag, A. *et al.* Stable pit formation on AA2024-T3 in a NaCl environment. *Corrosion Science* **52**, 90–103 (2010).
62. Larson, C., Smith, J. R. & Armstrong, G. J. Current research on surface finishing and coatings for aerospace bodies and structures – a review. *Transactions of the IMF* **91**, 120–132 (2013).
63. Shreir, L. L., Jarman, R. A. & Burstein, G. T. *Corrosion control*. (Butterworth-Heinemann, 1995).
64. Schweitzer, P. A. & Schweitzer, P. A. *Corrosion of linings and coatings: cathodic and inhibition protection and corrosion monitoring*. (CRC Press, 2007).
65. Bishopp, J. Chapter 4 Surface pretreatment for structural bonding. in *Handbook of Adhesives and Sealants* **1**, 163–214 (Elsevier, 2005).
66. Jones, D. A. Coatings and Inhibitors. in *Principles and prevention of corrosion* (Prentice Hall, 1996).
67. Presuel-Moreno, F., Jakab, M. A., Tailleart, N., Goldman, M. & Scully, J. R. Corrosion-resistant metallic coatings. *Materials Today* **11**, 14–23 (2008).
68. Juhl, A. D. Overview of anodizing in the aerospace industry. *Metal Finishing* **108**, 20–21 (2010).
69. Landolt, D. Protection of Engineering Systems Against Corrosion. in *Corrosion and surface chemistry of metals* (EPFL Press, 2007).
70. Whelan, M., Barton, K., Cassidy, J., Colreavy, J. & Duffy, B. Corrosion inhibitors for anodised aluminium. *Surface and Coatings Technology* **227**, 75–83 (2013).
71. *Aluminum: properties and physical metallurgy*. (American Society for Metals, 1984).
72. Qi, J.-T. *et al.* Trivalent chromium conversion coating formation on aluminium. *Surface and Coatings Technology* **280**, 317–329 (2015).
73. Ohya, Y. Aqueous Precursors. in *Handbook of sol-gel science and technology: processing, characterization and applications* **25** (2018).
74. Catauro, M., Mozzati, M. C. & Bollino, F. Sol–gel hybrid materials for aerospace applications: Chemical characterization and comparative investigation of the magnetic properties. *Acta Astronautica* **117**, 153–162 (2015).
75. Salazar-Banda, G. R., Moraes, S. R., Motheo, A. J. & Machado, S. A. S. Anticorrosive cerium-based coatings prepared by the sol–gel method. *Journal of Sol-Gel Science and Technology* **52**, 415–423 (2009).
76. Blohowiak, K. Y., Osborne, J. H. & Seebergh, J. E. Development and Implementation of Sol-Gel Coatings for Aerospace Applications. in (2009). doi:10.4271/2009-01-3208
77. Liu, J. *et al.* Effect of Surface Morphology on Crack Growth at a Sol-Gel Reinforced Epoxy/Aluminum Interface. *The Journal of Adhesion* **82**, 487–516 (2006).

Chapter I - Bibliographic review

78. Le Blanc, Luc, Campazzi, Elisa & Savigne, Patrick. Sol for Sol-gel Process Coating of a Surface and Coating Method by Sol-gel Process using same. *15* (2009).
79. Varley, R. J., Simmonds, E. K., Seebergh, J. E. & Berry, D. H. Investigation of factors impacting the in-service degradation of aerospace coatings. *Progress in Organic Coatings* **74**, 679–686 (2012).
80. Moghim, T. B., Abel, M.-L. & Watts, J. F. A novel approach to the assessment of aerospace coatings degradation: The HyperTest. *Progress in Organic Coatings* **104**, 223–231 (2017).
81. Klomjit, P. & Buchheit, R. G. Characterization of inhibitor storage and release from commercial primers. *Progress in Organic Coatings* **114**, 68–77 (2018).
82. Allahar, K. N., Battocchi, D., Bierwagen, G. & Tallman, D. Thermal Degradation of a Mg-Rich Primer on AA 2024-T3. in 75–89 (2009). doi:10.1149/1.3259800
83. van Ooij, W. J. & Puomi, P. Environmental and Solubility Issues Related to Novel Corrosion Control. in *Thermodynamics, solubility and environmental issues* (eds. International Association of Chemical Thermodynamics & International Union of Pure and Applied Chemistry) (Elsevier, 2007).
84. Cohen, S. M. Replacements for Chromium Pretreatments on Aluminum. *Corrosion* **51**, 71–78 (1995).
85. Svehla, G. Nomenclature of kinetic methods of analysis (IUPAC Recommendations 1993). *Pure and Applied Chemistry* **65**, 2291–2298 (1993).
86. Cordier, P., Tournilhac, F., Soulié-Ziakovic, C. & Leibler, L. Self-healing and thermoreversible rubber from supramolecular assembly. *Nature* **451**, 977–980 (2008).
87. Calle, L., Hintze, P., Li, W. & Buhrow, J. Smart Coatings for Autonomous Corrosion Detection and Control. in *AIAA SPACE 2010 Conference & Exposition* (American Institute of Aeronautics and Astronautics, 2010). doi:10.2514/6.2010-8877
88. White, S. R. *et al.* Autonomic healing of polymer composites. *Nature* **409**, 794–797 (2001).
89. Fickert, J., Rupper, P., Graf, R., Landfester, K. & Crespy, D. Design and characterization of functionalized silica nanocontainers for self-healing materials. *Journal of Materials Chemistry* **22**, 2286–2291 (2012).
90. Jackson, A. C., Bartelt, J. A., Marczewski, K., Sottos, N. R. & Braun, P. V. Silica-Protected Micron and Sub-Micron Capsules and Particles for Self-Healing at the Microscale. *Macromolecular Rapid Communications* **32**, 82–87 (2011).
91. Lee, M. W., Sett, S., Yoon, S. S. & Yarin, A. L. Self-healing of nanofiber-based composites in the course of stretching. *Polymer* **103**, 180–188 (2016).
92. Hillewaere, X. K. D. *et al.* Autonomous Self-Healing of Epoxy Thermosets with Thiol-Isocyanate Chemistry. *Advanced Functional Materials* **24**, 5575–5583 (2014).
93. Dong-Min Kim *et al.* Low-Temperature Self-Healing of a Microcapsule-Type Protective Coating. *Materials* **10**, 1079 (2017).
94. Thanawala, K., Khanna, A. S., Raman, R. K. & others. Development of Self-Healing Coatings Using Encapsulated Linseed oil and Tung Oil as Healing Agents. in *NACE Corrosion 2016* (NACE International, 2016).
95. Siva, T. & Sathiyarayanan, S. Self healing coatings containing dual active agent loaded urea formaldehyde (UF) microcapsules. *Progress in Organic Coatings* **82**, 57–67 (2015).
96. Szabó, T., Telegdi, J. & Nyikos, L. Linseed oil-filled microcapsules containing drier and corrosion inhibitor – Their effects on self-healing capability of paints. *Progress in Organic Coatings* **84**, 136–142 (2015).
97. Yang, J., Keller, M. W., Moore, J. S., White, S. R. & Sottos, N. R. Microencapsulation of Isocyanates for Self-Healing Polymers. *Macromolecules* **41**, 9650–9655 (2008).
98. Yi, H., Yang, Y., Gu, X., Huang, J. & Wang, C. Multilayer composite microcapsules synthesized by Pickering emulsion templates and their application in self-healing coating. *Journal of Materials Chemistry A* **3**, 13749–13757 (2015).
99. Haghayegh, M., Mirabedini, S. M. & Yeganeh, H. Microcapsules containing multi-functional reactive isocyanate-terminated polyurethane prepolymer as a healing agent. Part 1: synthesis and optimization of reaction conditions. *Journal of Materials Science* **51**, 3056–3068 (2016).
100. Khun, N. W., Sun, D. W., Huang, M. X., Yang, J. L. & Yue, C. Y. Wear resistant epoxy composites with diisocyanate-based self-healing functionality. *Wear* **313**, 19–28 (2014).
101. Keller, M. W., Hampton, K. & McLaury, B. Self-healing of erosion damage in a polymer coating. *Wear* **307**, 218–225 (2013).

Chapter I - Bibliographic review

102. Huang, M. & Yang, J. Salt spray and EIS studies on HDI microcapsule-based self-healing anticorrosive coatings. *Progress in Organic Coatings* **77**, 168–175 (2014).
103. Spernath, L. & Magdassi, S. Polyurea nanocapsules obtained from nano-emulsions prepared by the phase inversion temperature method. *Polymers for Advanced Technologies* **22**, 2469–2473 (2011).
104. Meng, L. M., Yuan, Y. C., Rong, M. Z. & Zhang, M. Q. A dual mechanism single-component self-healing strategy for polymers. *Journal of Materials Chemistry* **20**, 6030 (2010).
105. Kuhl, N. *et al.* Urethanes as reversible covalent moieties in self-healing polymers. *European Polymer Journal* **104**, 45–50 (2018).
106. Kötteritzsch, J. *et al.* One-Component Intrinsic Self-Healing Coatings Based on Reversible Crosslinking by Diels-Alder Cycloadditions. *Macromolecular Chemistry and Physics* **214**, 1636–1649 (2013).
107. Chyzewski, E. & Evans, U. R. The Classification of Anodic and Cathodic Inhibitors. *Transactions of The Electrochemical Society* **76**, 215 (1939).
108. Ali, M. R., Mustafa, C. M. & Habib, M. Effect of Molybdate, Nitrite and Zinc Ions on the Corrosion Inhibition of Mild Steel in Aqueous Chloride Media Containing Cupric Ions. *Journal of Scientific Research* **1**, (2008).
109. Jonassen, H. B. Zinc as a Cathodic Inhibitor. *Corrosion* **14**, 39–40 (1958).
110. Thornhill, R. S. Zinc, Manganese, and Chromic Salts as Corrosion, Inhibitors. *Industrial & Engineering Chemistry* **37**, 706–708 (1945).
111. Scully, J. R. & Jakab, M. A. Design of Cathodic Inhibitors for AA2024-T3 Guided by Understanding Heterogeneous Cathodic Reaction Kinetics. in **1**, 47–63 (ECS, 2006).
112. Aldykewicz, A. J. The Investigation of Cerium as a Cathodic Inhibitor for Aluminum-Copper Alloys. *Journal of The Electrochemical Society* **142**, 3342 (1995).
113. Matter, E. A., Kozhukharov, S., Machkova, M. & Kozhukharov, V. Comparison between the inhibition efficiencies of Ce(III) and Ce(IV) ammonium nitrates against corrosion of AA2024 aluminum alloy in solutions of low chloride concentration. *Corrosion Science* **62**, 22–33 (2012).
114. Li, X., Deng, S., Fu, H. & Mu, G. Synergistic inhibition effect of rare earth cerium(IV) ion and sodium oleate on the corrosion of cold rolled steel in phosphoric acid solution. *Corrosion Science* **52**, 1167–1178 (2010).
115. Nam, N. D., Hien, P. V., Hoai, N. T. & Thu, V. T. H. A study on the mixed corrosion inhibitor with a dominant cathodic inhibitor for mild steel in aqueous chloride solution. *Journal of the Taiwan Institute of Chemical Engineers* (2018). doi:10.1016/j.jtice.2018.06.007
116. Muster, T. H. *et al.* An investigation of rare earth chloride mixtures: combinatorial optimisation for AA2024-t3 corrosion inhibition. *Surface and Interface Analysis* **42**, 170–174 (2010).
117. Eaves, D., Williams, G. & McMurray, H. N. Inhibition of self-corrosion in magnesium by poisoning hydrogen recombination on iron impurities. *Electrochimica Acta* **79**, 1–7 (2012).
118. *Innovative pre-treatment techniques to prevent corrosion of metallic surfaces*. (CRC [u.a.], 2007).
119. Kendig, M., Jeanjaquet, S., Addison, R. & Waldrop, J. Role of hexavalent chromium in the inhibition of corrosion of aluminum alloys. *Surface and Coatings Technology* **140**, 58–66 (2001).
120. Le Bozec, N., Joiret, S., Thierry, D. & Persson, D. The Role of Chromate Conversion Coating in the Filiform Corrosion of Coated Aluminum Alloys. *Journal of The Electrochemical Society* **150**, B561 (2003).
121. Frankel, G. S. & McCreery, R. L. Inhibition of Al Alloy Corrosion by Chromates. *The Electrochemical Society Interface* **5** (2001).
122. Sastri, V. S. & Revie, R. W. *Green Corrosion Inhibitors: Theory and Practice*.
123. Refaey, S. A. M., Abd El-Rehim, S. S., Taha, F., Saleh, M. B. & Ahmed, R. A. Inhibition of chloride localized corrosion of mild steel by PO₄³⁻, CrO₄²⁻, MoO₄²⁻, and NO₂⁻ anions. *Applied Surface Science* **158**, 190–196 (2000).
124. Karim, S., Mustafa, C. M., Assaduzzaman, Md. & Islam, M. Effect of nitrite ion on corrosion inhibition of mild steel in simulated cooling water. *Chemical Engineering Research Bulletin* **14**, (2010).
125. Kakaroglou, A., Domini, M. & De Graeve, I. Encapsulation and incorporation of sodium molybdate in polyurethane coatings and study of its corrosion inhibition on mild steel. *Surface and Coatings Technology* **303**, 330–341 (2016).

Chapter I - Bibliographic review

126. Lopez-Garrity, O. & Frankel, G. S. Corrosion Inhibition of Aluminum Alloy 2024-T3 by Sodium Molybdate. *Journal of the Electrochemical Society* **161**, C95–C106 (2013).
127. Saji, V. S. & Shibli, S. M. A. Synergistic inhibition of carbon steel corrosion by sodium tungstate and sodium silicate in neutral aqueous media. *Anti-Corrosion Methods and Materials* **49**, 433–443 (2002).
128. Kader, J. M. A. E., Warraky, A. A. E. & Aziz, A. M. A. E. Corrosion inhibition of mild steel by sodium tungstate in neutral solution Part 1: Behaviour in distilled water. *British Corrosion Journal* **33**, 139–144 (1998).
129. Robertson, W. D. Molybdate and Tungstate as Corrosion Inhibitors and the Mechanism of Inhibition. *Journal of The Electrochemical Society* **98**, 94 (1951).
130. Lopez-Garrity, O. & Frankel, G. S. Corrosion Inhibition of AA2024-T3 By Sodium Silicate. *Electrochimica Acta* **130**, 9–21 (2014).
131. Valcarce, M. B. & Vázquez, M. Phosphate ions used as green inhibitor against copper corrosion in tap water. *Corrosion Science* **52**, 1413–1420 (2010).
132. Jakab, M. A., Presuel-Moreno, F. & Scully, J. R. Critical Concentrations Associated with Cobalt, Cerium, and Molybdenum Inhibition of AA2024-T3 Corrosion: Delivery from Al-Co-Ce(-Mo) Alloys. *Corrosion* **61**, 246–263 (2005).
133. Saranya, J. *et al.* N-heterocycles as corrosion inhibitors for mild steel in acid medium. *Journal of Molecular Liquids* **216**, 42–52 (2016).
134. Rose, K., Kim, B.-S., Rajagopal, K., Arumugam, S. & Devarayan, K. Surface protection of steel in acid medium by *Tabernaemontana divaricata* extract: Physicochemical evidence for adsorption of inhibitor. *Journal of Molecular Liquids* **214**, 111–116 (2016).
135. Ibrahim, T., Gomes, E., Obot, I. B., Khamis, M. & Abou Zour, M. Corrosion inhibition of mild steel by *Calotropis p. ropera* leaves extract in a CO₂ saturated sodium chloride solution. *Journal of Adhesion Science and Technology* **30**, 2523–2543 (2016).
136. De Souza, F. S. & Spinelli, A. Caffeic acid as a green corrosion inhibitor for mild steel. *Corrosion Science* **51**, 642–649 (2009).
137. Taj, S., Siddekha, A., Papavinasam, S. & Revie, R. W. Some Natural Products As Green Corrosion Inhibitors. in *NACE* (NACE International, 2007).
138. Eddy, N. O. & Odoemelam, S. A. Inhibition of corrosion of mild steel in acidic medium using ethanol extract of *Aloe vera*. *Pigment & Resin Technology* **38**, 111–115 (2009).
139. Abd-El-Nabey, B. A., Goher, Y. M., Fetouh, H. A. & Karam, M. S. Anticorrosive Properties of Chitosan for the Acid Corrosion of Aluminium: *Portugaliae Electrochimica Acta* **33**, 231–239 (2015).
140. Umoren, S. A., AlAhmary, A. A., Gasem, Z. M. & Solomon, M. M. Evaluation of chitosan and carboxymethyl cellulose as ecofriendly corrosion inhibitors for steel. *International Journal of Biological Macromolecules* **117**, 1017–1028 (2018).
141. Yang, S., Wen, Y., Yi, P., Xiao, K. & Dong, C. Effects of chitosan inhibitor on the electrochemical corrosion behavior of 2205 duplex stainless steel. *International Journal of Minerals, Metallurgy, and Materials* **24**, 1260–1266 (2017).
142. Choi, H., Kim, K. Y. & Park, J. M. Encapsulation of aliphatic amines into nanoparticles for self-healing corrosion protection of steel sheets. *Progress in Organic Coatings* **76**, 1316–1324 (2013).
143. Falcón, J. M., Batista, F. F. & Aoki, I. V. Encapsulation of dodecylamine corrosion inhibitor on silica nanoparticles. *Electrochimica Acta* **124**, 109–118 (2014).
144. Harvey, T. G. *et al.* The effect of inhibitor structure on the corrosion of AA2024 and AA7075. *Corrosion Science* **53**, 2184–2190 (2011).
145. Marathe, R. J. & Gite, V. V. Encapsulation of 8-HQ as a corrosion inhibitor in PF and UF shells for enhanced anticorrosive properties of renewable source based smart PU coatings. *RSC Advances* **6**, 114436–114446 (2016).
146. Kartsonakis, I. A. *et al.* Multifunctional epoxy coatings combining a mixture of traps and inhibitor loaded nanocontainers for corrosion protection of AA2024-T3. *Corrosion Science* **85**, 147–159 (2014).
147. Haase, M. F., Grigoriev, D. O., Möhwald, H. & Shchukin, D. G. Development of Nanoparticle Stabilized Polymer Nanocontainers with High Content of the Encapsulated Active Agent and Their Application in Water-Borne Anticorrosive Coatings. *Advanced Materials* **24**, 2429–2435 (2012).
148. Snihirova, D. *et al.* pH-sensitive polymeric particles with increased inhibitor-loading capacity as smart additives for corrosion protective coatings for AA2024. *Electrochimica Acta* **145**, 123–131 (2014).

Chapter I - Bibliographic review

149. Montemor, M. F. *et al.* Evaluation of self-healing ability in protective coatings modified with combinations of layered double hydroxides and cerium molybdate nanocontainers filled with corrosion inhibitors. *Electrochimica Acta* **60**, 31–40 (2012).
150. Kopeć, M. *et al.* Self-healing epoxy coatings loaded with inhibitor-containing polyelectrolyte nanocapsules. *Progress in Organic Coatings* **84**, 97–106 (2015).
151. Maia, F. *et al.* Corrosion protection of AA2024 by sol–gel coatings modified with MBT-loaded polyurea microcapsules. *Chemical Engineering Journal* **283**, 1108–1117 (2016).
152. Plawecka, M. *et al.* Self healing ability of inhibitor-containing nanocapsules loaded in epoxy coatings applied on aluminium 5083 and galvaneal substrates. *Electrochimica Acta* **140**, 282–293 (2014).
153. Balaskas, A. C., Curioni, M. & Thompson, G. E. Effectiveness of 2-mercaptobenzothiazole, 8-hydroxyquinoline and benzotriazole as corrosion inhibitors on AA 2024-T3 assessed by electrochemical methods. *Surface and Interface Analysis* **47**, 1029–1039 (2015).
154. Yu, D., Wang, J., Hu, W. & Guo, R. Preparation and controlled release behavior of halloysite/2-mercaptobenzothiazole nanocomposite with calcined halloysite as nanocontainer. *Materials & Design* **129**, 103–110 (2017).
155. Buchheit, R. G., Guan, H., Mahajanam, S. & Wong, F. Active corrosion protection and corrosion sensing in chromate-free organic coatings. *Progress in Organic Coatings* **47**, 174–182 (2003).
156. Pech-Canul, M. A. & Echeverria, M. Corrosion inhibition of steel in neutral chloride solutions by mixtures of N-phosphono-methylglycine with zinc ions. *Corrosion Engineering, Science and Technology* **38**, 135–138 (2003).
157. Snihirova, D., Taryba, M., Lamaka, S. V. & Montemor, M. F. Corrosion inhibition synergies on a model Al-Cu-Mg sample studied by localized scanning electrochemical techniques. *Corrosion Science* **112**, 408–417 (2016).
158. Giuliani, C. *et al.* Chitosan-based coatings for corrosion protection of copper-based alloys: A promising more sustainable approach for cultural heritage applications. *Progress in Organic Coatings* **122**, 138–146 (2018).
159. *Techniques for Corrosion Monitoring*. (CRC Press, 2008).
160. Gan, F., Tian, G., Wan, Z., Liao, J. & Li, W. Investigation of pitting corrosion monitoring using field signature method. *Measurement* **82**, 46–54 (2016).
161. Bardal, E. Corrosion Testing, Monitoring and Inspection. in *Corrosion and protection* (Springer, 2005).
162. *Corrosion control in the aerospace industry*. (CRC Press [u.a.], 2009).
163. Komorowski, J. P., Forsyth, D. S., Simpson, D. L. & Gould, R. W. Probability of Detection of Corrosion in Aircraft Structures. 9
164. Nascov, V., Samoila, C. & Ursutiu, D. Corrosion monitoring by optical inspection with coherent and incoherent light. *Optoelectronics and Advanced Materials - Rapid Communications* 9
165. Denissen, P. J. & Garcia, S. J. Cerium-loaded algae exoskeletons for active corrosion protection of coated AA2024-T3. *Corrosion Science* **128**, 164–175 (2017).
166. Kathy Riggs Larsen. Sensors Can Predict Corrosive Conditions in Military Aircraft. *NACE International* **54**, 32–36 (2015).
167. Prosek, T., Taube, M., Dubois, F. & Thierry, D. Application of automated electrical resistance sensors for measurement of corrosion rate of copper, bronze and iron in model indoor atmospheres containing short-chain volatile carboxylic acids. *Corrosion Science* **87**, 376–382 (2014).
168. Kouril, M., Prosek, T., Scheffel, B. & Dubois, F. High sensitivity electrical resistance sensors for indoor corrosion monitoring. *Corrosion Engineering, Science and Technology* **48**, 282–287 (2013).
169. Rocchini, G. Corrosion rate monitoring by the linear polarization method. *Corrosion Science* **34**, 2031–2044 (1993).
170. Choudhary, S., Garg, A. & Mondal, K. Relation Between Open Circuit Potential and Polarization Resistance with Rust and Corrosion Monitoring of Mild Steel. *Journal of Materials Engineering and Performance* **25**, 2969–2976 (2016).
171. Tan, Y. J., Bailey, S. & Kinsella, B. The monitoring of the formation and destruction of corrosion inhibitor films using electrochemical noise analysis (ENA). *Corrosion Science* **38**, 1681–1695 (1996).

Chapter I - Bibliographic review

172. Salinas-Bravo, V. M., Porcayo-Calderon, J. & Gonzalez-Rodriguez, J. G. Corrosion monitoring using electrochemical noise and linear polarization resistance in fuel oil combustion gas environment. *Russian Journal of Electrochemistry* **42**, 560–565 (2006).
173. Darowicki, K. & Majewska, J. Harmonic Analysis Of Electrochemical and Corrosion Systems - A Review. *Corrosion Reviews* **17**, (1999).
174. Bosch, R. W. Harmonic Analysis of Corroding Systems Considering Diffusion Phenomena. *Journal of The Electrochemical Society* **143**, 4033 (1996).
175. Le Thu, Q., Takenouti, H. & Touzain, S. EIS characterization of thick flawed organic coatings aged under cathodic protection in seawater. *Electrochimica Acta* **51**, 2491–2502 (2006).
176. Mansfeld, F. Use of electrochemical impedance spectroscopy for the study of corrosion protection by polymer coatings. *Journal of Applied Electrochemistry* **25**, (1995).
177. Li, B. Y. & Zhang, W. Metal corrosion monitoring with acoustic emission technique. *Materials Research Innovations* **19**, S8-873-S8-876 (2015).
178. Zou, F. & Cegla, F. B. On quantitative corrosion rate monitoring with ultrasound. *Journal of Electroanalytical Chemistry* **812**, 115–121 (2018).
179. Blackford, R. Performance demands on aerospace paints relative to environmental legislation. *Aircraft Engineering and Aerospace Technology* **70**, 451–455 (1998).
180. Edalati, K., Rastkhah, N., Kermani, A., Seiedi, M. & Movafeghi, A. The use of radiography for thickness measurement and corrosion monitoring in pipes. *International Journal of Pressure Vessels and Piping* **83**, 736–741 (2006).
181. Zscherpel, U. *et al.* Radiographic Evaluation of Corrosion and Deposits in Pipelines: Results of an IAEA Co-ordinated Research Programme. *European Conference on NDT* **15**
182. Sun, Y., Ouyang, T. & Udpa, S. S. Recent advances in remote field eddy current NDE techniques and their applications in detection, characterization, and monitoring of deeply hidden corrosion in aircraft structures. in (ed. Mal, A. K.) 200–210 (1999). doi:10.1117/12.339905
183. He, Y. *et al.* Steel Corrosion Characterization Using Pulsed Eddy Current Systems. *IEEE Sensors Journal* **12**, 2113–2120 (2012).
184. Sodano, H. A. Development of an Automated Eddy Current Structural Health Monitoring Technique with an Extended Sensing Region for Corrosion Detection. *Structural Health Monitoring: An International Journal* **6**, 111–119 (2007).
185. Legat, A. Monitoring of steel corrosion in concrete by electrode arrays and electrical resistance probes. *Electrochimica Acta* **52**, 7590–7598 (2007).
186. Bagavathiappan, S., Lahiri, B. B., Saravanan, T., Philip, J. & Jayakumar, T. Infrared thermography for condition monitoring – A review. *Infrared Physics & Technology* **60**, 35–55 (2013).
187. Yang, R., He, Y., Zhang, H. & Huang, S. Through coating imaging and nondestructive visualization evaluation of early marine corrosion using electromagnetic induction thermography. *Ocean Engineering* **147**, 277–288 (2018).
188. Opel, O., Eggerichs, T., Otte, T. & Ruck, W. K. L. Monitoring of microbially mediated corrosion and scaling processes using redox potential measurements. *Bioelectrochemistry* **97**, 137–144 (2014).
189. Colbert, R. & Reich, R. *Corrosion monitoring of a water based rolling facility with coupled multielectrode array sensors and the correlations with other process variables: Conductivity, pH, temperature, dissolved oxygen and corrosion potential.* (2008).
190. Nguyen, T. H. *et al.* Fluorescence based fibre optic pH sensor for the pH 10–13 range suitable for corrosion monitoring in concrete structures. *Sensors and Actuators B: Chemical* **191**, 498–507 (2014).
191. Liu, G. & Wheat, H. G. Use of a Fluorescent Indicator in Monitoring Underlying Corrosion on Coated Aluminum 2024-T4. *Journal of The Electrochemical Society* **156**, C160 (2009).
192. Uzundal, C. B. & Ulgut, B. Method for visualizing under-coating corrosion utilizing pH indicators before visible damage. *Progress in Organic Coatings* **122**, 72–78 (2018).
193. Banks, J., Reichard, K., Sinding, K., Ledford, K. & Tittmann, B. R. Embedded wireless corrosion detection technology. in *2016 IEEE Aerospace Conference* 1–7 (IEEE, 2016). doi:10.1109/AERO.2016.7500562
194. Deng, F., Huang, Y., Azarmi, F. & Wang, Y. Pitted Corrosion Detection of Thermal Sprayed Metallic Coatings Using Fiber Bragg Grating Sensors. *Coatings* **7**, 35 (2017).

Chapter I - Bibliographic review

195. Deng, F., Huang, Y. & Azarmi, F. Corrosion detection for steel with soft coating using in-line fiber Bragg grating sensor. in (ed. Lynch, J. P.) 101681R (2017). doi:10.1117/12.2260260
196. Dhole, G. S., Gunasekaran, G., Singh, S. K. & Vinjamur, M. Smart corrosion sensing phenanthroline modified alkyd coatings. *Progress in Organic Coatings* **89**, 8–16 (2015).
197. Dhole, G. S., Gunasekaran, G., Ghorpade, T. & Vinjamur, M. Smart acrylic coatings for corrosion detection. *Progress in Organic Coatings* **110**, 140–149 (2017).
198. Trinchi, A., Muster, T. H., Cole, I. S., Dunlop, J. B. & Collocott, S. J. Embedded magnetic nanoparticle sensors for monitoring primer failure beneath paint. *Sensors and Actuators B: Chemical* **210**, 446–452 (2015).
199. Farmer, J. C. Paint for Detection of Corrosion and Warning of Chemical and Radiological Attack. 13 (2011).
200. Zhang, J. & Frankel, G. S. Corrosion-Sensing Behavior of an Acrylic-Based Coating System. *Corrosion* **55**, 957–967 (1999).
201. Song-mei, L. Preparation and performance of fluorescent sensing coating for monitoring corrosion of Al alloy 2024. *Transactions of Nonferrous Metals Society of China* **6** (2006).
202. Orlicki, J. A., Williams, A. A., Labukas, J., Escarsega, J. A. & Placzankis, B. Nondestructive Early Detection of Metal Corrosion in Pigmented Coatings with Fluorescent Smart Materials (First-year Report). 24
203. Liu, G. Fluorescent Coatings for Corrosion Detection in Steel and Aluminum Alloys. (University of Texas, 2010).
204. Roshan, S., Sarabi Dariani, A. A. & Mokhtari, J. Monitoring underlying epoxy-coated St-37 corrosion via 8-hydroxyquinoline as a fluorescent indicator. *Applied Surface Science* **440**, 880–888 (2018).
205. Augustyniak, A., Tsavalas, J. & Ming, W. Early Detection of Steel Corrosion via “Turn-On” Fluorescence in Smart Epoxy Coatings. *ACS Applied Materials & Interfaces* **1**, 2618–2623 (2009).
206. Augustyniak, A. & Ming, W. Early detection of aluminum corrosion via “turn-on” fluorescence in smart coatings. *Progress in Organic Coatings* **71**, 406–412 (2011).
207. Galvão, T. L. P. *et al.* Improving the functionality and performance of AA2024 corrosion sensing coatings with nanocontainers. *Chemical Engineering Journal* **341**, 526–538 (2018).
208. Raps, D. *et al.* Electrochemical study of inhibitor-containing organic–inorganic hybrid coatings on AA2024. *Corrosion Science* **51**, 1012–1021 (2009).
209. Trask, R. S., Williams, G. J. & Bond, I. P. Bioinspired self-healing of advanced composite structures using hollow glass fibres. *Journal of The Royal Society Interface* **4**, 363–371 (2007).
210. Pang, J. W. C. & Bond, I. P. A hollow fibre reinforced polymer composite encompassing self-healing and enhanced damage visibility. *Composites Science and Technology* **65**, 1791–1799 (2005).
211. Xu, J. *et al.* Chloride removal and corrosion inhibitions of nitrate, nitrite-intercalated Mg Al layered double hydroxides on steel in saturated calcium hydroxide solution. *Applied Clay Science* **163**, 129–136 (2018).
212. Vert, M. *et al.* Terminology for biorelated polymers and applications (IUPAC Recommendations 2012). *Pure and Applied Chemistry* **84**, 377–410 (2012).
213. Bancroft, W. D. The Theory of Emulsification, I. *The Journal of Physical Chemistry* **16**, 177–233 (1911).
214. Griffin, C. William. Classification of Surface-Active Agents by ‘HLB’. *J. of Cosm. Sc.* **1**, 311–326 (1949).
215. Porter, M. R. *Handbook of Surfactants*. (Springer US, 1991). doi:10.1007/978-1-4757-1293-3
216. Arriagada, F. J. & Osseo-Asare, K. Synthesis of Nanosize Silica in a Nonionic Water-in-Oil Microemulsion: Effects of the Water/Surfactant Molar Ratio and Ammonia Concentration. *Journal of Colloid and Interface Science* **211**, 210–220 (1999).
217. Marie, E., Rothe, R., Antonietti, M. & Landfester, K. Synthesis of Polyaniline Particles via Inverse and Direct Miniemulsion. *Macromolecules* **36**, 3967–3973 (2003).
218. Li, W. *et al.* Microencapsulation of Corrosion Indicators for Smart Coatings. (2011).
219. Wald, S., Wurm, F., Landfester, K. & Crespy, D. Stabilization of Inverse Miniemulsions by Silyl-Protected Homopolymers. *Polymers* **8**, 303 (2016).
220. Calle, L. M. & Li, Wenyan. Coatings and Methods For Corrosion Detection And/Or Reuction. 5 (2010).

221. Pornsunthorntawe, O., Chavadej, S. & Rujiravanit, R. Solution properties and vesicle formation of rhamnolipid biosurfactants produced by *Pseudomonas aeruginosa* SP4. *Colloids and Surfaces B: Biointerfaces* **72**, 6–15 (2009).
222. Matsuda, T. *et al.* Self-healing ability and particle size effect of encapsulated cerium nitrate into pH sensitive microcapsules. *Progress in Organic Coatings* **90**, 425–430 (2016).
223. Sides, R., Yarwood, J. & Fox, K. An FTIR study of the adsorption of surfactants on silica. *Mikrochimica Acta* **95**, 93–96 (1988).
224. Rosenbauer, E.-M., Landfester, K. & Musyanovych, A. Surface-Active Monomer as a Stabilizer for Polyurea Nanocapsules Synthesized via Interfacial Polyaddition in Inverse Miniemulsion. *Langmuir* **25**, 12084–12091 (2009).
225. Myers, D. *Surfaces, Interfaces, and Colloids*. (John Wiley & Sons, Inc., 1999). doi:10.1002/0471234990
226. Koppula, K. S., Fan, R., Veerapalli, K. R. & Wan, J. Integrated microfluidic system with simultaneous emulsion generation and concentration. *Journal of Colloid and Interface Science* **466**, 162–167 (2016).
227. Kopeć, M., Szczepanowicz, K., Warszyński, P. & Nowak, P. Liquid-core polyelectrolyte nanocapsules produced by membrane emulsification as carriers for corrosion inhibitors. *Colloids and Surfaces A: Physicochemical and Engineering Aspects* **510**, 2–10 (2016).
228. Li, J., Mazumder, M. A. J., Stöver, H. D. H., Hitchcock, A. P. & Shirley, I. M. Polyurea microcapsules: Surface modification and capsule size control. *Journal of Polymer Science Part A: Polymer Chemistry* **49**, 3038–3047 (2011).
229. Maia, F., Tedim, J., Bastos, A. C., Ferreira, M. G. S. & Zheludkevich, M. L. Active sensing coating for early detection of corrosion processes. *RSC Advances* **4**, 17780 (2014).
230. Huang, M. & Yang, J. Facile microencapsulation of HDI for self-healing anticorrosion coatings. *Journal of Materials Chemistry* **21**, 11123 (2011).
231. Crespy, D., Stark, M., Hoffmann-Richter, C., Ziener, U. & Landfester, K. Polymeric Nanoreactors for Hydrophilic Reagents Synthesized by Interfacial Polycondensation on Miniemulsion Droplets. *Macromolecules* **40**, 3122–3135 (2007).
232. Lv, L.-P. *et al.* Redox Responsive Release of Hydrophobic Self-Healing Agents from Polyaniline Capsules. *Journal of the American Chemical Society* **135**, 14198–14205 (2013).
233. Lv, L.-P., Landfester, K. & Crespy, D. Stimuli-Selective Delivery of two Payloads from Dual Responsive Nanocontainers. *Chemistry of Materials* **26**, 3351–3353 (2014).
234. Vimalanandan, A. *et al.* Redox-Responsive Self-Healing for Corrosion Protection. *Advanced Materials* **25**, 6980–6984 (2013).
235. Tran, H. D. *et al.* The oxidation of aniline to produce “polyaniline”: a process yielding many different nanoscale structures. *J. Mater. Chem.* **21**, 3534–3550 (2011).
236. Li, J., Hitchcock, A. P., Stöver, H. D. H. & Shirley, I. A New Approach to Studying Microcapsule Wall Growth Mechanisms. *Macromolecules* **42**, 2428–2432 (2009).
237. Li, G., Feng, Y., Gao, P. & Li, X. Preparation of Mono-Dispersed Polyurea-Urea Formaldehyde Double Layered Microcapsules. *Polymer Bulletin* **60**, 725–731 (2008).
238. Huang, M. & Yang, J. Facile microencapsulation of HDI for self-healing anticorrosion coatings. *Journal of Materials Chemistry* **21**, 11123 (2011).
239. Maia, F., Tedim, J., Bastos, A. C., Ferreira, M. G. S. & Zheludkevich, M. L. Nanocontainer-based corrosion sensing coating. *Nanotechnology* **24**, 415502 (2013).
240. Liang, Y. *et al.* Development of Novel Urease-Responsive Pendimethalin Microcapsules Using Silica-IPTS-PEI As Controlled Release Carrier Materials. *ACS Sustainable Chemistry & Engineering* **5**, 4802–4810 (2017).
241. Wu, G. *et al.* Robust microcapsules with polyurea/silica hybrid shell for one-part self-healing anticorrosion coatings. *Journal of Materials Chemistry A* **2**, 11614–11620 (2014).
242. Liang, Y. *et al.* Facile Synthesis of Smart Nanocontainers as Key Components for Construction of Self-Healing Coating with Superhydrophobic Surfaces. *Nanoscale Research Letters* **11**, (2016).
243. Cui, L. *et al.* Template-assisted synthesis of biodegradable and pH-responsive polymer capsules via RAFT polymerization for controlled drug release. *Materials Chemistry and Physics* **148**, 87–95 (2014).
244. Neema, S., Selvaraj, M., Raguraman, J. & Ramu, S. Investigating the self healing process on coated steel by SVET and EIS techniques. *Journal of Applied Polymer Science* **127**, 740–747 (2013).

Chapter I - Bibliographic review

245. Brown, E. N., Kessler, M. R., Sottos, N. R. & White, S. R. In situ poly(urea-formaldehyde) microencapsulation of dicyclopentadiene. *Journal of Microencapsulation* **20**, 719–730 (2003).
246. Jia, Y. *et al.* A combined interfacial and in-situ polymerization strategy to construct well-defined core-shell epoxy-containing SiO₂-based microcapsules with high encapsulation loading, super thermal stability and nonpolar solvent tolerance. *International Journal of Smart and Nano Materials* **7**, 221–235 (2016).
247. Shchukin, D. G. *et al.* Layer-by-Layer Assembled Nanocontainers for Self-Healing Corrosion Protection. *Advanced Materials* **18**, 1672–1678 (2006).
248. Shi, H., Wu, L., Wang, J., Liu, F. & Han, E.-H. Sub-micrometer mesoporous silica containers for active protective coatings on AA 2024-T3. *Corrosion Science* **127**, 230–239 (2017).
249. Feng, Yuanchao & Cheng, Frank. Self-healing pipeline epoxy coating. in 12 (2016).
250. Wu, Q.-X. *et al.* Self-assembly of polyelectrolyte complexes microcapsules with natural polysaccharides for sustained drug release. *Cellulose* **24**, 4949–4962 (2017).
251. Tavernier, I., Patel, A. R., Van der Meeren, P. & Dewettinck, K. Emulsion-templated liquid oil structuring with soy protein and soy protein: κ -carrageenan complexes. *Food Hydrocolloids* **65**, 107–120 (2017).
252. Lam, R. S. H. & Nickerson, M. T. The properties of whey protein–carrageenan mixtures during the formation of electrostatic coupled biopolymer and emulsion gels. *Food Research International* **66**, 140–149 (2014).
253. Liu, Y. *et al.* Formation and characterization of natural polysaccharide hollow nanocapsules via template layer-by-layer self-assembly. *Journal of Colloid and Interface Science* **379**, 130–140 (2012).
254. Iwata, N., Neves, M. A., Watanabe, J., Sato, S. & Ichikawa, S. Stability control of large oil droplets by layer-by-layer deposition using polyelectrolyte dietary fibers. *Colloids and Surfaces A: Physicochemical and Engineering Aspects* **440**, 2–9 (2014).
255. Kamburova, K., Mitarova, K. & Radeva, T. Polysaccharide-based nanocapsules for controlled release of indomethacin. *Colloids and Surfaces A: Physicochemical and Engineering Aspects* **519**, 199–204 (2017).
256. Luo, Y. & Wang, Q. Recent development of chitosan-based polyelectrolyte complexes with natural polysaccharides for drug delivery. *International Journal of Biological Macromolecules* **64**, 353–367 (2014).
257. Kurukji, D., Norton, I. & Spyropoulos, F. Fabrication of sub-micron protein-chitosan electrostatic complexes for encapsulation and pH-Modulated delivery of model hydrophilic active compounds. *Food Hydrocolloids* **53**, 249–260 (2016).
258. Sarmiento, B., Ferreira, D., Veiga, F. & Ribeiro, A. Characterization of insulin-loaded alginate nanoparticles produced by ionotropic pre-gelation through DSC and FTIR studies. *Carbohydrate Polymers* **66**, 1–7 (2006).
259. Yu, S., Hu, J., Pan, X., Yao, P. & Jiang, M. Stable and pH-Sensitive Nanogels Prepared by Self-Assembly of Chitosan and Ovalbumin. *Langmuir* **22**, 2754–2759 (2006).
260. De, S. Polymer relationships during preparation of chitosan–alginate and poly-l-lysine–alginate nanospheres. *Journal of Controlled Release* **89**, 101–112 (2003).
261. Huang, X. *et al.* Resveratrol encapsulation in core-shell biopolymer nanoparticles: Impact on antioxidant and anticancer activities. *Food Hydrocolloids* **64**, 157–165 (2017).
262. Kemala, T., Budianto, E. & Soegiyono, B. Preparation and characterization of microspheres based on blend of poly(lactic acid) and poly(ϵ -caprolactone) with poly(vinyl alcohol) as emulsifier. *Arabian Journal of Chemistry* **5**, 103–108 (2012).
263. Dowding, P. J., Atkin, R., Vincent, B. & Bouillot, P. Oil Core–Polymer Shell Microcapsules Prepared by Internal Phase Separation from Emulsion Droplets. I. Characterization and Release Rates for Microcapsules with Polystyrene Shells. *Langmuir* **20**, 11374–11379 (2004).
264. Wang, J.-P. *et al.* Adaptive Polymeric Coatings with Self-Reporting and Self-Healing Dual Functions from Porous Core-Shell Nanostructures. *Macromolecular Materials and Engineering* **303**, 1700616 (2018).
265. Cao, Z. *et al.* Preparation of polymeric/inorganic nanocomposite particles in miniemulsions: I. Particle formation mechanism in systems stabilized with sodium dodecyl sulfate. *Colloids and Surfaces A: Physicochemical and Engineering Aspects* **516**, 199–210 (2017).

Chapter I - Bibliographic review

266. Garkhal, K., Verma, S., Jonnalagadda, S. & Kumar, N. Fast degradable poly(L-lactide-co- ϵ -caprolactone) microspheres for tissue engineering: Synthesis, characterization, and degradation behavior. *Journal of Polymer Science Part A: Polymer Chemistry* **45**, 2755–2764 (2007).
267. Stöber, W., Fink, A. & Bohn, E. Controlled growth of monodisperse silica spheres in the micron size range. *Journal of Colloid and Interface Science* **26**, 62–69 (1968).
268. Clerc, C. Etude du mécanisme d'inhibition de la corrosion du cuivre par le 2-mercaptobenzothiazol. (1983). doi:10.5169/seals-74981
269. Raps, D., Hack, T., Kolb, M., Zheludkevich, M. L. & Nuyken, O. Development of Corrosion Protection Coatings for AA2024-T3 Using Micro-Encapsulated Inhibitors. in *Smart Coatings III* (eds. Baghdachi, J. & Provder, T.) **1050**, 165–189 (American Chemical Society, 2010).
270. Blaiszik, B. J., Sottos, N. R. & White, S. R. Nanocapsules for self-healing materials. *Composites Science and Technology* **68**, 978–986 (2008).
271. Keller, M. W. & Sottos, N. R. Mechanical Properties of Microcapsules Used in a Self-Healing Polymer. *Experimental Mechanics* **46**, 725–733 (2006).
272. Zhang, Z. Mechanical strength of single microcapsules determined by a novel micromanipulation technique. *Journal of Microencapsulation* **16**, 117–124 (1999).
273. Mercadé-Prieto, R. *et al.* Failure of elastic-plastic core-shell microcapsules under compression. *AIChE Journal* **58**, 2674–2681 (2012).
274. Bohlender, C., Landfester, K., Crespy, D. & Schiller, A. Unconventional Non-Aqueous Emulsions for the Encapsulation of a Phototriggerable NO-Donor Complex in Polymer Nanoparticles. *Particle & Particle Systems Characterization* **30**, 138–142 (2013).
275. Radhakrishnan, K., Tripathy, J., Gnanadhas, D. P., Chakravorty, D. & Raichur, A. M. Dual enzyme responsive and targeted nanocapsules for intracellular delivery of anticancer agents. *RSC Adv.* **4**, 45961–45968 (2014).
276. Aguirre, G., Ramos, J., Heuts, J. P. A. & Forcada, J. Biocompatible and thermo-responsive nanocapsule synthesis through vesicle templating. *Polym. Chem.* **5**, 4569–4579 (2014).
277. Baghdachi, J., Perez, H. & Shah, A. Design and Development of Self-Healing Polymers and Coatings. in *Smart Coatings III* (eds. Baghdachi, J. & Provder, T.) **1050**, 3–20 (American Chemical Society, 2010).
278. Maia, F. *et al.* Silica nanocontainers for active corrosion protection. *Nanoscale* **4**, 1287 (2012).
279. Rahsepar, M., Mohebbi, F. & Hayatdavoudi, H. Synthesis and characterization of inhibitor-loaded silica nanospheres for active corrosion protection of carbon steel substrate. *Journal of Alloys and Compounds* **709**, 519–530 (2017).
280. Körpe, D. A., Malekghasemi, S., Aydın, U. & Duman, M. Fabrication of monodispersive nanoscale alginate–chitosan core–shell particulate systems for controlled release studies. *Journal of Nanoparticle Research* **16**, (2014).
281. Staff, R. H. *et al.* Patchy Nanocapsules of Poly(vinylferrocene)-Based Block Copolymers for Redox-Responsive Release. *ACS Nano* **6**, 9042–9049 (2012).
282. Siva, T., Kamaraj, K. & Sathiyarayanan, S. Epoxy curing by polyaniline (PANI) – Characterization and self-healing evaluation. *Progress in Organic Coatings* **77**, 1095–1103 (2014).
283. Choi, H., Song, Y. K., Kim, K. Y. & Park, J. M. Encapsulation of triethanolamine as organic corrosion inhibitor into nanoparticles and its active corrosion protection for steel sheets. *Surface and Coatings Technology* **206**, 2354–2362 (2012).
284. Maia, F., Tedim, J., Bastos, A. C., Ferreira, M. G. S. & Zheludkevich, M. L. Active sensing coating for early detection of corrosion processes. *RSC Advances* **4**, 17780 (2014).
285. Huang, M., Zhang, H. & Yang, J. Synthesis of organic silane microcapsules for self-healing corrosion resistant polymer coatings. *Corrosion Science* **65**, 561–566 (2012).
286. Liang, Y. *et al.* Facile Synthesis of Smart Nanocontainers as Key Components for Construction of Self-Healing Coating with Superhydrophobic Surfaces. *Nanoscale Research Letters* **11**, (2016).
287. Maia, F. *et al.* Incorporation of biocides in nanocapsules for protective coatings used in maritime applications. *Chemical Engineering Journal* **270**, 150–157 (2015).
288. Wang, J.-P. *et al.* pH-Responsive Polymer Coatings for Reporting Early Stages of Metal Corrosion. *Macromolecular Materials and Engineering* **302**, 1700128 (2017).

Chapter I - Bibliographic review

289. Latnikova, A., Grigoriev, D. O., Möhwald, H. & Shchukin, D. G. Capsules Made of Cross-Linked Polymers and Liquid Core: Possible Morphologies and Their Estimation on the Basis of Hansen Solubility Parameters. *The Journal of Physical Chemistry C* **116**, 8181–8187 (2012).
290. Zhao, D., Liu, D. & Hu, Z. A smart anticorrosion coating based on hollow silica nanocapsules with inorganic salt in shells. *Journal of Coatings Technology and Research* **14**, 85–94 (2017).
291. Yasakau, K. A., Ferreira, M. G. S. & Zheludkevich, M. L. Sol-Gel Coatings with Nanocontainers of Corrosion Inhibitors for Active Corrosion Protection of Metallic Materials. in *Handbook of Sol-Gel Science and Technology* (eds. Klein, L., Aparicio, M. & Jitianu, A.) 1–37 (Springer International Publishing, 2017). doi:10.1007/978-3-319-19454-7_141-2
292. Samadzadeh, M., Boura, S. H., Peikari, M., Kasiriha, S. M. & Ashrafi, A. A review on self-healing coatings based on micro/nanocapsules. *Progress in Organic Coatings* **68**, 159–164 (2010).
293. Geng, J. *et al.* A ratiometric fluorescent probe for ferric ion based on a 2,2'-bithiazole derivative and its biological applications. *Sensors and Actuators B: Chemical* **222**, 612–617 (2016).
294. Wang, N., Diao, X., Zhang, J. & Kang, P. Corrosion Resistance of Waterborne Epoxy Coatings by Incorporation of Dopamine Treated Mesoporous-TiO₂ Particles. *Coatings* **8**, 209 (2018).
295. Astruc, A. *et al.* Incorporation of kaolin fillers into an epoxy/polyamidoamine matrix for coatings. *Progress in Organic Coatings* **65**, 158–168 (2009).
296. Lang, S. & Zhou, Q. Synthesis and characterization of poly(urea-formaldehyde) microcapsules containing linseed oil for self-healing coating development. *Progress in Organic Coatings* **105**, 99–110 (2017).
297. Jones, M. H. & Woodcock, J. T. UV spectrophotometric determination of 2-Mercaptobenzothiazole (MBT) in flotation liquors. *CANADIAN METALLURGICAL QUARTERLY* **12**, 9 (1973).
298. Zheludkevich, M. L., Yasakau, K. A., Poznyak, S. K. & Ferreira, M. G. S. Triazole and thiazole derivatives as corrosion inhibitors for AA2024 aluminium alloy. *Corrosion Science* **47**, 3368–3383 (2005).
299. Yang, J., Yang, Y., Balaskas, A. & Curioni, M. Development of a Chromium-Free Post-Anodizing Treatment Based on 2-Mercaptobenzothiazole for Corrosion Protection of AA2024T3. *Journal of The Electrochemical Society* **164**, C376–C382 (2017).
300. Goudarzi, N. & Farahani, H. Investigation on 2-mercaptobenzothiazole behavior as corrosion inhibitor for 316-stainless steel in acidic media. *Anti-Corrosion Methods and Materials* **61**, 20–26 (2013).

CHAPTER II

—

Containers formation and characterization

Chapter II - Table of contents

CHAPTER II - Containers formation and characterization	77
Containers for the NC ₂ M: introduction	80
II.1. Equipment used.....	81
II.1.1. Synthesis of the nanocapsules	81
II.1.1.1. Sonication system.....	81
II.1.1.2. Stirring.....	81
II.1.2. Characterization	81
II.1.2.1. Dynamic Light Scattering (DLS).....	81
II.1.2.2. Zetametry	85
II.1.2.3. Spectroscopy techniques.....	87
II.1.2.4. Microscopy.....	87
II.2. Hydrophobic-core silica containers.....	88
II.2.1. Capsules formation	88
II.2.1.1. Materials.....	88
II.2.1.2. Formation procedure	88
II.2.2. Characterization of the suspension	89
II.2.2.1. Assessment of the capsules formation.....	90
II.2.2.2. Size measurement.....	93
II.2.2.3. Encapsulation efficiency and release.....	96
II.2.2.4. Stability.....	97
II.2.3. Size optimization.....	101
II.2.3.1. Sonication	102
II.2.3.2. Mechanical stirring.....	103
II.2.3.3. Composition	107
II.2.3.4. Summary	111
II.3. Hydrophilic-core polyurea containers.....	112
II.3.1. Capsules formation	112

Chapter II - Containers formation and characterization

II.3.1.1. Materials	112
II.3.1.2. Standard procedure.....	112
II.3.1.3. Importance of the surfactant	113
II.3.1.4. Suspension purification and transfer in water	114
II.3.2. Characterization of the PUa capsules	115
II.3.2.1. Surfactants	115
II.3.2.2. Addition of ethanol in the dispersed phase.....	122
II.3.2.3. Transfer of the suspension in water	123
II.3.2.4. Conclusions on the synthesis of PUa containers	126
Conclusions on the containers formation and characterization	127
References	128

Containers for the NC₂M: introduction

Several compounds have been identified in the literature for both protection and detection. Regardless their function, their solubility can be very different. Potential corrosion sensors and inhibitors such as bromothymol blue¹ and sodium molybdate are highly soluble in water while others such as FD1 and MBT², to mention just a few, are not³.

The process we set up requires to dissolve the encapsulated molecule prior to its encapsulation. Therefore, in order to enable the use of both water-soluble and water-insoluble compounds, two types of smart containers have been chosen. Both formation mechanisms are based on a miniemulsion process as described in this section. This chapter first focused on the description of the containers synthesis for both types of nanocontainers, and then on the adjustments we carried out in order to have a better knowledge of their formation. The obtained containers are then fully characterized, using mainly dynamic light scattering and microscopy techniques.

II.1. Equipment used

II.1.1. Synthesis of the nanocapsules

II.1.1.1. Sonication system

Sonication processing is carried out using a Q700 sonicator (QSonica) with a 1/2" diameter tip. The sonicator power is 700 W, working at a frequency of 20 kHz. The amplitude is adjustable from 0 to 100%, the maximum amplitude corresponding to 120 μm according to the manufacturer. In order to prevent overheating, a pulse regime is used with 20 s sonication pulses separated by 10 s pauses if not mentioned otherwise. For all sonication steps, the vessel is placed in an ice bath.

II.1.1.2. Stirring

When mechanical stirring is employed, a T18 ultra turrax dispersing device (IKA) is used, associated with one of the following tools:

- A S18 N-18G "large" dispersing tool, having stator and rotor diameters of 18 and 12.7 mm respectively, made of stainless steel;
- A S18 D-10G-KS "small" dispersing tool, having a stator diameter of 10 mm, made of polycarbonate (PC) and polyetheretherketon (PEEK).

For magnetic stirring, a 15-spots magnetic stirring plate (2mag) was used, enabling stirring speeds between 0 and 1200 rpm.

II.1.2. Characterization

II.1.2.1. Dynamic Light Scattering (DLS)

DLS is a non-invasive technique that enables a quick determination of the particles' size and polydispersity. Since various information can be extracted, and in order to correctly interpret our results, the base principles of DLS are here described.

i. Theory

DLS is based on the relationship between the speed of particles only moved by Brownian motion and their hydrodynamic diameter $d(H)$ (sometimes referred to as R_H). $d(H)$ corresponds to the diameter of a hard sphere that would diffuse at the same speed as the analyzed particles. It can be calculated according to the Stokes-Einstein equation (II.1).

$$d(H) = \frac{k_B T}{3\pi\eta D} \quad (II.1)$$

where D is the particles' translational diffusion coefficient ($m^2.s^{-1}$), k_B is Boltzmann's constant, T the absolute temperature and η the dispersant's viscosity.

Calculating the particles' hydrodynamic diameter thus requires to determine their diffusional coefficient. This is achieved using a laser going through a dispersion of particles. When encountering a particle, an incident photon induces oscillations in the particle's electron cloud and energy is then scattered in all directions, in an anisotropic way for particles whose size exceed a tenth of the laser's wavelength (according to Mie theory).

A photon-counting detector is then used in order to assess the time dependency of the scattered light. D and $d(H)$ being inversely proportional as seen in equation (II.1), the smaller the particles, the faster their movements and so the faster the scattered light intensity fluctuates. To measure that time dependency, the autocorrelation function $G(\tau)$ is built as defined in equation (II.2) for our system (slightly different mathematical expressions are sometimes seen).

$$G(\tau) = \frac{\langle I(t) \cdot I(t + \tau) \rangle}{\langle I(t_\infty) \rangle^2} \quad (II.2)$$

where I is the scattered light intensity, t the time and τ the delay time.

This autocorrelation function is then fitted to a theoretical mathematical form depending on the sample's nature⁴. To determine the translational diffusion of a monodisperse sample, equation (II.3) is used, while equation (II.4) is used for polydisperse samples.

$$G(\tau) = 1 + B e^{-2q^2 D \tau} \quad (II.3)$$

$$G(\tau) = A + B \sum e^{-2q^2 D \tau} \quad (II.4)$$

with B the baseline at infinite time, A the intercept, D the diffusion coefficient, τ the correlator delay time and $q = \frac{4\pi n}{\lambda_0 \sin(\frac{\theta}{2})}$ the scattering vector where n is the dispersant's refractive index, θ the detection angle and λ_0 the laser's wavelength

It is very important to note that two types of analysis exist to interpret the correlation function: the cumulants and distribution analysis. Depending on the method that is used, different results are obtained. The cumulants methods, defined in ISO 22412:2017, is the simplest one. It consists in fitting the initial part of the correlation function with a single-exponential model. A particle mean size (Z-average) and a polydispersity index (PdI) are calculated from this analysis. On the other hand, the distribution method fits the data set using a multi-exponential model and calculates a mean size and associated standard deviation for each detected peak. The cumulants and distribution analysis are therefore more suited for monodisperse and polydisperse samples respectively.

Limitations

Due to these principles, the size of a dispersion is represented by a single value, based on the assumption that spherical particles are analyzed. This has then to be assessed by a different technique. Moreover, the hydrodynamic diameter value is also affected by the particles' surface (presence of surfactant...) and the medium's composition⁵. When ions are present in the analyzed sample, a double layer is indeed formed at the particles' surface. This layer's thickness (Debye length), decreasing when the medium's ionic strength increases, affects the particles' diffusion speed and has to be controlled.

ii. Analysis procedure

The device used for this study is a Zetasizer Nano S90 manufactured by Malvern Panalytical and controlled with Zetasizer software 7.11. The laser source used on this model is a He-Ne one with a wavelength of 633 nm and operated at 4 mW max. The manufacturer specifies that the size range of use is between 0.3 and 6000 nm with an accuracy of $\pm 2\%$.

When water is used as a dispersant, the refractive index and viscosity are assumed to be 1.330 and 0.8872 cP respectively for measurements performed at 25°C. When cyclohexane is used, the temperature is set to 20°C and the refractive index and viscosity values used are 1.427 and 0.977 cP respectively⁶.

The following procedure is adopted to prepare the DLS samples: first, the analyzed suspension is placed in an ultrasonic bath for 10 min in order to avoid any aggregation due to storage that would not be representative of the suspension as we use in a formulation. The suspension as synthesized is then diluted 20 times right before the DLS measurement using milli-QTM water as the dispersant. It has been observed that for a wide range of dilution (from 1/100 to 1/10) the measured mean size did not vary whatever the suspension's concentration. The analysis is performed either in a disposable cell (DTS0012) or in a glass cell (PCS1115). No difference was observed in the results with either one or the other type of cell.

The set parameters are as follows: 3 to 5 runs are performed (depending on the experiment's aim) with attenuator and number of sub-runs left automatically determined by the software. The algorithms used is set to "general purpose", enabling a high noise tolerance as recommended when no information is known on the sample's distribution.

iii. Results of the DLS measurement

Different values or data will be discussed and chosen upon their relevance⁷.

Particles' size

When a single population is present, its size can be described by two values using the cumulants analysis: the Z-average size and polydispersity index (PdI), that are respectively determined from the correlation function's time of decay (using Stokes-Einstein equation) and from the decay's slope. The polydispersity index attributes a value to the broadness of the sample's size distribution. A PdI is dimensionless and scaled to be between 0 and 1. According to the manufacturer's advice, PdI below 0.08 are seldom obtained while values above 0.7 correspond to a broad distribution (meaning cumulant analysis could be unsuitable). Generally, a value below 0.4 is wished⁷.

Intensity distribution

When the analyzed dispersion contains several populations, the results will be presented as a size distribution, which is the plot of the relative intensity of light scattered by the particles sorted in size classes. There are 66 size classes for our system, from 0.4 to 5560 nm. From this plot are extracted a mean size and associated width for each peak. Only the intensity distribution results are presented and discussed since they are the measured value. As a consequence, no extrapolation to the relative volume or particle number can be achieved by measuring the relative height of peaks. The scattered light intensity being indeed non-linearly proportional to the particle's size, bigger particles scatter way more light than smaller ones. Calculating the number and size distribution then requires the suspension to be made of spherical and homogeneous particles having a similar density, but also to know their refractive index and absorbance. In order to be as clear as possible when showing the evolution of the intensity distribution, histograms are converted to line plots.

Correlogram

In order to evaluate the stability of the analyzed samples, a comparison of the size distribution obtained from successive runs might not be sufficient and will then be completed by the analysis of the correlograms. Figure II. 1 presents two correlograms obtained after a 5-run DLS measurement. The first one (left) corresponds to what we qualify a stable clean sample while for the second one, a slightly unstable sample is analyzed. This is highlighted by the variation in the correlation coefficient intercept for the successive runs, as well as by the noisy baseline. Both observations can reveal a slight natural tendency to aggregation and/or sedimentation from the sample, or the presence of bigger particles or aggregates in the dispersion. When the analyzed sample sediments, a variation in the number of particles in solution can indeed imply a variation in the correlogram's intercept.

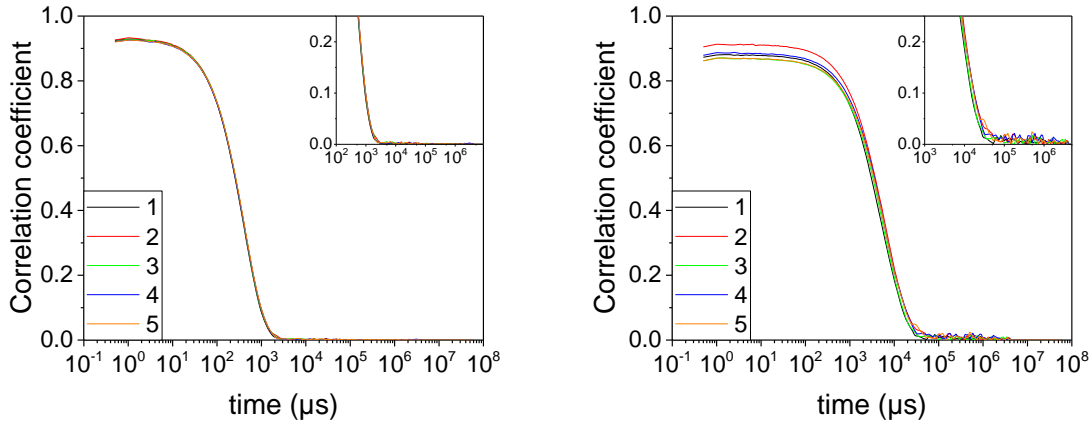


Figure II. 1: Example of correlograms obtained for the analysis of a monodisperse dispersion

Due to these explanations, DLS analysis is performed in our case in order to compare the different syntheses or as a routine check procedure before using the capsule suspension. Since the cumulants fit is less affected by the presence of bigger aggregates, the comparison of the Z-average values will be favored when possible. However, when used, Z-average values can only be compared amongst themselves and PdI will then be considered acceptable when below 0.4. Multimodal samples will be discussed in terms of peaks' mean size and standard deviation.

II.1.2.2. Zetametry

i. Theory

In order to assess the stability of a suspension, we study the repulsive potential of the colloids' double layer. According to DLVO theory, for particles undergoing Brownian motion the balance between this potential and Van der Waals force determines the suspension's stability⁸.

In a zetametry study, the electrical charge of the double layer surrounding particles is analyzed by applying an electrical field to the suspension. The particle's velocity is then measured by laser Doppler velocimetry, in order to deduce their electrophoretic mobility according to (II.5).

$$U_E = \frac{v}{E} \quad (II.5)$$

With v the particles' velocity and E the applied electrical field's strength.

The relationship between the electrophoretic mobility and zeta potential is then given by Henry equation, presented in (II.6):

$$U_E = \frac{2 \cdot \epsilon \cdot z \cdot F(ka)}{3 \cdot \eta} \quad (II.6)$$

With U_E the electrophoretic mobility, z the zeta potential, ϵ the dielectric constant, η the medium's viscosity and $F(ka)$ Henry's function which involves the ratio between the particles' radius and their

double layer's thickness. As often done in polar and/or high ionic strength media, we use Smoluchowski approximation, meaning we assume that the double layer's thickness is small compared to the particles' radius. In this case $F(ka)=1.5$, that leads to equation (II.7)⁹.

$$U_E = \frac{\epsilon \cdot Z}{\eta} \quad (II.7)$$

The absolute value of the zeta potential gives an insight of the suspension's behavior. It is generally admitted that a suspension is stable when its zeta potential is higher than 30 mV⁸, although the nature of the particles also has an importance since Van der Waals force has to be taken into account⁷. Moreover, the double layer's thickness and exact particles' size are not perfectly known for our system, and therefore Smoluchowski approximation can introduce errors. An "apparent" zeta potential value is then calculated this way.

ii Analysis procedure

Zeta potential studies have been carried out employing a Zetasizer Nano ZS90 (Malvern Panalytical) controlled with Malvern's Zetasizer Software v7.11. Measurements are performed in a disposable folded capillary cell (DTS1060, Malvern). For this, the analyzed suspension is diluted 100 times in the appropriate medium, using either HCl, KOH or NaOH for pH adjustments, and KCl or NaCl for the study concerning the influence of the ionic strength.

The number of runs per measurement is automatically determined by the software, between 10 and 30. Three consecutive measurements are performed for each sample in order to get reliable results but avoiding heating of the suspension due to prolonged exposure to the electrical field. The applied voltage is manually set to 50 V in order to avoid voltage-dependence of the electrophoretic mobility¹⁰. As discussed in the previous section, Smoluchowski model is used in order to convert the measured electrophoretic mobility to an apparent zeta potential.

iii. Results obtained from a zeta potential measurement

Using velocimetry measurements, an electrophoretic mobility distribution is obtained, from which is calculated the zeta potential (ZP) distribution of the suspension. An example of the electrophoretic mobility and calculated ZP plots is given in Figure II. 2. From these plots, we can assume that a ZP measurement is acceptable and that the sample is stable during the measurement, based on the low count rate evolution.

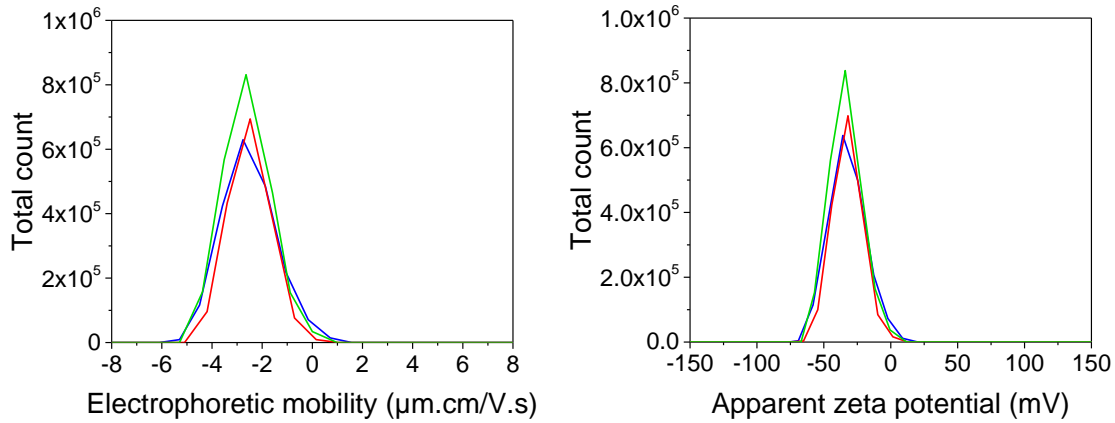


Figure II. 2: Example of electrophoretic mobility and deduced zeta potential distribution considered as good quality data

When discussing ZP results, we will then compare the mean zeta potential and its standard deviation, averaged over three measurements.

II.1.2.3. Spectroscopy techniques

i. Fourier-Transform Infrared Spectroscopy (FTIR)

Infrared spectra are recorded by Attenuated Total Reflectance (ATR), using a Nicolet iS50 FTIR Spectrometer (Thermo Scientific). Settings are as follows: 64 scans, resolution of 4 cm⁻¹ and spectra recorded from 4000 to 400 cm⁻¹. Analyses are performed placing the coating or powder sample on top of the diamond.

ii. UV-visible spectroscopy

For the determination of concentrations in MBT during the release experiments, UV-vis spectra have been recorded using an Evolution™ 60S UV-Visible Spectrophotometer manufactured by ThermoFisher Scientific. Scans are performed from 200 to 350 nm with 0.5 nm steps and a scan speed set as “medium”. Calibration data in neutral and alkaline media are given in appendix 1.

II.1.2.4. Microscopy

Scanning electron observations are performed using a FEI Quanta 200 FEG ESEM on a dried dispersion droplet placed on a glass substrate. The sample is then sputtered with gold. Operating conditions are as follows: 10.0 kV accelerating voltage, 9.9 mm working distance and 3.7 spot size.

Concerning Transmission Electron Microscopy (TEM), a JEM-2011 from JEOL operated at 200 kV is employed. For the observations, a 10-times diluted suspension is cast on a copper grid with a carbon film and left to dry at room temperature.

II.2. Hydrophobic-core silica containers

II.2.1. Capsules formation

II.2.1.1. Materials

The list of chemicals used for the different synthesis of silica nanocontainers discussed in this section and the purity taken into account for weight calculations are given in the appendices section (Appendix 2).

II.2.1.2. Formation procedure

Interfacial polymerization is carried out for the formation of oil-core capsules, using a direct mini-emulsion process as illustrated in Figure II. 3 and based on a procedure described elsewhere¹¹. Two solutions, constituting the two phases, are prepared as follows:

- The continuous phase is made dissolving 37 mg of dodecyl trimethylammonium bromide (DTAB) in pure water in a 40 mL-vial;
- The dispersed phase is prepared adding successively 1.15 mL of toluene, 162 μ L of hexadecane and 2.15 mL of tetraethylorthosilicate (TEOS) in a 4 mL-vial. When present, the potential payload is placed in the vessel prior to the addition of other chemicals.

The two solutions are homogenized under magnetic stirring during one hour. The oil phase is then added to the surfactant aqueous solution, and the mixture is immediately placed in an ice bath and sonicated for 180s in a pulse regime (20s sonication + 10s pause) at 60% amplitude. The final dispersion is then left under magnetic stirring at 750 rpm for at least 12h.

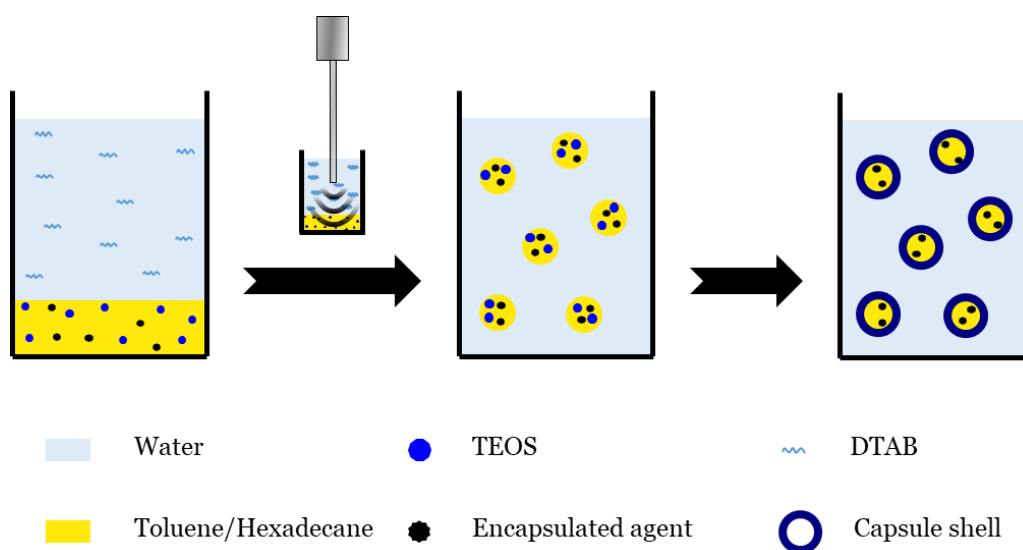


Figure II. 3: Silica capsules formation using an O/W mini-emulsion process

The formation of the silica capsules is based on the reaction occurring between the TEOS precursor and the water forming the continuous phase. The shell is formed by the hydrolysis and polycondensation of the alkoxy silane, following the reaction presented in Figure II. 4. The formation of an O/W mini-emulsion allows the precursor to be in contact with water only at the interface between the organic core and the aqueous continuous phase. Therefore, the control of the emulsion's size and stability leads to controlled capsules' size and morphology. This reaction is very well known and both acid and base-catalyzed^{12,13}. We assume that the dissolution of a compound in the organic phase before formation of the silica walls will enable its encapsulation, meaning that the selected molecules must be mainly soluble in the organic solvents during the formation of the silica wall.

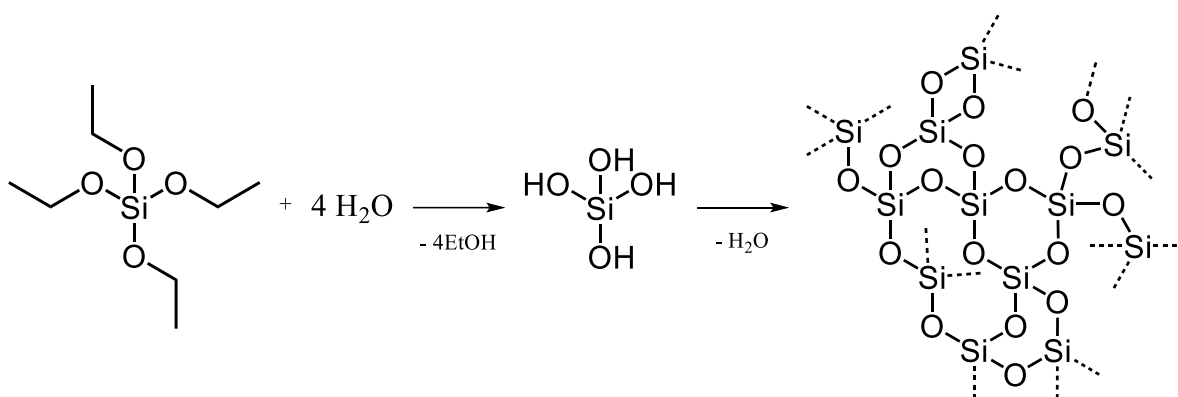


Figure II. 4: TEOS polycondensation reaction

The quantities used in our reference procedure are adapted to the sonication equipment employed, in order to have *ca.* 20 mL to process. Water is in high excess (86.8 equivalent versus TEOS), making the hydrolysis reaction all the more efficient, although interfacial polymerization implies that not all the water content is available for the reaction. Despite its confirmed toxicity, toluene is used as the major constituent of the oil phase to which hexadecane is added. Representing 12% of the dispersed phase's volume, hexadecane helps to prevent Ostwald ripening, hence increasing the emulsion's stability¹⁴. A last point to highlight is the formation of ethanol as a by-product of the hydrolysis step. That could play a role since MBT's solubility is very low in pure water (around 0.12 g.L⁻¹ at 25°C according to the supplier specifications) but increases with alkalinity or in alcohols. Therefore, a part of the MBT could be extracted by the ethanol that is produced.

II.2.2. Characterization of the suspension

Various types of analysis have been performed in order to exactly determine the nature and properties of the containers and to have a better understanding of their behavior once introduced in a varnish. In a second step, variations of the synthesis procedure have been performed in order to evaluate the importance of the involved parameters on the formation of the nanocontainers (NCs), but also with the objective of obtaining different sizes for the silica capsules.

II.2.2.1. Assessment of the capsules formation

The nanocontainers' shape is first determined using electron microscopy techniques. As presented in Figure II. 5, SEM observations confirmed the spherical shape of the synthesized particles. On SEM pictures, some capsules are broken, what is probably due to the observation conditions in high vacuum, and evidences the presence of a central cavity. Hollow capsules have therefore been synthesized. The size distribution seems monodisperse with diameters of a few hundreds of nanometers, what will be thoroughly detailed in the next section.

TEM analysis confirms the spherical shape of the silica-based nanocapsules. Figure II. 5.b. highlights that the internal part of the containers is empty and that the silica walls define the spherical shape of the containers. The electron diffraction pattern, as shown in the insert of Figure II. 5.b confirms the amorphous character of the silica shells. The capsules' diameter was evaluated between 50 and 150 nm, and TEM observations enable to estimate the walls' thickness to be 5 to 10 nm. A statistical analysis will be conducted later on.

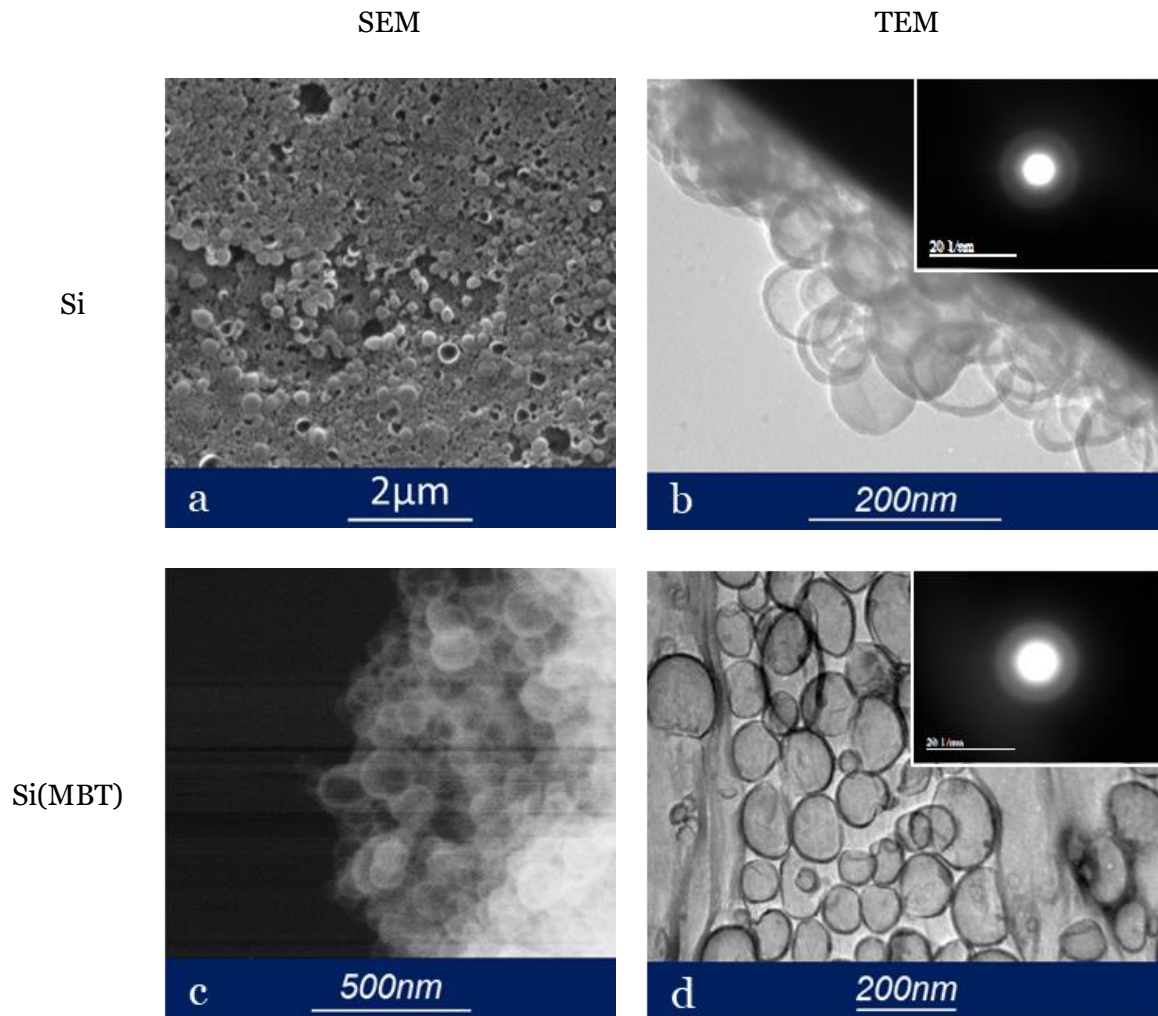


Figure II. 5: SEM (a & c) and TEM (b & d) observations of the unloaded (a & b) and MBT-loaded (c & d) Si NCs

Figure II. 5.c and d reveal that the addition of a payload like MBT does not affect the shape of the capsules and the shell formation, since there is no detectable porosity or holes in the shell. The average diameter is not affected by the addition of the MBT and the electron diffraction pattern reveals that the silica shells are still amorphous.

Another useful information is that the capsules' shell seems to be quite flexible, leading to apparently compact aggregates. On TEM images, as highlighted in Figure II. 6, some capsules appear flattened or bended, and suggest that the Si NCs can resist to deformations although this resistance has not been measured.

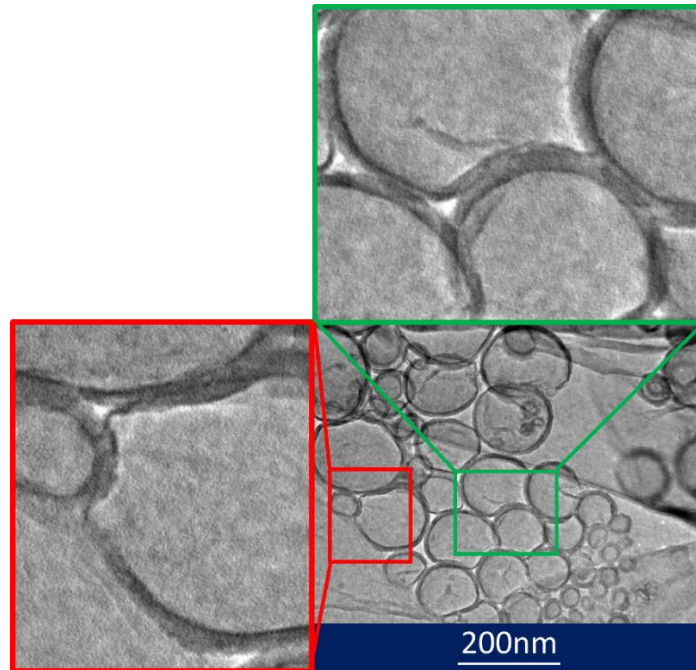


Figure II. 6: TEM observations of silica NCs and zoom in on deformed parts of the silica containers

The composition of the silica capsules has been studied by FTIR, for both “empty” silica nanocontainers and MBT-containing suspensions. Recorded spectra are presented in Figure II. 7 and the associated vibration frequencies are listed in Table II. 1. These results are in good agreement with the formation of a SiO₂ network by the TEOS hydrolysis/condensation according to literature^{15,16}. However, no signal corresponding to MBT could be identified, contrary to the work published by Maia *et al.*¹⁵. This is probably due to the low concentration in MBT used in our case, 3 to 5 times less concentrated than in the work of Maia *et al.* Moreover, they reported a yellow pale coloration when MBT is added in the suspension, what was not observed in our case.

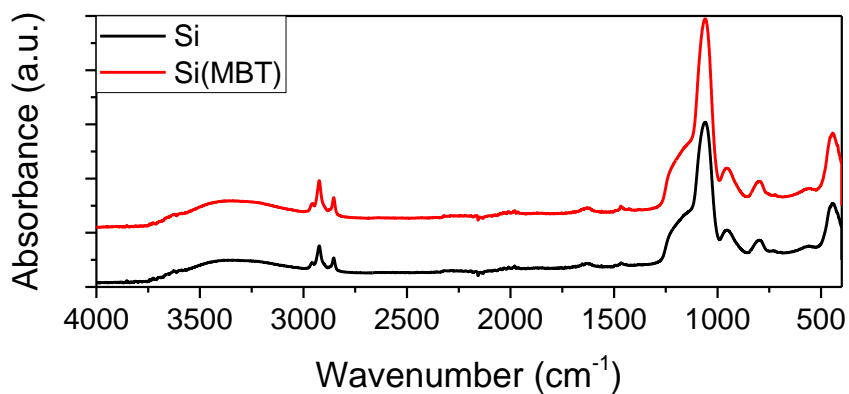


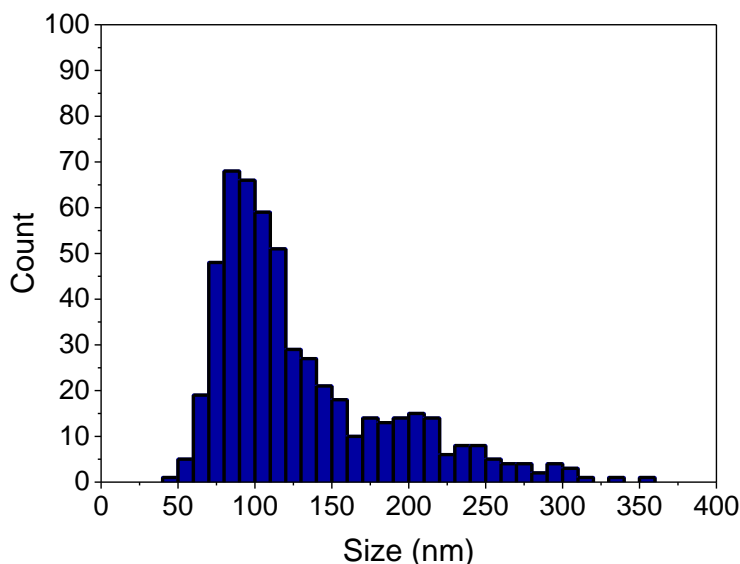
Figure II. 7: FTIR spectrum of silica NCs with and without encapsulated MBT

Table II. 1: Characteristic vibration frequencies in FTIR spectra of Si and Si(MBT) NCs

Vibration frequency (cm ⁻¹)	Type of vibration	Structural unit
3100 - 3500	O-H and Si-OH	-O-H...H ₂ O
2958	ν_s C-H	-CH ₃
2924	ν_{as} C-H	-CH ₂
2854	ν_s C-H	-CH ₂
1060	ν_{as} Si-O-Si	-Si-O-Si-
1245 - 1115	ν_{as} Si-O-Si	-Si-O-Si-
955	ν_β Si-O	-Si-OH
798	ν_s Si-O	-Si-O-Si-
455	δ O-Si-O	-O-Si-O-

II.2.2.2. Size measurement

A rough SEM image analysis performed on 539 capsules in Figure II. 5.a gives the size distribution presented in Figure II. 8. The measured sizes range from 45 to 350 nm with an average size of 130 ± 55 nm.

**Figure II. 8: Size distribution obtained from SEM image analysis**

Due to the low number of observed capsules, analysis of TEM images is not relevant for size measurement. However, it allows to analyze the walls' thickness, that is apparently not dependent on the capsules' size. Based on 19 analyzable capsules on TEM observations (spherical capsules out of aggregates), we measured the capsules' diameter (2 measurements per capsule) and the associated wall's thickness (10 measurement per capsule). The results, presented in Figure II. 9a,

show that for capsules diameters between 40 and 150 nm, the respective walls' thickness range is very narrow, between 4 and 15 nm and with a mean wall thickness of 8.7 ± 0.6 nm. Therefore, smaller capsules do not necessarily have thinner shells. This could be explained by the diffusion-governed interfacial polymerization. Once a critical thickness is obtained, the potential residual TEOS remains within the capsules and cannot further react.

An estimation of the free volume inside the capsules can be calculated using (II.8). This gives a broad range of free volumes, between 22 and 69% of the capsules' volume for the 19 analyzed capsules as shown in Figure II. 9b.

$$\%V_{\text{free}} = \frac{V_{\text{free}}}{V_{\text{tot}}} = \left(\frac{r - e}{r} \right)^3 \quad (\text{II.8})$$

with V_{tot} the volume of the capsule, r the capsule's radius and e the shell's thickness.

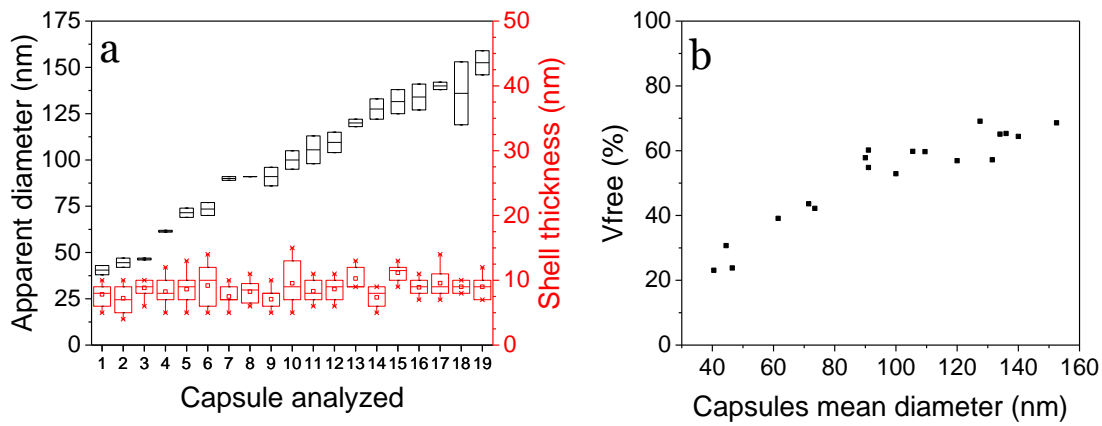


Figure II. 9: (a) Capsules' diameter and associated wall thickness from TEM images analysis and (b) the associated calculated free volume

Although microscopy techniques can give an estimation of the particles' size, the low number of analyzed particles and overlapping particles make necessary the use of a more accurate technique such as DLS for size analysis. Figure II. 10 shows the DLS measurements carried out on empty and MBT-loaded capsules. Several batches have been synthesized for capsules without any payload and capsules with MBT and correspond to the red and blue curves respectively. In order to keep a clear graph, only four batches are presented in Figure II. 10. For both types of capsules, a monomodal distribution is observed, what is consistent for an emulsion process. Since microscopy observations proved the sphericity of the particles, a mean hydrodynamic diameter value is then estimated.

On the intensity distribution curves, the error bars correspond to the four successive measurements performed for each sample. This gives an insight of the suspension's stability, highlighting the absence of agglomerating particles when the suspension is not stirred.

The measured sizes are 183.2 ± 11.9 nm for Si NCs and 192.7 ± 7.3 nm for Si(MBT) capsules. The absence of significant variation between the DLS curves and capsule shape when MBT is added

proves that it does not interfere with the capsule formation. These results suggest that the molecules should be located either in the capsules (encapsulated or adsorbed), in their surrounding environment or shared in both phases. In both cases, a single peak is observed. A cumulant analysis gives comparable polydispersity indexes of 0.151 ± 0.028 and 0.163 ± 0.035 for Si and Si(MBT) containers respectively, what corresponds to a narrow distribution, as desired.

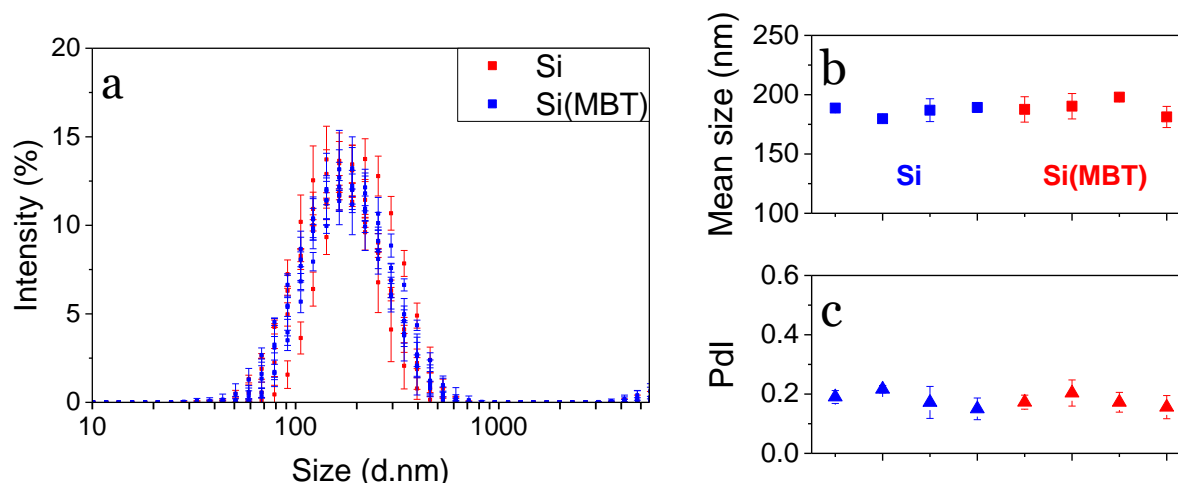


Figure II. 10: (a) DLS curves for Si and Si(MBT) NCs), and associated (b) mean sizes and (c) polydispersity indexes

Concerning the capsule's size, a slight difference is observed between SEM images and DLS measurements (from ~130 nm to ~190 nm), explained by the combination of few factors. First, the sample preparation and observation conditions: SEM and TEM samples are dried suspensions observed under vacuum whereas DLS samples is a diluted suspension. DLS analysis therefore takes dynamic parameters and aggregation into account, leading to higher size values. Secondly, when analyzing a SEM image, only the dried capsule size is measured, while the Z-average value given by DLS represents the hydrodynamic volume moving with the capsules^{17,18}.

As seen in Figure II. 10, a small increase in the scattered intensity at the limit of our equipment (above 6 μm) could denote a slight aggregation. However, the correlation function coefficient presented in Figure II. 11 showed no evolution of this parameter at high delay times, highlighting the absence of sedimentation. It can also be noticed that for each measurement a Y-intercept between 0.8 and 1 is obtained, confirming the good conditions of the DLS measurements and therefore the absence of multiple scattering.

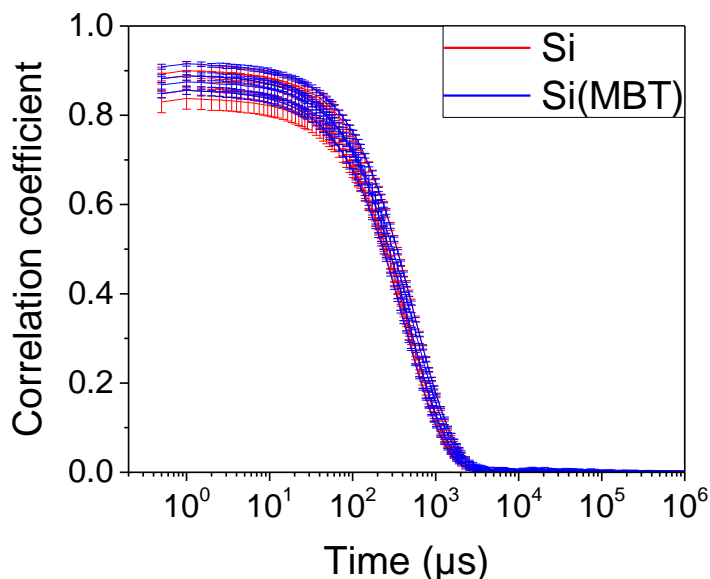


Figure II. 11: Correlograms obtained for DLS analyses of (red) Si and (blue) Si(MBT) containers

From the presented analysis, it is clear that monodisperse spherical hollow capsules have been formed through a reproducible oil-in-water process. Due to MBT's low solubility in pure water and neutral solutions, the major part should be inside the nanocontainers when MBT is first dissolved in the oil phase.

II.2.2.3. Encapsulation efficiency and release

The encapsulation study is carried out measuring the concentration in MBT by UV-vis spectroscopy. In order to measure the released amount, the suspension is filtered (Millex-VV, 0.1 μm , PVDF, 33 mm syringe filter unit, Merck). The filtrate is then diluted 20 times in water prior to analysis in order to avoid signal saturation.

The MBT dissolved in the medium surrounding the capsules being measured, the encapsulation efficiency (%EE) is determined using formula (II.9). Based on three different suspensions, an encapsulation efficiency of $84.5 \pm 2.1\%$ has been determined 24h after the emulsion formation and no difference was observed after 7 days under magnetic stirring.

$$\%EE = (1 - \%R) \times 100 \quad (II.9)$$

$$\text{With } \%R = \frac{m_{\text{MBT in filtrate}}}{m_{\text{MBT in suspension}}} \quad (II.10)$$

Release studies were then performed 24h after the sonication step and as follows: 9 g of the Si(MBT) suspension are left under stirring in a vial and 1.0 mL of 1 M sodium hydroxide solution is added. The pH of the final solution is 10.2 ± 0.2 . Performing regular measurements, the release rate is then calculated using (II.10). The results are presented in Figure II. 12. An important increase of the MBT concentration in the filtrate is already observed 30s after addition of the base, with 54% of the total

MBT content released during this period. A slower release then occurs, with a supplementary 21% total MBT released in the first two hours, leading to around 90% of the initial content released in the medium after 2h at pH 10.

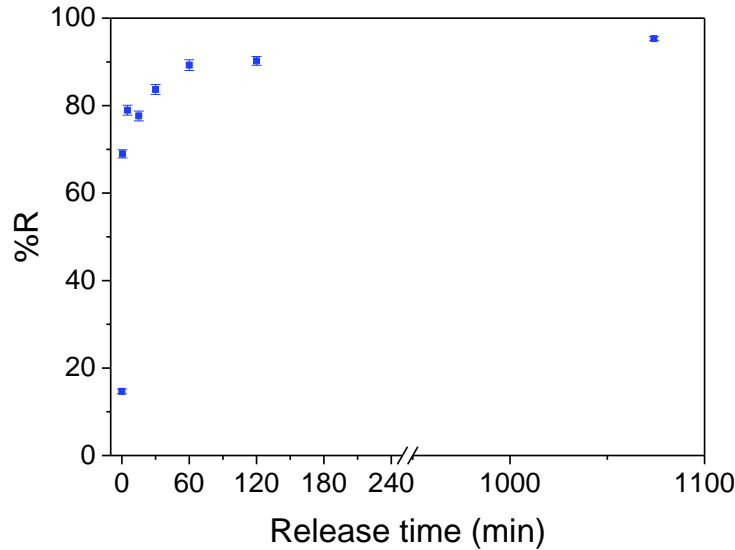


Figure II. 12: Release of MBT from silica NCs in an alkaline medium (pH=10.2)

With a very fast release in the presence of hydroxide ions, the developed silica nanocontainers seem to be very suitable for corrosion-related purposes. The encapsulation rate is quite high, although a not negligible amount of MBT remains in the solution after formation of the containers. This unencapsulated MBT could be harmful for the host matrix. The behavior of the suspension was studied in order to determine how and in which conditions the Si NCs can be used and eventually establish the involved release mechanism.

II.2.2.4. Stability

In the presented approach, the nanocontainers suspension will be used as prepared, without any purification step and therefore requires being stable when added to the formulation. It is assumed that the capsules can be synthesized on-demand during the formulation process and that therefore the suspension has to be stable for a few days only. The stability tests that have been carried out concern the evolution of the capsules' size over time, the influence of the environment's pH in a wide range and the influence of the encapsulation of MBT on the NCs' surface potential.

i. Stability over time

The suspensions' stability over time has been assessed by DLS checking the size, polydispersity and potential sedimentation of empty and MBT-loaded capsules. For this, two batches are prepared for each type of capsules, and analyzed by DLS 12h and 20 days after the emulsion formation. This is done diluting the suspension in pure water and performing the analysis right after dilution. Size

measurements and standard deviations over the four successive measurements are presented in Figure II. 13, based on a distribution fit.

A size increase of 13% and 9% is observed for Si and Si(MBT) capsules respectively, that could be attributed to a slight swelling of the capsules. An explanation is that over time the capsules' shell becomes permeable, and therefore diffusion of water through the silica shell makes it swell. Another possible explanation is that over time, the smaller particles would agglomerate or merge, leading to a slightly bigger suspension. However, electron microscopy observations did not allow to confirm this latter assumption. The comparison of the correlograms for the different syntheses did not evidence any agglomeration or sedimentation.

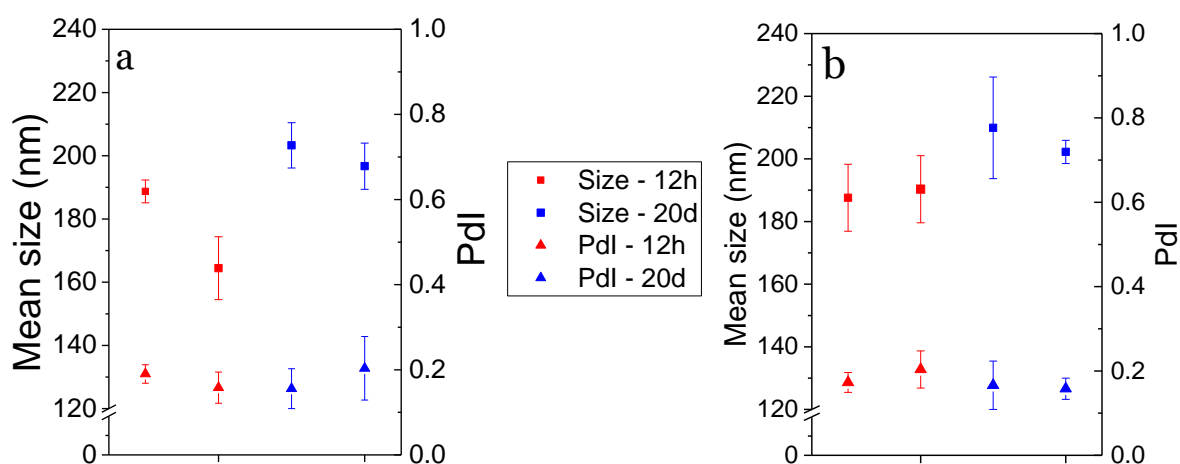


Figure II. 13: Mean size and polydispersity index obtained by DLS for (a) Si and (b) Si(MBT) containers 12h and 20 days after synthesis

This phenomenon, if linked to swelling, could be detrimental since it could lead to a premature release of the encapsulated compounds.

ii. Silica-based NCs' behavior as a function of pH

As seen in section II.2.2.4, the silica-based capsules are pH-sensitive and able to release their payload in alkaline media, what confers them a sensitiveness to corrosion processes. In order to determine the pH range of efficiency, the size of the capsules has been measured in 6 different pH conditions. The measurements have been performed first right after pH adjustment, and a second time 7 days later in order to observe any evolution as presented in Figure II. 14. The horizontal line corresponds to a hydrodynamic diameter of 185 nm, as observed for the suspension in the as-synthesized conditions (pH around 6.2). The size measurement allows to assess the good stability of the suspension in acidic conditions. The particles' size does not evolve even after 7 days of storage under stirring. However, for pH values of 8.8 and 10.7, the capsules' diameter increases from around 185 nm to 248 nm and 262 nm respectively, corresponding to an increase of 34% and 42% of the capsules' hydrodynamic diameter. It seems that the silica capsules instantly swell in alkaline media, what could explain their release ability. The diameter increase under alkaline conditions could favor

the formation of a porosity network that induces the release of the inhibitor. Interestingly, for the most alkaline conditions (pH = 12.5), the diameter increase represents only 23% of the initial size. This is probably due to the associated increase of the medium's ionic strength, thinning the electrical double layer. However, after 7 days in these conditions, a clear increase is seen for this pH condition as well, in good agreement with the values obtained for the other alkaline conditions.

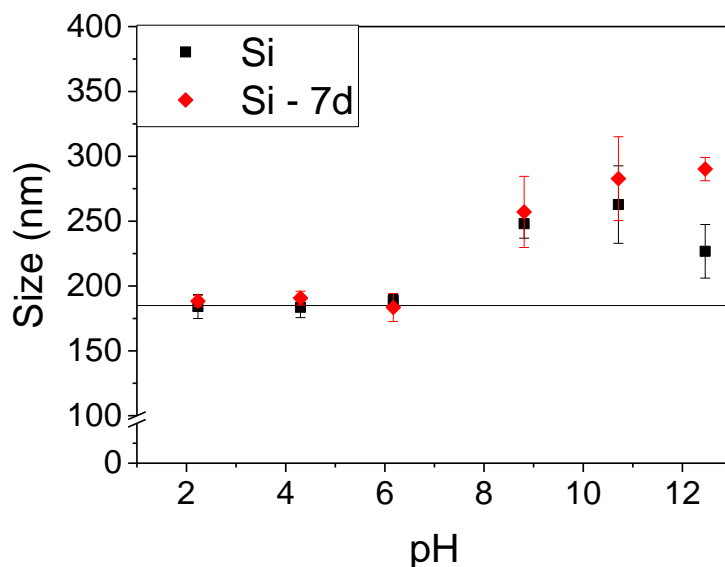


Figure II. 14: Evolution of the Si NCs hydrodynamic diameter as a function of pH and time

According to our results, we can assume that the hydroxide ions are able to diffuse through the silica shell that becomes permeable, and to reach the core of the capsule. This enables the release of the encapsulated compound. This mechanism is very rapid when the pH goes above 8.8, with, in the first steps, an apparent maximum swelling speed. However, for longer durations we observe that the higher the pH, the more important the swelling. This lets think that the release could also be more important. Moreover, we could not perform a DLS analysis 21 days after pH adjustment since no particles were detectable in alkaline media. Even visually, we observed a loss of opacity in the suspension when placed in alkaline media. These results and observations are in good agreement with a slow dissolution of the capsules' polymeric shells. The depolymerization of silica is furthermore reported in the literature^{19,20}. In a first step, a selective dissolution leads to a higher mobility of the silica chains, provoking the swelling of the shell. After a certain time, oligomers are formed and released in the medium, resulting in the disappearance of the scattered light signal.

Therefore, the addition of the containers to a host matrix, or analyses, have to be carried out in the first 7 days after formation of the capsules (since no extra-release was observed at this time). At this point the suspension is stable and controlled.

iii. Influence of the environment (Zetametry)

The stability of the suspension undergoing Brownian motion is only due to the electrostatic repulsion between the capsules, enhanced by adsorbed or covalently linked DTAB molecules. The formed dispersion should therefore be sensitive to pH changes and to the presence of ionic species. As seen previously, the dissolution of the particles occurs in alkaline media and has to be prevented during the formulation process. Zetametry can quantitatively determine the suspension's stability depending on the medium ionic strength for a given pH. Moreover, comparing the surface charges of Si and Si(MBT) suspensions can give an insight of the encapsulation of MBT (*i.e.* being in the core or adsorbed).

In order to keep a comparable ionic strength between experiments performed in acidic and alkaline media, the same quantity of HCl and KOH respectively has been used, with a final concentration of 10^{-3} M. ZP measurement for added KCl concentrations below this value hence does not make any sense. pH values of the samples are 3.15 ± 0.05 , 7.06 ± 0.34 and 9.51 ± 0.08 for acidic, neutral and alkaline conditions respectively. Apparent ZPs are plotted versus the concentration of added monovalent salt (KCl) in Figure II. 15.

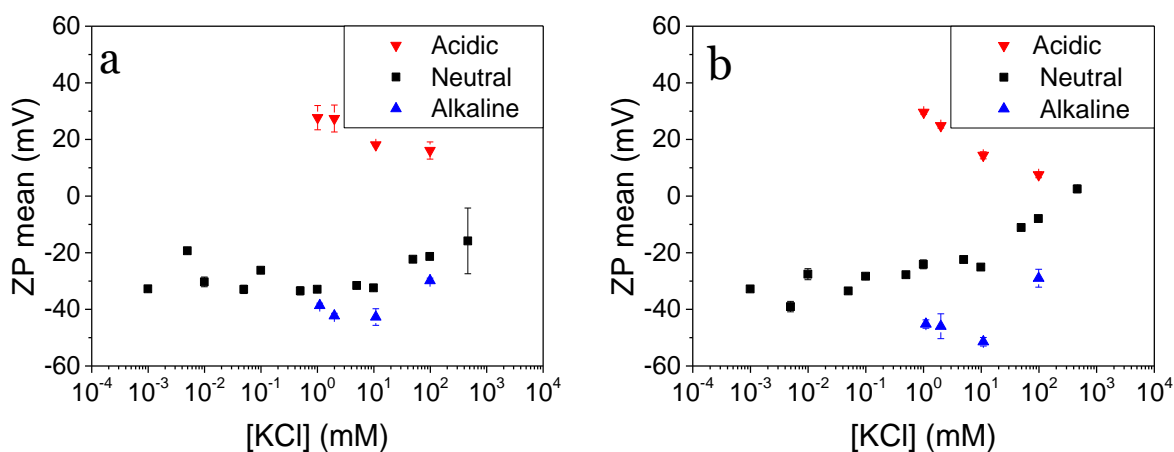


Figure II. 15: Zetametry study of the silica capsules, (a) without and (b) with MBT as a payload

The silica's surface being mainly composed of “-Si-O-Si-“ units and “Si-OH” silanol groups, they are part of a protonation/deprotonation equilibrium. When placed in an alkaline environment, the -Si-O⁻ groups are predominant, whereas protonated -Si-OH₂⁺ groups are responsible of the positive ZP values observed in an acidic medium²¹. This first piece of information given by zetametry is that the nanocapsules' shell as prepared is negatively charged with ZP values of *ca.* -30 mV in dilute electrolyte solutions, meaning that the particles' isoelectric point (IEP) is between 3 and 7. The PZC of silica PZC is generally between 1 and 3 and is affected by the colloid's size²². An IEP of 2 has been reported by Tseng²³ for 550 nm hollow silica particles²⁴. The presence of DTAB in the suspension would explain why our system's PZC should be slightly higher.

Concerning the suspension's stability, it is sometimes assumed that a stable colloid should have a ZP higher than 30 mV²⁵. Being near this value, the formed NCs might have a tendency to sediment after a certain period of time. However, in our case, we observed no aggregates in the samples after 24h when $|ZP| > 20$ mV, which is therefore our stability criterion. Two different behaviors are observed for both loaded and unloaded suspensions. For low electrolyte concentrations ($[KCl] < 10$ mM), ZP values are between -25 and -35 mV in a neutral medium, and slightly lower for pH 9.5. On the other hand, a positive value is measured in acidic conditions with a slightly lower absolute value (between +20 and +30 mV). For low ionic strength media, we can hence assume that the dispersion is stable and that no aggregation should occur.

However, when the electrolyte concentration goes above 10 mM, a decrease in $|ZP|$ is seen, what leads to quick flocculation of the particles, observed in the samples as soon as 1h after the preparation. Interestingly, the critical electrolyte concentration is 10 times lower when MBT is present in the dispersion. Moreover, the $|ZP|$ difference between measurements performed in neutral and alkaline media is higher when MBT is present. Our assumption is that a not negligible part of the MBT remains unencapsulated, and hence adsorbs on the capsules surface. When the medium pH goes beyond its pKa value of 7.03, MBT is deprotonated, and is therefore electrostatically repelled. This is not seen in neutral medium for which the adsorbed MBT implies a decrease in the apparent zeta potential.

This zetametry study tends to show that the dispersion is stable in the tested conditions. The silica capsules should therefore be dispersible without formation of aggregates in the absence of ionic species, and for pH values higher than 7.06. The determination of the suspension's isoelectric point however still has to be done. A difference of behavior between loaded and unloaded capsules could lead to a difference in compatibility of the NCs when added to a matrix.

This difference seems to highlight the adsorption of MBT molecules on the capsules' surface rather than proper encapsulation, for at least a part of the "encapsulated" MBT. However, based on ZP potential measurements, the accurate determination of the encapsulated and adsorbed part is not possible. It is also likely that the adsorbed molecule could hinder the diffusion of MBT molecules through the coating, and degrade the host matrix / silica capsules interface.

II.2.3. Size optimization

As seen in the previous parts, we succeeded in forming controlled silica nanocapsules with hydrodynamic diameters around 180 nm, having a hollow core that can be loaded with active molecules. In the case of corrosion inhibitors, a very important parameter is the amount of inhibitor that can be locally released. This release amount is naturally linked to the quantity and distribution of nanocapsules incorporated into the host coating. The size of the capsules would hence define the amount of loaded inhibitor. In order to evaluate the influence of the capsules' size on both the loaded

coating properties and the amount of inhibitor that is released, we tried to determine the importance of several factors and the effects of variations on the capsules' size.

Our first approach was devoted to the formation of a bigger emulsion by changing the emulsion formulation procedure. This is done either by making variations in the sonication parameters or using a high-shear disperser to mix the two phases. A second strategy consists in changing the system's composition to increase Ostwald ripening and get bigger oil droplets, leading to bigger capsules. In this section, in order to compare the different syntheses, the mean size and polydispersity are presented. However, since a distribution fit is used, the plotted size corresponds to the main peak mean size, while the polydispersity index of the main peak is calculated using

$PdI = \left(\frac{\text{Standard Deviation}}{\text{Mean Size}} \right)^2$, according to the manufacturer's advice for the analysis of a single peak.

II.2.3.1. Sonication

The use of ultrasounds generates cavitation that enables the formation of a stable mini-emulsion. For a given power (in our case 700 W), possible variations then concern the tip amplitude, and duration of the process. It has been evidenced that increasing the amplitude or process duration leads to a higher cavitation intensity, generating a smaller and more controlled suspension (as soon as the system is stable long enough for the shell to be fully formed), although optimization is necessary²⁶⁻²⁸. We therefore tried to reduce the sonication time, from 3 to 1 min, what did not allow us to see any difference. On the other hand, by changing the amplitude, differences in both the suspension's size and polydispersity are noticed, as presented in Figure II. 16.

Due to our setup, the amplitude is physically limited since we saw that for values below 40%, the processing of the formulation was not homogeneous and a clear supernatant was still present at the end of the process. An upper limit also exists since values higher than 70% produced splashing. We therefore tried amplitude of 42%, 60% and 70% corresponding to a membrane displacement of around 50 μm , 72 μm and 84 μm respectively. A small increase in the capsules' hydrodynamic diameter, from 150 to 180 nm roughly, is observed when the amplitude is increased from 42 to 60%. This is associated with a decrease in the PdI. A possibility is that increase in the amplitude can be linked to a temperature increase that favors the droplets coalescence²⁸. No further increase in size is observed for a 10% higher amplitude, although the suspension's stability is apparently increased since a lower standard deviation is observed between the different measurements.

Since the temperature is hardly measurable during the process but plays an important role, a batch of capsules has been synthesized using shorter pulses. This limits the heat increase, while the cooling down time is kept the same. In our reference procedure the vessel is placed in an ice bath and 20s pulses are separated by 10s pauses in order to allow heat dissipation. However, when shorter pulses were used, as presented in Figure II. 16 with 5s pulses, the obtained size is identical compared to the reference procedure. The final suspension is slightly more polydisperse, we can therefore assume

that the generated heat does not affect the emulsion formation or at least has a less pronounced effect than sonication duration.

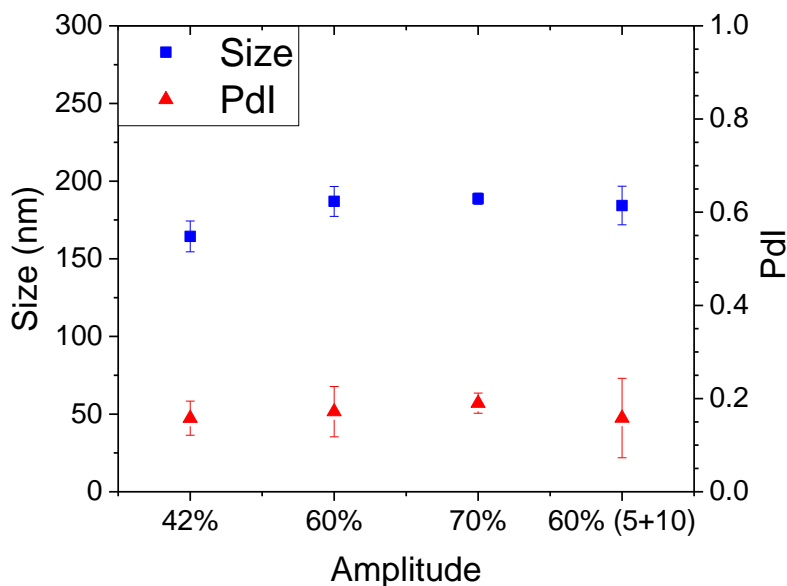


Figure II. 16: Influence of the sonication amplitude and pulse duration on the Si NCs size and polydispersity index for a total sonication duration of 3min

Although sonication settings are paramount parameters, the performed tests highlight the need to use optimized parameters to obtain a monodisperse reproducible dispersion rather than a possibility to tune the suspension's size.

II.2.3.2. Mechanical stirring

Sonication is generally preferred for the preparation of nanomaterials since it allows to reach smaller particles' sizes and to obtain highly monodisperse suspensions²⁹. We therefore logically attempted to use mechanical stirring in order to prepare bigger emulsions since less energy is brought to the system compared to sonication-induced cavitation.

i. Stirring speed

The assessment of the influence of the stirring speed has been done using an Ultra-turrax disperser equipped with a S18D-10G-KS tool (small dimension) during 5 min and using 4 different stirring speeds. Figure II. 17 records the size distributions obtained by DLS measurements. A colloidal suspension is obtained by mechanical stirring, with bigger particles' size as expected. However, for stirring speeds below 10 krpm, we can see a multimodal size distribution, with an out-of-range part or the suspension. Moreover, differences in the successive measurements show a clear instability of the suspension. This issue is fixed when a higher speed is employed: Figure II. 17c. and d. are indeed monomodal curves with reproducible measurements. A slight aggregation is noticed for 10 krpm mixing, while the suspension formed at 15 krpm seems stable. Concerning the hydrodynamic

diameter, the particles' mean size decreases from 399 ± 40 nm to 365 ± 6 nm when the stirring speed is increased from 10 to 15 krpm.

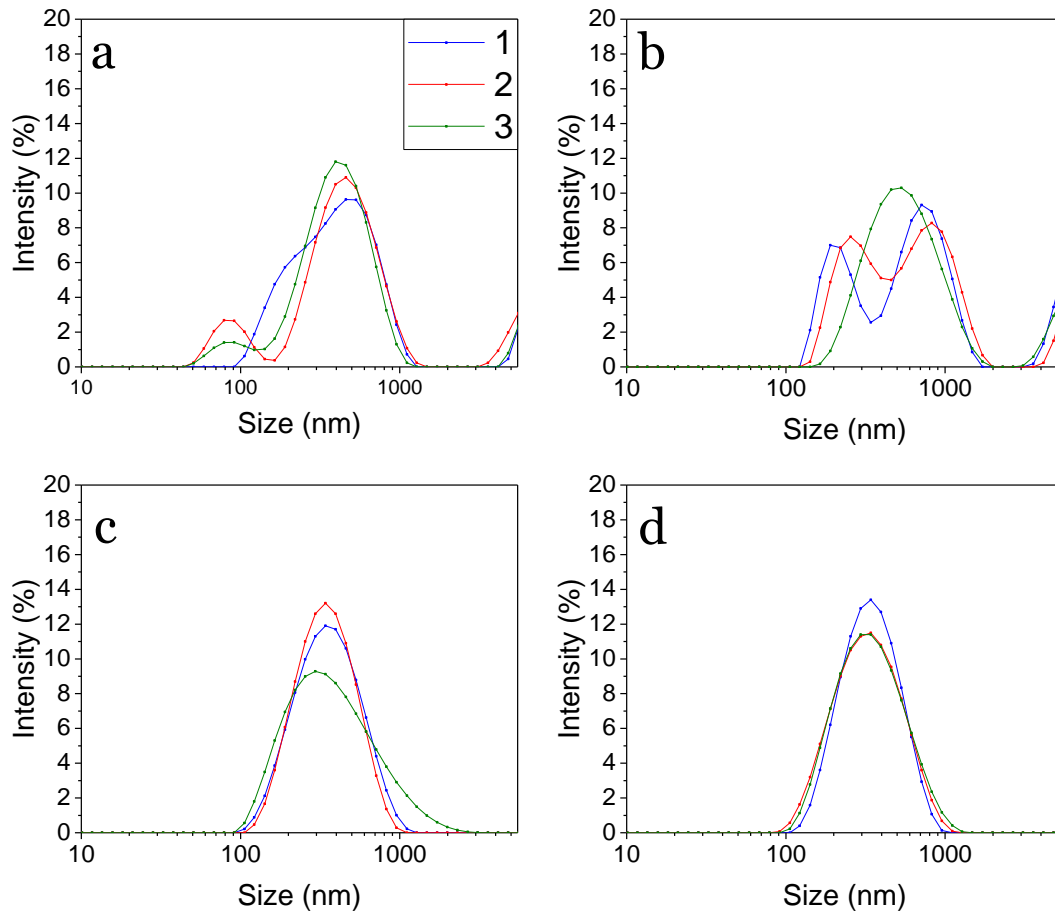


Figure II. 17: Size distribution of mechanically formed suspension for 5 min processing at (a) 3 krpm, (b) 7 krpm, (c) 10 krpm and (d) 15 krpm

Using a larger dispersing tool, the same kind of results could be achieved using lower stirring speed and time, what is presented in Figure II. 18, obtained by mechanical stirring at 7 krpm for 10 min. A monomodal distribution is obtain, with a similar mean size of approximately 370 nm but a narrower PdI of 0.03 compared to 0.21 obtained with the smaller tool. However, the analysis of the correlation function shows signs of sedimenting and/or aggregation (noisy baseline, varying intercept) that are not visible in the intensity distribution.

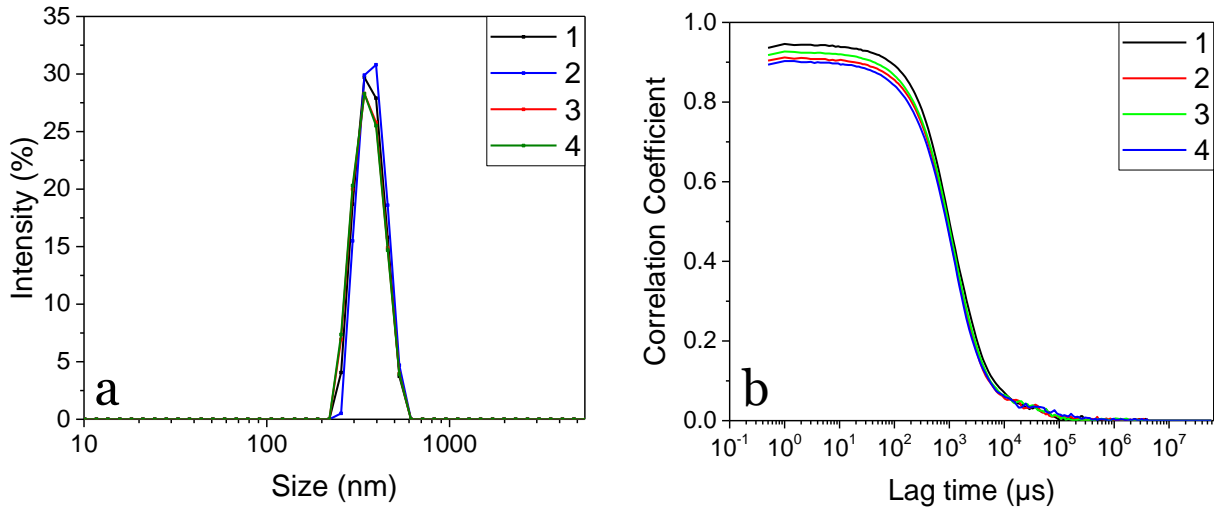


Figure II. 18: DLS (a) size distribution and (b) correlation function for a suspension mechanically formed by stirring at 7 krpm for 10 min

ESEM observations have been performed on this sample and are shown in Figure II. 19. On the pictures, we can detect the presence of spherical capsules, ranging from roughly 150 to 750 nm. These particles seem to be trapped in a shapeless matrix, probably due to the drying of unreacted monomer. A part of the initial TEOS has been shaped as particles during the emulsion formation. However, the formed emulsion is likely to be unstable over the polymerization reaction, what leads to a non-controlled reaction.

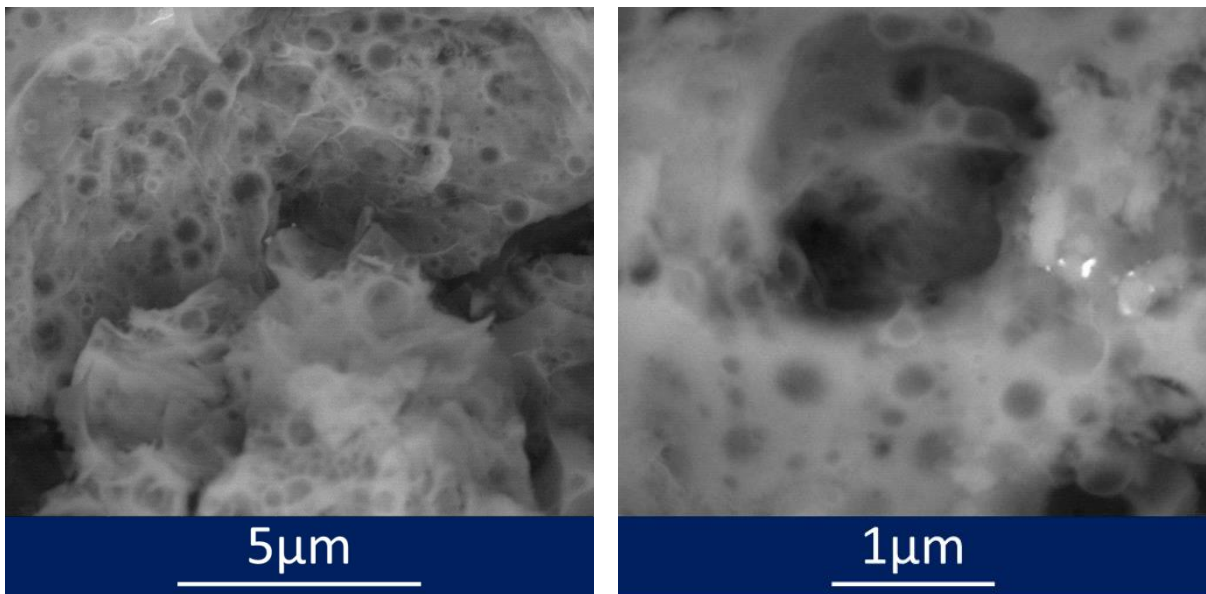


Figure II. 19: ESEM observations of a silica particle suspension obtained through a mechanically formed emulsion

From these observations, we can assume that in the tested conditions the use of a high shear rate disperser cannot form an emulsion stable enough to enable the formation of a monodisperse suspension. Moreover, even in the case that the suspension is purified (by dialysis or filtration for instance), this process implies an apparently low yield that is not affordable.

ii. Mixing duration

The previous results evidenced that a minimum speed is required in order to form a monodisperse suspension, but also that an important part of the precursors does not react. Increasing the stirring duration could be a way to enhance the reaction's yield and the suspension's polydispersity. Tests have therefore been performed fixing the stirring speed at 7 krpm for 5, 10 and 15 min processing. The suspensions looked visually the same after 24h. The results of the DLS measurements are plotted in Figure II. 20 for 5 and 15 min of stirring at 7 krpm and clearly show that in both cases a monodisperse suspension could not be obtained. Multiple peaks are indeed observed, with important differences between two successive runs in the same sample. Increasing the stirring time however apparently limits the sedimenting since no increase in the scattered intensity is observed for particles' sizes above 3000 nm for 15 min stirring contrary to the 5 min stirring suspension. This phenomenon is corroborated by the corresponding correlograms with a decrease in baseline noise and initial value variations for higher durations.

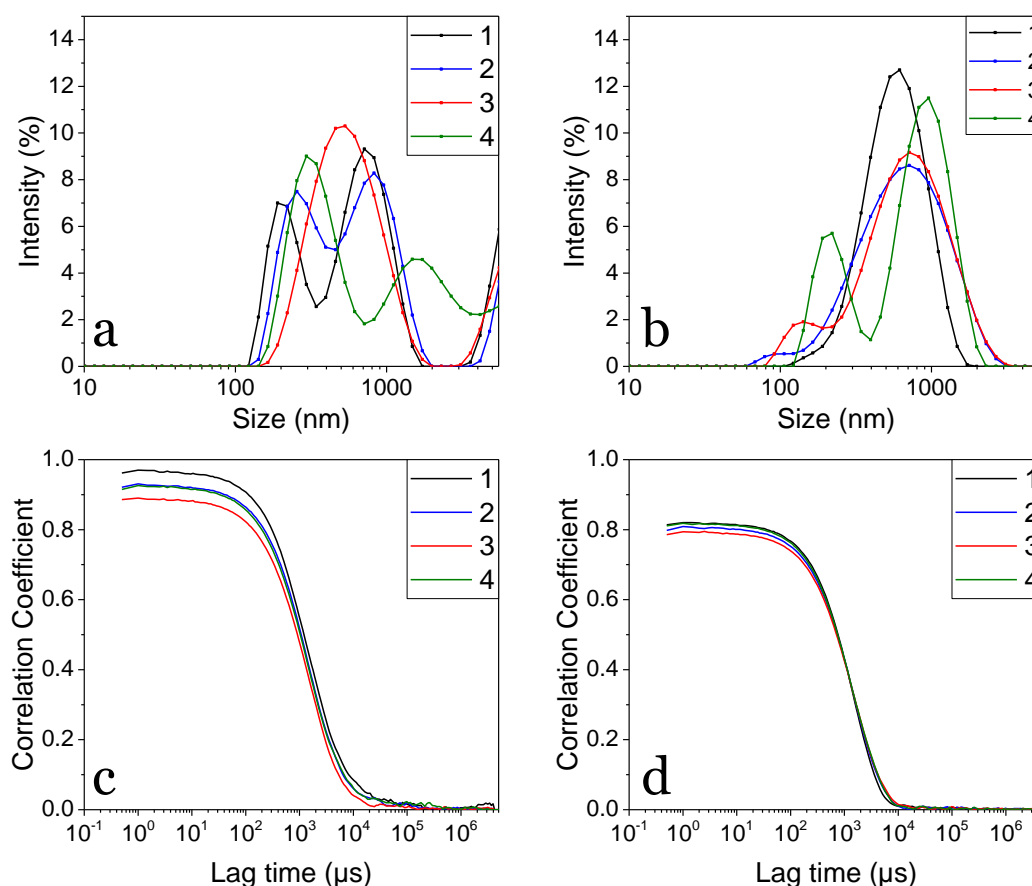


Figure II. 20: DLS analysis of a suspension formed using mechanical stirring at 7 krpm for (a & c) 5 min and (b & d) 15 min

Due to the ultra-turrax's design, longer stirring is not advised by the manufacturer and were not tried. It however looks like the stirring speed is the most influent parameters in order to obtain a

monodisperse suspension, while increasing the stirring time can increase the reaction yield. This has to be confirmed by microscopic observations

II.2.3.3. Composition

We have seen that a mechanical formation of the template emulsion is not viable without purification since it led to either non-controlled or partial interfacial polymerization. Tests have then been carried out making variations in the medium's composition, in order to obtain a controlled bigger suspension. The considered key parameters are the concentration in surfactant and its chain's length, the ratio between the two phases' volumes and the mounts of hexadecane and TEOS.

i. Surfactant

As presented in the state of art, the choice of surfactant and its amount highly influence the emulsion's size, morphology and polydispersity. It is commonly accepted that for a known surfactant able to form a stable emulsion, an increase in the surfactant concentration leads to a decrease in the size of the particles. Figure II. 21 shows the size and the polydispersity of the suspensions obtained for four different concentrations of DTAB, varying from 2 to 24 mM. The DTAB's critical micellar concentration (CMC) is around 14 mM in pure water³⁰. In a second study, the length of the surfactant's tail has been modified, keeping the trimethylammonium head nature in order to preserve the interface interactions. A concentration of 8 mM has been used based on the reference procedure.

As expected, the measured suspension's size decreases when the surfactant concentration increases with 151 ± 6 nm DLS mean size obtained at 24 mM. Logically, decreasing the surfactant concentration allowed the formation of slightly bigger capsules: a hydrodynamic diameter around 210 ± 8 nm was obtained for a 2 mM DTAB concentration, against 187 ± 10 nm for the reference synthesis (8 mM). However, a minimum surfactant concentration is mandatory in order to obtain a viable suspension since the absence of DTAB leads to a non-controlled TEOS reaction, and hence formation of a bulk polymer.

Concerning the dispersion's polydispersity, a monomodal dispersion is obtained whatever the DTAB concentration ($PdI < 0.2$). The slight increase that is observed when increasing the surfactant concentration is here mathematically due to the shift toward lower sizes: Since the PdI is the ratio $(\text{standard deviation} / \text{mean size})^2$, a decrease in size while keeping a constant standard deviation indeed leads to higher PdI values. A variation of the DTAB concentration then hardly influences the capsules' sizes, with a diameter difference of 60 nm between the extreme values obtained.

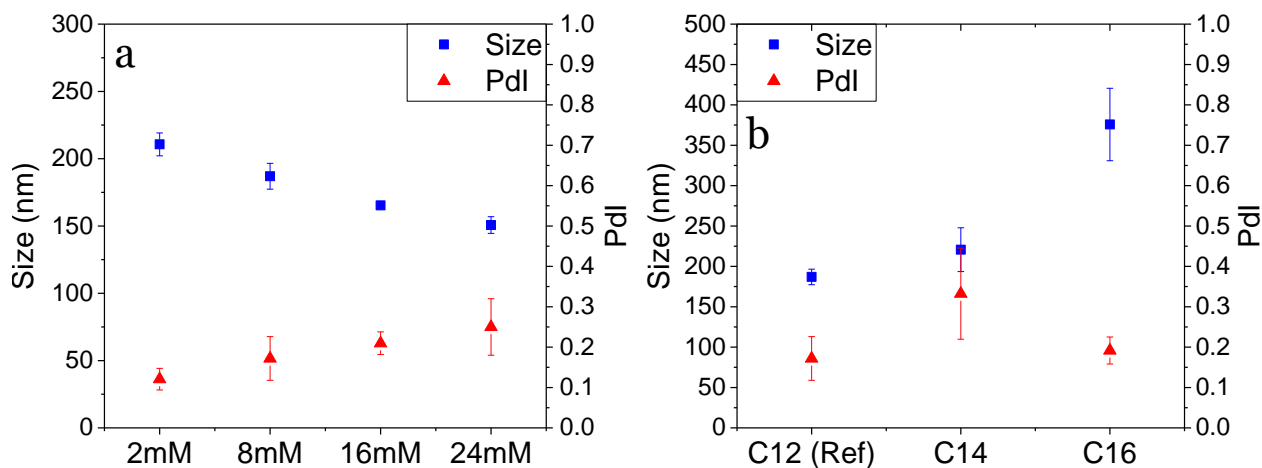


Figure II. 21: Influence of (a) the DTAB concentration and (b) surfactant carbon-chain's length on the final suspension's size

Another strategy to reach higher sizes is the use of a different surfactant. Due to availability and in order not to change the interface interactions, other alkyl trimethylammonium bromide surfactants have been used, presenting a carbon chain longer than that of DTAB. The concentration used is 8 mM based on our reference procedure. Molecules with tails made of 12, 14, 16 and 18 carbon atoms have been tested and looked similar 24h after sonication. However, the first 3 only enabled the formation of a stable dispersion according to the DLS analysis. The sample prepared with OTAB (C₁₈ chain) formed flocs upon dilution and therefore could not be analyzed. SEM observations did not allow to observe controlled architectures.

The increase in the chain's length implies an increase in both the dispersion's size and polydispersity. The sizes indeed range from 187 ± 10 nm for DTAB (C₁₂) to 376 ± 45 nm for HTAB (C₁₆). An assumption is that due to steric hindrance, less molecules can adsorb per surface area unit and that this lower coverage favors the stabilization of a bigger emulsion. The higher associated standard deviation observed however highlights a tendency to agglomerate or a potential instability of the dispersion. This might be enhanced as seen previously by increasing the surfactant concentration. Another idea is to use a combination of water-soluble and oil-soluble surfactants³¹, but this has not been tried. Despite this instability, particles with a diameter twice as high as the reference synthesis have been obtained.

ii. Medium's composition

In addition to the surfactant, the nature of the emulsion's phases (especially the solvent polarity) or volume may induce changes in the mode of action and efficiency of the surfactant, and also in the mixing efficiency (sonication being sensitive to the volume to be processed). The influence of several parameters have then been studied in order to have a better understanding of our medium while trying to tune the capsules' size.

In a first step, we evaluated the effect of the dispersed phase's composition, changing either the precursor or the hexadecane amount. We noticed on TEM observations that the thickness of the capsules' shell is quite constant, whatever the capsules' diameter. Our assumption is that a decrease in the TEOS amount can still enable the formation of capsules and could imply differences in the dispersion's size, stability and dispersion. Another try concerns the use of hexadecane in the dispersed phase. According to the work of Fickert and colleagues¹¹, hexadecane is added to toluene in the reference procedure in order to prevent Ostwald ripening and then permit to obtain smaller particles. By decreasing the hexadecane content, the promotion of coalescence of the droplets might then lead to bigger capsules. Figure II. 22 shows the DLS analysis of the dispersion obtained with 33% less TEOS (*i.e.* 1.43 mL instead of 2.15 mL) and 40% less hexadecane (*i.e.* 77 μ L instead of 162 μ L).

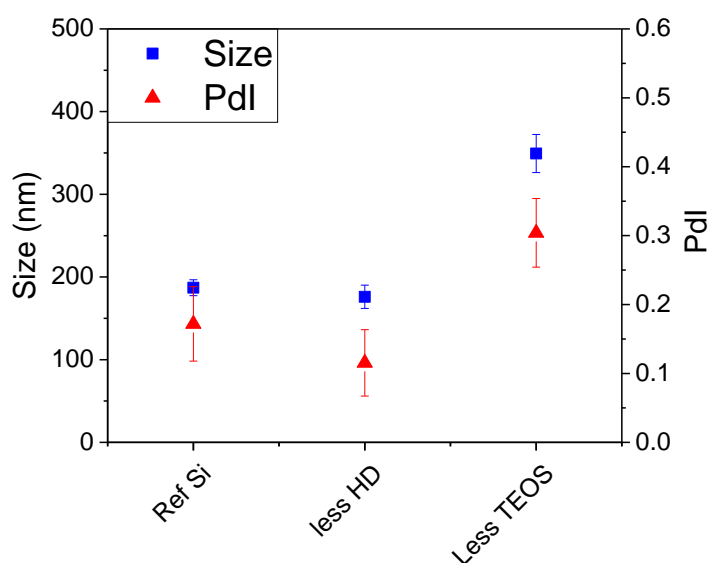


Figure II. 22: Influence of hexadecane and TEOS amounts on the dispersion's size and polydispersity

We noticed that a diminution of the TEOS amount leads to an increase in both the capsules' mean size and polydispersity. An assumption is that reducing the TEOS amount, the reaction is slowed down enough for particles to coalesce during the polymerization reaction. This could perhaps allow the formation of non-spherical particles but SEM observations of this sample were not successful. This could be the result of sintering of the particles over drying. Because we were unable to visually assess the particles formation and because polydispersity was increasing, this approach was not further developed.

On the other hand, the influence of hexadecane seems to be less important since a 40% decrease in the hexadecane amount does not affect significantly the final dispersion's size. Hexadecane is however mandatory in order to limit the droplets coalescence during the shell formation. In the absence of hexadecane, the final mixture was indeed not analyzable by DLS since the polymerization was not controlled. Figure II. 23 shows a SEM observation of a synthesis carried out without using hexadecane and shows open capsules from a few microns to around 10 μ m.

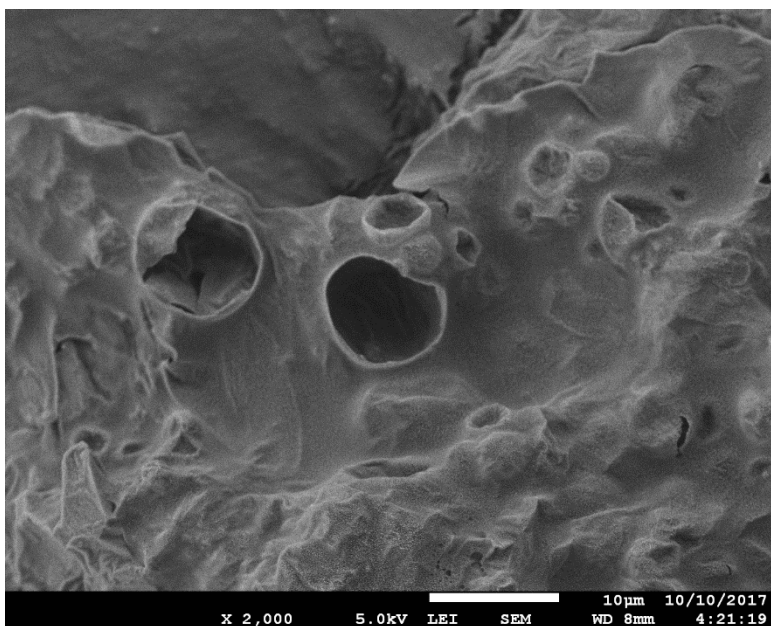


Figure II. 23: SEM observation of a sample prepared without hexadecane in the dispersed phase

From these results, we can assume that the quantity of hexadecane and TEOS cannot be further optimized since variations induced destabilization of the suspension. Another approach then consists in keeping the same relative amount of chemicals in the dispersed phase but changing the volume or phase volume ratio. Doing that, we change the probability of encounter between droplets, in order to induce coalescing. The conducted tests consist in doubling the amount in each component in order to assess that the observed changes are not dependent on the volume processed. We then tried to use twice and four times as high quantities of dispersed phase compounds. Moreover, the surfactant needed quantity being dependent on the total O/W interface area, an attempt in adapting the amount of surfactant was performed, using 2.6 mM DTAB against 8 mM for the reference procedure. DLS analysis, when usable, is presented in Figure II. 24 and shows *in fine* only little variations in the dispersion's size and polydispersity.

First, this proves that the total processed volume has almost no influence on the way the emulsion is produced since mean sizes around 180-190 nm are obtained with polydispersity indexes below 0.2 when doubling all quantities, similarly to the reference suspension. The increase of the total volume induced when increasing the dispersed phase volume is hence not responsible for the differences in the dispersion. Moreover, doubling only the dispersed phase's volume, a hardly bigger suspension with a lower PDI is obtained with a 195 ± 9.0 nm mean size and a PDI of 0.136 ± 0.038 against a 187 ± 9.6 nm mean size and a 0.172 ± 0.054 PDI for the reference procedure. Interestingly, combining the dispersed phase's volume increase with a lower concentration in surfactant, a higher capsules' mean size, of 265 ± 7.0 nm, was obtained, keeping a very low PDI (below 0.1).

A further increase of the dispersed volume destabilized the emulsion and a gel was obtained 24h after sonication.

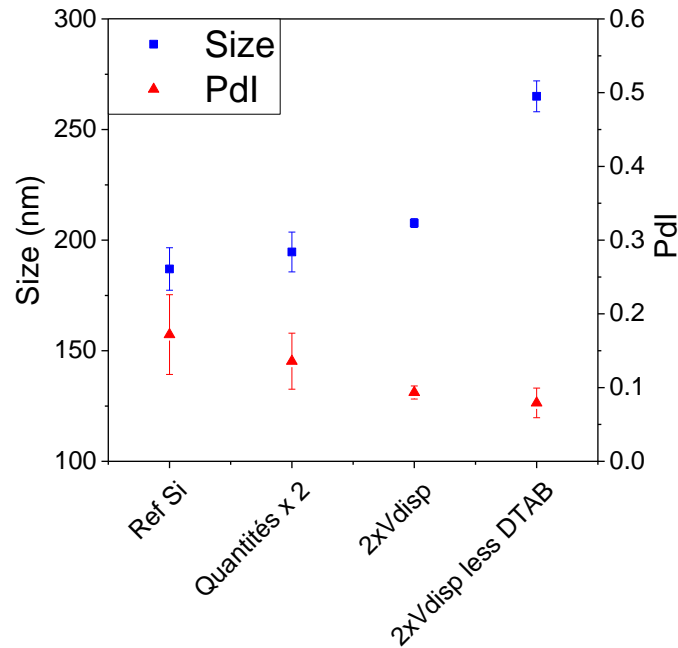


Figure II. 24: Influence of the total dispersion's volume and the dispersed phase's relative volume on the final dispersion's size and polydispersity

II.2.3.4. Summary

A summary of the optimization tries performed is given in the appendices section (Appendix 3). The experiments that have been carried out did not allow to obtain a clear increase in the capsules' size, keeping a moderate polydispersity index. However several interesting results have to be highlighted and must be pursued:

- Mechanical stirring enables the formation of a bigger emulsion, but a minimum stirring speed is required in order to get a stable dispersion (15 krpm in our case), while the stirring duration has a lower influence. However, due to either a lower reactivity (because of the absence of heating compared to US) or a too low emulsion's stability, a not quantified part of TEOS does not lead to the formation of capsules. This has to be optimized by varying either the surfactant or the involved volume. A purification step could also help to remove the bulk polymer. A controlled heating associated with mechanical stirring could also be an option.
- Choice of surfactant is probably the paramount parameter. The use of trimethyl ammonium bromides with longer carbon skeleton led to bigger apparent capsules, but the quantity of surfactant has to be optimized in order to get a stable controlled dispersion.
- The best result we got so far consists in increasing the dispersed phase volume, adjusting the concentration in surfactant, in order to favor and control Ostwald ripening. This way we got particles with hydrodynamic mean sizes of 265 ± 7 nm.

II.3. Hydrophilic-core polyurea containers

II.3.1. Capsules formation

II.3.1.1. Materials

A list of the chemicals used for the synthesis of polyurea (PUa) containers is given in the appendices section (Appendix 2).

II.3.1.2. Standard procedure

The encapsulation of water-soluble compounds is carried out through a W/O emulsion process, illustrated in Figure II. 25, in order to form hollow water-core capsules. In the process we use, developed at Max Planck Institute (Mainz, Germany), three solutions are prepared:

- 100 mg of Lubrizol® U, an oil-soluble surfactant are dissolved in 9.63 mL of cyclohexane that constitutes the continuous oil phase (solution A);
- 100 µL of 1,4-diaminobutane (DAB) and the potential payload are dissolved in 1.30 mL of water that is the dispersed phase (solution B);
- 215 µL of 2,4-toluene diisocyanate (TDI) are dissolved in 3.21 mL of cyclohexane (solution C).

After 1h of homogenization under magnetic stirring (750 rpm), the solution B is added dropwise to the solution A under stirring. The emulsion is then formed right away using a sonication probe. If not specified, sonication is performed in a pulse regime (each pulse during 20s, with 10s pauses) for 180s at 90% amplitude, the vessel being placed in an ice bath. Immediately, the vessel is placed under magnetic stirring and the solution C is added dropwise to the emulsion. The final suspension is then left under magnetic stirring at 750 rpm for 24h.

Unlike for the synthesis of silica capsules, the second monomer is added after the emulsion is formed. Being soluble different phases, the two monomers react at the O/W interphase, hence forming the capsules' shells. The size of the emulsion is then governed by the sonication parameters, the nature of the surfactant and its concentration. In this process, the encapsulated molecule is dissolved in the dispersed phase and the capsules are therefore loaded *in-situ*. This kind of containers have mainly been designed for the encapsulation of pH indicators (thymolphthalein and phenolphthalein) as sensing molecules. Due to the poor solubility of these molecules in pure water, ethanol is added to the dispersed phase solution when they are used.

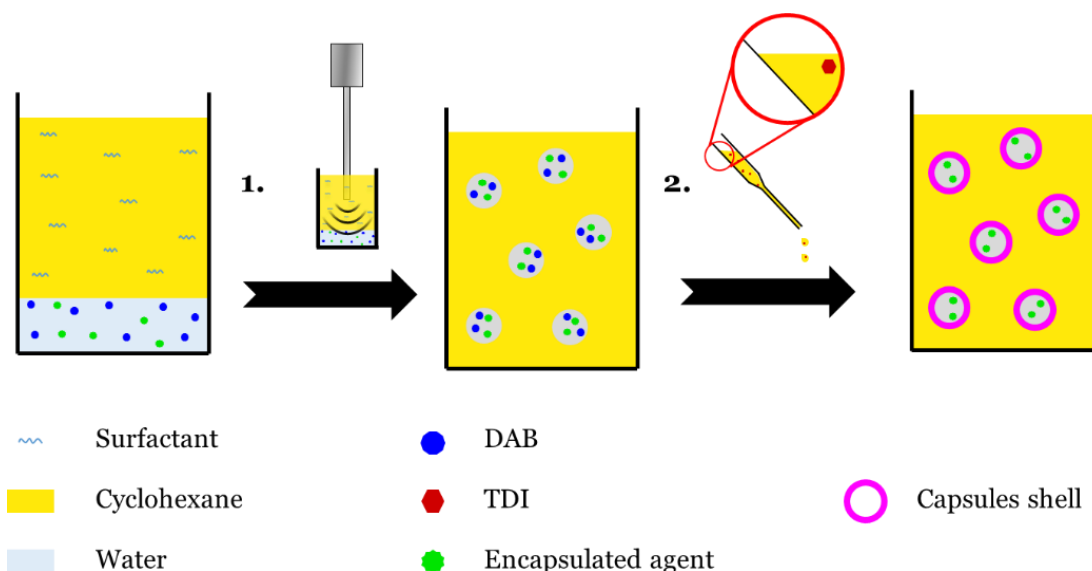


Figure II. 25: Schematic representation of the W/O emulsion and polyurea capsules formation

The quantities given for the solvents and monomers concern our reference procedure. The quantity and nature of the surfactant and encapsulated agent varying, they will be discussed later on. The melting temperatures of TDI and DAB are 21.8 and 27°C respectively, what is slightly above the storage temperature. The vessels are therefore placed in a water-bath filled with hot tap water for 20 min before the takings. Importantly, only a range of molar weight is known for the surfactant used in our reference procedure, namely Lubrizol® U.

The formation reaction of the capsules occurring at the water/cyclohexane interphase is the polyaddition involving a diamine, DAB, and a diisocyanate, TDI. This reaction is well known and is quick enough so it does not require a catalyst³². Since the dispersed phase is water, the hydrolysis of the isocyanate also occurs as a parallel reaction, leading to the formation of the corresponding primary amine. The reactivity of DAB being higher, the mentioned reaction, presented in Figure II. 26, is the most favorable³³. Using an excess of TDI, DAB is then entirely consumed and the remaining isocyanate reacts with water to form isocyanato-methylaniline (IMA) as an intermediate. IMA reacts with either TDI, IMA or polymeric chains to form new PUa units^{34,35}.

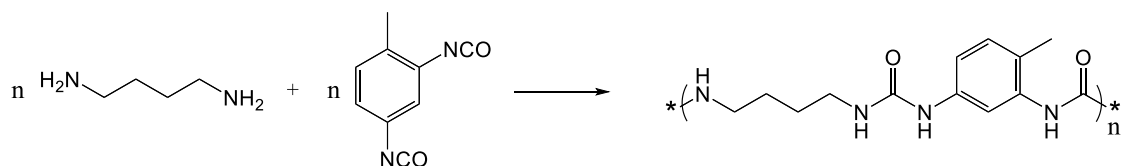


Figure II. 26: Polymerization of DAB with TDI leading to the formation of polyurea shell

II.3.1.3. Importance of the surfactant

A second reaction is due to the surfactant employed. As explained for instance by Rosenbauer and coworkers³⁶, surfactants can possess reactive groups and participate in the polymerization reaction. This would lead to covalent bonds between the polyurea chains and the surfactants molecules.

Developed at the Max Planck Institute (Mainz), our process was first using a commercial surfactant named “Lubrizol® U”, whose structure is presented in Figure II. 27. With five available amine groups, the molecule possesses reactive nucleophilic sites that can react. Therefore, besides stabilizing the W/O emulsion, the surfactant forms covalent bonds with the capsules’ shell.

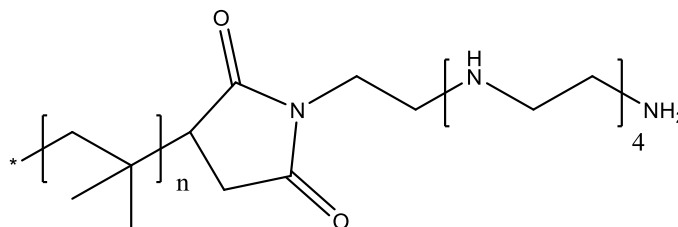


Figure II. 27: Polyisobutylene succinimide pentamine structure of Lubrizol® U used for the synthesis of PUa capsules, with $n=1-10$, according to ³⁶

The nature of the employed surfactant is then crucial. However, due to supply issues, an alternative to Lubrizol® U had to be found and so different surfactants were tested.

II.3.1.4. Suspension purification and transfer in water

Since the presence of unreacted reactants or free polymer chains can interact with the capsules, the dispersion is purified 24h after its formation using a cellulose dialysis tubing membrane. In a typical experiment, around 10 g of the PUa dispersion are placed in a cleaned dialysis membrane, closed by knots at both ends. The dialysis bag is then placed in a beaker containing 200 mL of cyclohexane under magnetic stirring at 300 rpm. The cyclohexane is renewed after 24h and 48h, the surrounding cyclohexane being whitish. After 72h, the dialysis is stopped and the purified dispersion retrieved.

After their formation and purification, the PUa capsules naturally exist as a suspension in cyclohexane, what is not convenient for uses such as the addition to a paint formulation. The capsules are therefore redispersed in water. This is achieved by diluting the PUa capsules in water and using a second surfactant to stabilize the dispersion, while the cyclohexane is evaporated. According to the literature³⁷, sodium dodecyl sulfate (SDS) is used as a water-soluble surfactant. The PUa capsules walls are likely to be cationic³⁸, SDS then electrostatically adsorb on them. Solutions are prepared with different concentrations in SDS, whose pH is adjusted using either citric acid or sodium hydroxide solutions. The dispersion is added to the surfactant solution under stirring at 300 rpm. The dispersion/water ratio is 1/9.

The mixture is then sonicated for 1 min in a pulse regime (10s sonication + 5s pause) and the vial is left open under magnetic stirring at 300 rpm and 70°C for 30 min. Mass loss measurements showed that the evaporated mass is higher than that of the initial dispersion placed in the vial. All the cyclohexane is therefore assumed to be removed.

II.3.2. Characterization of the PUa capsules

II.3.2.1. Surfactants

As explained, the choice of a surfactant has to be made depending on its ability to stabilize the emulsion, but also on the available reactive groups that could take part in the shell formation reaction. A list of the surfactants we chose is given in

Table II. 2. Three strategies were adopted:

- Sorbitan esters are well-known surfactants for the stabilization of W/O emulsions. Based on the literature, Span[®] 80 and Span[®] 85 were tested³⁹. Both are non-ionic surfactants that should stabilize the emulsion during the polymerization reaction. Moreover, these surfactants possess hydroxyl groups and might therefore be considered as “surfmers”, forming polyurethane linkages when reacting with TDI;
- In case the tested Spans were not efficient enough to stabilize the water/cyclohexane emulsion, and enable the formation of PUa capsules, Tween[®] 80 is dissolved in the water phase and combined with the equivalent span. This allows to modify the surfactant system’s HLB that can be controlled to fit our system³⁹;
- According to the supplier’s recommendation, and given the available information, two commercially available surfactants with properties similar to that of Lubrizol[®] U were tested: Lubrizol[®] 5625 and 5620B. Both possess a polyisobutylene succinic anhydride (PIBSA) structure. Lubrizol[®] 5625 is functionalized with sulfonate groups.

Table II. 2: List of the surfactants used to stabilize W/O emulsions and their properties

Commercial name	Supplier	Structure	Soluble in	HLB	M (g.mol ⁻¹)
Lubrizol [®] ‘U’	Lubrizol	PIB-succinimide pentamine	Oil	< 7	400 - 900
Lubrizol [®] 5625	Lubrizol	PIB succinic anhydride skeleton	Oil	10.6	~1000
Lubrizol [®] 5620B	Lubrizol	PIB succinic anhydride skeleton	Oil	10.6	~1000
Span [®] 80	Croda	Sorbitane monooleate	Oil	4.3	429
Span [®] 85	Croda	Sorbitane trioleate	Oil	1.8	957
Tween [®] 80	Croda	Polysorbate	Water	15.0	605

*PIB: PolyIso Butylene

i. Sorbitan esters

Span and Tween surfactants are composed of an alkyl hydrophobic chain and a polar moiety that contains hydroxyl groups. The use of such compounds should then enable the formation of polyurethane functions with TDI. Span® 85 possesses one “-OH” group per molecule while Span® 80 has 3.

Since the molecular weight of both compounds is close to the targeted molecule, the same quantity as in our reference procedure has been employed. When Tween® 80 is dissolved in the dispersed phase in order to enhance the template emulsion stability, the total quantity (Span® 80 + Tween® 80) is kept constant with a Span/Tween ratio of 80/20. This ratio is calculated in order to obtain a mean HLB slightly lower than 7, adapted to a W/O emulsion. Figure II. 28 shows representative DLS correlograms obtained for the tried parameters while the quantities used for optimization are recorded in Table II. 3.

Table II. 3: Quantity of surfactants tried in order to form PUa capsules using Span® 80 and Tween® 80

Surfactant 1	m_1 (mg)	n_1 (mmol)	Surfactant 2	m_2 (mg)	n_2 (mmol)	$n_{\text{surf}}/n_{\text{TDI}}$
Span® 80	80	0.19	Tween® 80	20	0.033	0.15
Span® 80	450	1.05	Tween® 80	150	0.248	0.87

The formation of capsules has not been successful in the samples containing only a sorbitan ester (Span 80 or Span 85). Sedimenting was observed in the reaction vial, and the analysis of the homogeneous part of the sample by DLS was not successful (correlograms a and b). This is probably due to an important aggregation, potentially combined with the formation of too big particles, as evidenced by the DLS analysis (difficulty to reach baseline, intercept above 1).

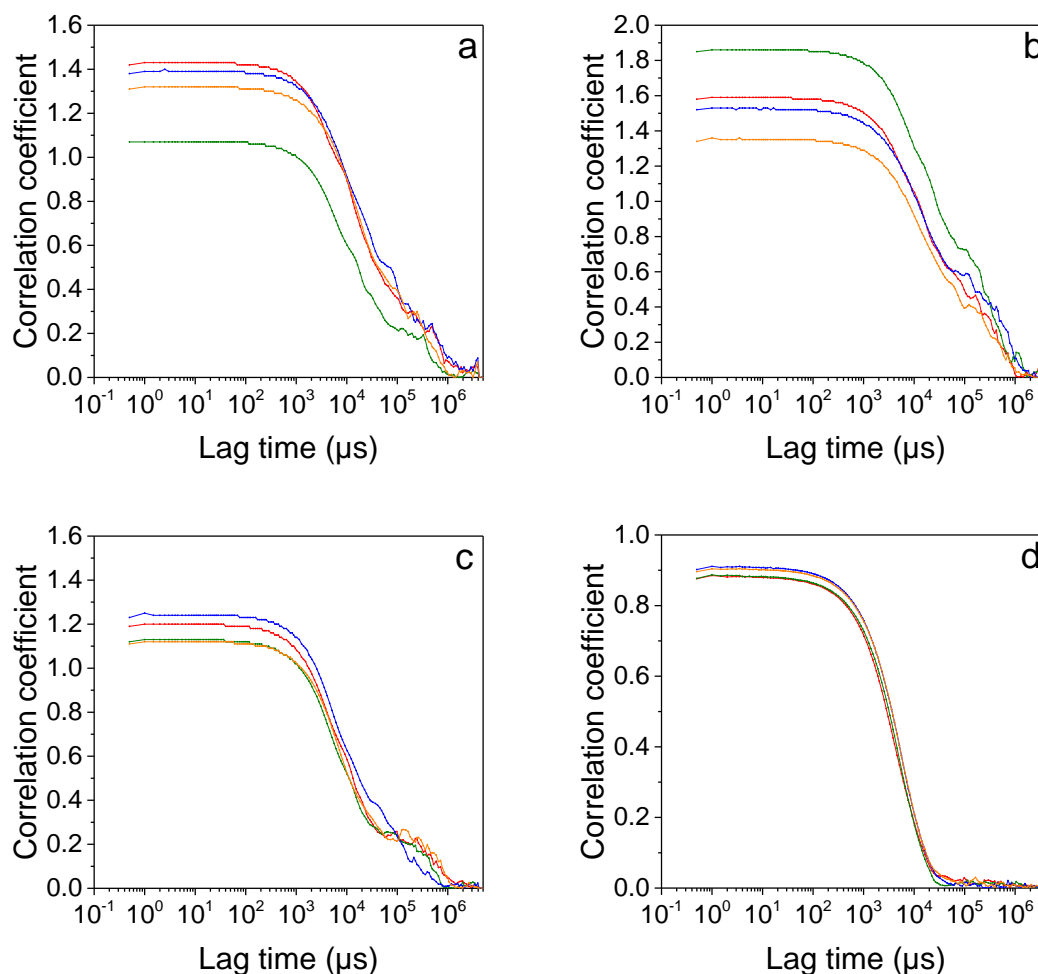


Figure II. 28: DLS correlograms obtained for the emulsions formed with (a) Span 80, (b) Span 85, (c) Span 80+Tween 80 0.15 eq. and (d) Span 80 + Tween 80 0.87 eq.

Since the impossibility to form a stable dispersion is likely to be due to an unstable emulsion, the quantities of surfactants have been increased for the combination of Span and Tween 80. When the total surfactants quantity reaches a 1:1 ratio versus TDI, a homogeneous mixture is obtained. DLS analysis cannot give a size distribution despite an exploitable correlogram evidencing a homogeneous dispersion. The main hypothesis is that particles with diameters exceeding $10\ \mu\text{m}$ could have been synthesized. The formation of a stable emulsion, as well as the formation of particles can be explained by the reaction between the surfactants' polyols and TDI, as seen for instance in a study performed by Kakaroglou and coworkers³⁹.

Although the use of a combination of Span 80 and Tween 80 seems promising, the size of the obtained particles exceed our expectations. Moreover, differences in the shell nature would necessitate further works in order to assess the potential of these architectures for our applications.

ii. PIBSA

Polyisobutylene succinic anhydride (PIBSA) surfactants are polymeric emulsifiers suitable for the stabilization of W/O emulsions. Trying to mimic the mode of action of Lubrizol[®] U, PIBSAs

(Lubrizol® 5625 and 5620B) have been chosen for their structural similarity and for their eventual reactivity toward the diamine precursors we used. PIBSAs general structure is presented in Figure II. 29⁴⁰. This base structure can then be functionalized in different ways. The chemicals we used being commercial ones, very few information were available. However, Lubrizol® 5625 and 5620B have a succinic anhydride group that can react with amine functions to form amide groups^{41,42}. Since the reactive groups in the Lubrizol® U's structure are amines, *in situ* formation of amine-functionalized PIBSA could be of great interest.

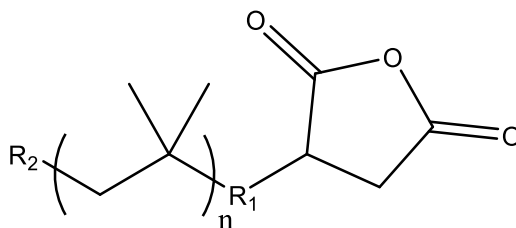


Figure II. 29: generic structure of PIBSA surfactant molecules

As for the previous surfactant tries, syntheses have been carried out with different quantities of surfactants. The supplier giving an approximate molar weight of 1000 g.mol⁻¹ for the PIBSA surfactants, two different ratios were used in order to get close to our reference procedure. 0.067 and 0.20 equivalent toward TDI are used. The DLS results of four syntheses are presented in Figure II. 30. It has to be mentioned that DLS measurements failed right after dilution, except in the last case (0.2 eq. of Lubrizol® 5620B), and were possible only after the suspension stays for a few minutes in the cuvette. This highlights a high instability of the suspension, but in order to compare the four conditions, the time between the preparation of the sample and the measurement is kept constant.

A net improvement in the dispersion's homogeneity is seen when increasing the surfactant concentration in both cases. For the lower concentration, the successive runs give very different size distributions, highlighting a very high polydispersity and an unstable dispersion. When Lubrizol® 5625 is used, the autocorrelation function cannot be fitted due to important variations. It tends to show that only a part of the medium led to the formation of particles while impurities and aggregates are present. On the other hand, the suspension made with Lubrizol® 5620B seems to contain analyzable particles with several populations and a wide polydispersity.

An increase of the surfactant concentration (c and d) leads to smooth autocorrelation function curves and repeatable DLS runs. However, Lubrizol® 5625 shows that a part of the particles in the dispersion is out of range and cannot be analyzed. In the case of Lubrizol® 5620B, a major peak is seen in the size distribution with a mean size of 2650 ± 210 nm that does not evolve during the measurement.

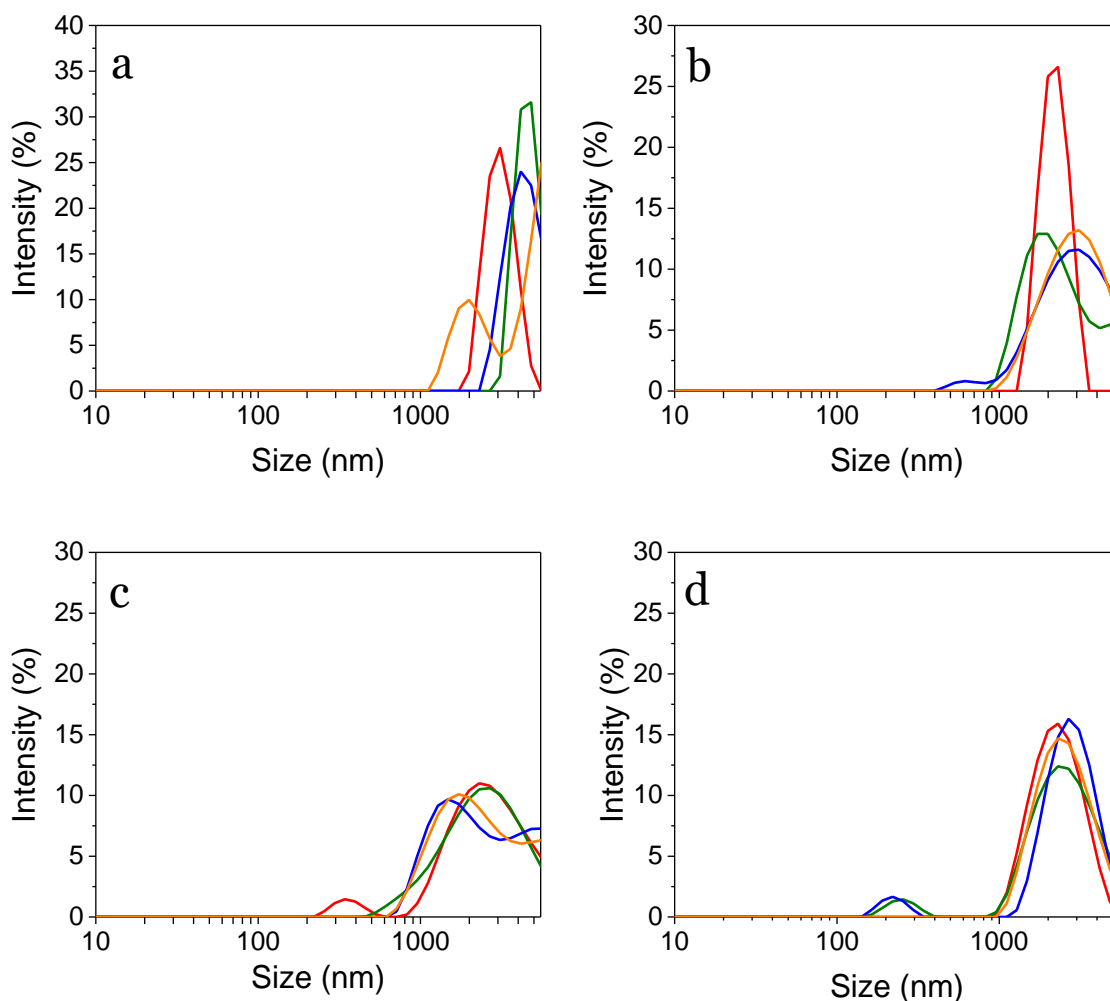


Figure II. 30: DLS size distributions of PUa syntheses carried out using PIBSA-based surfactants Lubrizol® 5625 (a and c) and Lubrizol® 5620B (b and d) using 0.067 (a and b) and 0.2 (c and d) equivalent versus TDI

Even though the particles' sphericity cannot be assessed, a stable emulsion can apparently be obtained, meaning we probably reached the minimum quantity required to stabilize the emulsion and carry out the polymerization reaction. However, even if the smaller peak (corresponding to 200 nm particles) can probably be neglected, a part of the emulsion is out of range and several populations could coexist. The particles' size is moreover higher than the targeted diameter of 500-1000 nm, that we obtained in a previous work. Since the role of the reactive groups, especially amines, in the carbon chain has been put forward, FTIR analysis has been performed on both Lubrizol® 5625 and 5620B and on a sample of Lubrizol® U. Spectra are shown in Figure II. 31 and interpreted peaks recorded in Table II. 4.

Based on the formula of Lubrizol® U, the main difference with Lubrizol® 5625 is the absence of amine functions in Lubrizol® 5625. The existence of peaks between 3200 and 3400 cm^{-1} and at 1227 cm^{-1} , related to aliphatic amines might explain the better results obtained with Lubrizol® 5620B. On the other hand, an important difference concerns the succinic anhydride group that is

present in PIBSA molecules and could take part in the particles formation, while Lubrizol® U has an amide function.

Table II. 4: Comparison of FTIR spectra for the PIBSA and Lubrizol® surfactants

Wavenumber (cm ⁻¹)	Deformation	Group	U	5620B	5625
3500 - 3200	O-H stretch	hydroxyl	Y	Y	Y
3400 - 3200	N-H stretch	Amine II	Y	Y	N
1750 - 1730	C=O stretch	Ester or carboxylic acid	N	Y	Y
1660	C=O stretch	Amide III	Y	N	N
1227	C-N stretch	Aliphatic amine	Y	Y	N

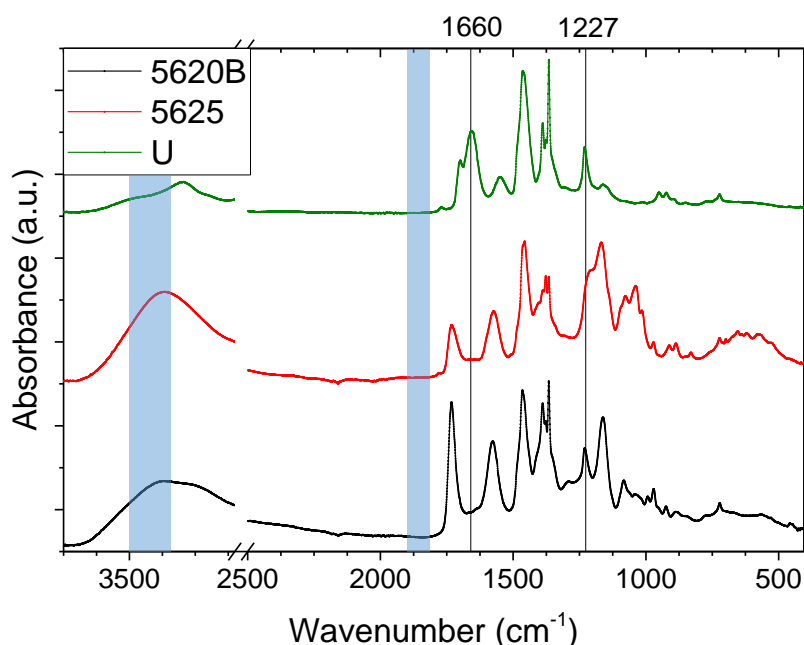


Figure II. 31: FTIR spectra of the employed PIBSA-based surfactants and reference Lubrizol® U

In order to assess the particles shape, ESEM observations, presented in Figure II. 32, have been carried out on dried dispersions, synthesized using Lubrizol® 5620B in the two previous ratios. Observations of samples with the lower amount of surfactant (II. 32 a and II. 32 b) show a compact structure, with spheroidal shapes entrapped in a shapeless matrix. The first supposition would be that particles and aggregates are present in the dispersion and that, upon drying, the unreacted monomers and aggregates merge, forming the continuous film. The size of the spheroidal parts is roughly between 1 and 5 μm , corresponding to the DLS measurements.

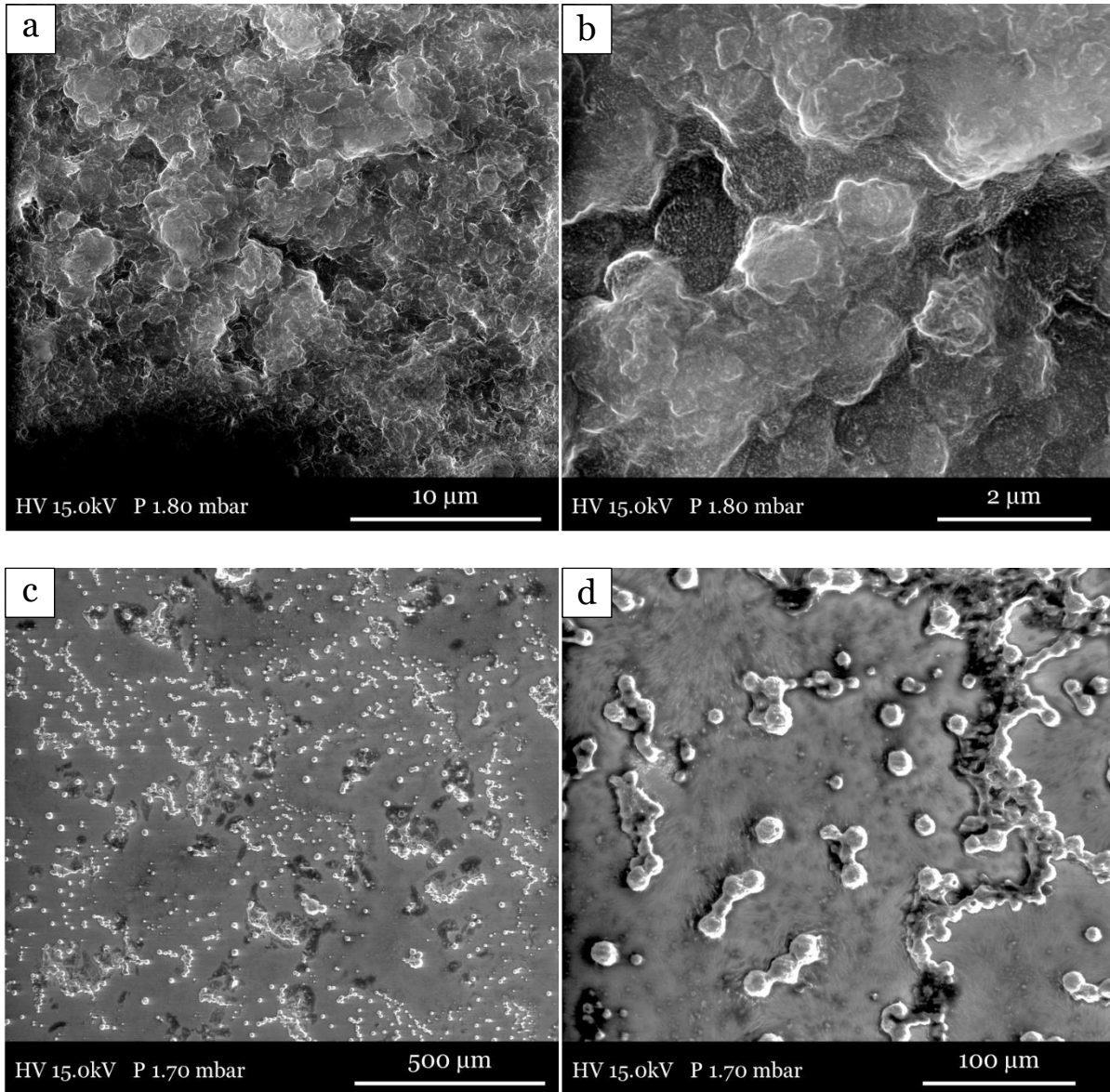


Figure II. 32: ESEM observations of dispersions of capsules formed with (a and b) 0.067 and (c and d) 0.2 equivalents of L5620B respectively

As expected from the DLS analysis, when the quantity of L5620B increases, a cleaner dispersion is obtained, and the observation of isolated particles is enabled, as seen in pictures II. 32 c and d. These observations allow to conclude that spherical particles are prepared, with a pretty rough surface. Shapeless parts are also seen in this sample, but to a lower extent, what leads to the formation of strings of particles and aggregates. Using image analysis based on 781 analyzed particles in picture c, a size distribution analysis is performed, presented in Figure II. 33. It gives a mean diameter of $8.9 \pm 3.2 \mu\text{m}$ for particles ranging from 2.5 to 24.8 μm , what is naturally higher than DLS values since DLS fitting algorithms hardly operate above 5 μm and so bigger particles are not analyzed. It is also possible that the particles' shape changes during the preparation of the sample, and that eventually unreacted species would bind to the particles, making them swell.

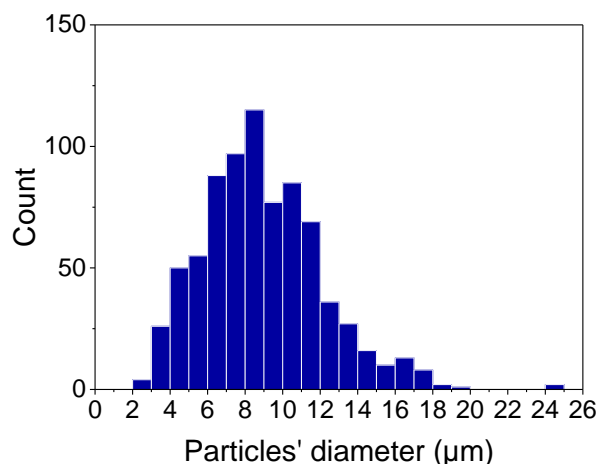


Figure II. 33: Particle size distribution obtained by image analysis on 781 particles from an ESEM observation of particles using 0.2 equivalent of Lubrizol 5620B

Despite not being identical to the previously developed microcontainers, the PUa particles formed using Lubrizol 5620B as a surfactant seem viable, and were therefore used for the following experiments. The next objective is to assess the possibility to load the microcapsules, and to study their reactivity in media at different pH.

II.3.2.2. Addition of ethanol in the dispersed phase

The first purpose of the synthesized water-core capsules is to encapsulate thymolphthalein and phenolphthalein as corrosion sensors. However, both molecules present a low solubility in pure water, but that can be enhanced by the addition of ethanol in the dispersed phase. Since ethanol could react through its hydroxyl groups, the capsules synthesis has then been performed adding ethanol to the reference formulation in order to assess the viability of the process. The total volume of the dispersed phase is kept constant and water:ethanol ratios of 91:9 and 79:21 are tested. At the end of the reaction, an important sedimenting is observed at the reaction vessel's bottom and on its walls. A DLS analysis was not possible. However, when 9.0% ethanol is used a homogeneous mixture is obtained, whose DLS analysis is presented in Figure II. 34. Despite a size peak shift over the four consecutive runs, a single population is observed with a tendency to aggregate. This behavior is similar to what has been previously seen, corroborated by a noisy correlogram baseline.

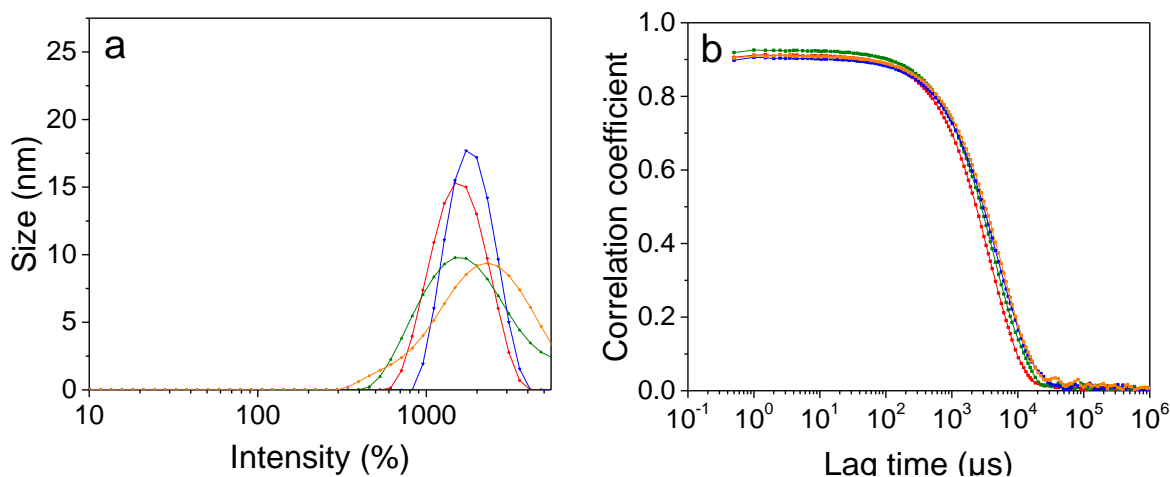


Figure II. 34: DLS (a) size distribution and (b) associated correlograms

When a too high proportion of ethanol is used in the dispersed phase, forming the microparticles was not successful. This can be due to changes in the dispersed phase's polarity, inducing a loss of the emulsifier stabilization. Ethanol being soluble in both water and cyclohexane, and susceptible to react with the isocyanate groups, the control of the emulsion is then hindered, what leads to bulk polymerization.

II.3.2.3. Transfer of the suspension in water

Since the PUa capsules are intended to be added to a water-based paint and that the addition of a non-negligible amount of cyclohexane to the formulation is not achievable, a change of dispersant, *i.e.* transfer in water, is required. This is performed in two steps: first, the dispersion is purified by dialysis, and secondly the suspension is transferred in water using an anionic surfactant: sodium dodecyl sulfate (SDS).

i. Purification of the suspension by dialysis

A non-negligible amount a surfactant or residual monomers could remain in solution at the end of the synthesis. The suspension dialysis is performed in order to prevent any unwanted reaction that could occur between these undesired compounds and water or with the SDS. The suspension used for re-dispersion was prepared using Lubrizol® 5620 in the ratio 0.2 versus TDI since the best results were obtained with these parameters as discussed before. The DLS size distributions of the dispersion before and after dialysis are given in Figure II. 35.

The size distribution obtained before dialysis (a) is slightly different compared to the one of section II.3.2.1. This is due to the difference in the time between the sample preparation and the analysis because of the instability of the suspension. However, a very clear difference is seen after dialysis: the major peak is a very narrow one that represents more than 95% of the scattered light intensity

for every measurement. The corresponding mean size is 189 ± 9 nm while the main peak is between 500 and 1000 nm before dialysis.

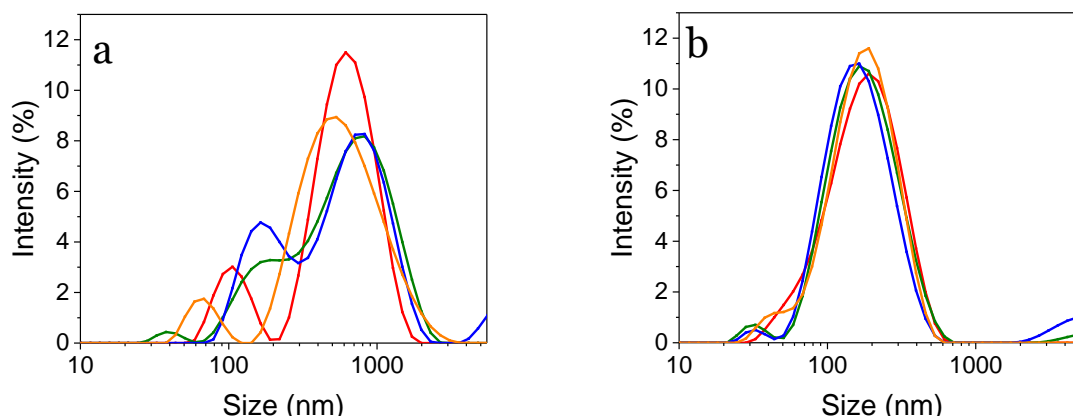


Figure II. 35: DLS size distribution of the reference PUa capsules, (a) before and (b) after purification by dialysis

From these results, we can conclude that the synthesized PUa capsules are highly aggregated, what explains the differences and repeatability issues in the measurements performed before purification. The dialysis in cyclohexane allows to get rid of the unreacted material and to detect what, we assume, are the single capsules, whose mean size is around 190 nm.

ii.. Redispersion in water using SDS

The purified suspension is then dispersed in water using SDS as a surfactant to stabilize the capsules in the aqueous environment. The efficiency of SDS being highly dependent on the capsules' size and nature, different concentrations were tried.

Moreover, a change in pH is the targeted release stimulus, with a supposed degradation of the capsules' shell in presence of a base. Since the pH also has an effect on the surfactants' mode of action, redispersion was carried out in SDS solutions at acidic, neutral or alkaline pH. The pH was adjusted to 3.8 ± 0.20 , 6.9 ± 0.14 , and 11.0 ± 0.13 respectively. Results are shown in Figure II. 36.

Different trends are seen here, what, we assume, is due to the surfactant's action depending on the particles' surface charge. For SDS concentration below 0.2%, the particles are probably not individually stabilized, and a large shifting peak is seen in the size distributions curves for size above 350 nm. However, the critical micellar concentration for SDS is between 7 and 10 mM, what represents a weight concentration of 0.20 to 0.29%. The SDS concentration is then probably not sufficient.

For a SDS concentration around the CMC (0.3%), similar results are obtained whatever the medium's pH, with sizes between 250 and 300 nm and slightly above what had been measured in cyclohexane. This slight increase can be due to adsorbed SDS that increases the hydrodynamic volume of the particles. Close results are observed for higher SDS concentrations in either alkaline

or acidic media. The stability of these suspensions, especially in an alkaline medium is an issue since we expected the capsules to open and release their content in the presence of hydroxide ions. The fact that the efficiency of SDS is the same in acidic and alkaline solutions probably means that our particles' surface is cationic in both conditions and that the pKa of the shell groups is above 11.

Concerning the redispersion carried out in a neutral medium, an increase of the measured size with the SDS concentration is observed with sizes of around 280, 415 and 450 nm for SDS concentration of 0.3, 0.5 and 0.7% respectively. This highlights the influence of the medium's ionic strength on the particles' dispersion. Increasing the SDS concentration, two phenomena compete: the dispersion destabilization, due to changes in the medium's ionic strength, and its stabilization, thanks to the adsorption of surfactant molecules. When a trigger value is obtained (between 0.7 and 0.9% SDS), the stabilization dominates and the measured sizes are in agreement with the initial values.

For 1.0% added SDS, the same particles' size as in cyclohexane is obtained, meaning that we probably succeed in stabilizing the dispersion in water. A lower particles' mean size is observed in neutral medium than in acidic or alkaline medium, but it was not possible to link this to a potential swelling of the capsules' shell.

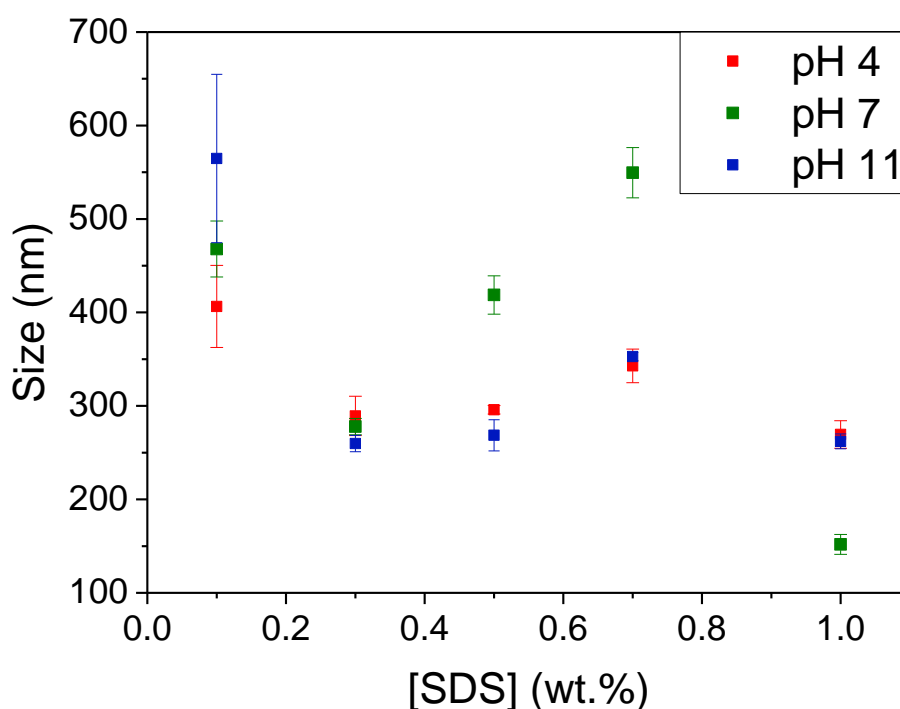


Figure II. 36: Effect of the surfactant concentration and pH of the environment on the capsules' mean size (only the major peak's mean size is considered)

The assumptions we made are compatible with the ESEM observations carried out after redispersion in neutral pH and with 0.5% SDS, presented in Figure II. 37, which show almost spherical agglomerated particles. Despite being hardly accurately measurable, the sizes of the smallest units are between 200 and 400 nm, what corresponds to the lower capsules' size measured

by DLS for 1.0% SDS. The irregular shapes observed are probably caused by the agglomeration of smaller particles.

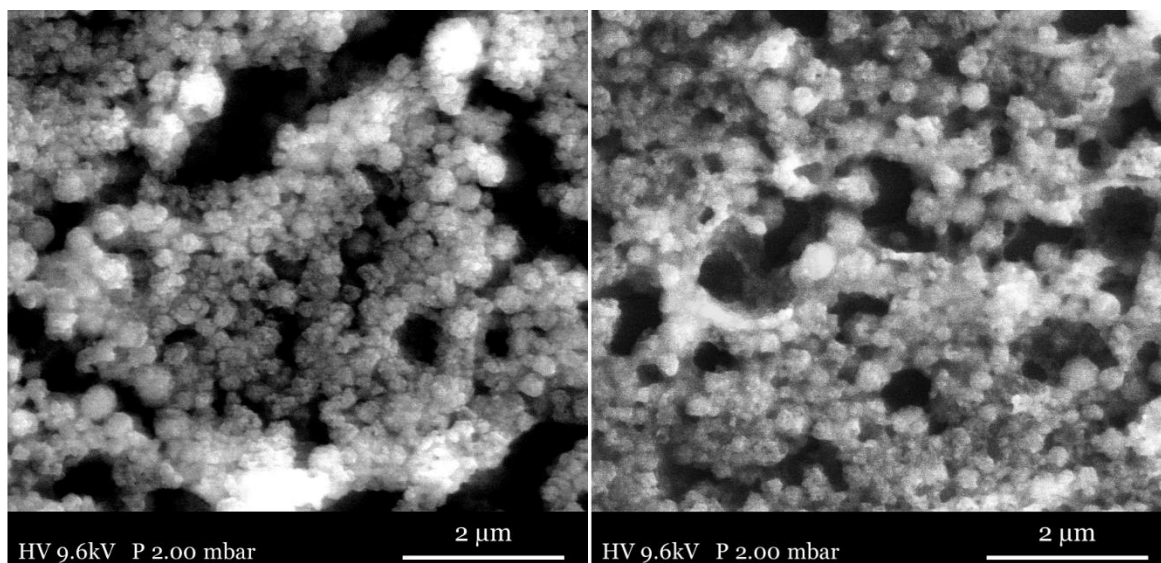


Figure II. 37: ESEM observations of PUa capsules after dialysis and transfer in water using 0.5% SDS

II.3.2.4. Conclusions on the synthesis of PUa containers

The different experiments carried out in this section showed that we succeeded in forming nanoparticles through polymerization of TDI and DAB, involving a W/O emulsion process. In a second step, the particles have successfully been purified and transferred into water, a dispersant that would be compatible with the considered matrices.

However, we noticed repeatability issues, highlighted by variations in the capsules' sizes from an experiment to another. This process, and especially the sonication step, seems to be very sensitive. Moreover, the major drawback of our process is the unevaluated role of the surfactant used that definitely takes part in the shell formation reaction. Determining the exact reactions occurring would require to know the exact structure of the surfactant molecule, what is not the case for commercial Lubrizol® 5620B and Lubrizol® 5625. Given the work it would imply, and since no acceptable results were obtained for known surfactants, this type of container was abandoned. Moreover, the described process involving substances of high concern for their toxicity (TDI and cyclohexane are classified as CMR, DAB is a toxic compound), important changes would have to be made. This type of containers was therefore set aside.

Conclusions on the containers formation and characterization

The aim of this chapter was to understand the formation and properties of the nanocontainers based on a mini-emulsion process. In the framework of NC2M, in order to enable the encapsulation of either water-soluble or water-insoluble compounds, two types of smart nanocontainers have been designed and studied.

First, molecules that are soluble in organic solvents and with a low solubility in pure water are loaded in silica nanocontainers. We showed that, through an oil-in-water mini-emulsion, spherical nanocontainers with an average mean size around 180 to 200 nm are obtained. These particles are formed of a central cavity and a silica wall that is around 10 nm-thick, based on TEM observations. It has then been proved that in alkaline media, when the pH exceed 8, the silica suspension is destabilized, what leads to the release of the capsules' payload. This has been done for the release of 2-mercaptobenzothiazole, highlighted at pH 10.2. In these conditions, around 95% of the total MBT is released within 2 hours. This is explained by a dissolution of the amorphous silica shell in alkaline media. This can therefore likely be used for corrosion-triggered responses.

A second process, based on a water-in-oil emulsion this time, has then been designed in order to encapsulate water-soluble compounds (such as colored agents and ionic chemicals). Polyurea architectures are formed from the polyaddition reaction of toluene 2,4-diisocyanate with 1,4-diaminobutane, in presence of a surfactant participating in the polymerization reaction. This leads to the formation of a polyurea shell that can be hydrolyzed in alkaline conditions. However, due to the unavailability of the originally used surfactant, alternative compounds have been tried but were not able to form reactive controlled capsules in the desired size range ($< 1 \mu\text{m}$). Since the used chemicals present some toxicity issues, it has then been decided not to further investigate this type of containers.

Due to these results, silica nanocontainers have been used and integrated in the NC2M coating in the next steps of our study. 2-mercaptobenzothiazole being encapsulated with a high yield (~85% encapsulation efficiency) and released in the wished conditions, we focused on the inhibition function of the NC2M coating. Assuming that a sensing molecule with the same solubility parameters than MBT could be encapsulated and released following the same mechanism and rate, the obtained results could possibly be adapted for corrosion detection.

References

- Zhang, J. & Frankel, G. S. Corrosion-Sensing Behavior of an Acrylic-Based Coating System. *Corrosion* **55**, 957–967 (1999).
- Maia, F. *et al.* Corrosion protection of AA2024 by sol–gel coatings modified with MBT-loaded polyurea microcapsules. *Chemical Engineering Journal* **283**, 1108–1117 (2016).
- Nguyen Thuy, D., To Thi Xuan, H., Nicolay, A., Paint, Y. & Olivier, M.-G. Corrosion protection of carbon steel by solvent free epoxy coating containing hydrotalcites intercalated with different organic corrosion inhibitors. *Progress in Organic Coatings* **101**, 331–341 (2016).
- Ford, N. C. Light Scattering Apparatus. in *Dynamic Light Scattering* (ed. Pecora, R.) (Springer US, 1985). doi:10.1007/978-1-4613-2389-1
- Lim, J., Yeap, S., Che, H. & Low, S. Characterization of magnetic nanoparticle by dynamic light scattering. *Nanoscale Research Letters* **8**, 381 (2013).
- CRC handbook of chemistry and physics: a ready-reference book of chemical and physical data.* (CRC Press, 1994).
- Bhattacharjee, S. DLS and zeta potential – What they are and what they are not? *Journal of Controlled Release* **235**, 337–351 (2016).
- Antonio Alves Júnior, J. & Baptista Baldo, J. The Behavior of Zeta Potential of Silica Suspensions. *New Journal of Glass and Ceramics* **04**, 29–37 (2014).
- Hunter, R. J. The Calculation of Zeta Potential. in *Zeta Potential in Colloid Science* 59–124 (Elsevier, 1981). doi:10.1016/B978-0-12-361961-7.50007-9
- Chassagne, C. & Ibanez, M. Electrophoretic mobility of latex nanospheres in electrolytes: Experimental challenges. *Pure and Applied Chemistry* **85**, 41–51 (2012).
- Fickert, J., Rupper, P., Graf, R., Landfester, K. & Crespy, D. Design and characterization of functionalized silica nanocontainers for self-healing materials. *Journal of Materials Chemistry* **22**, 2286–2291 (2012).
- Cihlář, J. Hydrolysis and polycondensation of ethyl silicates. 1. Effect of pH and catalyst on the hydrolysis and polycondensation of tetraethoxysilane (TEOS). *Colloids and Surfaces A: Physicochemical and Engineering Aspects* **70**, 239–251 (1993).
- Zhou, H. H., Xue, W., Li, F. & Qin, Y. F. Study on the Sol-Gel Process of TEOS by React-IR. *Applied Mechanics and Materials* **110–116**, 1401–1405 (2011).
- Sadtler, V. M., Imbert, P. & Dellacherie, E. Ostwald Ripening of Oil-in-Water Emulsions Stabilized by Phenoxy-Substituted Dextrans. *Journal of Colloid and Interface Science* **254**, 355–361 (2002).
- Maia, F. *et al.* Silica nanocontainers for active corrosion protection. *Nanoscale* **4**, 1287 (2012).
- Al-Oweini, R. & El-Rassy, H. Synthesis and characterization by FTIR spectroscopy of silica aerogels prepared using several Si(OR)₄ and R''Si(OR')₃ precursors. *Journal of Molecular Structure* **919**, 140–145 (2009).
- Bootz, A., Vogel, V., Schubert, D. & Kreuter, J. Comparison of scanning electron microscopy, dynamic light scattering and analytical ultracentrifugation for the sizing of poly(butyl cyanoacrylate) nanoparticles. *European Journal of Pharmaceutics and Biopharmaceutics* **57**, 369–375 (2004).
- Eaton, P. *et al.* A direct comparison of experimental methods to measure dimensions of synthetic nanoparticles. *Ultramicroscopy* **182**, 179–190 (2017).
- Greenberg, S. A. The Depolymerization of Silica in Sodium Hydroxide Solutions. *The Journal of Physical Chemistry* **61**, 960–965 (1957).
- Dove, P. M., Han, N., Wallace, A. F. & De Yoreo, J. J. Kinetics of amorphous silica dissolution and the paradox of the silica polymorphs. *Proceedings of the National Academy of Sciences* **105**, 9903–9908 (2008).
- Sulpizi, M., Gageot, M.-P. & Sprik, M. The Silica–Water Interface: How the Silanols Determine the Surface Acidity and Modulate the Water Properties. *Journal of Chemical Theory and Computation* **8**, 1037–1047 (2012).
- Puddu, V. & Perry, C. C. Interactions at the Silica–Peptide Interface: The Influence of Particle Size and Surface Functionality. *Langmuir* **30**, 227–233 (2014).

Chapter II - Containers formation and characterization

23. Khan, A. M. *et al.* Surface modification of colloidal silica particles using cationic surfactant and the resulting adsorption of dyes. *Journal of Molecular Liquids* **274**, 673–680 (2019).
24. Tseng, W. J., Tsai, P. & Lin, T.-E. Electrophoretic movement of hollow silica particles under DC electric fields. *Journal of the Ceramic Society of Japan* **118**, 309–313 (2010).
25. Blaiszik, B. J., Sottos, N. R. & White, S. R. Nanocapsules for self-healing materials. *Composites Science and Technology* **68**, 978–986 (2008).
26. Hashtjin, A. M. & Abbasi, S. Optimization of ultrasonic emulsification conditions for the production of orange peel essential oil nanoemulsions. *Journal of Food Science and Technology* **52**, 2679–2689 (2015).
27. Mahdi Jafari, S., He, Y. & Bhandari, B. Nano-Emulsion Production by Sonication and Microfluidization—A Comparison. *International Journal of Food Properties* **9**, 475–485 (2006).
28. Kaltsa, O., Gatsi, I., Yanniotis, S. & Mandala, I. Influence of Ultrasonication Parameters on Physical Characteristics of Olive Oil Model Emulsions Containing Xanthan. *Food and Bioprocess Technology* **7**, 2038–2049 (2014).
29. Ramisetty, K. A. & R Shyamsunder. Effect of Ultrasonication on Stability of Oil in Water Emulsions. (2014). doi:10.13140/RG.2.1.1654.4160
30. Bahri, M. A. *et al.* Investigation of SDS, DTAB and CTAB micelle microviscosities by electron spin resonance. *Colloids and Surfaces A: Physicochemical and Engineering Aspects* **290**, 206–212 (2006).
31. Lee, Y.-G., Oh, C., Yoo, S.-K., Koo, S.-M. & Oh, S.-G. New approach for the control of size and surface characteristics of mesoporous silica particles by using mixed surfactants in W/O emulsion. *Microporous and Mesoporous Materials* **86**, 134–144 (2005).
32. Pannone, M. C. & Macosko, C. W. Kinetics of isocyanate amine reactions. *Journal of Applied Polymer Science* **34**, 2409–2432 (1987).
33. Torini, L., Argillier, J. F. & Zydowicz, N. Interfacial Polycondensation Encapsulation in Miniemulsion. *Macromolecules* **38**, 3225–3236 (2005).
34. Ni, H., Nash, H. A., Worden, J. G. & Soucek, M. D. Effect of catalysts on the reaction of an aliphatic isocyanate and water. *Journal of Polymer Science Part A: Polymer Chemistry* **40**, 1677–1688 (2002).
35. Tawa, T. & Ito, S. Preparation and reactions of hydrophilic isocyanate micelles dispersed in water. *Colloid and Polymer Science* **283**, 731–737 (2005).
36. Rosenbauer, E.-M., Landfester, K. & Musyanovych, A. Surface-Active Monomer as a Stabilizer for Polyurea Nanocapsules Synthesized via Interfacial Polyaddition in Inverse Miniemulsion. *Langmuir* **25**, 12084–12091 (2009).
37. Crespy, D., Stark, M., Hoffmann-Richter, C., Ziener, U. & Landfester, K. Polymeric Nanoreactors for Hydrophilic Reagents Synthesized by Interfacial Polycondensation on Miniemulsion Droplets. *Macromolecules* **40**, 3122–3135 (2007).
38. Li, J., Mazumder, M. A. J., Stöver, H. D. H., Hitchcock, A. P. & Shirley, I. M. Polyurea microcapsules: Surface modification and capsule size control. *Journal of Polymer Science Part A: Polymer Chemistry* **49**, 3038–3047 (2011).
39. Kakaroglou, A., Domini, M. & De Graeve, I. Encapsulation and incorporation of sodium molybdate in polyurethane coatings and study of its corrosion inhibition on mild steel. *Surface and Coatings Technology* **303**, 330–341 (2016).
40. van der Merwe, M. M., Landman, M., van Rooyen, P. H., Jordaan, J. H. L. & Otto, D. P. Structural Assignment of Commercial Polyisobutylene Succinic Anhydride-based Surfactants. *Journal of Surfactants and Detergents* **20**, 193–205 (2017).
41. Coleman, L., Bork, J. & Dunn, H. Notes. Reaction of Primary Aliphatic Amines with Maleic Anhydride. *The Journal of Organic Chemistry* **24**, 135–136 (1959).
42. Pirouz, S., Wang, Y., Chong, J. M. & Duhamel, J. Characterization of the Chemical Composition of Polyisobutylene-Based Oil-Soluble Dispersants by Fluorescence. *The Journal of Physical Chemistry B* **118**, 3899–3911 (2014).

CHAPTER III

—

Obtaining homogeneous coatings loaded with silica nanocontainers

Chapter III - Table of contents

Introduction	134
III.1. Materials and methods	135
III.1.1. Materials	135
III.1.1.1. Resins.....	135
III.1.1.2. Substrates.....	136
III.1.2. Capsules incorporation.....	138
III.1.2.1. Approach.....	138
III.1.2.2. Formulation preparation.....	138
III.1.3. Coating application	139
III.1.3.1. Bar coating onto steel panels.....	139
III.1.3.2. Spraying onto AA panels	139
III.1.4. Coating characterization	140
III.1.4.1. Fourier-transform infrared (FTIR) spectroscopy	140
III.1.4.2. Microscopic observations.....	140
III.1.4.3. Thickness measurement.....	141
III.1.4.4. Micro-X-ray fluorescence (μ -XRF).....	141
III.1.4.5. ToF-SIMS	141
III.2. Film formation and optimization.....	142
III.2.1. Epoxy coating.....	142
III.2.1.1. Addition of water to the epoxy formulation	142
III.2.1.2. Addition of silica nanocontainers	149
III.2.1.3. Conclusion on the use of epoxy.....	152
III.2.2. Polyurethane coating	152
III.2.2.1. Low carbon steel: bar-coating.....	152
III.2.2.2. AA2024-T3 Aluminum alloy: Spray.....	155
III.3. Polyurethane coatings analysis	158
III.3.1. Amount of added capsules and inhibitor	158

Chapter III - Obtaining homogeneous coatings loaded with silica nanocontainers

III.3.2. Evaluation of the silica-loaded coatings	159
III.3.2.1. FTIR.....	159
III.3.2.2. μ -XRF	160
III.3.2.3. SEM observations.....	164
III.3.2.4. Time-of-Flight Secondary Ion Mass Spectrometry (ToF-SIMS).....	165
Conclusions and outlook	167
References	169

Introduction

Since the formation of capsules, usable for corrosion purposes, was successful, the next step of this work consists in their incorporation inside a polymeric coating. As seen in section I.4.4., various processes can be considered for the containers dispersion and several parameters such as the polymer's nature, mixing technology and application technique have to be taken into account. This work focuses on nanocontainers incorporation techniques and coating application technologies that could be scaled up. Moreover, an innovative and important point is that the nanocapsules are added as a suspension to the resin.

Since their characterization requires reproducible homogeneous coatings, this section firstly deals with the optimization of the application process in order to obtain visually acceptable coatings. Epoxy and polyurethane waterborne resins were used since both are used as primers in the aerospace industry.

After obtaining homogeneous and defect-free coatings, the dispersion of the silica containers was assessed. The main objectives of this chapter are then to identify the steps that are involved in the preparation process of capsules-loaded coatings, and to determine how to optimize them in order to get a viable system. The dispersion of the containers was performed using high-shear dispersion and sonication, while either bar coating or spraying were used for the formulation. The evaluation of the containers dispersion was carried out by micro-X-ray fluorescence (μ -XRF) using the signal of silicon as representative of the nanocontainers, and complemented by SEM observations and ToF-SIMS analysis.

III.1. Materials and methods

III.1.1. Materials

III.1.1.1. Resins

As explained in the project presentation, the NC2M system possesses two functionalities. Although this manuscript is mainly dedicated to corrosion protection purposes, the choice of the resins has been made in order to allow and to assess the efficiency of the capsules incorporation for both protection and detection. Therefore, the specifications taken into account are:

- Use of a transparent polymer in order to enable the detection of defects such as capsules aggregation or underlying corrosion products development. In further steps, the transparency also facilitates the detection of a coating degradation;
- Possible addition of water into the polymer formulation in order to use the nanocontainers as a suspension rather than as dried powders, avoiding the drying steps that could modify the properties of the nanocontainers;
- Application of the organic coating could be made either by bar coating or spraying depending on the size and geometry of the samples;
- Use of a formulation adapted to structural steel and aluminum alloys.

In order to reach these requirements, a simplified commercial paint to which fillers and pigments were removed was selected. The formulation of the best appropriate matrix is not part of the presented work, and therefore no attention has been paid to the intrinsic anticorrosion properties of the coating. These coatings are then used as tools to assess the containers dispersion and allow to notice even slight changes in the coating's properties but not as a final viable solution.

i. Epoxy resin

The formulation used is a two-component epoxy-amine paint. The epoxide base is mainly made of a bisphenol A derivative epoxide and 10 to 20% of butan-2-ol as a solvent. The hardener's major constituents are at least 50% of a polyamide dispersion and 10 to 20% of nitroethane, probably used to obtain a water-reducible polyamide¹.

According to the information provided by the supplier, the base/hardener stoichiometric ratio (w/w) used is 100/19. The formulation can be diluted with water in order to either adjust its viscosity or add the desired water-dispersed pigments, however no specific water quantity is specified. Curing of the epoxy coating is carried out at 60°C for 4h after a 15 min solvent evaporation step at room temperature.

ii. Polyurethane

The polyurethane varnish used in this study is also a bi-component system. The first component is an acrylic polyol dispersion while the hardener contains at least 50% of poly(hexamethylene diisocyanate) and 25 to 50% of 1-ethoxy-2-propyl acetate as a solvent. Importantly, the base component can contain up to 10% silicon dioxide, what has to be taken into account when assessing the quantity of incorporated silica.

According to the supplier's advice, the formulation requires the addition of water. The base/hardener/water ratio (w/w/w) used is 100/50/40. More water could supposedly be added. Curing of the applied polyurethane formulation is carried out at 60°C for 12h after a 4h solvent evaporation step at room temperature.

III.1.1.2. Substrates

In the Nc2M project, the capsules-loaded coating should be usable with carbon steel and aluminum alloy (AA), and should be applicable either by spray or brush. The nature of the alloys used is detailed in this section. In order to reduce the number of parameters at first, it was chosen to apply the coating onto the steel samples using a bar coater and onto the aluminum alloy using a spray. This is representative of the application methods that exist at ArianeGroup for both substrates. This naturally implies that the nature and size of steel and AA samples are different, according to the application method. Therefore, the comparison of results obtained with steel and aluminum alloys samples is not possible.

i. Structural steel

S355 structural steel is frequently used by ArianeGroup. However, in order to get a reproducible surface preparation, SAE 1008/1010 steel Qpanels (reference R36, Labomat Essor, France) were used since they possess a composition that is close to that of S355, as shown in Table III. 1, but with a controlled surface roughness. The panels dimensions (LxWxT) are 152 x 76 x 0.81 mm. The electrochemical behaviors of S355 and SAE1008/1010 substrates are given in the appendices section for comparison (Appendix 4).

Table III. 1: Composition of S355 and the used steel Qpanels in wt.%

Grade	C	Mn	P	S	Si
S355	0.23	1.60	0.05	0.05	0.05
SAE 1010/1008	0.15	0.6	0.03	0.035	-

Steel Qpanels are rinsed with ethanol, then with ultrapure water (18.2 MΩ), and dried with air 1h to 2h before application of the formulation. Figure III. 1 shows the surface's aspect of a R36 steel Qpanel. Uneven areas are observed, with hills that are a few microns to a few hundreds of microns

wide. The mean roughness, specified by the supplier, is ranging from 0.64 to 1.65 μm . The mean values, measured with a SJ-201M surface roughness tester (Mitutoyo), for roughness parameters are given in Table III. 2.

Table III. 2: Roughness parameters of degreased uncovered steel Qpanels, in μm

Ra	Rq	Rt
0.93 ± 0.06	1.15 ± 1.15	5.99 ± 0.39

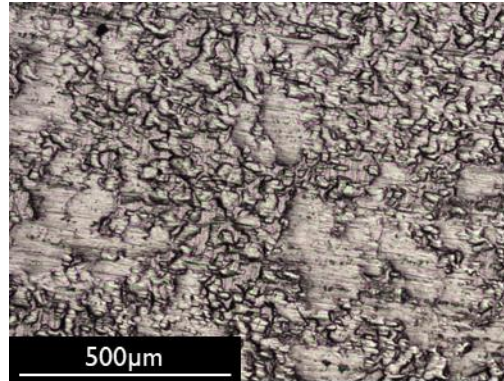


Figure III. 1: Optical microscopic observation of the uncoated steel Qpanels' surface

ii. AA2024-T3 Aluminum alloy

20 mm-diameter AA2024-T3 rods (Services Centres Aero, France) are used for spray applications. The composition of the alloy is presented in Table III. 3., determined on a rod's cross-section by μ -XRF. Due to overlapping between the silicon and aluminum peaks, the content in silicon is apparently underestimated.

Table III. 3: Composition of the used AA2024-T3 determined by μ -XRF

	Al	Cu	Mn	Fe	Zn	Ti	Si	Mg	Cr	P
AA2024-T3	92.83	4.63	0.80	0.16	0.14	-	0.01	1.37	0.05	0.02

The substrates are prepared as follows: first the AA rods are sawed, then a screw is placed on a roughly grinded face and pasted using silver conductive paint. The whole sample is then embedded in a cold mounting epoxy resin (Struers). Before application of the coating, the surface is prepared by grinding (SiC #4000 grinding paper), followed by 5 min of sonication in ethanol (ultrasonic bath), and finally rinsing with ultrapure water and drying by air spray. A blueprint of the samples prepared as described is shown in Figure III. 2.

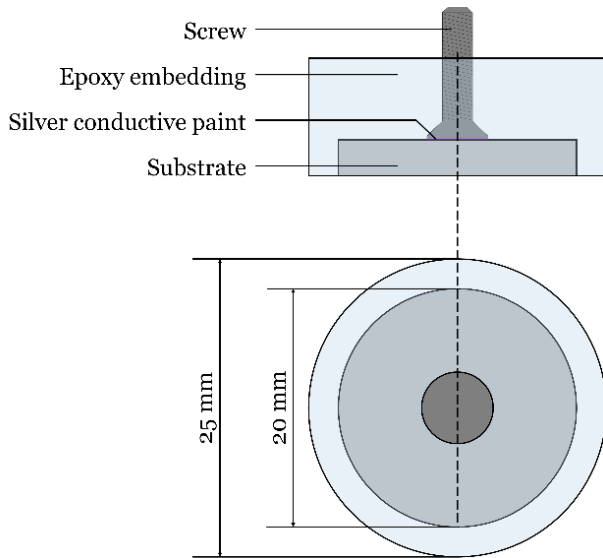


Figure III. 2: AA2024-T3 samples used for coating application

III.1.2. Capsules incorporation

III.1.2.1. Approach

The efficiency of coatings loaded with containers naturally depends on the quantity of active agents that is present. This content can be increased playing with the containers' nature (size, encapsulation efficiency, release efficiency) as seen in chapter II, or with the quantity of loaded capsules. However, although the employed formulations are dilutable with water, this can only be done up to a certain threshold. This limits the added quantity of silica nanocontainers that could not reach values seen in the literature for the addition of capsules as a powder (often above 10 wt.%),^{2,3}. We assume that getting over this limit could be done by concentrating the suspension, what has not been done in the presented results. Therefore, the aim of this section is to obtain homogeneous coatings, adding the maximal quantity of water (or Si NCs suspension) in the formulation. From this will be determined the capsules weight content.

As seen in the literature (see chapter I), obtaining a good dispersion by mixing sometimes involves long-duration magnetic stirring. We, however, could not afford this, since the addition of the silica suspension to either one or the other or both components provokes a fast evolution of the formulation. This is why a high-performance dispersing device was used. The incorporation then deals with the process, meaning the components addition order, mixing technology and parameters

III.1.2.2. Formulation preparation

For mechanical stirring, an IKA ultra turrax T18 dispersing device is employed with a S18 D-10G-KS dispersing tool. This tool is made of a stator ($\text{Ø}_{\text{int}} = 7.2 \text{ mm}$ and $\text{Ø}_{\text{ext}} = 10 \text{ mm}$) and a rotor ($\text{Ø}_{\text{int}} = 4.75 \text{ mm}$ and $\text{Ø}_{\text{ext}} = 6.75 \text{ mm}$) whose speed can be set from 0 to 24 krpm (equivalent to a

8.5 m.s⁻¹ circumferential speed). This produces high shear and thrust forces as well as turbulences, likely to be able to break potential aggregates.

Since bubbles were observed, degassing has been tried, either applying vacuum or sonication to complement the mechanical dispersion. Vacuum equipment is either a vacuum desiccator connected to a diaphragm pump (ILMVAC FB65455) or a resin-mounting machine (Presi). When used, sonication was applied using the same 700 W sonication system as for the capsules formation, equipped with a ½” tip. The set amplitude is 20%, lower than for the NCs preparation. This way, deterioration of the silica containers does not occur. Since sonication generates heat in the sample, the vessel is placed in an ice bath in order not to shorten the formulation’s pot life.

In order to optimize our process, we compared formulations containing either pure water as a reference, or a silica nanocontainers dispersion. No difference in the coatings’ homogeneity was observed whatever MBT-loaded silica capsules (Si(MBT) or empty capsules (Si) were added. Tests were then conducted with Si NCs.

III.1.3. Coating application

Bar coating and spraying were considered in this work. As previously mentioned, different substrate’s sizes were used for the two techniques.

III.1.3.1. Bar coating onto steel panels

A four sided film applicator (Elcometer 3540) was used. The enabled wet thicknesses are 30, 60, 90 and 120 µm. For some tests, in order to get a higher wet thickness, one or two layers of a 40 µm-thick adhesive tape are applied on the substrate’s edges. The tape thickness is controlled to be constant (± 1 µm) using an Elcometer 415 thickness gauge (10 measurements performed along the substrate’s length). After application of the formulation, the coatings are left under a fume cupboard during the solvent evaporation time before being cured in a heating oven. For each condition, a minimum of 3 similar samples is coated. In order to compare the different coatings, we used their dried thickness and solid volume. Assuming that the wet formulation has been homogeneously applied and that the applicator is well calibrated, the solid volume is calculated as:

$$\%VS = 100 \times \frac{\text{Dry thickness}}{\text{Wet thickness}}$$

III.1.3.2. Spraying onto AA panels

An airbrush (A4709, Aztek) equipped with a gravity feed was used to spray the formulation. The adjustable flow (dial) is set to the maximum and the trigger fully pushed so the sprayed quantity is only controlled by the spray duration, pressure and nozzle opening. The pressure is adjusted to 1.0 bar using water, and 0.70 mm and 1.02 mm nozzles are used.

In order to get reproducible results, the AA2024-T3 samples described before are placed in a mold filled with modelling clay. A piston is then applied in order to ensure the substrate's surface planeness despite non-parallel faces as shown in Figure III. 3. The spraying step is then carried out handling manually the airbrush at a distance of around 10 cm with an angle of 45°. This distance was chosen in order to have an apparent homogeneous coverage with the formulation while keeping a sufficiently wide spot size. Coated samples are then covered and left under a fume cupboard during the solvent evaporation before being placed in a heating oven for the curing step.

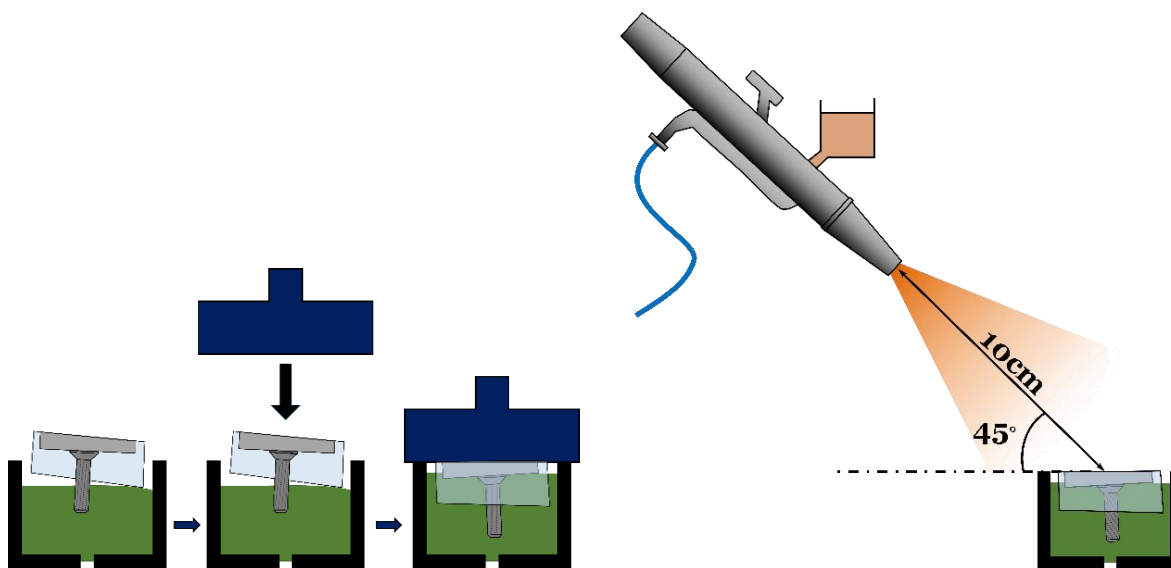


Figure III. 3: (left) AA2024-T3 samples preparation and (right) spraying set-up

III.1.4. Coating characterization

III.1.4.1. Fourier-transform infrared (FTIR) spectroscopy

Infrared spectra are recorded by Attenuated Total Reflectance (ATR), using a Nicolet iS50 FTIR Spectrometer (Thermo Fisher Scientific). Settings are as follows: 64 scans, resolution of 4 cm^{-1} and spectra recorded from 4000 to 400 cm^{-1} . Analyses are performed covering the apparatus' diamond with a piece of coating.

III.1.4.2. Microscopic observations

Pictures have been taken either with a stereo microscope M165C equipped with a DFC 290 numeric camera (Leica®) for low magnification observations, or with a digital microscope DM 6000M equipped with a DMC 2900 camera (Leica®) for higher magnifications. Both are controlled with the software Leica Application Suite.

III.1.4.3. Thickness measurement

The dry films thickness is measured with an Elcometer 415 thickness gauge. For embedded rods, 15 measurements are randomly performed on the whole covered surface. For bar-coated samples, the resin-covered area is divided in 3 equal areas along the substrate length. 30 measurements are performed in each of these 3 zones.

III.1.4.4. Micro-X-ray fluorescence (μ -XRF)

Elemental analyses have been performed by micro-X-ray fluorescence using a M4 Tornado (Bruker). Operating conditions were as follows: Rh excitation tube voltage: 30 kV; current: 160 μ A. For local analyses, one-point measurements have been carried out with a 25 μ m spot size. For area composition measurements, the mean value is calculated over a total area of 3 x 3 mm², analyzed with 30 μ m steps.

III.1.4.5. ToF-SIMS

ToF-SIMS was tried in order to get an idea on the silica dispersion within the layer's volume. Measurements were performed by an external laboratory (PLACAMAT, Bordeaux, France), using a TOFS-SIMS⁵ instrument, manufactured by IONTOF. An argon cluster source is used for sputtering, the energy is fixed at 10 keV.

III.2. Film formation and optimization

The addition of the suspension to a complex formulation could destabilize the suspension, or interfere with the varnish components. This will likely promote the formation of defects due to aggregation or uncontrolled cross-linking. That is why optimization of the formulation process is needed since no additive is used. As observed in the literature, pigments are often first mixed in a component of the formulation for long duration (up to several hours) to formulate such coatings^{4,5}. In our case however, the silica capsules being dispersed in water, they possess a reactive surface. When mixing the suspension with either the base or the hardener of one of the considered resins (magnetic stirring, 1000 rpm), a heterogeneous mixture containing particles is obtained after at most 15 min.

We then tried to increase the mixing efficiency in order to quickly obtain a homogeneous formulation before application. The formulation being opaque, the films are formed and cured before the dry transparent coatings are observed. The epoxy resin was first tried in order to define the mixing process and its parameters for coating made on steel substrates. The same process was next applied to the polyurethane formulation, either bar coated and sprayed. In this section, Qpanel substrates are used for bar-coating applications, and AA2024-T3 embedded rods for spraying.

III.2.1. Epoxy coating

For this development, the first step in our approach is to assess the effect of dilution on the film formation. We then incorporated the suspension instead of pure water and dried different solutions in order to get defect-free homogeneous coatings. All the coatings presented in this section have been obtained by bar coating.

III.2.1.1. Addition of water to the epoxy formulation

i. Wet thickness and shrinkage

Since no recommended quantity of water to add was given by the supplier for the epoxy varnish, we first assessed the effect of the dilution on the epoxy formulation. In order to be able to compare the two formulations, the added quantity has been fixed to 20 wt.% of the total formulation's weight. The mixing ratio is then 100/18/31 (base/hardener/water), and the coating is compared to a pure epoxy formulation containing 18 g of hardener for 100 g of base, since water is not required. Mixing is carried out by magnetic stirring at 1000 rpm for 5 min. Moreover, vacuum treatment was used in order to limit the formation of bubbles and voids by placing the formulation in a desiccator under vacuum for 15 min as a routine procedure. During this vacuum step, foaming is observed in the vessel. After application and curing, the coatings look matt.

The first coatings were made by bar coating on steel Qpanels. The box chart presented in Figure III.4.a shows the measured thickness of the epoxy films after curing for different wet thicknesses ranging from 30 to 120 μm , for the pure epoxy formulation (black boxes) and from 30 to 200 μm for the diluted one (red boxes). Due to a higher viscosity when no water is added to the formulation, important differences are observed in the thicknesses homogeneity. More reproducible coatings are obtained with the diluted formulation. An addition of up to 20% of the total weight still allows the formation of apparently homogeneous coatings; hence, this value will be kept for our study. It has to be reminded that the total height of the Qpanels substrates' profile (Rt) is around 6 μm , what explains the quite important standard deviation we observe.

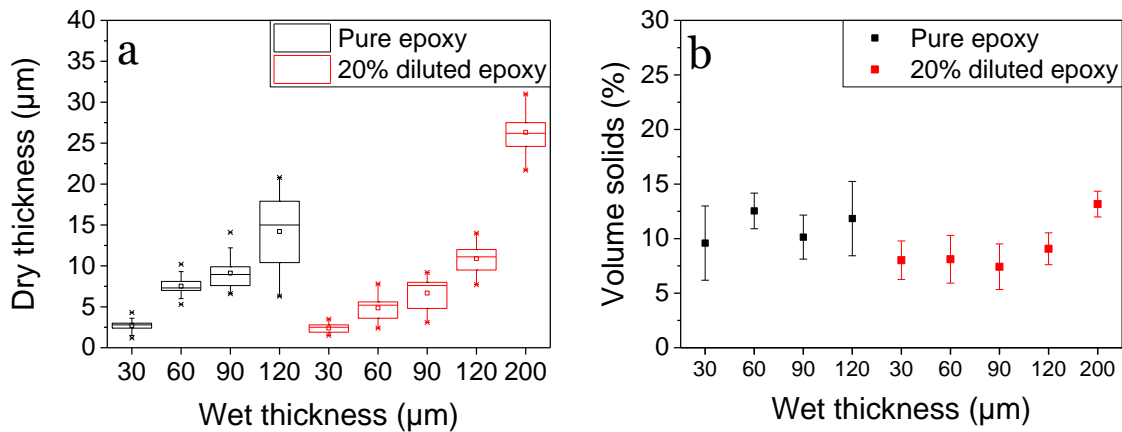


Figure III.4: (a) Dry thicknesses of the pure and 20% diluted epoxy coatings depending on the applied formulation's wet thickness and (b) corresponding relative dry/wet ratio.

Interestingly, as evidenced in Figure III.4.b, only 5 to 15% of the initial wet thickness remains after curing for the pure formulation. This value is naturally lower, between 5 and 10% for the diluted formulation. Moreover, a dry content of $29.8 \pm 4.8\%$ was measured by gravimetric analysis in this case. This corresponds to an important loss since most of the commercial water-based protective primers generally have a volume solid above 30% and up to 60%^{6,7}. The shrinkage observed with the epoxy formulation leads to the formation of thin films that can hardly reach a dry thickness of 15 μm for a 120 μm wet thickness. Moreover, this could induce defects at the epoxy/silica interface when capsules are inserted in the polymer network.

The volume solid for a homogeneous coating layer should be constant. However a slight increase is observed for the 200 μm tries for which a $26.3 \pm 2.4 \mu\text{m}$ thickness is obtained once dry. This likely means that either evaporation is not complete for this too high wet thicknesses, or that the coating contains defects. Figure III. 5 presents the optical observations of the 120 μm and 200 μm coatings that are representative of the whole coating's surface. This confirms the presence of numerous defects, likely due to air bubbles in the formulation. When comparing the pure and diluted formulations applied with a 120 μm wet thickness, we notice that adding water to the resin seems to increase the number of defects while slightly reducing their size. The diameter of the visible craters

Chapter III - Obtaining homogeneous coatings loaded with silica nanocontainers

is between 5 and 20 μm for the diluted formulation whilst it reaches 30 to 35 μm in the pure formulation. This difference is likely due to a decrease in the formulation's viscosity. Increasing the applied wet thickness however hinders the air removal and coatings obtained from 200 μm of formulation show less but bigger defects with diameters ranging from 15 to 60 μm roughly.

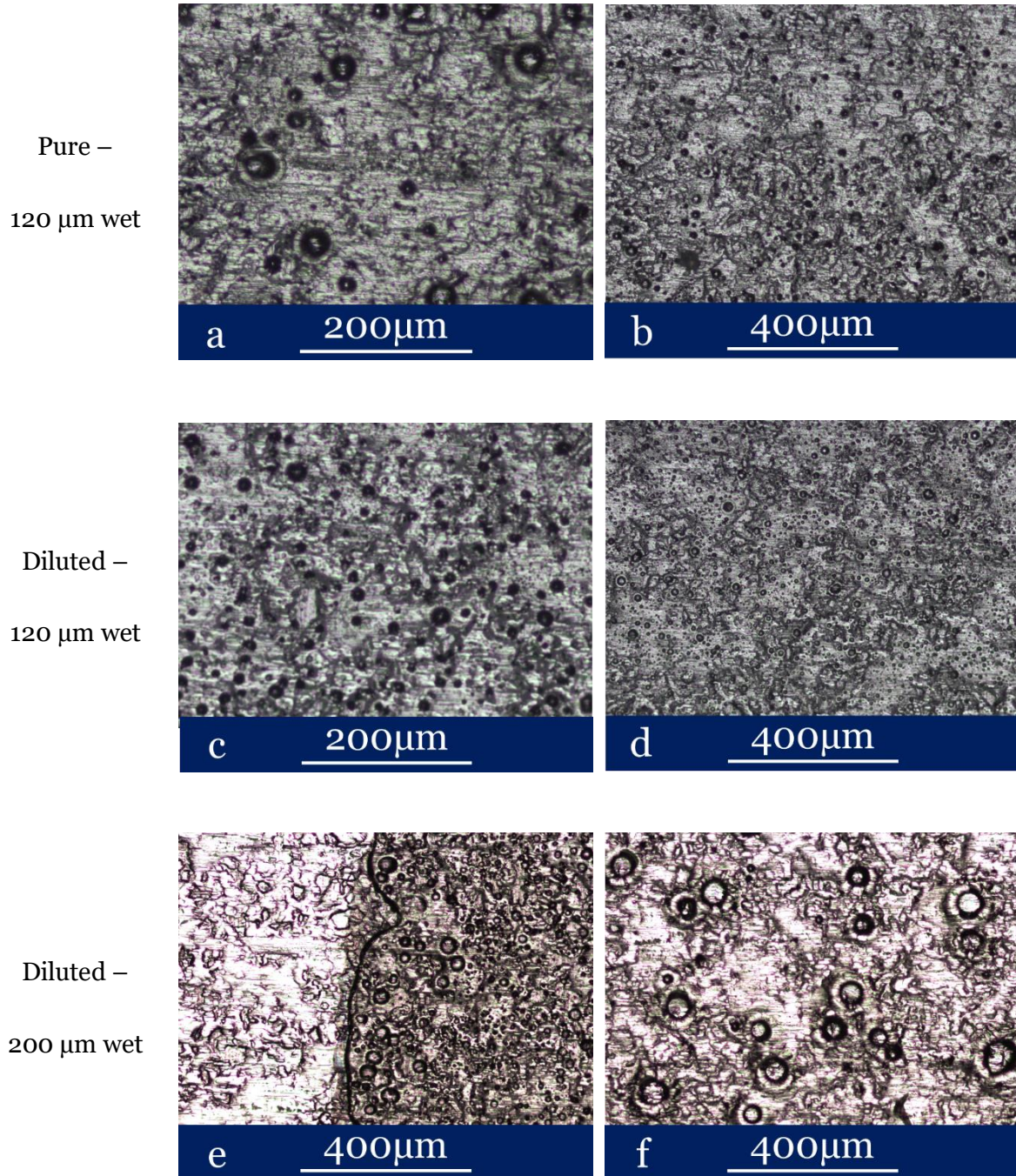


Figure III. 5: Microscopy observations of (a,b) pure and (c,d,e,f) diluted epoxy coatings applied by bar coating on top of steel Qpanels with (a,b,c,d) 120 μm and (e,f) 200 μm wet thickness

For this 200 μm -wet thickness of diluted formulation, it also appears that the substrate is uncovered at the center of some defects that look brighter. However, observations of a sample cross-section presented in Figure III. 6 showed that although the coating layer thickness is not constant, the substrate is always coated.

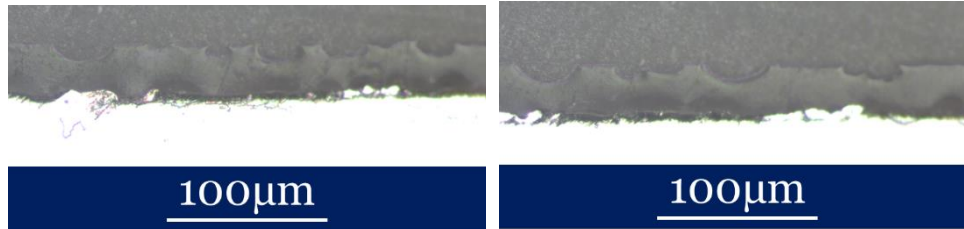


Figure III. 6: Observation of a 200 μm wet epoxy sample cross-section

Since the increase in wet thickness led to bigger defects, a 120 μm wet thickness is used in the next bar-coating experiments.

ii. Evaporation time

Solvent evaporation plays an important role in the formation of organic films and requires appropriate conditions. An insufficient evaporation time could indeed freeze the coating layer entrapping incorporated air. Optimization has been done with the diluted formulation. Figure III. 7 presents pictures representative of the coatings cured after 2 and 12h evaporation duration at room temperature. Even if a slight decrease in the defects' size is apparently observed when increasing the evaporation time, no clear improvement in the coating's final appearance was observed. The final coating still presents defects and therefore this could not constitute a solution.

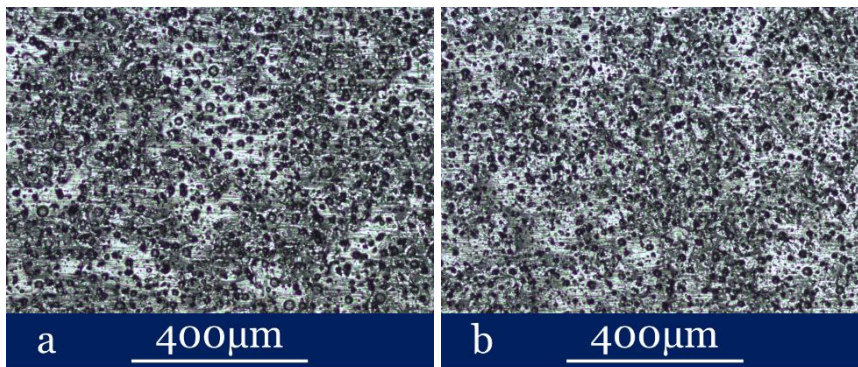


Figure III. 7: Appearance of epoxy coatings formed and cured at 60°C after (a) 2h and (b) 12h solvent evaporation at RT (bar coating, 120 μm wet)

iii. Influence of the mixing technique

Our assumptions are that a more efficient mixing technique could lead to the formation of smaller bubbles that could more easily leave the formulation. We here compared three ways to stir: manually, using a blade stirrer or a high-performance Ultra-Turrax disperser. The mixing time is fixed at 5 min and the stirring speed is visually determined in order to avoid the formation of a

Chapter III - Obtaining homogeneous coatings loaded with silica nanocontainers

vortex. As a reference, the formulation is manually stirred and visually homogeneous during application. Appearance of the coatings is presented in Figure III. 8.

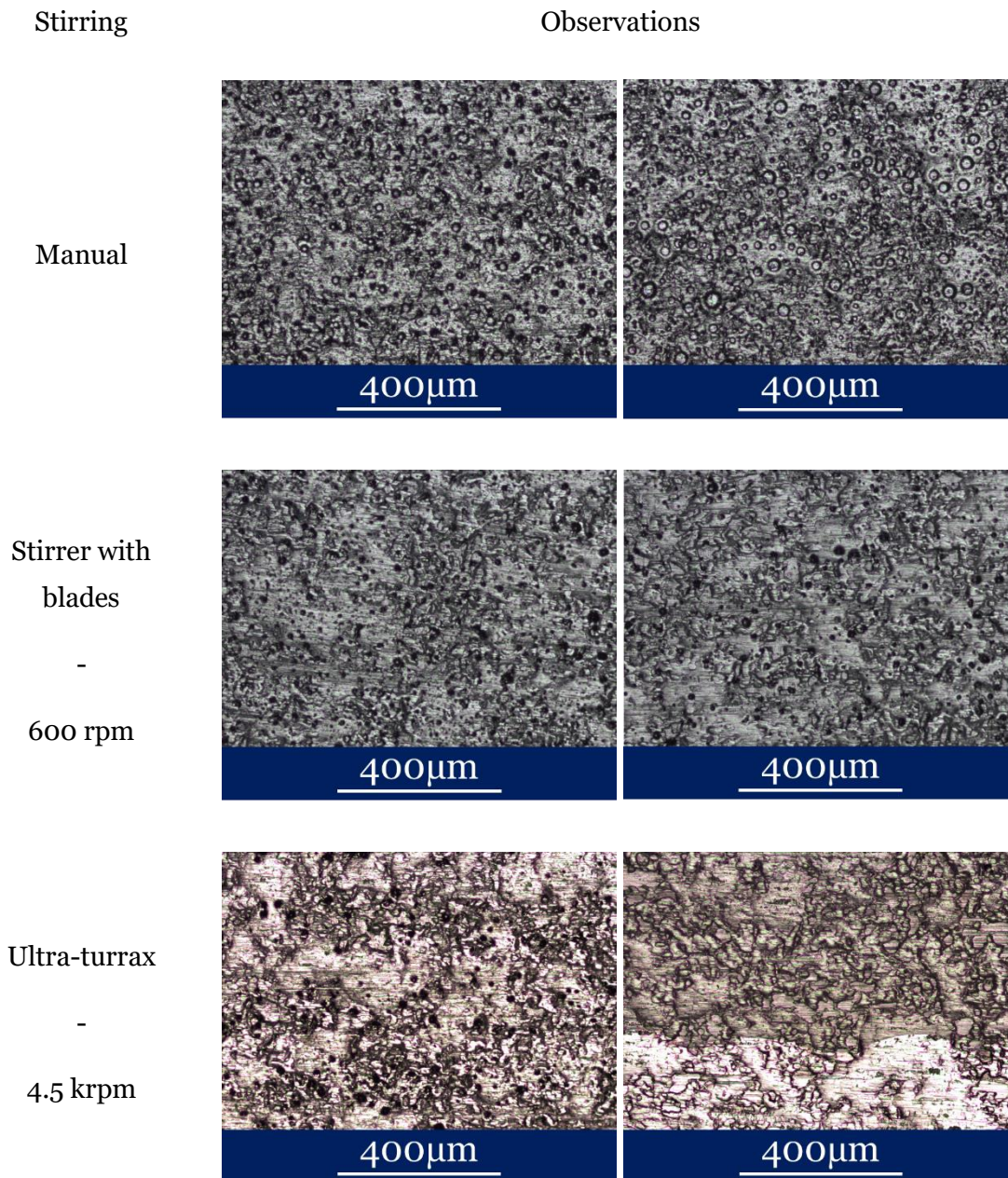


Figure III. 8: Appearance of epoxy coatings for three mixing techniques, applied by bar coating with a 120 µm wet thickness

The first conclusion is that none of the considered techniques allows to form defect-free coatings. In order to compare these three methods and magnetic stirring seen in the first section, the size of defects was evaluated on zones that we assumed to be representative of the whole coatings. Image analysis is carried out with the software imageJ on at least 100 defects, measuring the rings' diameters. Since only a part of the samples is analyzed, the defects quantity is only qualitatively assessed; results are presented in Table III. 4.

We observed that manual stirring leads to the formation of defects with various sizes that cover the whole surface. The use of a more efficient dispersing tool significantly reduces both the diameter and number of formed voids. If the sizes are comparable, the best results concerning the density of defects were obtained using the Ultra-Turrax dispersing tool. Interestingly, a perfectly clear coating is observed on the edges of the coated area (likely to be thinner than at the center of the substrate).

Table III. 4: Size and qualitative assessment of the number of defects present in epoxy coatings depending on the mixing technique, from microscope observations

	Defects' mean size (μm)	Defects' min. size (μm)	Defects' max. size (μm)	Quantity of defects
Magnetic	10 \pm 4	3	28	++
Manual	19 \pm 6	9	42	+++
Blades	13 \pm 5	4	29	++
Ultra-Turrax	15 \pm 4	5	21	+

Ultra-turrax and stirrer with blades are the most controlled techniques and show comparable results, they were then further considered for optimization. Since mixing was not enough to get rid of the air, degassing was used.

iv. Optimization of the degassing step

After around 30 min under vacuum in a desiccator, the solution became too viscous to be handled. Moreover, it does not allow to control the pressure in the vessel. We therefore used a mounting machine that allows to set a controlled 100 mbar pressure. Tests have shown that after 1h in these conditions the formulation became too thick to be correctly applied. We therefore set the maximum time to 45 min and compared formulations stirred with either a high-performance stirring device or a blade stirrer. The appearance of the obtained coatings is presented in Figure III. 9 and shows an important reduction of the number of defects in the coating layer in both cases. While almost no defects were detected for the formulation processed with the ultra-turrax disperser, dots with diameters ranging from 8 to 25 μm are noticeable for the formulation stirred with blades. This vacuum technique however avoids the formation of the smaller voids observed before.

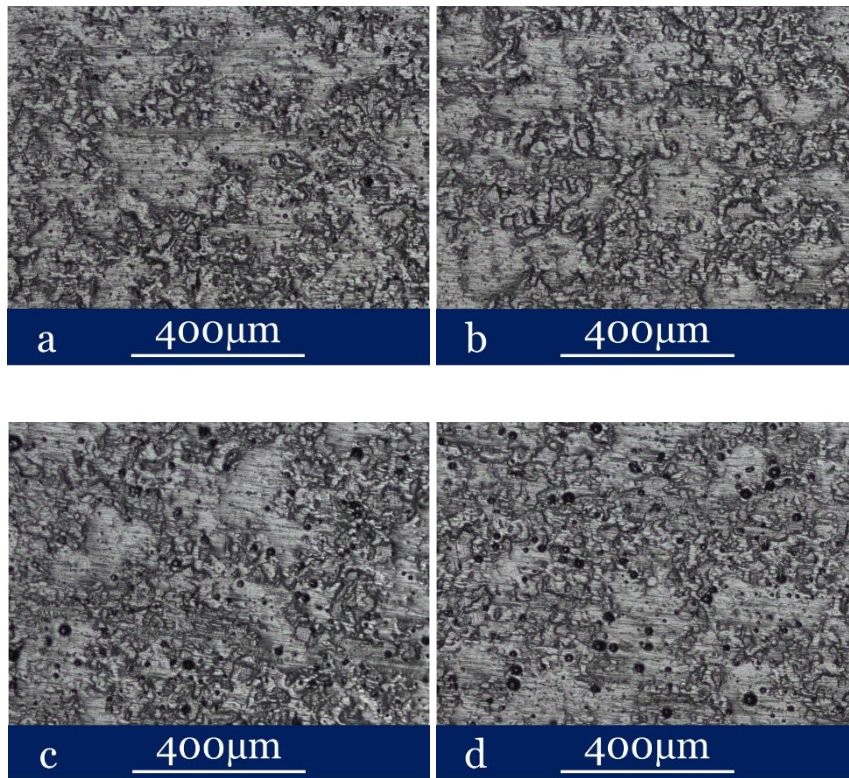


Figure III. 9: Appearance of coatings formed from a formulation stirred with (a & b) an Ultra-turrax or (c & d) a stirrer with blades after a 45 min degassing in a mounting-machine

An alternative solution to degas liquids, already used for industrial applications is sonication. Cavitation generates bubbles in the processed liquid. The dissolved gas diffuses to these bubbles that then migrate to the surface⁸. The main advantages of sonication, compared to the application of vacuum, are that it should require a shorter period of time to be efficient and also enhance the dispersion of the silica NCs. However, sonication induces local heating that could threaten the formulation's pot life or trigger cross-linking. Figure III. 10 shows the appearance of coatings obtained after 60s and 90s-processing (in a pulse regime with 10s sonication and 10s pause), with an amplitude fixed at 20%. As one can see, the cured coatings are free of defects for a short sonication time, while 90s sonication leads to a thicker formulation that does not cure properly. On this second type of coatings, holes are observed with a diameter of $100 \pm 36 \mu\text{m}$.

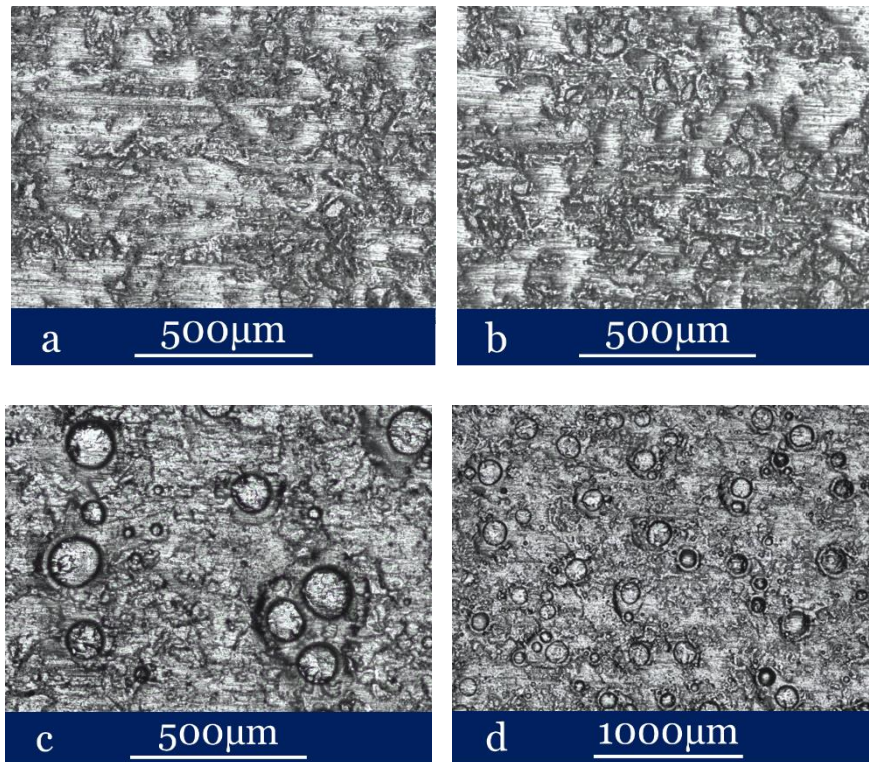


Figure III. 10: Appearance of epoxy coatings made from a formulation degassed using (a & b) 60s and (c & d) 90s of sonication

From these results, the sonication of the formulation enables the formation of coatings free of defects, although the use of ultrasounds proposed is limited to short durations.

III.2.1.2. Addition of silica nanocontainers

i. Replacement of water by the Si NCs suspension

Addition of the nanocontainers was carried out following the previous protocol. The first attempt consisted in mixing the three components of the formulation, replacing water by the silica containers dispersion. The aim is here to see how stirring could disperse the Si NCs in the formulation. Degassing is carried out with a mounting machine in the conditions of the previous section. Right after application, grains are visible in the wet film, attributed to aggregates that are due to the silica capsules. Observations of the coatings after curing are presented in Figure III. 11. Despite homogeneous areas on the layer's edges, aggregates are visible in the epoxy layer, the largest exceeding 200 µm. Pinholes are also evidenced.

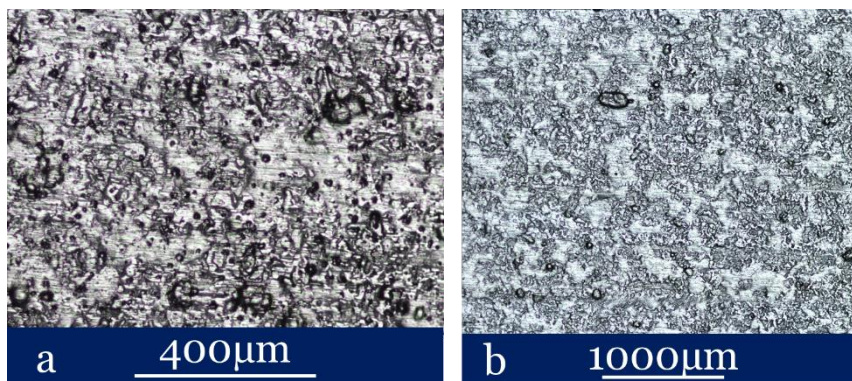


Figure III. 11: Observations of epoxy films loaded with silica NCs after Ultra-Turrax dispersion and vacuum degassing. Grains are visible in the epoxy layer.

These aggregates were not observed with pure water. They are therefore likely due to reactions between the silica containers and either one or the other component of the varnish. Indeed, the amine component could react at room temperature and lead to the dissolution/precipitation of silica⁹. Reactions with epoxy have also been observed but require heating¹⁰. Another possibility is that the silica containers induced the introduction of air, and notably CO₂, in the system as proposed by Eckstein and Dreyfuss¹¹. Carbon dioxide can react with some amines and lead to the observed defects. However, our knowledge about the components' chemistry does not allow to conclude on this. The addition of the silica suspension to either one or the other component prior to the addition of the second one should give an insight on this.

ii. Order of addition

If silica capsules can react preferentially with one or the other component, the order of mixing should have an influence on the aggregation that occurred during the mixing step. Due to the white color of both the resin and the capsules suspension, any heterogeneity of the formulation is hardly detectable to the naked eye before application. For these experiments, the silica suspension (S) is added to either the base (B) or the hardener (H) and stirred using the Ultra-Turrax tool in the same conditions as before (4.5 krpm, 5 min). The third component is then added and the mixing step repeated. Pictures of the two options are presented in Figure III. 12. While no clear difference was noticed when the suspension is added to the hardener first, both the number and size of the clusters decrease when the suspension is added to the base in a first step. This reinforces the idea that interactions occur preferentially between the silica and the polyamide hardener. Some aggregates are however still visible in the coatings that therefore need further improvement.

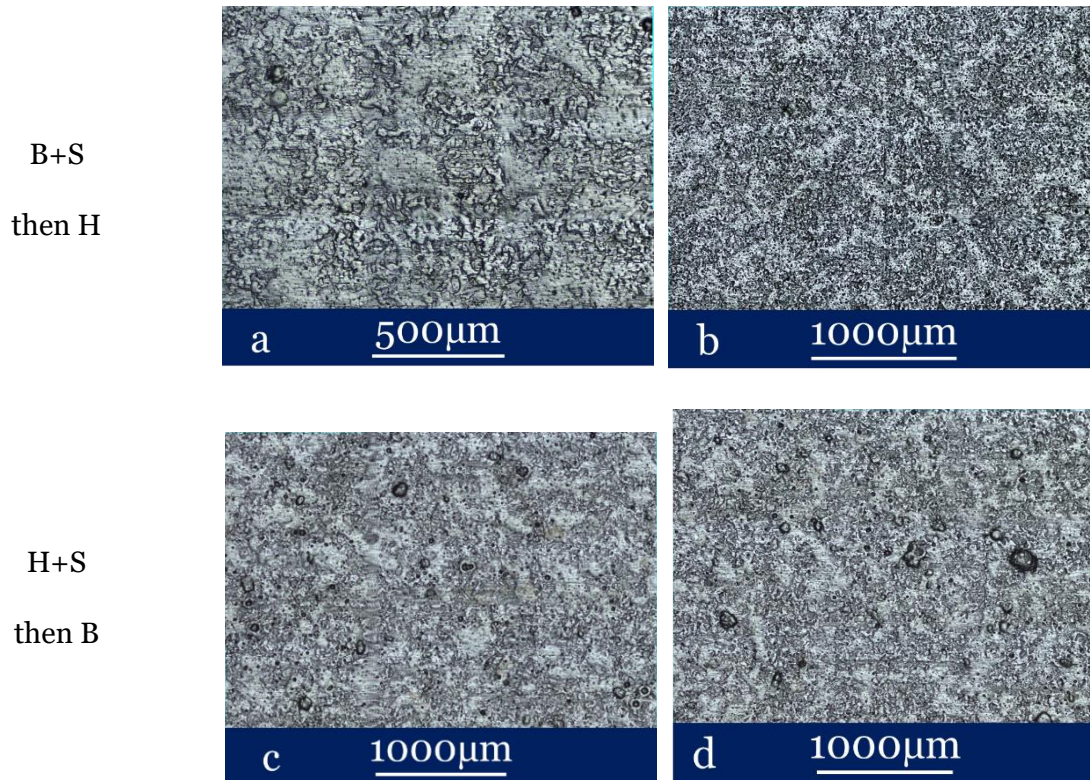


Figure III. 12: Effect of the order of addition of the silica NCs suspension with addition of the suspension (S) first to (a & b) Base (B) and (c & d) Hardener (H)

iii. Use of a sonication probe

When sonication is used in order to complement high-speed dispersion and replace vacuum degassing, the obtained coating are free of clusters as shown in Figure III. 13. Interestingly, although sonication was effective to get rid of bubbles with only water added to the formulation, pinholes are observed in the epoxy coatings when the suspension is present. The main assumptions to explain these defects are that the silica containers can entrap air, or that the residual surfactants molecules stabilize gas bubbles in the formulation. However, as previously, an increase in the sonication time made impossible the application of the formulation by bar coating.

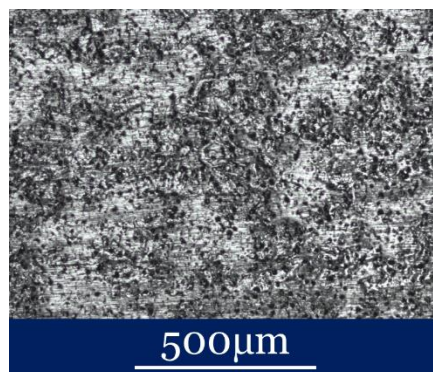


Figure III. 13: Presence of defects in the silica NCs-loaded epoxy coating after US degassing

The incorporation and dispersion of the Si NCs suspension into the epoxy formulation therefore seems to be enhanced by the use of ultrasounds, able to avoid the formation of clusters in the epoxy layer. However, bubbles are visible in the coatings in which the suspension has been added.

III.2.1.3. Conclusion on the use of epoxy

Obtaining a clear epoxy layer was possible using a process involving high performance dispersion and ultrasonic degassing. The waterborne formulation is transparent, and adding 20 wt.% water to the original formulation was successful with only differences in the coatings' dry thickness.

Added water was next replaced by the suspension of Si NCs, applying the same process. High performance mixing was not sufficient to obtain a correct physical aspect and led to the formation of aggregates, likely due to interactions between the nanoreservoirs and the paint's components. Sonication visually enabled a suitable dispersion of the capsules but could not, however, prevent the formation of small defects (pinholes) in the organic layer. Further improvements, required to form suitable coatings, would probably require the purification of the suspension in order to remove the residual surfactants. If the observed defects are however due to the incorporation of air, vacuum treatment or mixing under inert conditions should be considered, but are not realistic in the case of industrial applications.

III.2.2. Polyurethane coating

Polyurethane was considered as a second possible host matrix. It was studied the same way as the epoxy one and applied by bar coating onto steel Qpanels. In a second step, we then adapted the protocol for an application by spray onto AA2024-T3 substrates

III.2.2.1. Low carbon steel: bar-coating

Unlike for the epoxy resin, the water amount to add to the formulation is fixed to 20.1% of the total formulation by the manufacturer. After assessing the volume solid of the formulation, the coating application has been studied using the same approach as for the previous experiment.

i. Polyurethane formulation

The polyurethane formulation containing water was applied on top of steel Qpanels with wet thicknesses of either 60 or 120 μm . For this, the formulation is stirred using an Ultra-Turrax disperser (4.5 krpm, 5 min) and degassed either in a desiccator under vacuum or with an ultrasound probe (20%, 1 min, 10s pulses with 10s pauses). After curing, the polyurethane layer is perfectly clear and free of any visible defect, as shown in Figure III. 14, whether the wet thickness applied is 60 μm (a) or 120 μm (b & c), and whatever the degassing technique used.

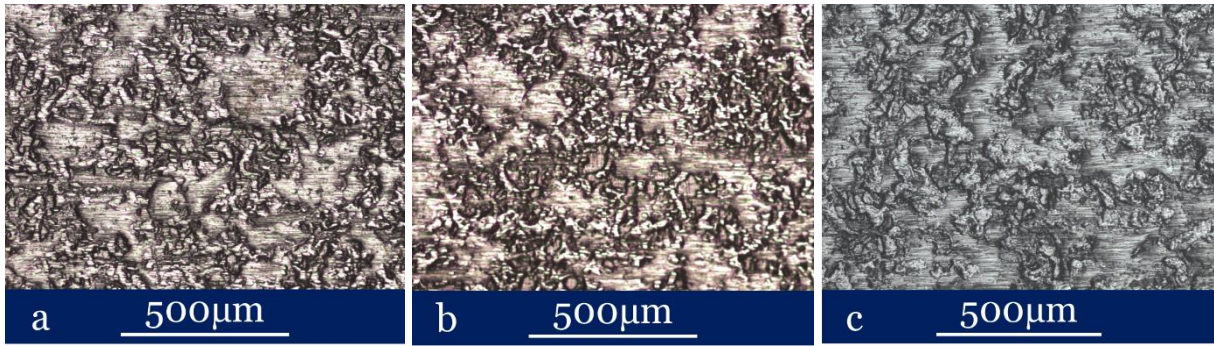


Figure III. 14: Observations of neat PU coatings applied by bar coating with a (a) 60 μm and (b) 120 μm wet thickness degassed (a & b) in a desiccator or (c) by sonication

Thickness measurements performed on three samples for each system are recorded in Figure III. 15, and allowed to determine a volume solid of $17.9 \pm 2.50\%$ and $20.8 \pm 1.51\%$ for wet thicknesses of 60 μm and 120 μm respectively. Measurements showed a homogeneous thickness all over the coated area. Due to the absence of significant differences between the coatings, a 120 μm wet thickness was chosen for the next optimization and characterization steps.

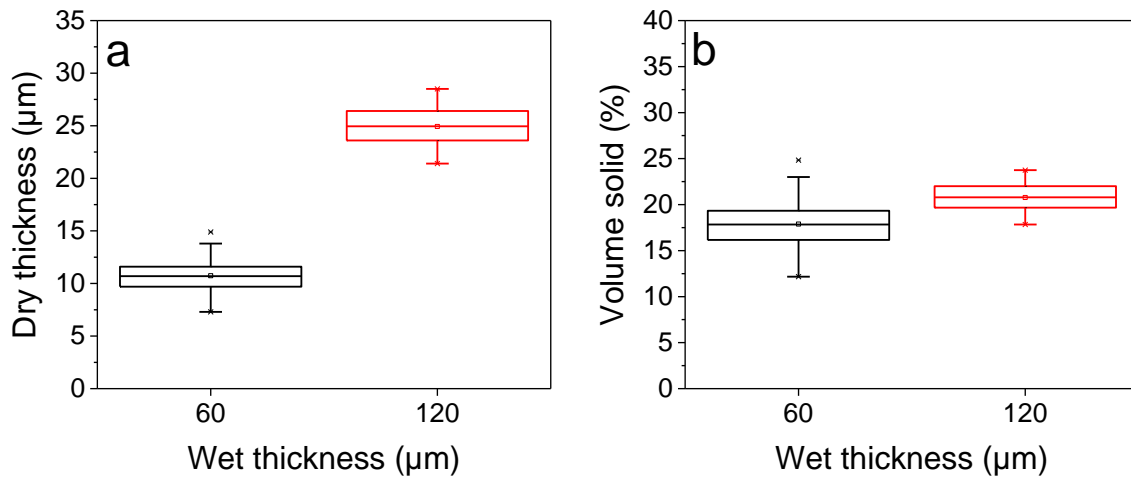


Figure III. 15: (a) Thickness of pure PU layers after curing and (b) corresponding volume solid, for 60 and 120 μm wet thickness

ii. Addition of silica containers to the formulation

The addition of the silica NCs suspension instead of water was tried either adding the suspension to the PU's base or to the mixture of base and hardener. Adding the suspension to the hardener led to the immediate formation of a precipitate, probably due to the reaction of the diisocyanate with the silica surface's silanol groups. Reactions between silanol and PU through hydrogen bonding^{12,13} or leading to the formation of covalent bonds between silanols and isocyanates¹⁴ have indeed been reported. Even after 10 min of stirring, lumps were seen in the solution. This order of addition was then discarded. No heterogeneity was detected for the other cases.

However, after application, grains are seen already in the wet film, and observable to the naked eye after curing. The number of aggregates is more important when the capsules are first added to the polyol dispersion, as represented in Figure III. 16.

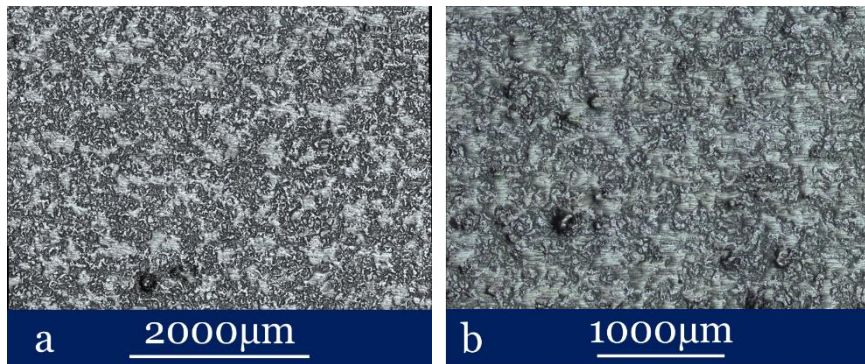


Figure III. 16: Observations of defects in PU coatings loaded with Si NCs, the suspension being added (a) to the blend of base and hardener and (b) first in the base before addition of the hardener

The composition of clusters and apparently defect-free zones have been analyzed using μ -XRF. Images and performed measurements are shown in Figure III. 17 and Table III. 5 respectively. Although differences are seen from a cluster region to another as evidenced here, a 1.5 to 3.5 higher amount of silicon is detected in the visible aggregates compared to the clear areas next to it. These Si-rich areas are therefore likely formed from the reaction of the silica capsules. The difference observed before depending on the order of addition let us think that a better dispersion of the capsules could prevent the formation of such defects.

Table III. 5: Elemental composition of the previously determined spots, determined by μ -XRF (in wt.%)

	1	2	3	4
Fe	90.21	96.98	96.13	97.75
Si	9.5	2.7	3.57	1.96
Mn	0.25	0.28	0.26	0.25
Cr	0.04	0.04	0.04	0.04

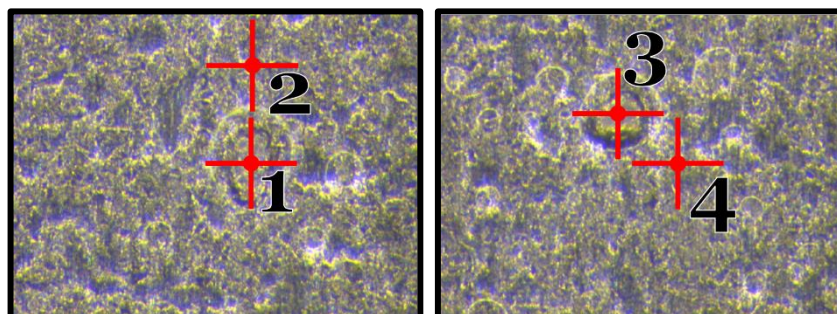


Figure III. 17: Observations of clusters in a PU-Si coating and spots analyzed by μ -XRF

In order to enhance the capsules dispersion, ultrasounds were used like in the previous section (1 min, 20% amplitude, 10s pulses with 10 pauses). However, unlike the epoxy resin, the polyurethane formulation was applicable even after longer sonication steps (at least 2 min). An

example of coating's appearance and the associated cross-section are given in Figure III. 18. Microscopic observations highlighted the homogeneity of coatings loaded with Si NCs dispersed this way, as well as a good apparent adhesion of the PU layer on the substrate. Moreover, the surface of the coating is apparently flat. Defects are seen in the mounting resin as well as in the PU layer and are due to the sample preparation. Image analysis as well as gauge thickness measurements gave a dry thickness of $26 \pm 2 \mu\text{m}$, similar to those obtained with the neat PU formulation.

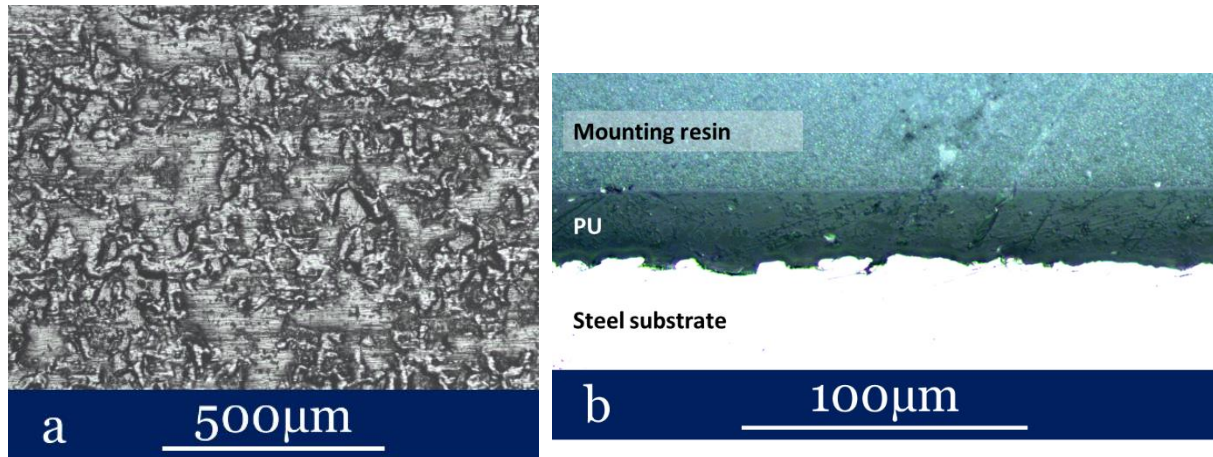


Figure III. 18: (a) Appearance and (b) cross-section of a PU-Si coating, after US processing of the formulation

III.2.2.2. AA2024-T3 Aluminum alloy: Spray

i. Formulation dilution

Since bar coating is limited to wide enough surfaces with a limited length, spraying was also considered as a technique that could be scaled-up. The same PU formulation without NCs as for bar coating was first used, using a 0.7 mm nozzle opening. In order to visually obtain a total coverage of the sample surface, a minimum 4-second spraying time was required. An example of a PU layer obtained after curing is presented in Figure III. 19. An important part of the sample (circled in red) is highly inhomogeneous in terms of thickness. In this area, bubbles are seen (b). An increase of the spraying duration from 4 to 6s increased the number of bubbles (c) and therefore we limited this value to 4s.

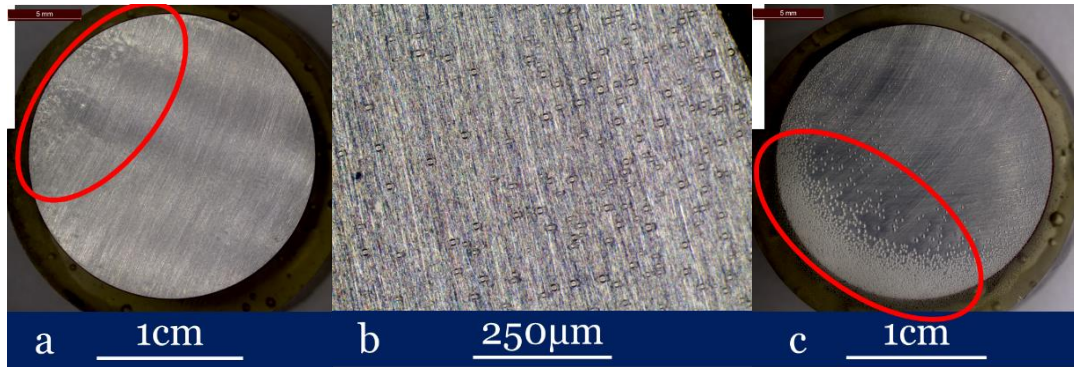


Figure III. 19: Appearance of AA samples after (a & b) 4s and (c) 6s-spraying of a 10/5/4 (B/H/W) PU formulation

Thickness measurements presented in Figure III. 20 corroborated these observations with important thickness variations in both cases, and an absence of reproducibility between samples of the same batch. Since the formulation used is quite viscous, this thickness inhomogeneity is probably due to a non-uniform deposition and to the effect of the pressure (the thicker part being due to the formulation “pushed” by the flow). The dilution of the formulation enabled a better distribution of the formulation after application, and led to uniform coatings free of voids with dry thicknesses of $65 \pm 14 \mu\text{m}$. On the other hand, a change in the applied pressure from 0.8 to 1.2 bar (measured with water) did not induce any change in the final appearance and homogeneity of the coatings. Below this range, random sputtering of droplets was observed, while above 1.2 bar the formulation was wavy and pushed off the substrate. Thereafter, the pressure was then set at 1 bar.

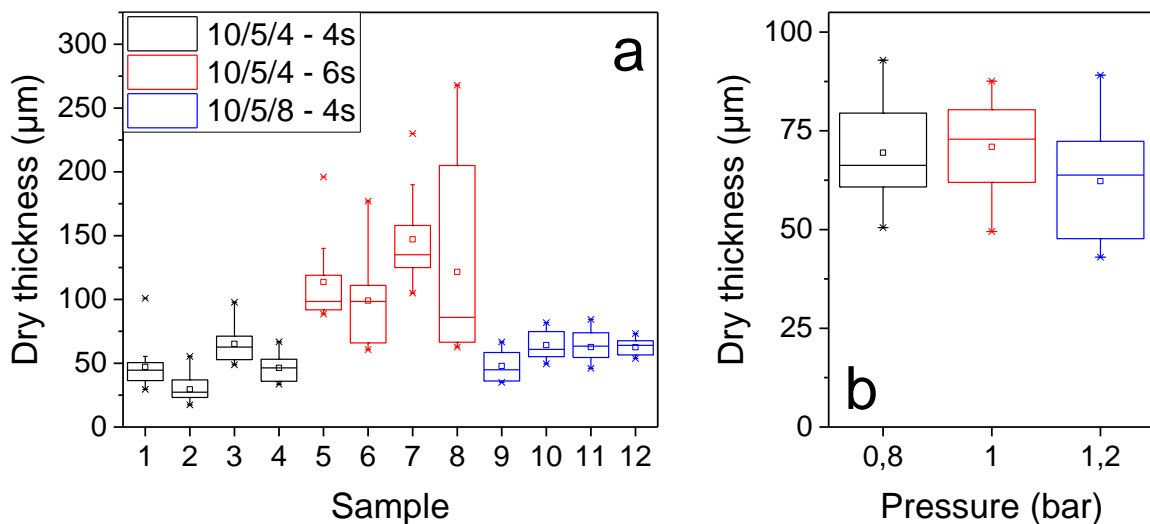


Figure III. 20: (a) Thickness of PU coatings sprayed on AA2024-T3 samples depending on the spraying time and formulation and (b) influence of the pressure applied

ii. Incorporation of the silica capsules suspension

The addition of the suspension is realized the same way as before. However, although the neat PU coatings were homogeneous, the addition of the NCs suspension instead of water has a detrimental effect on the mixture. This induces splatters and the appearance of clusters in the silica

Chapter III - Obtaining homogeneous coatings loaded with silica nanocontainers

nanocapsules-loaded polyurethane (PU-Si) layer, as shown in Figure III. 21 (a & b). This issue was overcome by increasing the nozzle opening (from 0.7 to 1.02 mm). This increase allows a better spray that led to the coatings shown in Figure III. 21 (c & d). Using a different nozzle also has an impact on the sprayed quantity, but since the coatings are homogeneous in thickness and structure, we did not adapt the other parameters (spraying time and pressure). The coatings' thickness was therefore increased: the measured dry thicknesses are plotted in Figure III. 22 and range from 70 to 90 μm . No difference is observed between the polymer only (PU) and the matrix loaded with either empty nanocontainers (PU-Si) or MBT-loaded nanocontainers (PU-Si(MBT)). The blue chart box in Figure III. 22 corresponds to coatings for which the SiNCs suspension has been diluted twice before addition. This shows that there is an upper limit for the quantity of capsules we can add (limited by the formulation's stability and viscosity).

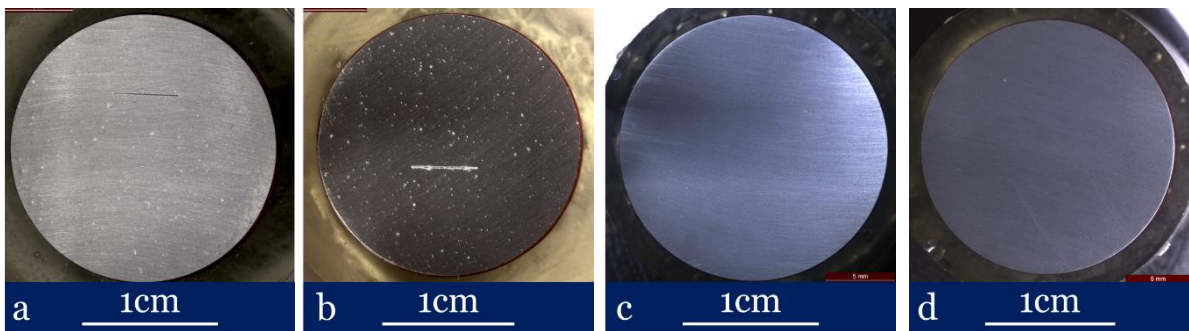


Figure III. 21: PU-Si coatings on AA substrate obtained with (a & b) 0.7 mm and (c & d) 1.02 mm nozzle openings

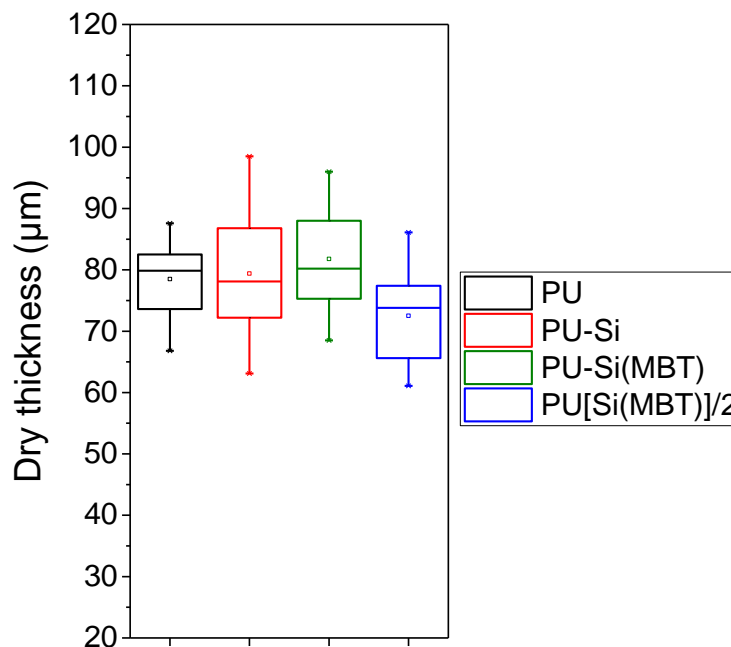


Figure III. 22: Thickness of sprayed PU, PU-Si and PU-Si(MBT) coatings on top of AA2024-T3 substrates

III.3. Polyurethane coatings analysis

Since we could not form a homogeneous and viable layer using the epoxy matrix loaded with Si NCs, the next steps of the work focused on the polyurethane resin. Before looking at the corrosion resistance of the composite coating, we tried to determine its capsules content, and so the related inhibitor amount that the coating can contain. This parameter is indeed the first one to take into account when speaking of corrosion inhibition. In the following steps, the capsules dispersion was assessed by μ -XRF

III.3.1. Amount of added capsules and inhibitor

The incorporated amount of capsules is estimated from dry content measurements, making the assumption that during the curing step the resin and suspension have the same behavior mixed than taken separately. With the previous weight ratio (10/5/8 in base/hardener/water respectively), the polyurethane's dry content is $40.8\% \pm 1.2\%$, measured by weight loss measurements, while its density is 1.02. Its volume solid is assumed to be 20.8%, determined from the bar coating thickness measurements. The silica nanocontainers suspension's dry content is 3.48% (measured after evaporation at 60°C). We can then estimate that the amount of silica capsules in the system is:

$$\begin{aligned} \text{wt. \%}_{\text{caps}} &= \frac{m_{\text{NCs}}}{m_{\text{coating}}} = \frac{m_{\text{suspension}} \times \text{DC}_{\text{suspension}}}{m_{\text{suspension}} \times \text{DC}_{\text{suspension}} + m_{\text{formulation}} \times \text{DC}_{\text{PU}}} \\ &= \frac{8 \times 0.0348}{8 \times 0.0348 + 15 \times 0.408} = 4.35\% \end{aligned}$$

With $\text{wt. \%}_{\text{caps}}$ the silica capsules content, m_{NCs} the weight of nanocapsules, m_{coating} the weight of the coating layer, $m_{\text{suspension}}$ and $\text{DC}_{\text{suspension}}$ the weight and dry content respectively for the suspension added to the formulation, and $m_{\text{formulation}}$ and DC_{PU} the weight and dry content respectively of the polyurethane formulation

If we assume the best-case scenario, all the water, ethanol that is formed and solvents evaporate during the curing step. In theory, the residual suspension should hence contain 3.60% of MBT and have a dry content of 1.53%. Yet, experimentally the suspension's dry content we measured is 3.48%. This difference has to be taken into account when calculating the content in MBT of the dry suspension, and so we have:

$$\mathbf{m_{\text{MBT th}} = m_{\text{MBT exp}}} \quad \text{(III.1)}$$

$$\text{yet} \quad \mathbf{m_{\text{MBT}} = m_{\text{caps}} \times \%_{\text{MBT in caps}} = \text{DC}_{\text{susp}} \times m_{\text{susp}} \times \%_{\text{MBT in cap}}} \quad \text{(III.2)}$$

Where m_{caps} is the weight of the NCs

$\%_{\text{MBT in caps}}$ is the weight percent of MBT in the dried capsules

DC_{susp} is the suspension dry content

And therefore, replacing (III.2) in (III.1):

$$(\%MBT_{in\ caps})_{calculated} = \frac{(\%MBT_{in\ cap})_{th} \times (DC_{susp})_{th}}{(DC_{susp})_{exp}} = 3.60 \times \frac{1.53}{3.48} = 1.58\%$$

the amount of MBT in the final coating can therefore be approximated as:

$$\%MBT_{in\ PU} = \%caps_{in\ PU} \times \%MBT_{in\ caps} = 0.0435 \times 0.0158 = 6.9 \cdot 10^{-2} \%$$

meaning that $[MBT]_{in\ PU} = 690\text{ppm}$.

In order to estimate the maximum MBT concentration in a surrounding solution, we can roughly link the PU coating's thickness to its weight. This allows to determine the maximum concentration of MBT that is released by the system for an exposed area A:

$$\begin{aligned} m_{coating} &= m_{formulation} \times DC_{PU} \\ &= V_{formulation} \times d_{PU} \times DC_{PU} = \left(\frac{V_{coating}}{\%S_{PU}} \right) \times d_{PU} \times DC_{PU} \end{aligned}$$

With $V_{coating} = A \times t$

Therefore we have:

$$m_{coating} = \frac{(1.02 \times 0.408)}{0.208} \times A \cdot t = 2.00 \text{ mg} \cdot \text{cm}^{-2} \cdot \mu\text{m}^{-1}$$

With t the coating's thickness in μm

A the considered area in cm^2

And so $m_{caps} = 8.70 \cdot 10^{-2} \text{ mg} \cdot \text{cm}^{-2} \cdot \mu\text{m}^{-1}$ and $m_{MBT} = 1.38 \cdot 10^{-3} \text{ mg} \cdot \text{cm}^{-2} \cdot \mu\text{m}^{-1}$.

Although this section only aims at describing the coating, it seems that a non-negligible amount of capsules and inhibitor can be incorporated in the PU layer. However, the loaded amount of MBT is not sufficient to suppose that the system is efficient. An active protection indeed requires a homogeneous dispersion of the NCs over the covered surface as well as a release of the inhibitor in the defect or through the defective PU matrix.

III.3.2. Evaluation of the silica-loaded coatings

III.3.2.1. FTIR

Infrared spectroscopy is used in order to assess the potential effect of the addition of silica NCs in the PU on its structure. Figure III. 23 shows the FTIR spectra of the PU, PU-Si and PU-Si(MBT) coating.

The absence of band in the 2280-2260 cm^{-1} region highlights the absence of residual isocyanate, whether capsules were added to the formulation or not. Almost no difference is seen in the spectra, meaning that the addition of silica capsules do not have a crucial effect on the polymer network's structure. Bands at 3350 cm^{-1} and 1235 cm^{-1} are attributed to N-H stretching and C-N stretching respectively, and are seen as expected for the three coatings. Asymmetric Si-O-S vibrations appear in the region between 1075 and 1125 cm^{-1} for both PU-Si and PU-Si(MBT) coatings¹⁵.

However, the spectrum of the PU coating presents a large band at 1568 cm^{-1} that is shifted to 1529 cm^{-1} upon addition of the silica NCs. This peak is attributed to N-H bending vibrations as well as C-N stretching, in the urethane bond. This region being especially sensitive to H-bonding¹⁶, this slight shift could hence be due to interactions between the capsules' silanol groups and the PU's urethane groups.

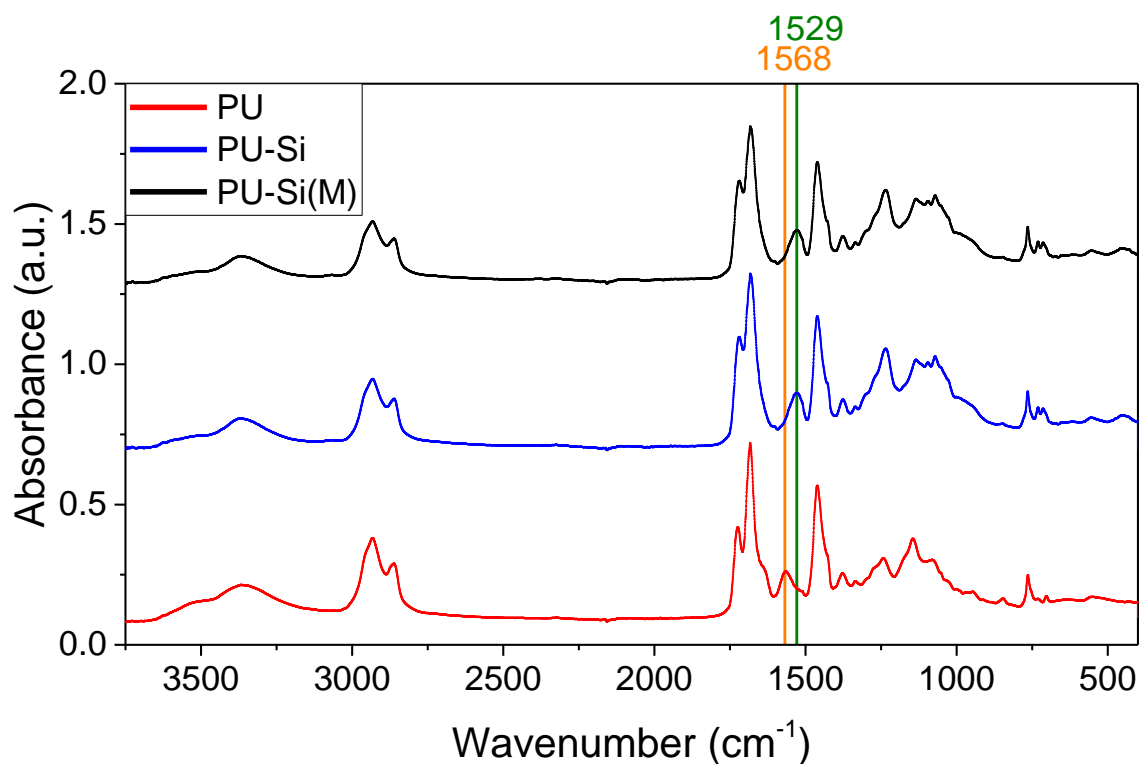


Figure III. 23: FTIR spectra of the neat PU and Si-loaded PU coatings

Despite this little difference in the FTIR spectra in presence of silica containers, the chemical structure of the PU layer is not significantly affected by the incorporation of capsules.

III.3.2.2. μ -XRF

In order to assess the homogeneous dispersion of the capsules at a lower scale than before, scanning electron microscopy was first considered. Micro x-ray fluorescence (μ -XRF) spectroscopy measurements were performed while other tests were conducted in order to try to assess the dispersion within the coating's thickness.

i. Cured formulation

The sensitivity of the equipment enables the detection of elements from sodium to uranium. Therefore, when analyzing the Si NCs-loaded PU itself (cured in a vial), as shown in Figure III. 24, only silicon and bromine are identified. The presence of bromine is due to the residual surfactant molecules (DTAB), while the detected silicon is due to both the incorporated nanocontainers and silica-based pigments of the formulation.



Figure III. 24: μ -XRF analysis of the cured Si-loaded PU resin

μ -XRF hence allows to compare the silicon content on several spots of the coatings, what gives a good insight of the distribution. It is however not possible to determine if the Si NCs are likely to stay at the coating's surface or at the metal/coating interface.

ii. Steel bar-coated Qpanels

Measurements have been performed on bar coated steel substrates for similar PU coating's thicknesses of *ca.* 25 μ m in order to be able to compare the measured amounts. The values presented in Table III. 6 are mean values obtained from a 3 x 3 mm² analyzed area. These results highlight the presence of 0.14% of silicon in the unloaded polyurethane formulation and a tiny amount in the steel substrate (0.03%). The increase in the silicon signal, from 0.14% in the pure PU to 3.8 and 4.1%, in the PU-Si and PU-Si(MBT) coating respectively is significant and due to the incorporated silica nanocontainers. Moreover, the measured amounts are comparable in both cases. Sulphur was also detected, only when MBT is present in the suspension, and with a measured amount compatible with the ratio MBT/Si.

Table III. 6: Thickness and composition of PU coatings determined by μ -XRF in the absence (PU) and presence of Si NCs, without (PU-Si) and with a payload (PU-Si(MBT) respectively), in wt%

	Thickness (μm)	Fe	Si	Mn	P	Br	Cr	S
Qpanel	-	99.51	-	0.33	0.09	0.01	-	0.03
PU	15.9 \pm 1.8	99.51	0.14	0.32	-	-	0.04	-
PU-Si	15.2 \pm 1.6	95.42	4.11	0.32	0.07	0.04	0.04	0.00
PU-Si(MBT)	16.0 \pm 1.9	95.61	3.87	0.33	0.06	0.03	0.04	0.05

In order to assess the capsule distribution, a μ -XRF mapping of a random part of a PU-Si coating's surface is shown in Figure III. 25. Although the probe is 25 μm wide, therefore not compatible with the capsules' size, the color map does evidence the absence of cluster or silicon-rich areas. A correct dispersion has hence been obtained over the covered area, validating our process for bar coating application.

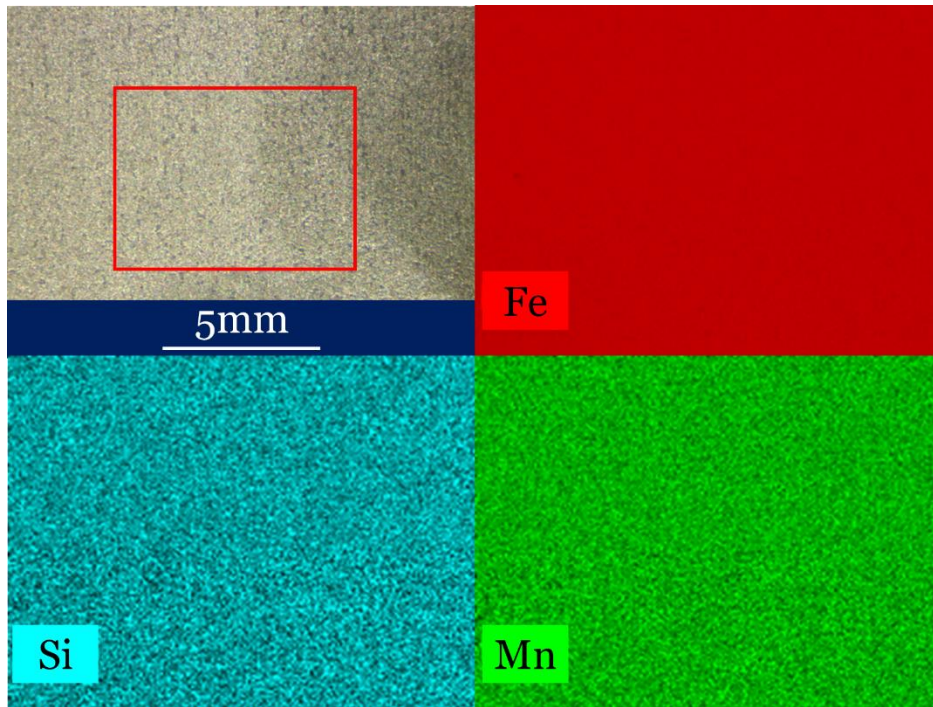


Figure III. 25: μ -XRF assessment of the silicon capsules distribution in a PU-Si coating made on top of a steel substrate.

iii. AA2024-T3 spray-coated samples

Analyses were performed on spray coated AA2024-T3 substrates. An observation of the analyzed sample is presented in Figure III. 26, the red crosses being the 6 analyzed spots, with their elemental composition given in weight percent in Table III. 7. The coating's thickness is $40 \pm 2 \mu\text{m}$. μ -XRF performed in our conditions gives the elemental composition of the coating layer and the underlying substrate. However, a screening effect clearly occurs, what distorts the quantification, as proved by an apparent copper content above 18% that does not make sense. Aluminum emission being less

energetic than that of copper (aluminum has a $K\alpha$ spectral line energy of 1.486 keV, compared to the 8.046 keV of copper), its content measurement is more influenced. This is corroborated by measurements performed in a scratched area (spots 5 and 6), for which the measured elemental composition does agree with the one of AA2024-T3. Concerning the silicon content measurements, the measured amount is similar at the randomly chosen locations but quantification is not usable because of the screening phenomenon.

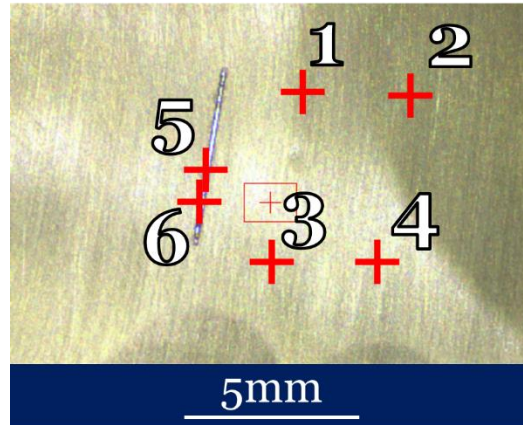


Figure III. 26: Observation of a PU-Si sample analyzed by μ -XRF

Table III. 7: Elemental composition (in wt.%) of a PU-Si covered AA2024-T3 sample, from μ -XRF measurements

#	Al	Si	Mg	Mn	Fe	Cu	Zn	Cr	Ni
1	76.49	0.68	0.25	2.68	0.25	18.84	0.61	0.18	0.02
2	77.02	0.73	0.20	2.53	0.22	18.46	0.63	0.16	0.03
3	75.22	0.75	0.09	2.47	0.22	20.39	0.68	0.16	0.01
4	73.59	0.81	0.16	2.32	0.31	21.99	0.65	0.15	0.03
5	93.74	0.01	1.27	0.66	0.09	4.03	0.14	0.05	0.01
6	93.57	0.01	1.37	0.68	0.10	4.08	0.13	0.05	0.01

This screening effect is moreover highly dependent on the organic layer's thickness. Measurements performed on an $80 \pm 5 \mu\text{m}$ -thick PU-Si coating (around twice as thick as the previous one) are recorded in Table III. 8 and indeed show an even lower aluminum amount, while the silicon, manganese, copper and zinc relative amounts are highly overestimated. μ -XRF then allows to compare the silicon local concentration for samples with comparable thicknesses but requires identical thicknesses to accurately compare measurements. Here also, after removal of the coating, the chemical composition expected for AA2024-T3 is measured.

Table III. 8: Elemental composition (in wt.%) measured by μ -XRF of a 80 μm PU-Si layer sprayed on top of an A2024-T3 substrate

	Al	Si	P	Ti	Mn	Fe	Cu	Zn	Br	Zr
PU-Si	6.06	26.78	0.29	0.09	5.25	1.29	57.71	1.90	0.32	0.32

III.3.2.3. SEM observations

The silica dispersion being assessed at a larger scale, scanning electron microscopy was employed to detect silica containers and potentially observe small aggregates, or areas free of capsules. All observations are carried out at 10 kV. Figure III. 27.a and b show surface observations for which some sort of relief whose sizes roughly correspond to the nanocontainers' are seen. In order to get more information, sputtering of argon ions was performed in order to remove around 150 nm of the coating. Figure III. 27.c shows a sputtered area. interestingly, holes appeared in place of the capsules. This tends to prove that the capsules are inserted within the host matrix but that only weak interactions exist between the resin and the silica shells. The removal of the organic binder hence leads to debonding of the capsules from the matrix. This highlights the absence of aggregation, that can sometimes be observed for not functionalized silica particles¹⁷. The magnification used here is however not sufficient to assess the wettability of the capsules by the matrix, that can cause the formation of voids surrounding the particles¹⁸.

Concerning the dispersion, Figure III. 27a. and b. are representative of a NCs-rich and a NCs-poor area respectively. Although an important difference in the capsules concentration is seen, most of the observed surface has been filled with Si NCs. The entire covered surface should therefore be protected.

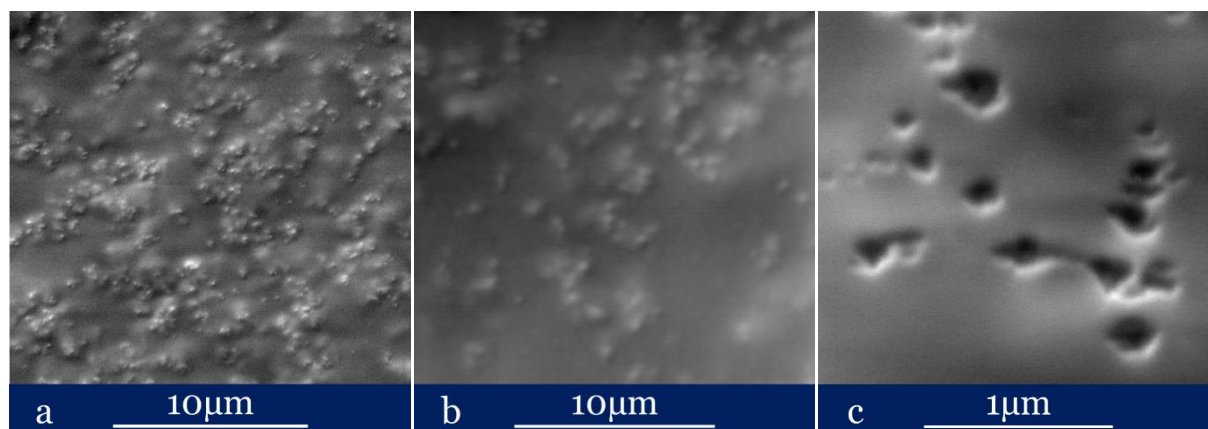


Figure III. 27: SEM observations of the surface of a sprayed PU-Si coating (a,b) before and (c) after removal of 150 nm of coating by Ar-sputtering

However, even though the encapsulated compound is present in the whole coating, such disparities could be detrimental to the system's properties. Indeed, the local concentration in Si NCs could exceed the critical pigment volume concentration, leading to an insufficient quantity of binder and

a loss in the coating's barrier properties⁴⁹. An in-depth analysis of the organic layer would moreover be useful in order to complement these observations. However, the evaluation of the Si NCs dispersion in the coating's depth by observation of a cross-section was not successful.

III.3.2.4. Time-of-Flight Secondary Ion Mass Spectrometry (ToF-SIMS)

ToF-SIMS consists in sputtering the coating's surface with primary ions (Bi^{3+} in our case) and then analyze the secondary ions that are ejected from the sample. The spatial resolution of this technique is not suited to the detection of the nanocapsules themselves, but ToF-SIMS can nonetheless give an insight on the presence of capsules beneath the coating's surface.

Figure III. 28 is a depth profile of a sprayed PU-Si coating. The analyzed area is $200 \times 200 \mu\text{m}^2$, and sputtering of Argon cluster is performed between two consecutive measurements in order to remove an estimated $1 \text{ nm}\cdot\text{s}^{-1}$. A progressive increase in the silicon-containing ions is observed during the first 100s, corresponding to the ionization of the superficial PU layer. Once this has been done, only small fluctuations are observed in the signal of SiO_2^- , SiHO_3^- and Si_2HO_5^- secondary ions. Over the estimated 300 nm analyzed, the silicon, and so the capsules, mean concentration is then quite constant.

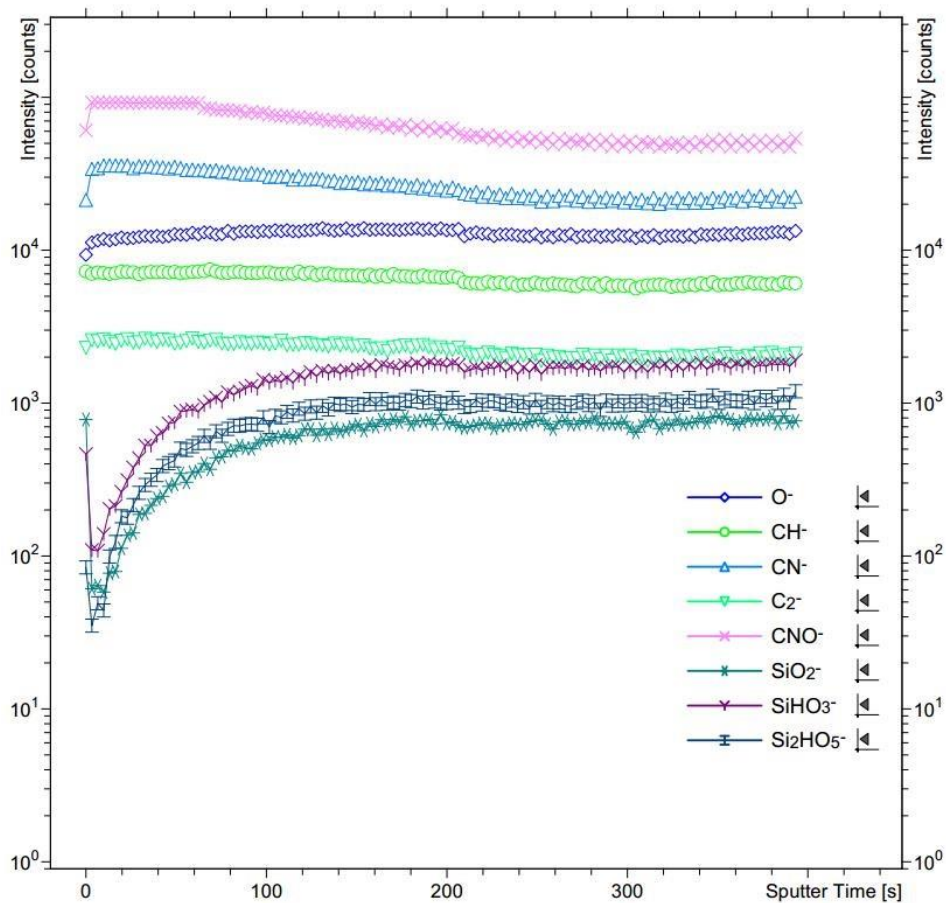


Figure III. 28: Depth profile of a PU-Si coating

A mapping of the surface after sputtering is shown in Figure III. 29 in order to assess not only the mean value but also the spatial repartition of silicon. The colored scale correspond to the intensity of the emitted Si^+ ion. Silicon is detected on the whole analyzed area. Some differences are however observed, leading to the same conclusions that for the sample's surface, with the existence of richer areas. Since the silica distribution seems random, we can assume that a correct dispersion has been obtained in the evaluated volume.

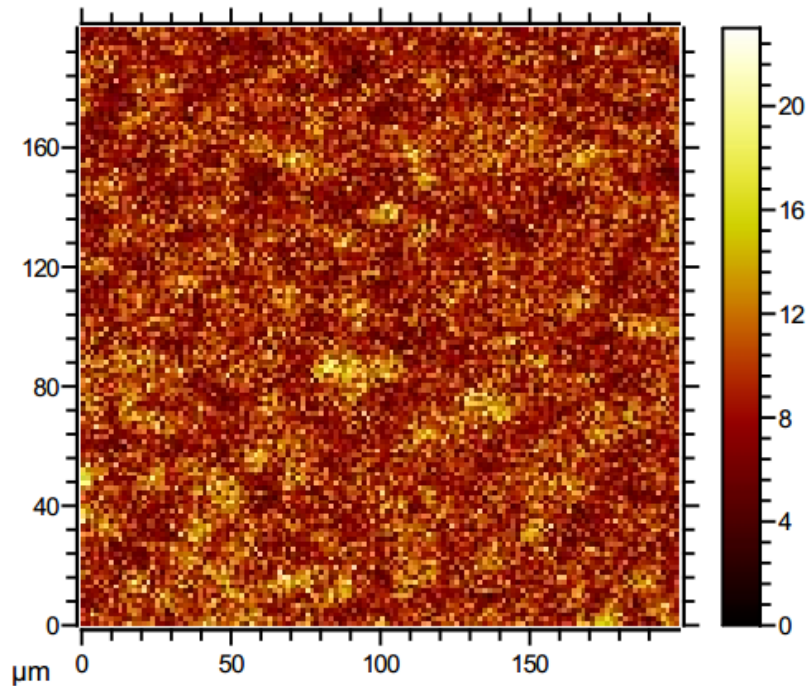


Figure III. 29: TOF-SIMS surface mapping of a PU-Si coating sprayed on AA2024-T3 after Ar-sputtering.

As seen in this section, the PU coatings loaded with silica capsules have the same composition as the reference coating. Moreover, a homogeneous silica content has been measured over the substrate by mean of μ -XRF. At a lower scale, SEM evidenced some areas that are richer in silica nanocontainers, but a 3D random dispersion of the nanocontainers should prevent the formation of silica-free zones.

Conclusions and outlook

In this section, we reported the development and systematic optimization of the process used to incorporate silica nanocontainers in a paint formulation. Either epoxy or polyurethane matrices were considered, both being waterborne commercial simplified formulations that should be dilutable with water. The addition of the nanocontainers consists in adding the suspension in a liquid form, using industrially applicable technologies. The main results of this work are that:

- The dilution of the epoxy formulation led to its destabilization and formation of defects in the polymer layer;
- The use of a sonication probe to complement high-performance dispersion was efficient to degas the formulation and obtain homogeneous coatings when only water is added, and aggregate-free coatings when the Si NCs are incorporated. However, due to either the presence of residual surfactant molecules or the presence of entrapped air, bubbles remained in the NCs-loaded epoxy coatings. It was hence decided not to further develop the epoxy system;
- The application of the same protocol to the polyurethane waterborne formulation led to defect-free coatings whether the suspension was loaded in the formulation or not;
- The application of the PU formulation was successful both by bar coating on steel substrates and by spray on AA2024-T3 substrates;
- Due to an important evaporation after curing, 25 μm -thick coatings were obtained by bar coating, while the thickness is increased up to 80 μm when spraying is employed.

We estimated that, with respect to the ratio used, the capsules weight content in the Si NCs-loaded PU coatings is around 4.3%. Moreover, assuming the best-case scenario, the system with MBT-loaded capsules should contain $1.4 \cdot 10^{-3}$ mg of MBT per covered cm^2 and per μm of thickness, equivalent to a concentration of $14 \text{ g} \cdot \text{L}^{-1}$ in the polymer layer. These values will be compared to the inhibitor's efficiency in the next chapter.

It was shown that the addition of the dispersion did not imply significant changes in the polymer's structures; while the dispersion of the nanocontainers was evaluated by μ -XRF, SEM observation and ToF-SIMS. It was evidenced that, despite some local disparities, no important capsules clusters were detected and that the whole coating's surface is loaded with nanocapsules.

Outlooks

The presented protocol has been optimized fixing several parameters, amongst which the quantity of suspension (and therefore capsules) added. Tries with different quantities of suspension might evidence the existence of an optimal quantity in order to enhance dispersion. Since the maximum amount of water that can be added to the formulation is limited, concentration of the suspension should be considered in case that the coatings' response is not high enough.

Sputtering evidenced that capsules can be detached from the host matrix, meaning that only weak bonds exist between the silica shells and the PU matrix, and might also highlight a detrimental interface. The assessment of these interfaces and potential improvements could be carried out. An option is the use of a formulation with a higher volume solid in order to potentially avoid the formation of voids at the capsules' surfaces. Secondly, in order to increase the matrix/NCs compatibility and enable a good dispersion and cohesive interfaces, surface modification is usually achieved²⁰ and should be considered, taking into account the nature of both the containers and the host matrix.

It has to be reminded that the formulation used are simplified paint and therefore are not optimized for application. Longer-term outlook include the use of a higher-viscosity polymer in order to enable the coating of non-planar geometries. The addition of the silica suspensions in a sol-gel layer should also be investigated since the similar chemistry should enhance the capsules incorporation.

References

1. Albers, R. A. Water-reducible epoxy coating compositions without emulsifier. *12* (1982).
2. Jackson, A. C., Bartelt, J. A., Marczewski, K., Sottos, N. R. & Braun, P. V. Silica-Protected Micron and Sub-Micron Capsules and Particles for Self-Healing at the Microscale. *Macromolecular Rapid Communications* **32**, 82–87 (2011).
3. Huang, M. & Yang, J. Salt spray and EIS studies on HDI microcapsule-based self-healing anticorrosive coatings. *Progress in Organic Coatings* **77**, 168–175 (2014).
4. Astruc, A. *et al.* Incorporation of kaolin fillers into an epoxy/polyamidoamine matrix for coatings. *Progress in Organic Coatings* **65**, 158–168 (2009).
5. Shi, H., Wu, L., Wang, J., Liu, F. & Han, E.-H. Sub-micrometer mesoporous silica containers for active protective coatings on AA 2024-T3. *Corrosion Science* **127**, 230–239 (2017).
6. Cook, M. Formulating novel aqueous epoxy. *6th Nürnberg Congress* **8** (2001).
7. Flick, E. W. *Water based paint formulations*. **4**, (Noyes, 1997).
8. Eskin, D. G. Ultrasonic degassing of liquids. in *Power Ultrasonics* 611–631 (Elsevier, 2015). doi:10.1016/B978-1-78242-028-6.00020-X
9. Patwardhan, S. V., Tilburey, G. E. & Perry, C. C. Interactions of Amines with Silicon Species in Undersaturated Solutions Leads to Dissolution and/or Precipitation of Silica. *Langmuir* **27**, 15135–15145 (2011).
10. Xue, G., Ishidab, H. & Koenigb, J. L. Chemical reactions in the bulk of the epoxy-functional silane hydrolyzate. *Die Angewandte Makromolekulare Chemie* **8**
11. Eckstein, Y. & Dreyfuss, P. Role of Amines in Adhesion of Polybutadiene to Glass Substrates. II. Reactions of Amines with Trimethoxysilanol and/or Fumed Silica. *The Journal of Adhesion* **15**, 163–178 (1983).
12. Heck, C. A., dos Santos, J. H. Z. & Wolf, C. R. Hybrid silicas/waterborne polyurethane composite properties: In situ formation vs. grafting methods. *Journal of Sol-Gel Science and Technology* **81**, 505–513 (2017).
13. Nunes, R. C. R., Fonseca, J. L. C. & Pereira, M. R. Polymer–filler interactions and mechanical properties of a polyurethane elastomer. *Polymer Testing* **19**, 93–103 (2000).
14. Zhang, G. *et al.* Isocyanate-crosslinked silica aerogel monoliths: preparation and characterization. *Journal of Non-Crystalline Solids* **350**, 152–164 (2004).
15. Wu, G. *et al.* Robust microcapsules with polyurea/silica hybrid shell for one-part self-healing anticorrosion coatings. *Journal of Materials Chemistry A* **2**, 11614–11620 (2014).
16. Wang, F. C., Fève, M., Lam, T. M. & Pascault, J.-P. FTIR analysis of hydrogen bonding in amorphous linear aromatic polyurethanes. II. Influence of styrene solvent. *Journal of Polymer Science Part B: Polymer Physics* **32**, 1315–1320 (1994).
17. Zhang, S., Yu, A., Song, X. & Liu, X. Synthesis and characterization of waterborne UV-curable polyurethane nanocomposites based on the macromonomer surface modification of colloidal silica. *Progress in Organic Coatings* **76**, 1032–1039 (2013).
18. Bansal, A. *et al.* Quantitative equivalence between polymer nanocomposites and thin polymer films. *Nature Materials* **4**, 693–698 (2005).
19. Mirmohseni, A., Akbari, M., Najjar, R. & Hosseini, M. Self-healing waterborne polyurethane coating by pH-dependent triggered-release mechanism. *Journal of Applied Polymer Science* **136**, 47082 (2019).
20. Lin, W. C., Yang, C. H., Wang, T. L., Shieh, Y. T. & Chen, W. J. Hybrid thin films derived from UV-curable acrylate-modified waterborne polyurethane and monodispersed colloidal silica. *Express Polymer Letters* **6**, 2–13 (2012).

Chapter IV

—

Corrosion protection and performances of capsules-loaded polyurethane coatings

Chapter IV - Table of contents

Introduction	174
IV.1. Materials and methods	174
IV.1.1. Materials.....	174
IV.1.1.1. Chemicals.....	174
IV.1.1.2. Metal samples	174
IV.1.2. Electrochemical measurements	175
IV.1.2.1. Set-ups.....	175
IV.1.2.2. Procedures and data analysis	177
IV.2. Considered inhibitors	179
IV.2.1. Protection of structural steel	179
IV.2.1.1. MBT	179
IV.2.1.2. Sodium molybdate (Na_2MoO_4).....	181
IV.2.2. Protection of AA2024-T3	184
IV.2.2.1. MBT.....	184
IV.2.2.2. Cerium dibutylphosphate $\text{Ce}(\text{dbp})_3$	187
IV.2.2.3. Conclusions on the inhibitors to use	190
IV.3. Interactions of the silica capsules with the metallic substrates.....	192
IV.3.1. Effect on the corrosion behavior of steel	192
IV.3.2. Effect on the corrosion behavior of AA2024-T3.....	194
IV.4. Inhibition properties of the coatings	199
IV.4.1. On steel	199
IV.4.1.1. Intact coatings.....	199
IV.4.1.2. Artificially damaged coatings	205
IV.4.2. On AA2024-T3.....	208
IV.4.2.1. Reference polyurethane coating (PU).....	208
IV.4.2.2. PU coating loaded with “empty” Si NCs (PU-Si)	209
IV.4.2.3. PU coating loaded with MBT-loaded Si NCs (PU-Si(MBT))	211

Chapter IV - Corrosion protection and performances of capsules-loaded polyurethane coatings

IV.4.2.4. Comparison of the performances of the three systems212

IV.5. Conclusion on the system's performances216

References217

Introduction

The incorporation of the nanoreservoirs into the polyurethane matrix led to homogeneous and visually defect-free coatings after optimization of the deposition procedure. The aim of this chapter is to assess the corrosion protection brought by the developed system using open circuit potential monitoring and Electrochemical Impedance Spectroscopy (EIS)

As a first step, we looked at the effect of inhibitors on corrosion processes on both steel and aluminum alloy when placed in a chlorinated medium. Since it was successfully encapsulated, 2-mercaptobenzothiazole was employed, before looking at potential alternatives, namely sodium molybdate for steel and cerium dibutylphosphate for aluminum alloys. Existing interplays between the silica suspension and metallic substrate was also investigated.

In a second step, the PU coatings loaded with silica nanocontainers were studied. Both bar-coated steel and sprayed AA samples were analyzed. The three systems presented in chapter III allowed to assess the impact of the addition of nanocapsules into the matrix, and the importance of the encapsulated MBT.

IV.1. Materials and methods

IV.1.1. Materials

IV.1.1.1. Chemicals

The list of the chemicals used for the preparation of the electrolytes and inhibitor solutions are given in the appendices section (see Appendix 2). Since it was not commercially available, cerium dibutylphosphate was synthesized according to a procedure described by Scholes¹.

IV.1.1.2. Metal samples

The two kinds of substrates used for the electrochemical study are AA2024-T3 aluminum alloy and carbon steel (either S355 or SAE 1008/1010).

The embedded aluminum alloys coupons are those presented in Section III.1.1.2. For uncoated embedded substrates, the samples are grinded (P4000 SiC abrasive paper), placed in ethanol in an ultrasound bath for 3 min, then rinsed with deionized water and dried with air. For some experiments, non-embedded substrates have been used. In this case, 2 mm-thick AA2024-T3 plates have been cut, grinded (P1200 abrasive paper) and placed for 3 min in ethanol in an ultrasound bath.

The steel substrates used for the inhibitors' effect study are made of S355. A plate is cut in order to get a 15 mm-large square cross section that is then embedded in a cold-mounted epoxy resin. A copper cable is welded on the backside of the plate as presented in Figure IV. 1 for electrical measurements. These coupons are then grinded (P1200 abrasive paper), placed in ethanol in an ultrasound bath for 3 min, then rinsed with deionized water and dried using air.

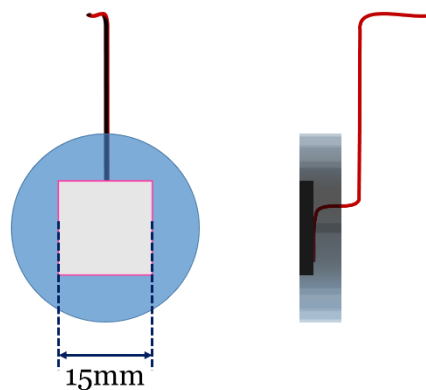


Figure IV. 1: Scheme of a S355 steel sample prepared for inhibitor testing

In order to get a reproducible surface preparation for bar coated steel samples, SAE 1008/1010 steel Qpanels are used. Before immersion, Qpanels are rinsed with ethanol and deionized water.

IV.1.2. Electrochemical measurements

IV.1.2.1. Set-ups

Depending on the samples used, three setups are employed in order to perform electrochemical measurements.

i. Stirred cell

A conventional 3-electrode electrochemical cell was used where a glass vessel is filled with 250 mL of electrolyte under magnetic stirring (300 rpm). The analyzed metal is placed vertically and constitutes the working electrode (WE), while a saturated calomel electrode (SCE) is used as a reference and a platinum grid as the counter-electrode (CE).

The measurements are performed with a PGSTAT302N (Metrohm Autolab®) potentiostat/galvanostat controlled with GPES and FRA softwares for stationary and impedance measurements respectively.

ii. Opto-EIS setup

This setup is a home-made three-electrode electrochemical cell built at TU Delft². It is composed of a Ag/AgCl reference electrode, a 6.6 mm-diameter graphite rod as counter electrode and the measured sample as a working electrode. The sample is clamped vertically in the electrochemical cell with a copper block. The exposed area, through a hole made on one side of the cell is an 8 mm-diameter disc, and an electrolyte volume of 100 mL is required. The three-electrode electrochemical cell is placed in a Faraday cage in order to avoid external interferences.

Electrochemical measurements were performed with a PGSTAT302 (Metrohm Autolab®) potentiostat/galvanostat controlled with NOVA v1.11.1 software.

iii. Paint test cell

A Gamry PTC1 paint test cell is used. For coated Qpanels, the cell is placed on a homogeneous area and clamped while a lined part of the substrate is connected to the potentiostat. The exposed area is then defined by an O-ring, whose internal diameter and cross section are 40.87 mm and 3.53 mm respectively. The assumed exposed area is then 15.5 cm². For Sprayed coatings, a setup presented in Figure IV. 2 is used. The sample is screwed on a support, and electrically connected to a banana plug. The paint cell is then placed on top and the considered area is the AA's cross section, *i.e.* 3.14 cm².

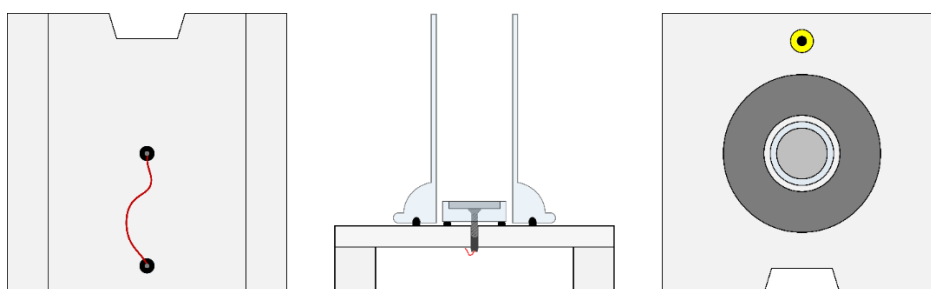


Figure IV. 2: (a) bottom view, (b) face cross section, and (c) top view of the electrochemical cell used for EIS measurements

For coated samples, a 6.6 mm-diameter graphite rod is employed as counter and pseudo-reference electrode. This two-electrode cell is used in order to avoid any interferences from a classic reference electrode when working with high frequencies or low currents. For the uncoated samples used with this setup as a reference, the graphite electrode is replaced with a SCE as a reference and a platinum grid as a counter electrode.

Before immersion, the samples are placed at 40°C under vacuum for 3h, then cooled down under vacuum for 3h in order to get rid of any moisture before the measurements. The electrochemical cell is placed in a Faraday cage in order to avoid external interferences.

Electrochemical measurements were performed with a PGSTAT302N (Metrohm Autolab®) potentiostat/galvanostat controlled with GPES and FRA softwares for classic electrochemical and electrochemical impedance measurements respectively.

iv. Use

Table IV. 1 records the different types of substrates employed in this section, as well as the purpose of the experiments carried out with each system. All electrochemical measurements have been carried out in NaCl 0.05M as the electrolyte.

Table IV. 1: Electrochemical setups used and their purpose

Set-up	Substrate			Purpose
	Nature	Area	Orientation	
Stirred vessel	Embedded S355	2.25 cm ² square	Vertical	Inhibitors evaluation
Opto-EIS setup	AA2024-T3	0.50 cm ² disc	Vertical	Inhibitors evaluation
	Bare Qpanels	0.50 cm ² disc	Vertical	Suspension interactions
	Scratched PU	0.50 cm ² disc	Vertical	Coating evaluation
Gamry Paint- Cell	Embedded AA2024-T3 disc	3.14 cm ² disc	Horizontal	Coating evaluation
	Bar-coated intact PU	13.07 cm ² disc	Horizontal	Coating evaluation

IV.1.2.2. Procedures and data analysis

i. Inhibition assessment by linear polarization measurements

Linear Polarization Resistance (LPR) measurements are performed after 0.5, 1, 2, 4, 6, 10, 16, and 24h of immersion in an electrolyte made of 0.05M NaCl to which is added a certain amount of inhibitor. The Open Circuit Potential (OCP) is recorded between LPR measurements. The parameters used for LPR measurement are: ± 20 mV around the metal's OCP, 1.95 mV steps, 2 mV.s⁻¹ sweep. The polarization resistance R_p is then calculated using: $R_p = \frac{\Delta E}{\Delta i}$.

ii. Impedance measurements for coated substrates

Electrochemical Impedance Spectroscopy (EIS) measurements are performed from 10⁵ to 10⁻² Hz, with an amplitude of 15 mV RMS over the measured OCP. The number of points per decade could vary from 8 to 12 and is specified when results are presented. During an EIS experiment, the system's OCP is recorded between two measurements.

Analysis of the impedance plots was then carried out with the software ZView 3.5b, using the appropriate Equivalent Electrical Circuits (EEC).

iii. Water uptake assessment

Since free films could not be obtained, a gravimetric analysis of the applied coatings over immersion was not possible. However, water uptake of an organic coating can be measured by EIS, using the equation developed by Brasher and Kingsbury³. The coating can be assimilated to a dielectric whose

capacitance C_{coat} is defined by (IV.1), and it is therefore assumed that changes in the coating's capacitance are proportional to changes in permittivity if geometrical quantities are constant.

$$C_{coat} = \frac{A \cdot \epsilon_0 \cdot \epsilon_r}{d} \quad (IV.1)$$

With A the coating's area,

d its thickness,

ϵ_r its relative permittivity,

ϵ_0 the vacuum permittivity ($8.854 \cdot 10^{-12} \text{ F} \cdot \text{m}^{-1}$).

A polymer's relative permittivity being lower than 10 while the permittivity of water is 80.2 at 20°C, the system's permittivity increases as water progresses into the coating. Brasher and Kingsbury³ then proposed that the water uptake (in vol.%) can be calculated by:

$$X_v = 100 \cdot \frac{\log\left(\frac{C_t}{C_0}\right)}{\log(\epsilon_w)} \quad (IV.2)$$

Where C_t is the film capacitance at time t,

C_0 the dry film's capacitance,

ϵ_w the permittivity of water.

The coating's capacitance can then be calculated from a fixed frequency measurement in the high frequency domain⁴. Indeed, in this domain, the total impedance of the system is governed by the coating's capacitance^{5,6}. The capacitance C_t can therefore be calculated⁷ using (IV. 3), while the dry film's capacitance C_0 is extrapolated⁸ from the initial linear part of the capacitance time evolution $C_t=f(t)$.

$$C_t = \frac{-Z''}{2\pi f((Z')^2 + (Z'')^2)} \quad (IV.3)$$

Where Z' and Z'' are the real and imaginary part of the impedance respectively.

However, if these relations are widely used for paints immersed in salt solutions^{9,10}, they are based on assumptions, amongst which two are hardly measurable:

- The swelling of the paint can be ignored;
- The distribution of water within the paint is random and uniform.

In reality, the swelling of the polymer can be quite important in our case, whilst the incorporation of the silica containers can lead to a non-uniform water ingress. An absolute water uptake value therefore cannot be obtained¹¹, but a comparison between our systems can give insights on the impact of the capsules incorporation on the film's properties.

In order to evaluate the coatings' water uptake, quick measurements are repeated every one minute in the high frequency domain, from 10^5 to 10^3 Hz, with an amplitude of 15 mV RMS over the measured OCP.

IV.2. Considered inhibitors

Due to the encapsulation process and results presented in Chapter II, an oil-soluble inhibitor, namely 2-mercaptobenzothiazole (MBT), was encapsulated. Before looking at the performances of the composite coatings, we assessed the effect of MBT and our ability to detect it during corrosion for the substrates we focused on.

IV.2.1. Protection of structural steel

The results presented in this section (IV.2.1.) were obtained using an electrochemical cell under magnetic stirring.

IV.2.1.1. MBT

MBT is only slightly soluble in neutral aqueous solutions. Therefore, the maximum obtained concentration in order to have a clear solution was 25 ppm, equivalent to a molar concentration of $1.5 \cdot 10^{-4} \text{ M}$. This has also been observed by Lamaka¹² for instance that reported a saturation concentration below 0.05 g/L for MBT in pure water.

Figure IV. 3 shows the evolution of the steel's OCP over around 24h immersion in presence or not of MBT. In the solution free of inhibitor, a slight shoulder is observed in the first few hours with an equilibrium around -650 mV/SCE reached after 5h. In presence of 25 ppm of MBT the OCP stabilization occurs in around 2.5h and the OCP value is 50 mV higher than in the NaCl solution. This slight shift is in good agreement with studies carried out in acidic media^{13,14} and tends to show that MBT is predominantly an anodic inhibitor.

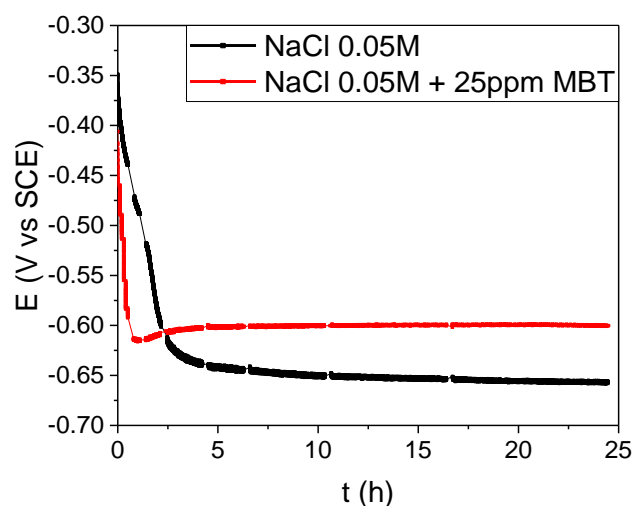
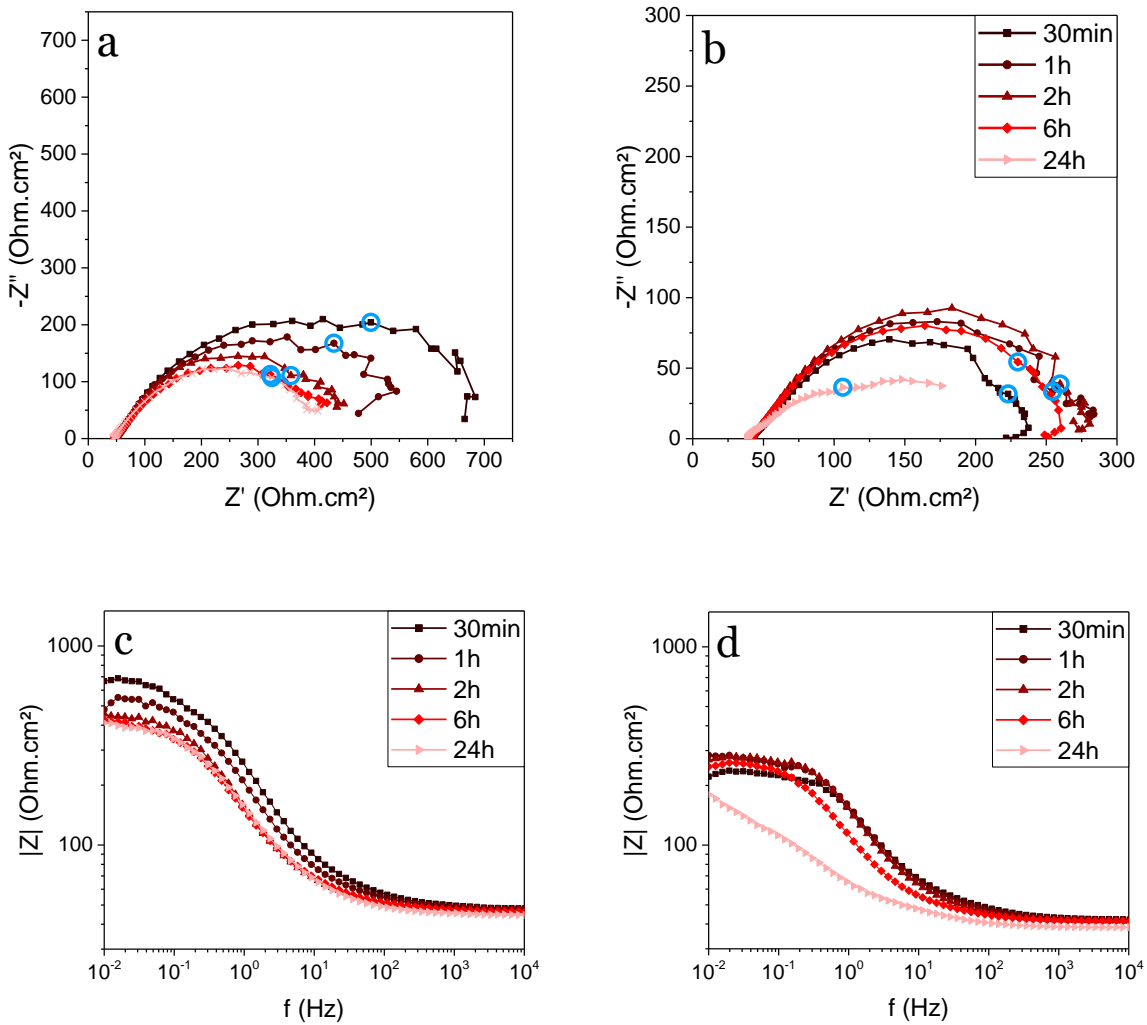


Figure IV. 3: Evolution of S355's OCP in 0.05M NaCl with and without 2-MBT

EIS measurements have been performed for both systems over immersion. The results are presented in Figure IV. 4. The impedance values for both systems cannot directly be compared since the

temperature is not well controlled. However, the behavior of the two systems is clearly different. The EIS spectra show an apparent simple RC behavior (one loop), with a continuous decrease in the impedance of the bare S355 substrate over the 24h of immersion. The low-frequency (LF) modulus (0.1 Hz) is almost half-reduced (from 700 to 400 ohm.cm²) after 24h of immersion. On the other hand, the addition of the inhibitor to the electrolyte leads to EIS spectra showing a RC behavior and an inductive response in LF, which is characteristic of adsorbed species at the metal's surface. A slight increase in the system's impedance is observed during the first few hours, followed by a decrease initiated after around 5h of immersion.



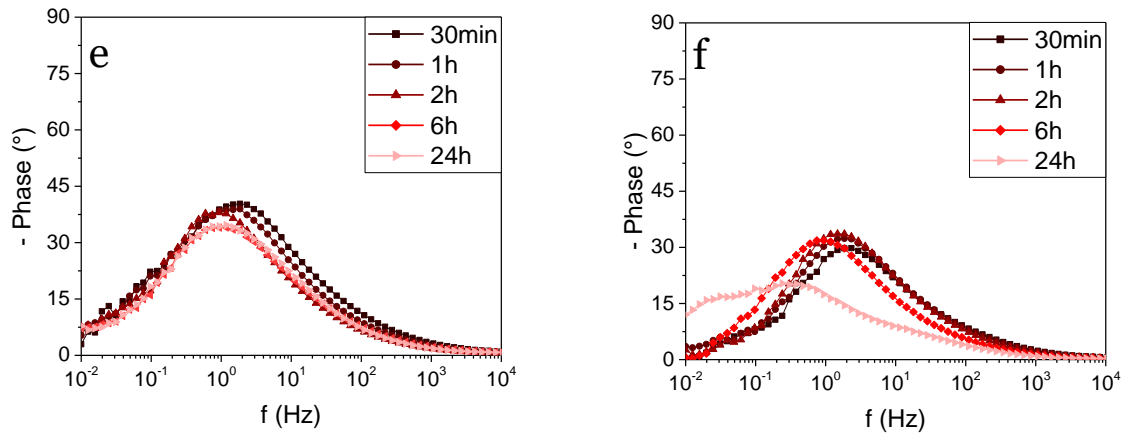


Figure IV. 4: Evolution with time of EIS spectra with (a,b) Nyquist plots, (c,d) moduli and (e,f) phase angle for the bare S355 substrate in (a,c,e) absence and (b,d,f) presence of 25 ppm of MBT. Spectra are taken with 10 pts/decade, the 0.1 Hz measurement is circled in the Nyquist plots

From these experiments, it seems that MBT has only a limited efficiency on steel in neutral conditions and at the apparent maximum concentration obtained. However, differences in the OCP values and in the impedance behavior during the first times of immersion have been evidenced and show an inhibiting effect, preferentially anodic as seen elsewhere^{14,15}. This effect is attributed to chemical adsorption through the heteroatoms of MBT (N and S), for the protonated form of the inhibitor¹⁶.

IV.2.1.2. Sodium molybdate (Na_2MoO_4)

Since MBT shows limited results, the efficiency of Na_2MoO_4 as a non-toxic inhibitor has been assessed for potential use with S355 structural steel. Figure IV. 5 shows the evolution of the system's OCP and polarization resistance (from LPR) over 24h of immersion in an electrolyte containing sodium molybdate amounts ranging from 50 to 1000 ppm ($2.1 \cdot 10^{-4}$ to $4.13 \cdot 10^{-3}$ M). For a concentration as low as 50 ppm, there is a clear increase in the open circuit potential of around 100 mV after 24h of immersion. An increase in the Na_2MoO_4 concentration moreover leads to an increase in OCP. This shows that sodium molybdate is an anodic inhibitor for S355 steel as expected from results on other mild steels^{17,18}. LPR measurements highlight this inhibition with a clear increase in the initial polarization resistance in presence of Na_2MoO_4 . However the conferred protection in this case is a short-term one since R_p rapidly decreases. Molybdate acts by forming a protective film at the steel surface due to its polycondensation¹⁹. A threshold concentration of MoO_4^{2-} is therefore continuously required to overcome the destruction or dissolution of this protective film²⁰, potentially sped up by the stirring of the electrolyte.

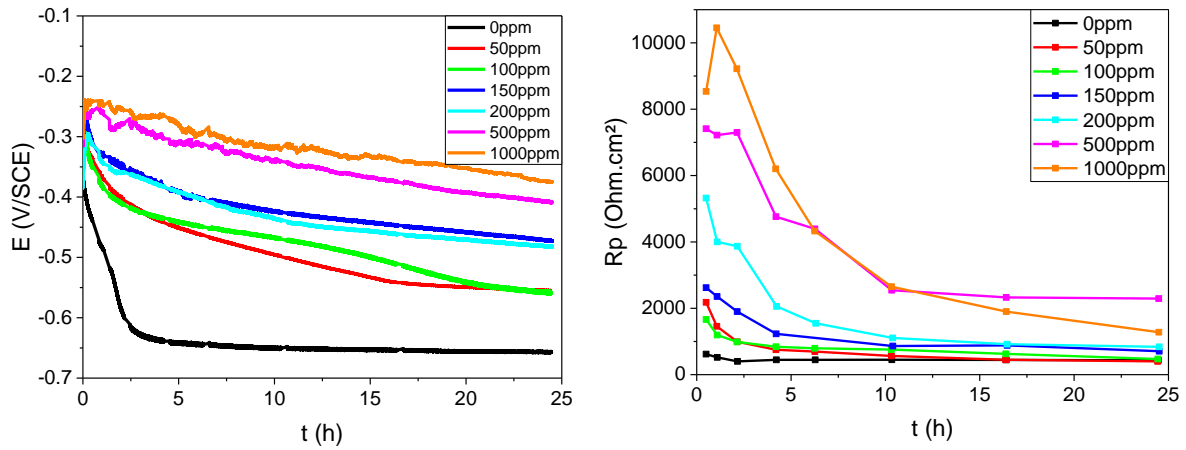


Figure IV. 5: OCP and R_p (measured by LPR) of S355 steel immersed in 0.05M NaCl with different amounts of sodium molybdate

Analysis of the impedance behavior of the same system was carried out. Three relevant spectra are presented in Figure IV. 6 and show a single time-constant. The impedance spectra have therefore been fitted using the Randles electrical equivalent circuit (EEC) presented in Figure IV. 7. This EEC is composed of a resistance R_s related to the solution and equipment's resistances, in series with a charge transfer resistance R_{ct} that can be assimilated to the system's polarization resistance R_p . The capacitance in parallel with R_p is the double layer capacitance C_{dl} linked to the substrate/electrolyte interface. The fitting of the impedance measurements allows to plot the evolution of R_p as a function of the immersion time shown in Figure IV. 7, and corroborate the LPR results, showing a short-term protection brought by sodium molybdate.

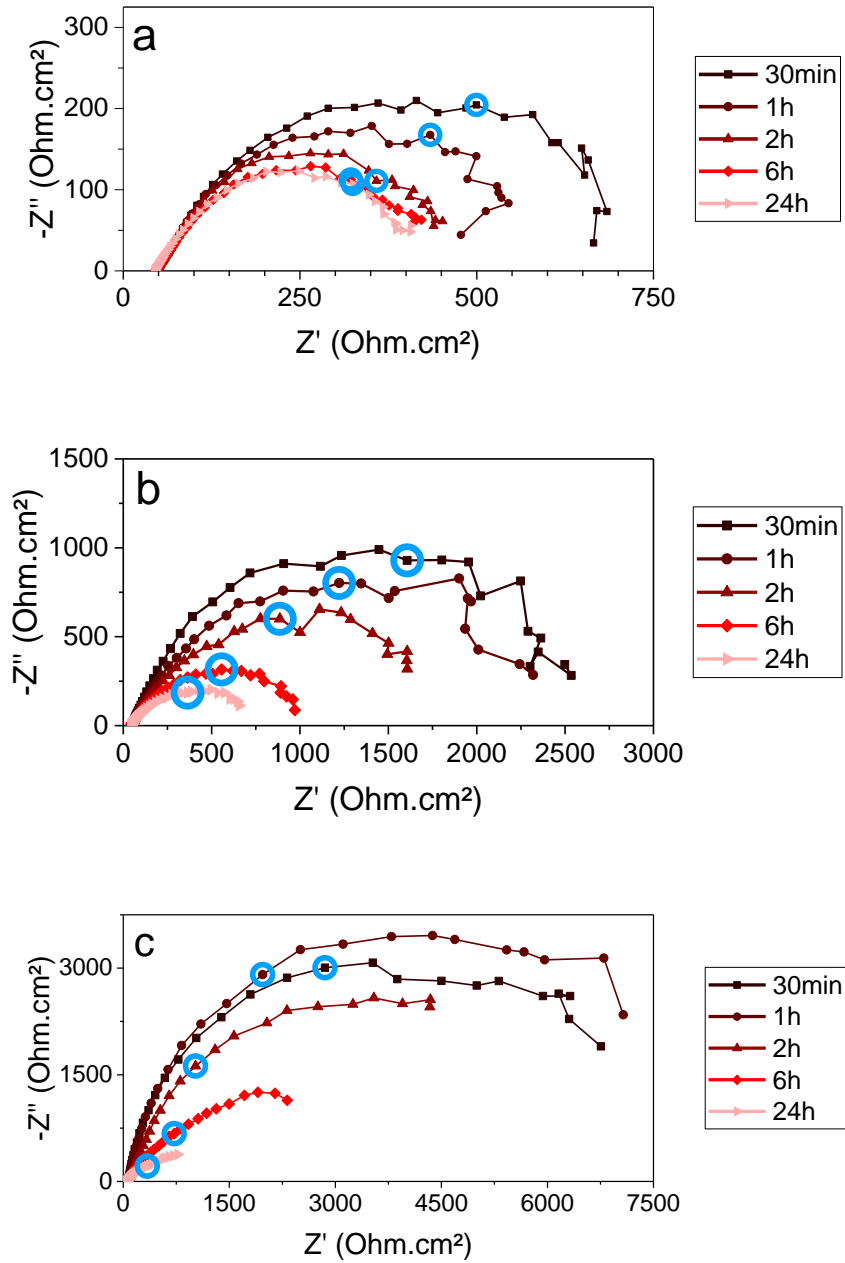


Figure IV. 6: EIS spectra of S355 immersed in 0.05M NaCl (a) without inhibitor and with (b) 150 ppm and (c) 1000 ppm of Na_2MoO_4 . Spectra contain 10 pts/decade; the measurement taken at 0.1Hz is circled

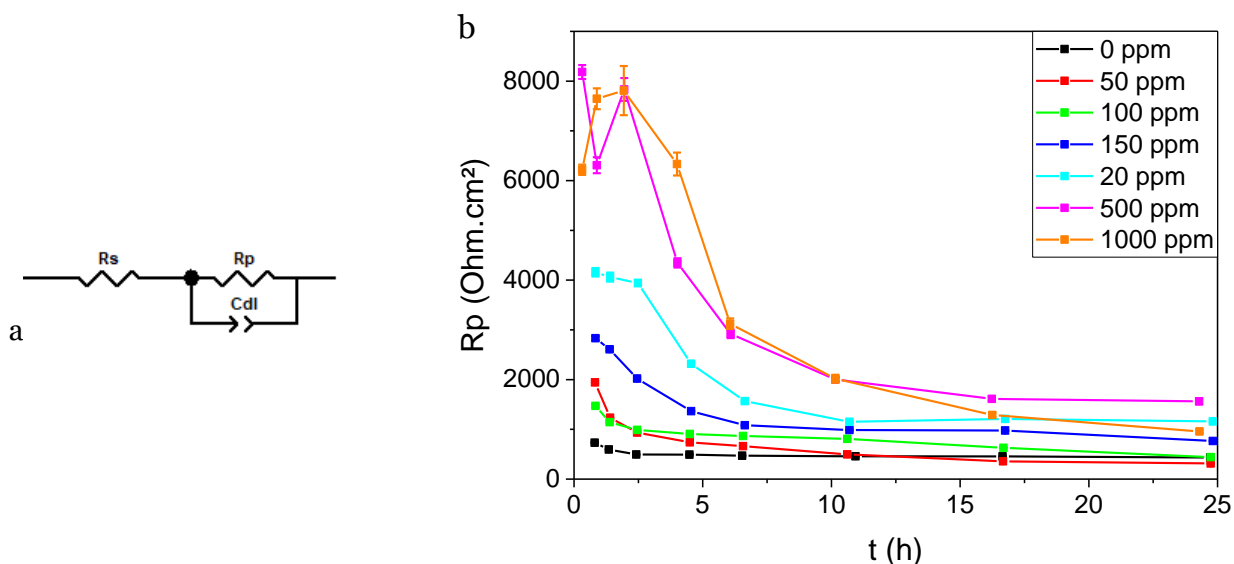


Figure IV. 7: (a) EEC used to fit the EIS spectra and (b) calculated R_p for S355 immersed in 0.05M NaCl without different amounts of Na_2MoO_4 corrosion inhibitor

Sodium molybdate has an effect on corrosion processes during the first few hours of immersion in these conditions, that were arbitrarily chosen. Shams El Din²⁰ showed that this loss of protection (and decrease in OCP) depends on both the concentration in inhibitor and the presence of aggressive species in the medium. This decrease in resistance is likely due to the consumption of inhibitor, whose concentration goes below a threshold value. This is however relevant for immersion, whereas a far lower amount should be enough to provide long-term corrosion protection in atmospheric corrosion conditions. Moreover, sodium molybdate is non-toxic²¹, what makes it a relevant choice. Nonetheless, this compound is highly soluble in water (up to 650 g.L⁻¹ at 25°C²²), what makes it unsuitable for encapsulation in the silica nanocontainers. MBT was then used in the next sections, keeping in mind that the application on steel could necessitate to replace the smart containers used.

IV.2.2. Protection of AA2024-T3

The results presented in this section (IV.2.1.) were obtained using the opto-EIS setup.

IV.2.2.1. MBT

Since MBT was successfully encapsulated in Si nanocontainers that were incorporated in the polyurethane coating, we first assessed its effects on bare aluminum in order to later identify its potential effect when integrated in the polymer layer. The evolution of the AA2024's open circuit potential in the presence of MBT is compared to the reference OCP in Figure IV. 8. As one can see, the measured OCP of bare AA2024-T3 is quite noisy, due to rapid processes occurring at the metal's surface. The OCP value is oscillating around -500 mV vs Ag/AgCl for around 15h, then slowly collapses to reach a value around -700 mV vs Ag/AgCl. These values are in good accordance to those found in the literature²³, although only few studies report the monitoring of the OCP for immersion

duration longer than a few hours. This behavior has nonetheless been reported before for AA2024-T3 immersed in low concentration NaCl electrolytes^{24,25}. The plateau observed for the first hours of immersion shows fluctuations due to the high surface activity. This is linked to the formation and passivation of metastable pits. The subsequent decrease corresponds to the following attack of the surface after breakdown of the oxide film. A very different behavior is observed when the electrolyte contains MBT: an initial drop of the system's OCP is measured, followed by an increase up to a potential plateau around -550 mV that only slightly decreases with increasing immersion time. This would mean that corrosion is prevented, what is in good agreement with the ability of MBT to bond with copper²⁶, stabilizing the MBT adsorbed layer and competing with the adsorption of chlorides^{27,28}. An OCP value above -650 mV, higher than in the absence of MBT, is observed for durations up to 65h.

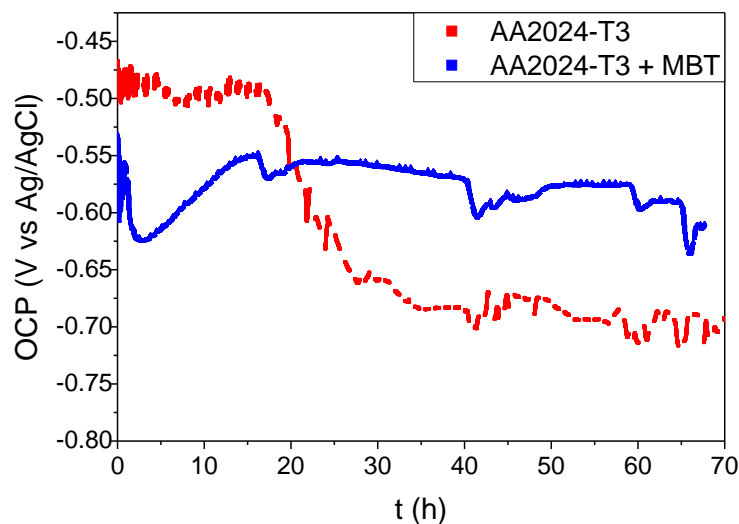


Figure IV. 8: OCP of AA2024-T3 in 0.05M NaCl without and with 25 ppm of MBT

Plots of the EIS measurements performed are shown in Figure IV. 9 for bare substrates immersed in an electrolyte with and without MBT. The Nyquist plot obtained for NaCl only (a) presents two capacitive loops that can be attributed to the charge transfer reactions for the higher frequencies, and to corrosion processes at lower frequencies as described by Queiroz²⁹ in low concentration electrolytes. The LF response goes from a capacitive response for short immersion times to a diffusive one, as evidenced for pitting^{29,30}. This second process is not seen in the presence of MBT: the addition of MBT to the electrolyte leads to a clear capacitive loop with an inductive loop at lower frequencies. A possible physical meaning of this inductive loop is the adsorption of a molecule on the metal, and could highlight the action of MBT. Indeed, although inductive behaviors have been reported for short immersion durations and associated to anodic dissolution due to aggressive species³¹ or to pitting propagation³², this phenomenon is still observed after 67h of immersion.

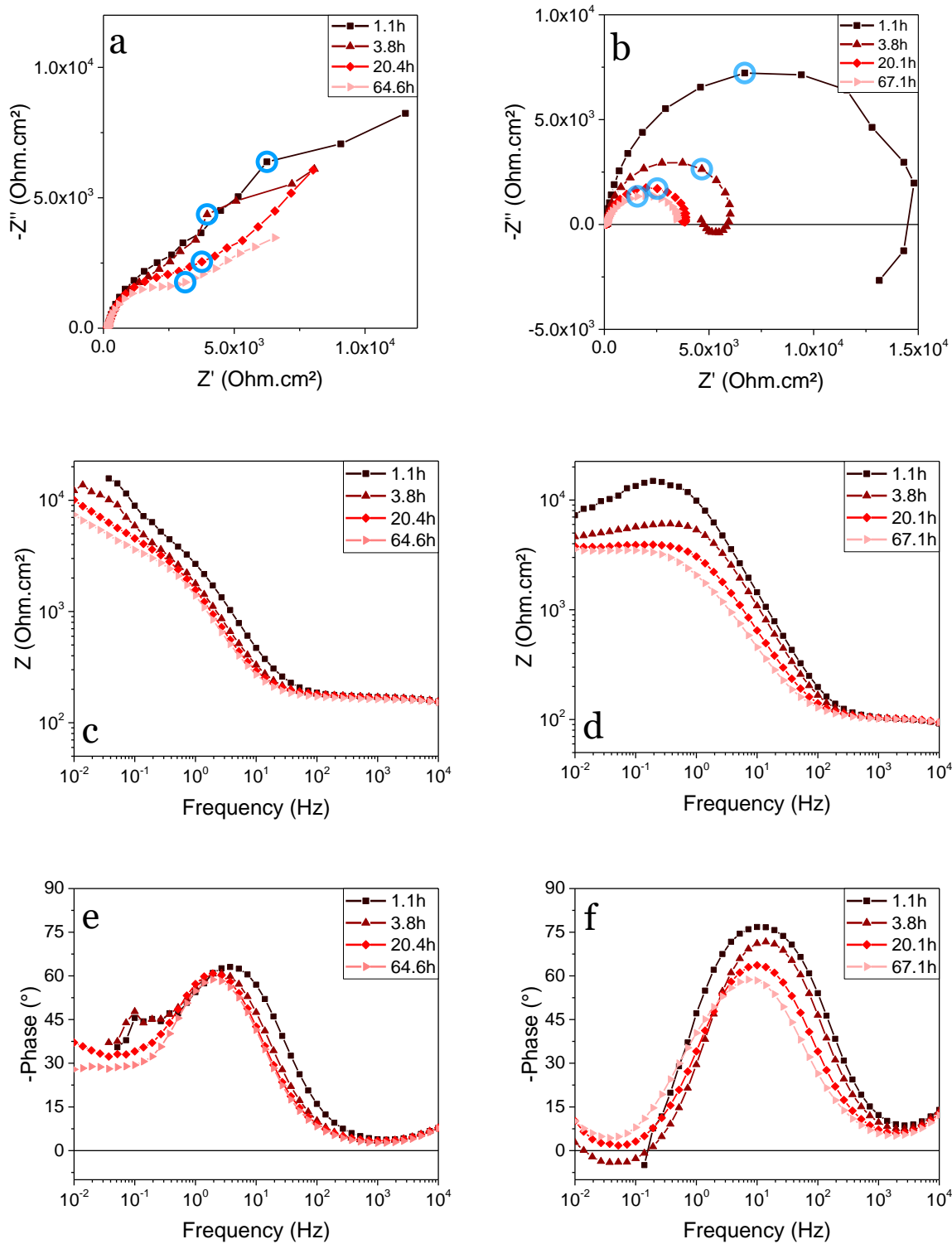


Figure IV. 9: Evolution of EIS spectra for bare AA2024-T3 immersed in (a,c,e) 0.05M NaCl and (b,d,f) 0.05M NaCl with 25 ppm of MBT. Spectra contain 8pts/decade, circled points correspond to measurements taken at (a) 0.1Hz and (b) 1Hz

If we discard the low frequency processes and only consider the medium frequency time constant that is present with and without MBT, the systems can be fitted using the Randles circuit, as shown in Figure IV. 7.a. The charge transfer resistances can then be compared. The fitting results, presented in Figure IV. 10, show a resistance around three times higher at the beginning of

immersion in the presence of MBT. This resistance drops as soon as the immersion starts, and reaches a pretty stable value around 4000 ohm.cm². This value is similar to the one obtained without inhibiting specie after 2-3h of immersion. This short-term protection is probably due to a low concentration in inhibitor species. Obtaining a solution that is more concentrated in MBT must however be achievable using a different preparation process. Although our electrolyte was apparently saturated at around 25 mg.L⁻¹, Abdollah Zadeh *et al.*³³ and Zheludkevich *et al.*³⁴ showed results for *ca.* 160 and 300 mg.L⁻¹ respectively. With these concentrations, they reported a resistance 10 times higher in presence of MBT than in 0.05M NaCl after 48h³³ and 300h³⁴ respectively.

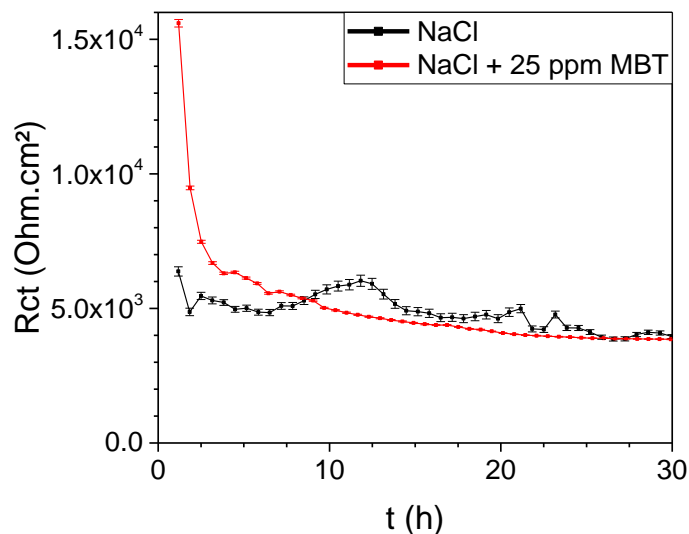


Figure IV. 10: Evolution of the charge transfer resistance of bare AA2024-T3 in 0.05M NaCl without and with 25 ppm of MBT, calculated from the EIS spectra fit

IV.2.2.2. Cerium dibutylphosphate Ce(dbp)₃

Despite being an effective corrosion inhibitor for AA2024-T3, MBT presents an aquatic toxicity and could raise concern for human health. If this inhibitor was selected for the demonstration of the NC2M system, alternatives have to be kept in mind. Amongst the existing ecofriendly inhibitors, cerium dibutylphosphate seems to be a very promising candidate^{24,25}. This compound is soluble in water but requires a long dissolution time³⁵, what can enable long-term protection but makes it tricky to encapsulate. In order to have an idea of the efficiency of Ce(dbp)₃ compared to MBT, the same concentration than the one used for MBT was employed. An electrolyte solution containing 0.05M NaCl and 1.5.10⁻⁴ M Ce(dbp)₃ (equivalent to 110 mg.L⁻¹) was prepared for these experiments.

The OCP of bare AA2024-T3 in this electrolyte is presented in Figure IV. 11. This potential decreases from -550 to around -700 mV vs Ag/AgCl in a few hours, compared to the 15h observed in the absence of inhibitor. This could be an insight of inhibition due to cerium cations that precipitate on the cathodic sites, hindering the oxygen reduction³⁶. At the beginning of immersion, an oscillating signal was measured and could be due to the cathodic precipitation of cerium competing with the

anodic adsorption of dibutylphosphate anions. Indeed, Ho *et al.*²⁴, in a 0.01M NaCl electrolyte and Garcia *et al.*²⁵ using 1 mM Ce(dbp)₃ reported a clear initial decrease in the OCP followed by an increase before describing the same behavior as reported here.

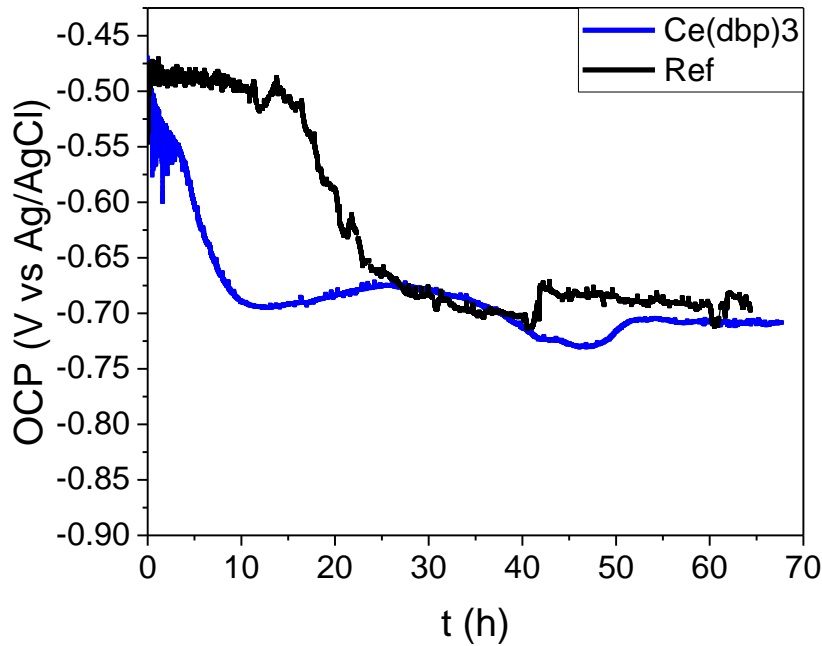


Figure IV. 11: OCP of bare AA2024-T3 immersed in a 0.05M NaCl electrolyte without and with 110 ppm of Ce(dbp)₃

EIS spectra obtained over the 65h of immersion are presented in Figure IV. 12. The Nyquist plots present a single capacitive loop for immersion time up to 5h. After 5h, a second phenomenon appears at lower frequencies, and could be related to a diffusion process. The total impedance value, taken in the low frequency domain, is around $5 \cdot 10^5 \text{ ohm.cm}^2$ at first, more than an order of magnitude higher than in the absence of inhibitor.

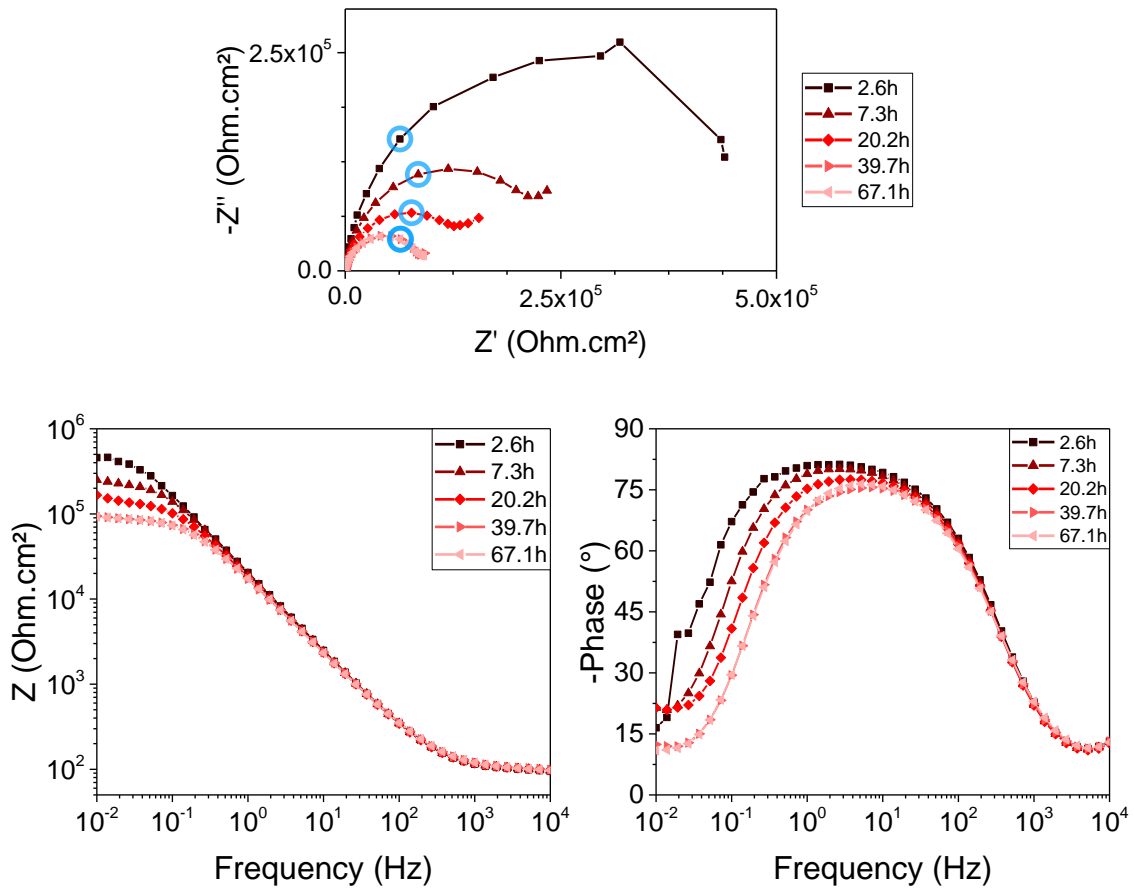


Figure IV. 12: Evolution of the impedance of AA2024-T3 in 0.05M NaCl + 110ppm Ce(dbp)₃ over immersion time. 8pts/decade are measured, measurements taken at 0.1Hz are circled.

As for bare S355 and MBT, the spectra have been fitted using a Randles EEC in order to compare the systems' charge transfer resistances. Results plotted in Figure IV. 13 show a different behavior than with MBT or no inhibitor: during the first few hours, there is a slight increase in the resistance, followed by a decrease and stabilization between 10⁵ and 2.10⁵ ohm.cm², what is approximately 20 times higher than the alloy alone.

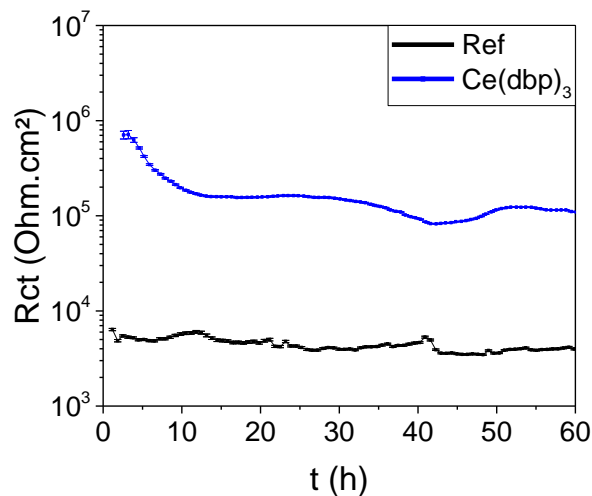


Figure IV. 13: Evolution of the charge transfer resistance R_{ct} for AA2024-T3 immersed in 0.05M NaCl + 110ppm of Ce(dbp)₃, calculated from EIS data.

From the electrochemical study presented here, we can say that MBT and $\text{Ce}(\text{dbp})_3$ both have an inhibiting role in the tested conditions. The effect of $\text{Ce}(\text{dbp})_3$ is more remarkable since the total impedance and charge transfer resistance are more than 10 times higher than for MBT, what lasts for a few hours compared to at least 60h in the case of $\text{Ce}(\text{dbp})_3$. However, although the same molar concentration of MBT and $\text{Ce}(\text{dbp})_3$ is used, $\text{Ce}(\text{dbp})_3$ dissociates into water to form dibutylphosphate and cerium (III)³⁵, both acting as inhibitors²⁵, what can reinforce its efficiency. *In-situ* observations of the AA's surface at the initial stage and after 24h and 38h of immersion at OCP are recorded in Figure IV. 14. Without any inhibitor, the alloy's surface is clearly attacked after 24 hours of immersion in the chloride solution, while with the two inhibitors, no visible corrosion products are observed after 38h of immersion. This confirms that the low impedance increase and the presence of an inductive loop in the impedance spectra obtained with MBT are related to a protection of the AA substrate.

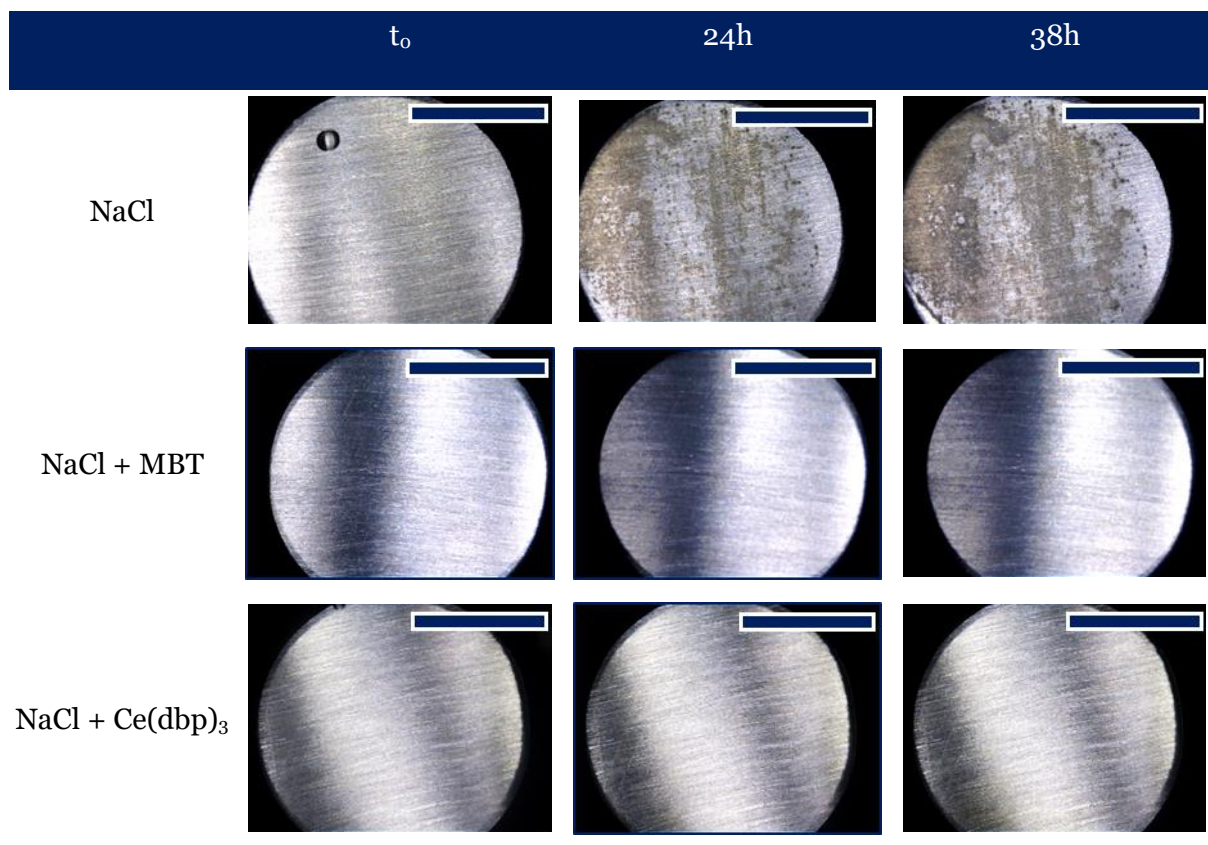


Figure IV. 14: Appearance of AA2024-T3 substrate's surface, immersed in 0.05M NaCl, NaCl with 25 ppm of MBT and NaCl with 25 ppm of $\text{Ce}(\text{dbp})_3$ after 0, 24 and 38h of immersion. Scale bars represent 4 mm

IV.2.2.3. Conclusions on the inhibitors to use

An electrochemical study has been carried out in order to assess the activity of MBT with the considered substrates in a neutral medium. MBT showed limited results with structural steel, mainly increasing its open circuit potential. The differences seen in the impedance behavior of the bare metal in presence of MBT (mainly stabilization of the total resistance) however highlight the

existence of interactions between the inhibitor and the steel's surface. On the other hand, MBT seems to be a good corrosion inhibitor for concentrations as low as 25 ppm for AA2024-T3.

MBT was used because its action should be detectable, and that its encapsulation was successful. However, its use could be hindered by the molecule's toxicity, low solubility and limited efficiency in neutral medium on S355. For these reasons, alternatives have been looked at, and we showed that sodium molybdate and cerium dibutylphosphate are good candidates for steel and aluminum protection respectively.

IV.3. Interactions of the silica capsules with the metallic substrates

Before being trapped in the polymeric network, the metallic substrate is in direct contact with the suspension. Moreover, when a defect is created locally in the polymer layer, a realistic scenario in the case of nanocontainers is that the shell is not broken but that the nanocontainers themselves are released from the coating in the electrolyte. It is hence of great interest to evaluate the interaction between the nanocontainers and the substrate. A destructive interaction could for example lead to the destruction of containers or to a non-random dispersion within the matrix. We therefore evaluated the effect of a 10 vol.% silica suspension addition in the electrolyte by monitoring the open circuit potential and performing regular EIS measurements. Due to the opacity of the solution, *in situ* observations of the surface of the substrate were not possible.

IV.3.1. Effect on the corrosion behavior of steel

Evolution of the OCP of the steel substrate immersed in the electrolyte containing the Si NCs suspension is presented in Figure IV. 15. and compared to the reference without NCs. In the sodium chloride electrolyte, the reference OCP decreases from -370 mV vs Ag/AgCl to 600 mV vs Ag/AgCl in around 3h, corresponding to the dissolution of the metal and the progressive formation of corrosion products^{37,38}. In presence of the capsules, this drop in OCP is very rapid from around -420 mV to -650 mV vs Ag/AgCl in 20s. This highlights an effect of the silica suspension that could catalyze the metallic dissolution and formation of corrosion products. The OCP then slightly shifts towards more positive values, and reaches a steady-state value at around -610 mV vs Ag/AgCl. This slight ennoblement of the OCP seems to suggest that the composition of the corrosion products is changed due to the presence of the silica capsules in solution.

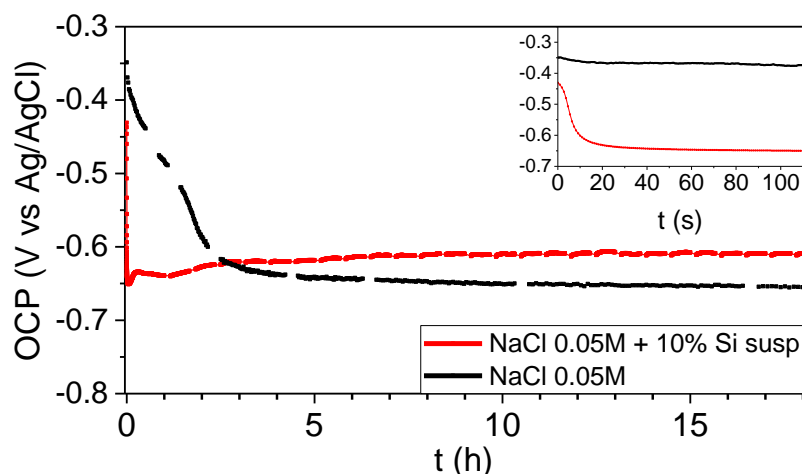


Figure IV. 15: Evolution of steel's OCP immersed in 0.05M NaCl with and without addition of 10% Si NCs suspension

The impedance plots are shown in Figure IV. 16. The Nyquist diagram presents a single capacitive loop whose diameter increases with the immersion time. This is associated with an increase in the

system's total impedance with a 0.01 Hz modulus increasing from roughly 1600 to 2600 ohm.cm² over 6h of immersion and then stabilizes. This phenomenon is probably due to the reaction of the silica onto the metal's surface and coincides with the evolution of the OCP. Adsorption of the silica capsules onto the steel's surface during the growth of a corrosion products film could explain the low frequency inductive behavior seen on the Nyquist plots. This is supported by the affinity of silica with iron (III) species^{39,40}, allowing the capsules to hence bond with the metal's surface or iron oxides, protecting it. The substrate's resistance therefore increases over time.

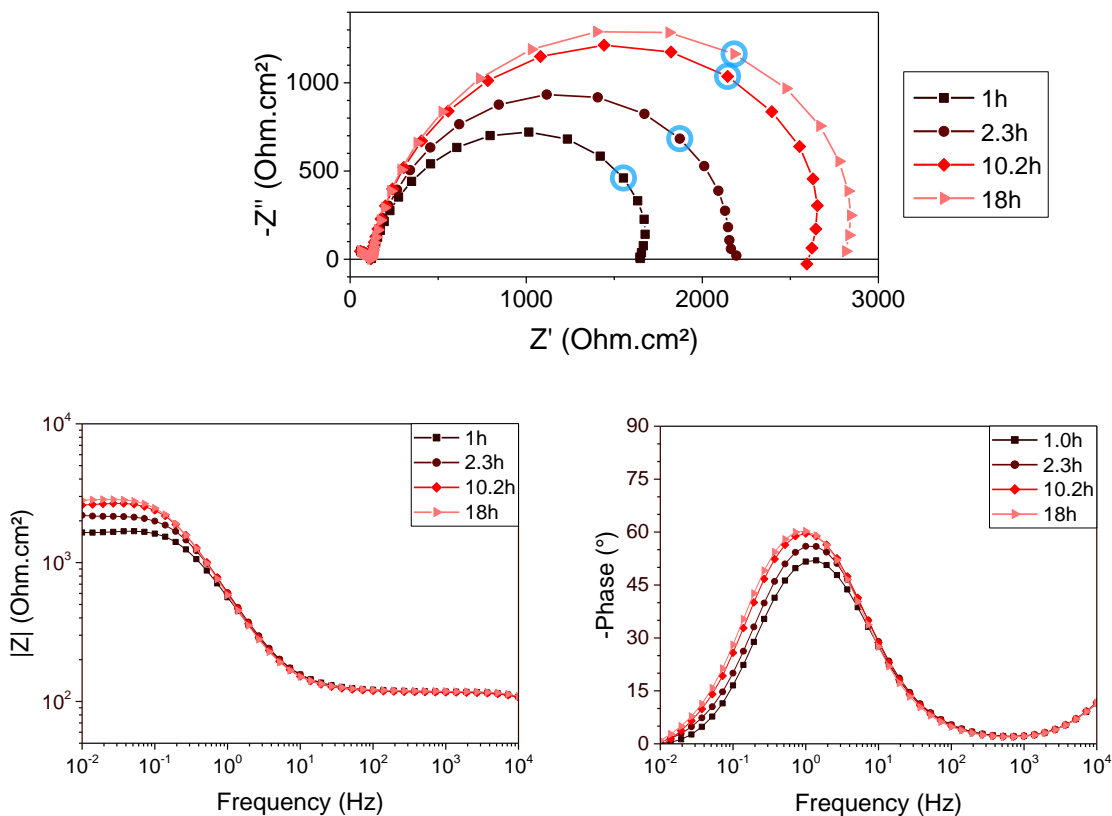


Figure IV. 16: Nyquist and Bode diagrams of a steel Qpanel immersed in an electrolyte containing 10 vol.% silica capsules suspension, measured using 8 pts/decade. Measurements taken at 0.1 Hz are circled

Observations of the substrate before and after immersion are shown in Figure IV. 17. After a gentle rinsing using deionized water, a sticky-looking layer remains on the steel's surface, whose color evidences corrosion products mixed with silica. The NCs are likely incorporated within the corrosion products and confer somehow protection. From the previous results, this layer has likely been formed during the first 5 to 6h of immersion. Since the substrate is vertically placed, this layer is not due to sedimenting of the suspension but to the mentioned interactions. Interestingly, this layer crackled upon drying and scaled off, as seen in picture c, what allowed to see that the substrate beneath this layer is barely damaged.

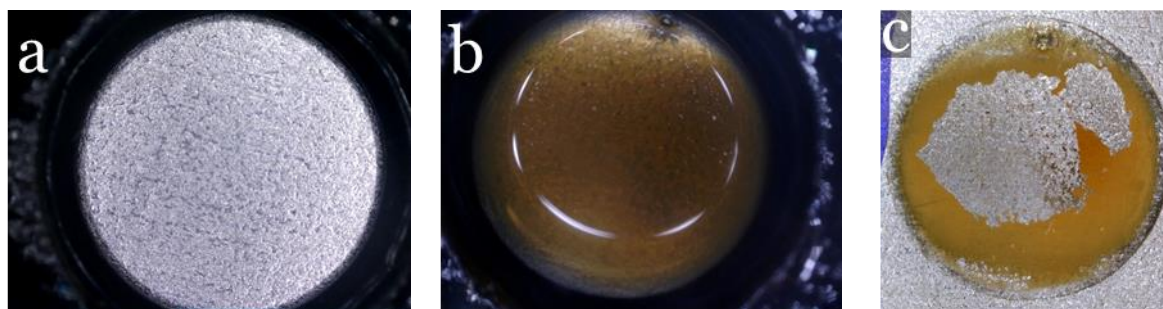


Figure IV. 17: Observations of a steel Qpanel (a) before, (b) after immersion in an electrolyte containing silica nanocontainers, and (c) after drying

As seen in II.2.2.4., in a 50 mM neutral electrolyte, the zeta potential of the capsules is barely affected and remains around -20 mV. Therefore, aggregation is limited and the suspension is stable. The formation of this layer is hence only due to electrostatic forces and to the affinity of silica with the metallic cations.

Concerning our application, these interactions are not likely to exist in the polymer. Upon defect, however, if capsules come loose, they could be attracted by the metal's surface and potentially deliver their payload there. This should be kept in mind for detection purposes since the identified sensor's fluorescence is triggered by complexation with iron (III) ions⁴¹.

IV.3.2. Effect on the corrosion behavior of AA2024-T3

The same protocol has been set up for the study with the AA, except that we studied the silica suspension (Si) as well as the MBT-loaded silica NCs suspension (Si(MBT)). We then proceeded the same way, monitoring the system's OCP for 20h as shown in Figure IV. 18. The alloy's OCP in NaCl 0.05M is assumed to be constant around -500 mV vs Ag/AgCl during this period. As one can see, when the electrolyte contains the Si suspension, an important drop from -500 to -850 mV vs Ag/AgCl occurs during the first hour of immersion, followed by an increase up to -550 mV after 7h roughly. This drop could be due to preferential adsorption of the silica particles on the intermetallics supporting the cathodic activity. This leads to a strong cathodic shift of the potential. The subsequent increase is then to be linked with the increasing coverage of the metal's surface.

This drop could be due to the preferential adsorption of silica particles on the native passive film formed on AA2024. This is supported by the electrical negative charge of the silica particles, while the point of zero charge of alumina is around 9⁴². Therefore, the film is positively charged in the electrolyte (pH 5.5). The partial and localized coverage of the surface by the silica capsules may favor the adsorption of chlorides on the unprotected part, what seems to increase the localized degradation of the passive film at the beginning of the immersion. After an hour of immersion, a progressive ennoblement of the OCP is observed, due to the formation of a more protective film probably composed of a mixture of silica and alumina. A second drop is then observed before the OCP increases again. This drop observed after 7h of immersion suggests a rupture of the protective film probably due to the adsorption of chloride anions or to the presence of internal stresses⁴³. A

competition occurs between the destruction of the protective film and its formation, that finally leads to the reinforcement of the protective film after 12h of immersion. It seems that the incorporation of silica particles on the aluminum-based passive film thoroughly changed the aluminum reactivity in this saline solution.

With the Si(MBT) suspension, the system behaves differently: the OCP first slightly decreases and stabilizes at around -600 mV vs Ag/AgCl. This shape is comparable with the one we previously obtained with MBT or $\text{Ce}(\text{dbp})_3$ dissolved in the electrolyte solution. Therefore, it seems that the MBT is able to counterbalance the drawbacks due to the adsorption and incorporation of silica into the aluminum-based passive film.

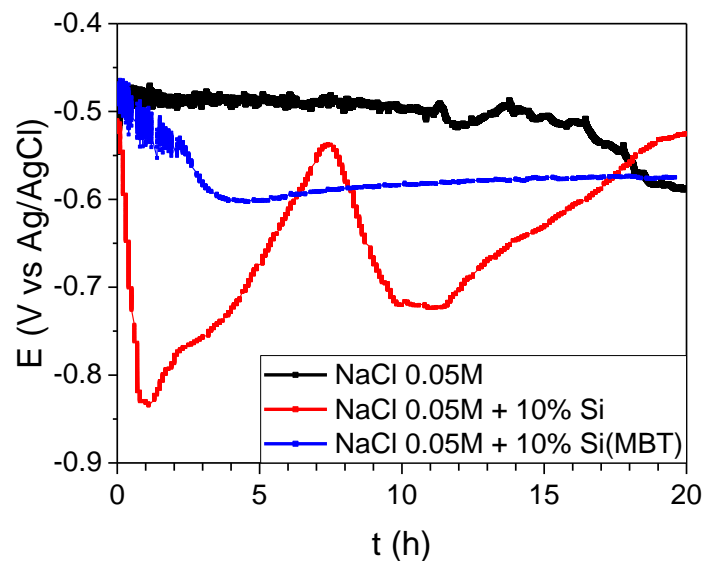


Figure IV. 18: Evolution of AA2024-T3's OCP in presence of 10 vol.% of "empty" (Si) or MBT-loaded (Si(MBT)) silica nanocontainers dispersion

The same behaviors are seen by EIS. The impedance plots are presented in Figure IV. 19. The formation of a silica-based layer is assessed for the Si suspension by the changes in the system's total impedance that first increases for up to 7h where it reaches its higher value. It then decreases before increasing again. This is in good agreement with the OCP evolution and the formation of a silica layer on top of the electrode that interacts with the reactivity of the aluminum alloy. When MBT is present in the solution, it dominates the system's evolution: as for experiments carried out in section IV.2.2.1., a large capacitive loop is observed in the first stages of immersion. This is associated with a high modulus at low frequencies around 10^5 ohm.cm^2 at 0.01 Hz. This is more than one order of magnitude higher than the values obtained in the absence of MBT in the suspension. This total impedance then continuously decreases over immersion.

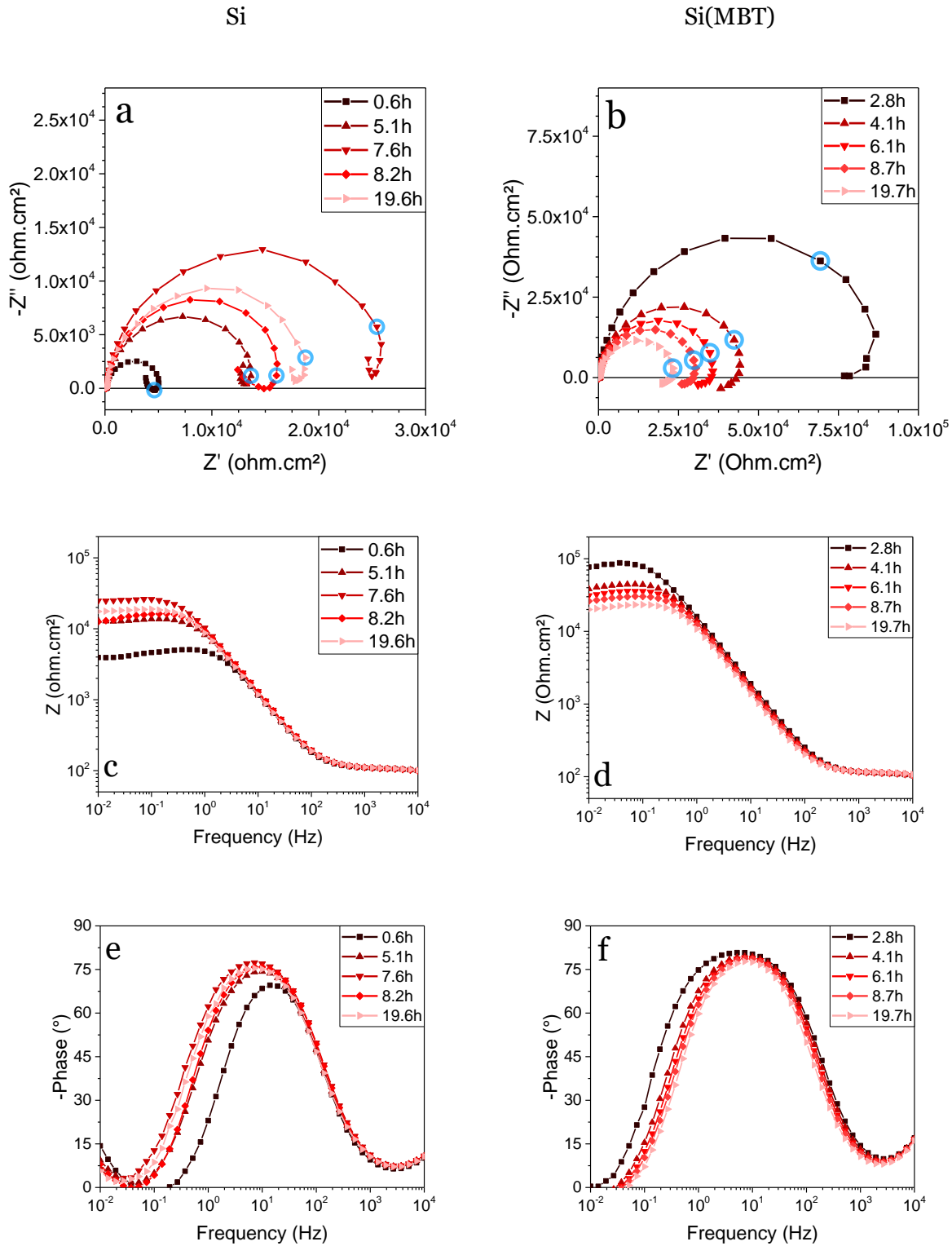


Figure IV. 19: (a,b) Nyquist and (c,d,e,f) Bode diagrams of AA2024-T3 immersed in 0.05M NaCl with 10 vol.% of (a,c,e) Si or (b,d,f) Si(MBT); Spectra acquired with 8pts/decade. Measurements taken at 0.1 Hz are circled

As for the experiments conducted with steel, a sticky layer is formed on the metal's surface. This white layer, once dried, crackles the same way and was analyzed by SEM-EDS in order to determine its composition. Figure IV. 20.a. shows a representative area of the layer formed with visible scales formed by the cracks. Elemental EDX mapping confirmed that this layer is mainly composed of

silicon oxide. Similar results have been obtained whether MBT was present or not. More importantly, Figure IV. 20.b. shows a part of the layer formed by the Si(MBT) suspension where a scale fell down upon drying. SEM observations underline the fact that the film formed during the immersion is thicker than the passive film normally formed on AA2024 in saline solution. Elemental analysis highlights the presence of sulfur on the AA's surface beneath the silica layer. Sulphur being likely due to the adsorption of inhibitor, it confirms that MBT quickly adsorbs on the AA's surface, before the silica layer is formed.

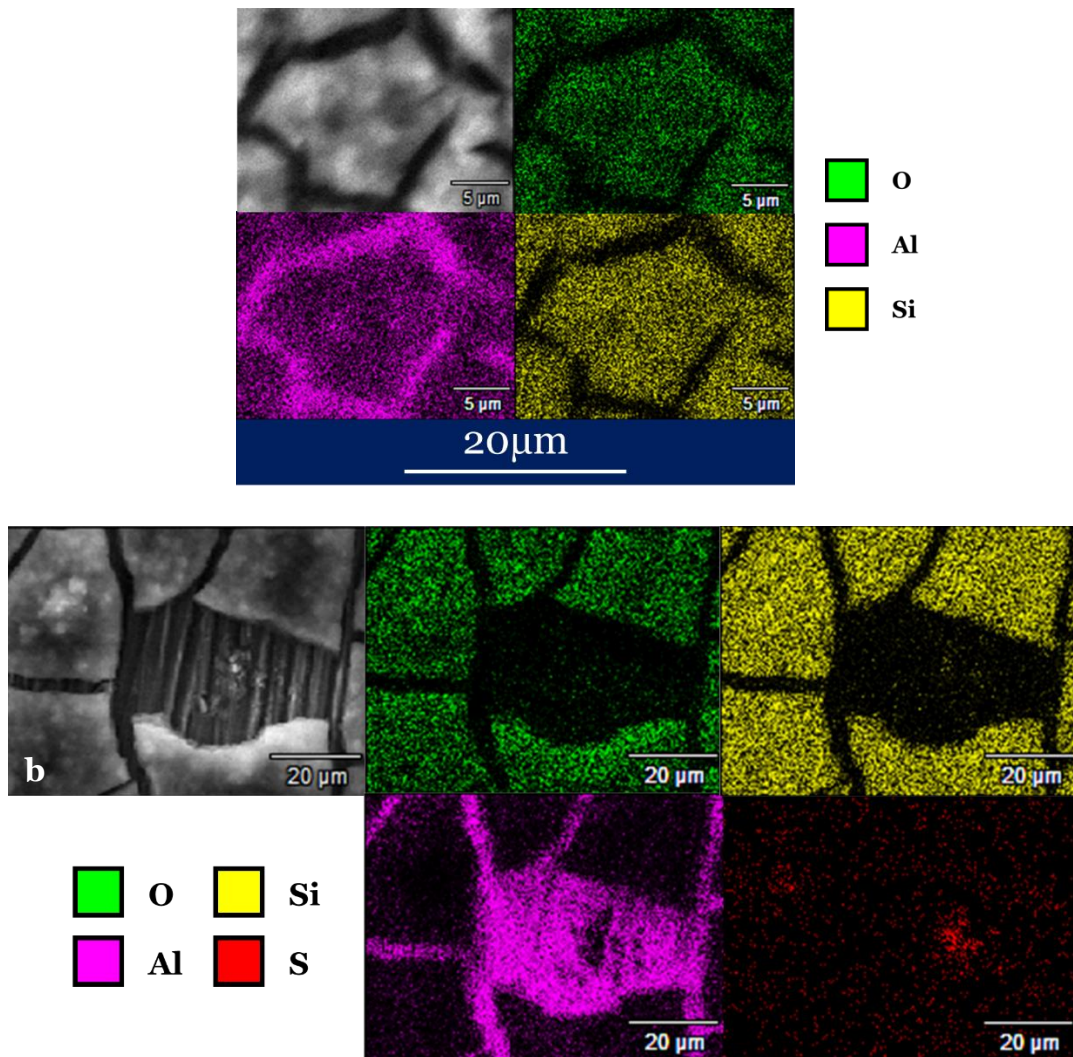


Figure IV. 20: EDS analysis of the silica layer deposited on AA2024-T3 after 24h immersion in 0.05M NaCl + 10 vol.% of Si(MBT) suspension

It has to be noticed that these results were obtained for 10 vol.% suspension added to a 0.05M NaCl solution, what involves changes in the suspension's ZP although the suspension's stability was demonstrated in these conditions. However, the formation of a silica layer was also reported when the Si NCs suspension is diluted in pure water. This layer however looked less opaque and thick, meaning that chlorides probably play a role in the layer formation. This was not further investigated.

Chapter IV - Corrosion protection and performances of capsules-loaded polyurethane coatings

As for steel, the silica nanocontainers have an affinity for AA2024-T3 that could be beneficial in case of loose Si NCs when the coating is damaged, and should be kept in mind for corrosion detection. Moreover, the clear difference between the behaviors of the silica and MBT-loaded silica containers highlights the effect of the free inhibitor. The not-encapsulated part of MBT could interact with the metal's surface, and can therefore interfere with the polymer during the formulation step.

IV.4. Inhibition properties of the coatings

The results of this section have been carried out employing a Gamry® paint test cell PTC1.

In this section, the efficiency of the MBT that is released will be discussed. As we evidenced, MBT has an inhibiting effect at low concentration (25 ppm). The thickness of bar-coated steel substrates is *ca.* 20 μm while the thickness of sprayed AA is *ca.* 80 μm . The exposed area is 15.5 cm^2 in both cases. According to the estimation presented in section III.3.1., the maximum amount of MBT in the immersed volume is hence at most $1.38 \cdot 10^{-3} \times 15.5 \times 20 = 0.43$ mg for bar-coated systems and 1.7 mg for sprayed samples. Locally, the MBT concentration is therefore above the solubility limit we saw in pure neutral water, what should enable protection of the substrate by MBT.

IV.4.1. On steel

IV.4.1.1. Intact coatings

i. Performances

Electrochemical impedance spectroscopy has been performed over 60h of immersion in order to assess the impact of the incorporation of silica capsules in the polyurethane coating. Three systems have been compared: neat polyurethane (PU), PU with Si NCs incorporated (PU-Si) and PU with MBT-loaded Si NCs incorporated (PU-Si(MBT)). Nyquist diagrams obtained for these three systems are presented in Figure IV. 21. At first glance, the Nyquist diagram of the PU system shows a single capacitive loop of around $2 \cdot 10^8$ $\text{ohm} \cdot \text{cm}^2$. The slight fluctuations of the spectra with time can be related with the temperature that is not controlled and/or the swelling of the coating. For the coatings containing NCs, the Nyquist plots show a capacitive loop, with a second phenomenon at low frequencies for PU-Si and, to a lower degree, for PU-Si(MBT). This second phenomenon could be related to a diffusional process. Impedance values decrease with time for both NC-loaded coatings. It can be seen that impedance values of the PU coating are more than 100 times higher than those of the coatings loaded with Si NCs, what may mean that the incorporation of NCs leads to the formation of porous coatings, because the interface between the NCs and the polymer matrix is not optimal.

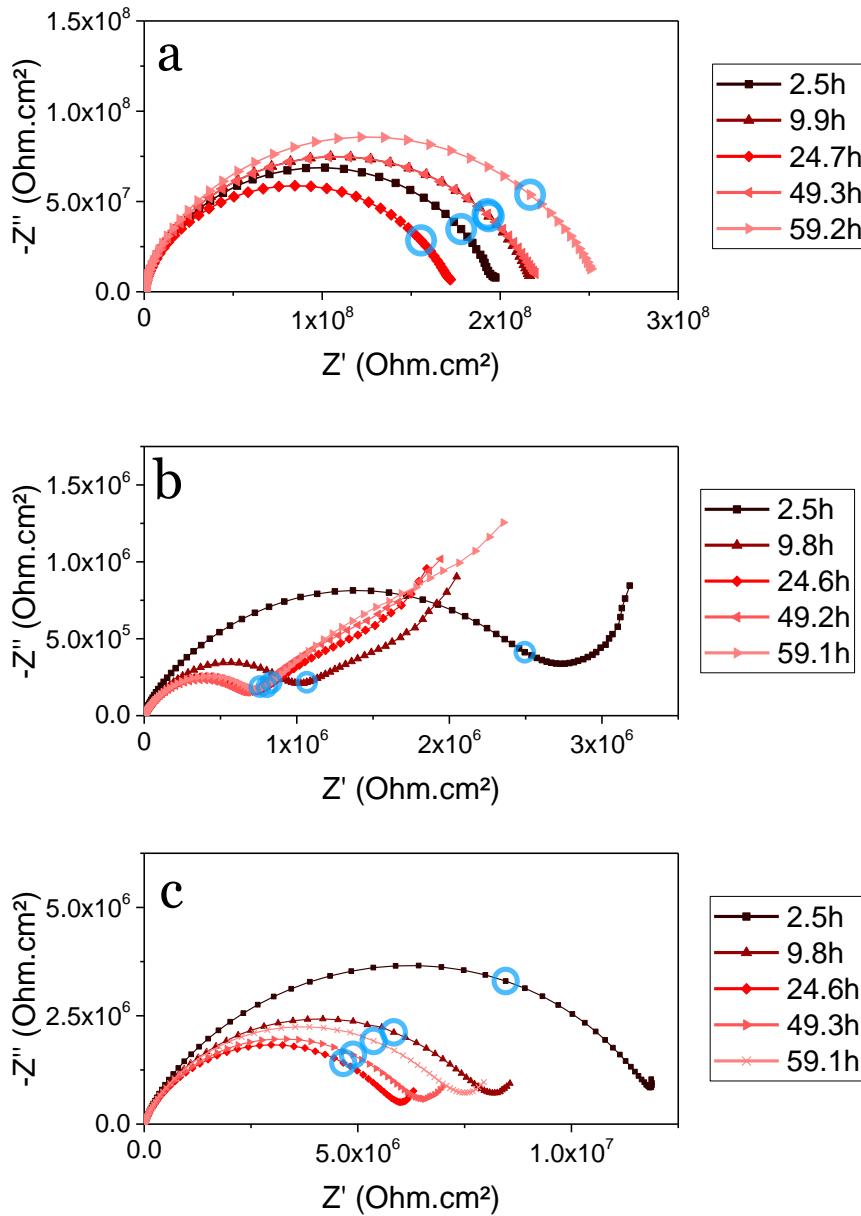


Figure IV. 21: Nyquist diagrams of steel Qpanels coated with (a) PU, (b) PU-Si and (c) PU-Si(MBT) systems. 12 pts/decade have been recorded, the circled values are taken at (a) 0.1 Hz and (b,c), 1 Hz

Concerning the Bode diagrams shown in Figure IV. 22, the PU coating presents impedance modulus values around 2.10^8 ohm.cm² and relatively constant for 60h. An apparent one time-constant behavior can be observed but two time-constants were needed to fit properly the impedance spectra of the PU coating onto steel. These two time-constants can be attributed to the PU coating (R_{coat} , C_{coat}) in the high frequency (HF) domain and to the charge transfer (R_{ct}) in parallel to the double layer (C_{dl}) in the lower frequency (LF) domain (Model a, Figure IV. 23).

The PU-Si coating shows much lower low-frequency modulus values (3 to 2.10^6 ohm.cm²) and several time-constants, with especially a well-defined diffusion time-constant in the LF domain. It confirms that the incorporation of the silica NCs leads to a drastic decrease of the PU coating's barrier properties. Despite the apparent homogeneity of the coating, this highlights preferential water ingress paths created by the incorporation of the nanocontainers. Another assumption that

was not investigated during this study could be associated to the formation of defects of crosslinking, caused by the capsules surface's silanol groups that could interact with the PU network formation. Moreover, corrosion spots were visually observed beneath the PU-Si coating after 60h of immersion. EIS spectra were first fitted using model b from Figure IV. 23, accounting for the PU-Si coating (R_{coat} , C_{coat}), the faradic impedance and double layer capacitance (R_{ct} , C_{dl}) and diffusion. Then, after 5h, another time-constant was seen so the model c (Figure IV. 23) was considered in order to take into account corrosion products (C_{ox} , R_{ox}) formed onto the steel substrate.

For the PU-Si(MBT) coating, the low frequency impedance modulus evolves from 10^7 to 5.10^6 ohm.cm² during immersion. These values are lower than those observed with the PU coating but are higher than that of the PU-Si coating. Moreover, no clear diffusion process can be detected. The spectra present an apparent one time-constant behavior but like for the PU coating, two time-constants were needed to fit the EIS curves (model b, Figure IV. 23).

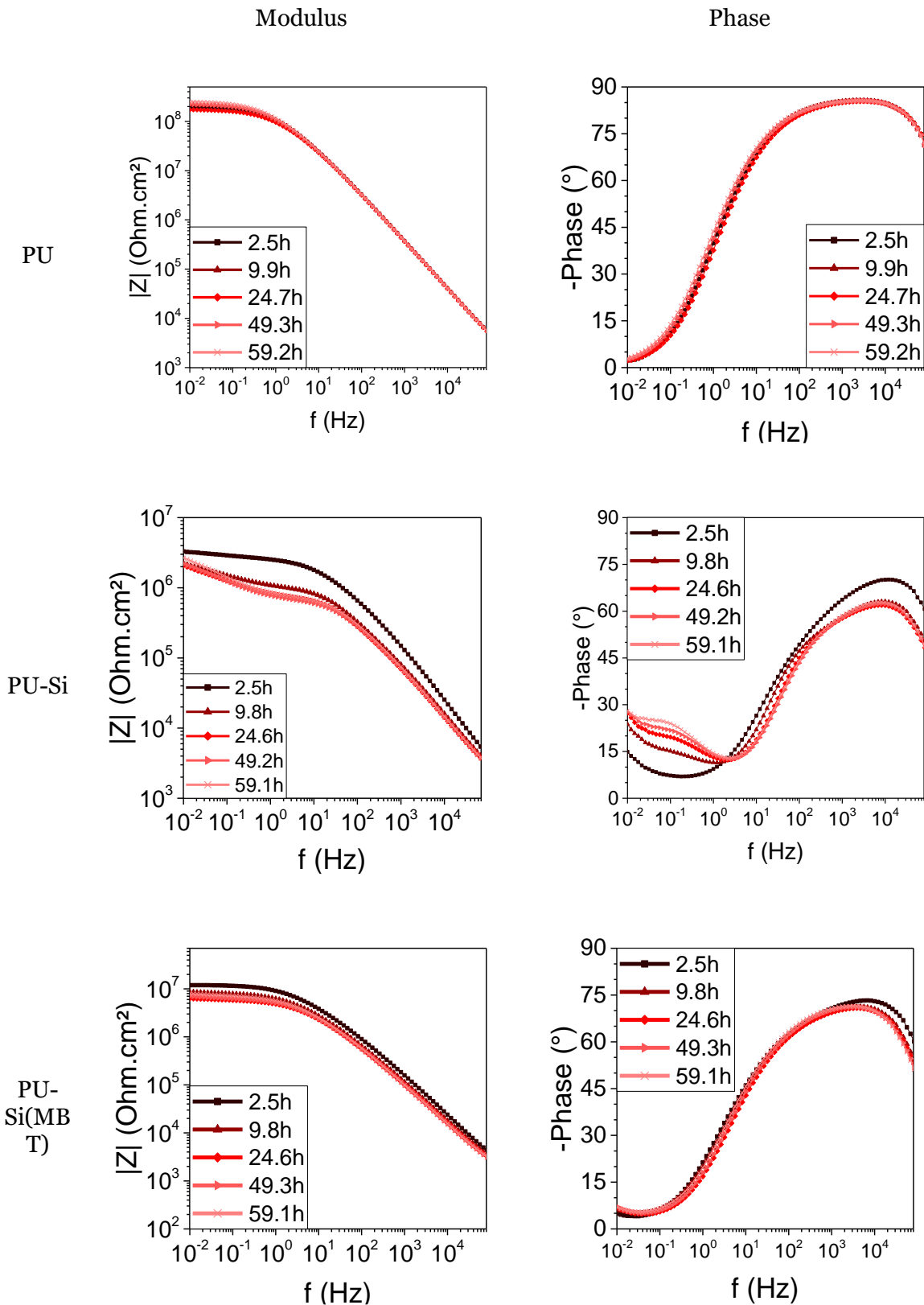


Figure IV. 22: Bode diagrams obtained for steel Qpanels coated with (a) PU, (b) PU-Si and (c) PU-Si(MBT) systems

The different equivalent circuits (EECs) are presented in Figure IV. 23. Capacitors were replaced by Constant Phase Elements (CPE) because of the inhomogeneous physical properties of the coatings.

These models allowed to extract fitted parameters, especially the coating's resistance R_{coat} and the charge transfer resistance R_{ct} .

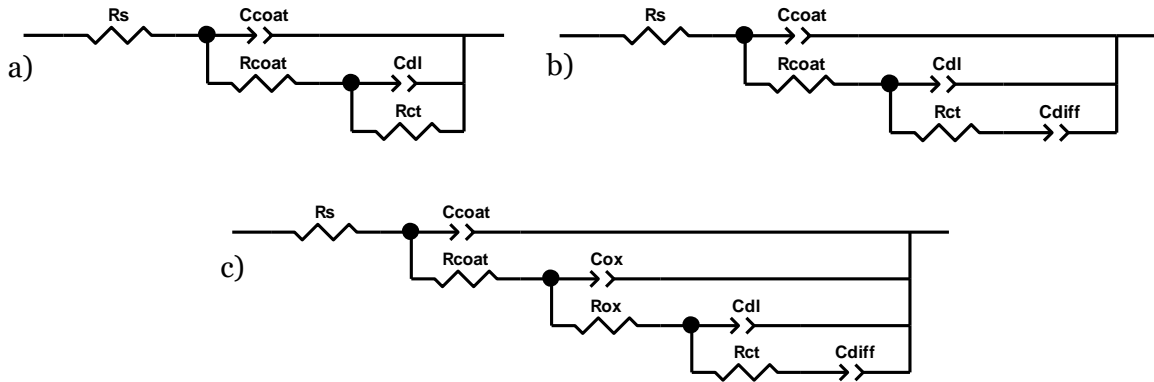


Figure IV. 23: Equivalent circuits used for the impedance plots of coated substrates with (a) 2 time constants (b) 2 time constants and diffusion (c) 3 time constants and diffusion

From the spectra fitting, the coating's resistance R_{coat} and charge transfer resistance R_{ct} have been plotted versus the immersion time in Figure IV. 24. R_{coat} is associated with the resistivity of the solution that fills the coating's porosity. It is therefore not surprising to find lower R_{coat} values for the PU-Si(MBT) than for the PU-Si coating, since MBT can be hydrolyzed when water penetrates ($pK_a = 6.95^{44}$). The most interesting result is the 10 times higher R_{ct} values for the PU-Si(MBT) than for the PU-Si coating. This can be related to the very local release of MBT and to the inhibition effect of MBT onto the steel's surface⁴⁵.

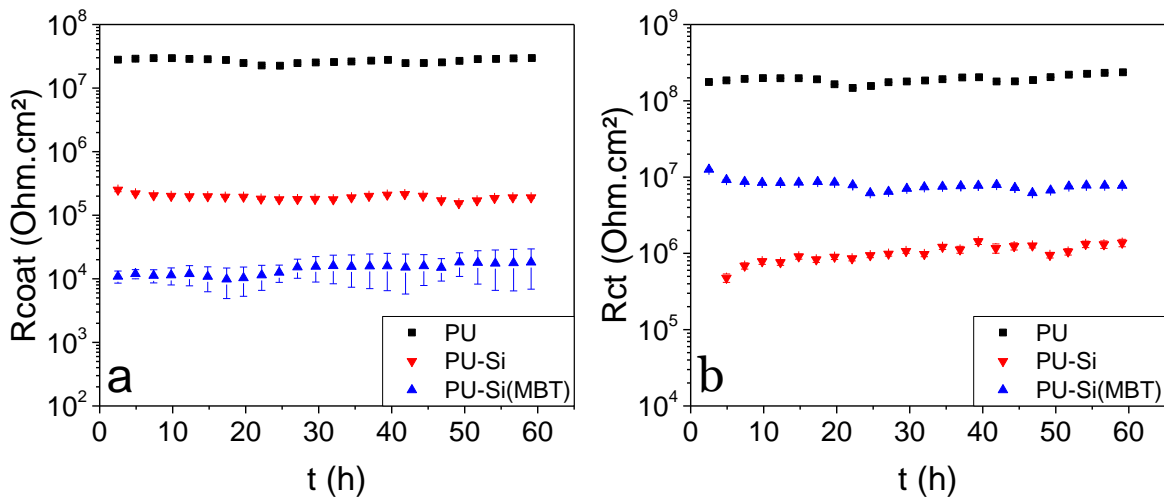


Figure IV. 24: Evolution of (a) the coating's resistance and (b) the charge transfer resistance for PU, PU-Si and PU-Si(MBT) systems, calculated from the adequate electrical equivalent circuits

ii. Water uptake assessment

The decrease in the PU coating's barrier properties upon addition of Si NCs could be due to an increase in the coating's porosity that could enable a higher and quicker water uptake from the polymer layer. The Brasher and Kingsbury equation has been applied to our systems in order to

compare their evolution. Since not all requirements are fulfilled to use this formula in the proper conditions, the absolute calculated value cannot be relevant and has to be handled carefully. Calculated water uptake (in volumetric percent) is plotted in Figure IV. 25 as a function of $\tau = \sqrt{t}/d$, with t the immersion time and d the coating's thickness. Using τ instead of the immersion time allows taking into account the thickness of the coatings that are $14.8 \pm 2.7 \mu\text{m}$, $16.1 \pm 1.3 \mu\text{m}$ and $15.4 \pm 1.6 \mu\text{m}$ for PU, PU-Si and PU-Si(MBT) coatings respectively. We can assume that in the first stages of water ingress, the PU coating respects Brasher and Kingsbury's conditions and so a rapid water uptake is seen, followed by a plateau around 7.5 vol%. This is compatible with a water uptake of 9.4% reported by Rezaei *et al.*⁴⁶ for 250 μm -thick PU coatings. On the other hand, the PU-Si and PU-Si(MBT) systems have a similar behavior, with a comparable "apparent" water uptake two times as high as the neat PU coating's one. This confirms the probable increased porosity due to the addition of the nanocontainers.

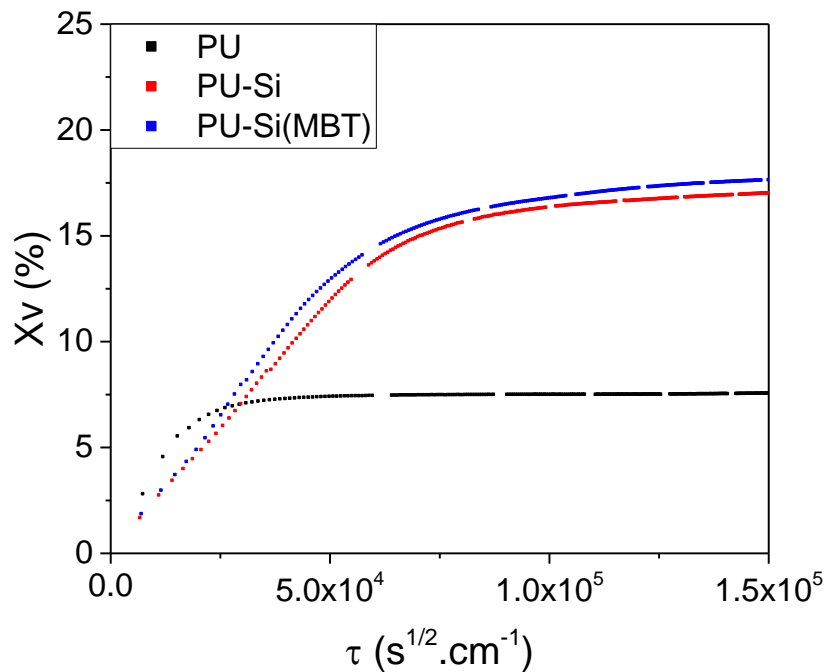


Figure IV. 25: Apparent water uptake of unloaded and Si NCs-loaded PU coatings applied by bar coating on top of steel Qpanels

This detrimental effect of the incorporation of Si NCs explains why such low resistances were observed for loaded coatings. Since the water uptake occurs at once as soon as the coating is soaked, the porosity cannot be due to the dissolution of silica containers we observed for alkaline media and duration longer than 24h. The preferential ionic paths formed by the silica nanocapsules are then due to the creation of heterogeneity at the PU / Si interface either because chemicals nature are not compatible or because of undetected aggregates.

IV.4.1.2. Artificially damaged coatings

It has been evidenced that the Si NCs can deliver their payload in an alkaline environment in chapter II. Moreover, we underlined in the previous section that PU-Si(MBT) coatings allow an increase of the system's R_{ct} that could be due to an inhibition effect. It hence seems interesting to study the coating's behavior in presence of an artificial defect.

It is possible that MBT cannot diffuse in the PU network, what could explain the absence of protection. An optical monitoring of the three previous systems was performed on samples with an artificial defect. The same scratch parameters have been used to create the defects but different defect lengths were finally obtained, because the tip did not reach the substrate's surface all over the scratch. However, the scratch width was about 200 μm for all 16 μm thick coatings. As one can see for each system on Figure IV. 26, the coating is severely damaged around the scratch, whether silica containers have been added to the PU or not. This affected region tends to show that the coating's cohesion is quite poor since a superficial part of the PU is torn off, while the surface is still covered. The addition of the silica capsules suspension to the polymeric matrix hence did not lead to a significant lack of adhesion of the coating. Reflection was enough to assume that the metal substrate was reached, although remains of the scratched coating were still present in some areas of the defect. Even if the exposed area is not exactly the same, the aim of this part is to qualitatively assess MBT-linked inhibition.

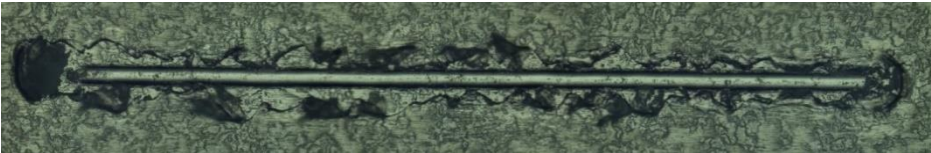
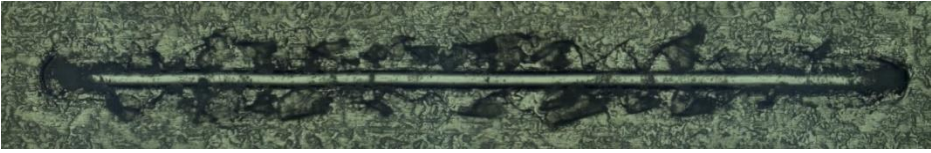

Sample name	Added suspension	Observation
PU	-	
PU-Si	Empty silica capsules	
PU-Si(MBT)	MBT-loaded silica capsules	

Figure IV. 26: Artificial defects made in PU coatings before opto-EIS measurements

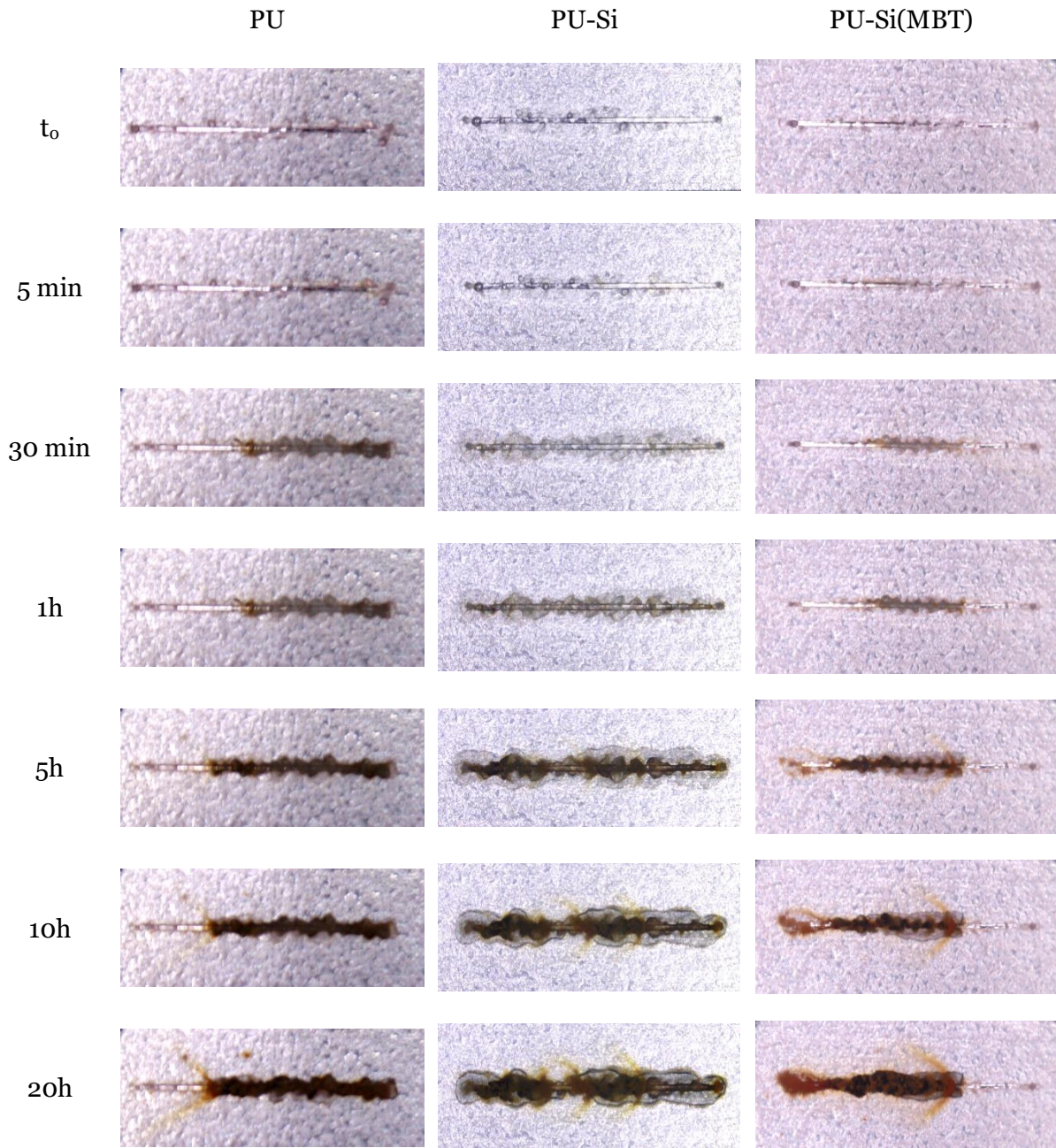


Figure IV. 27: Observation of the exposed area during EIS analysis

During immersion, the open circuit potential is monitored between two impedance spectroscopy measurements. No difference in the evolution of the OCP was seen between the different samples. From this data, the action of the MBT cannot be detected as it could be expected if MBT was released from the coating and directly adsorbed on the metal's surface.

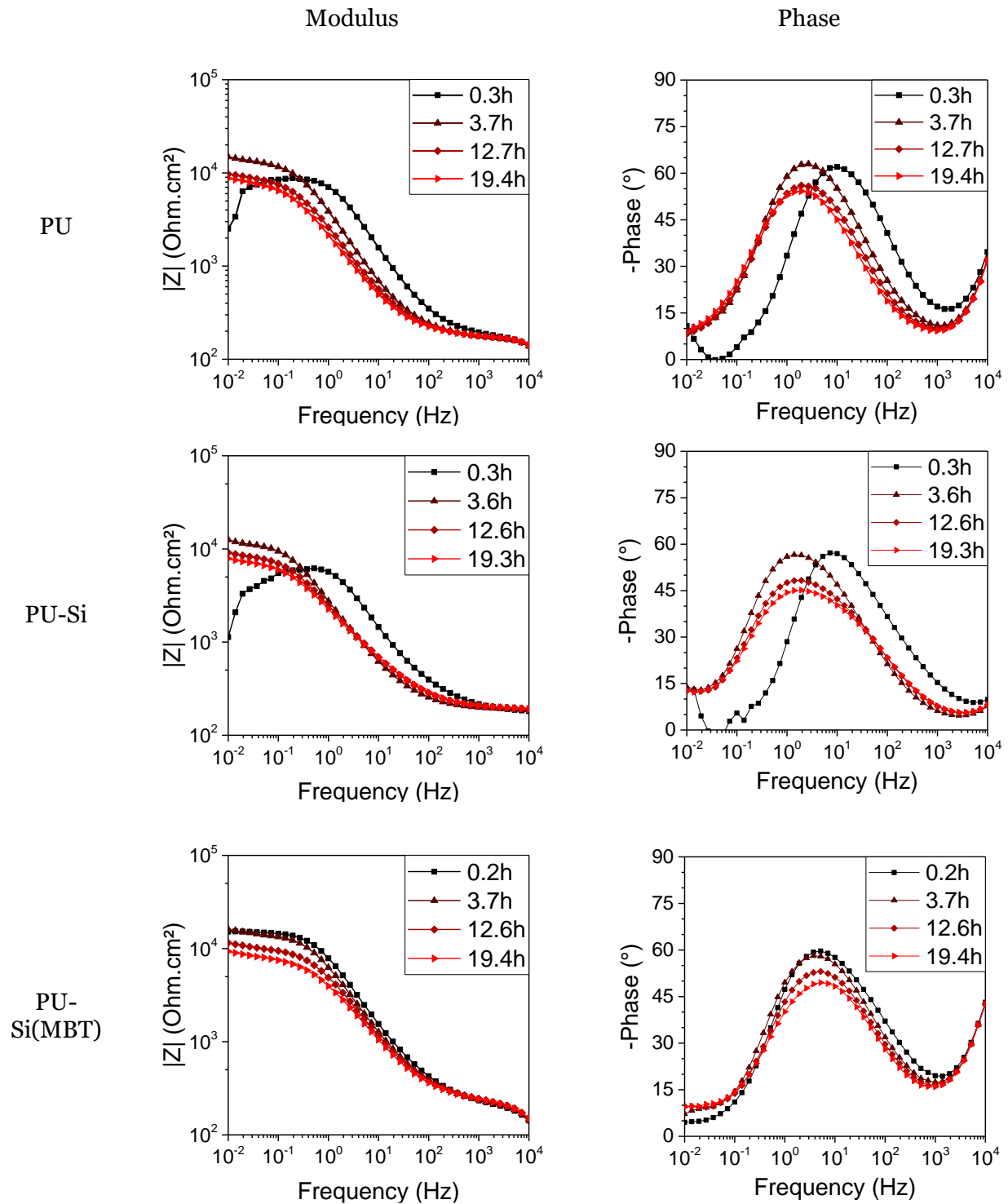


Figure IV. 28: EIS results from opto-EIS analysis for PU coatings

From the results presented in Figure IV. 28 and Figure IV. 27, the exposed area was corroded soon after immersion for all the coatings and no differences were observed in the EIS spectra. This absence of protection and the apparent same corrosion rate for the three samples mean that the PU-Si(MBT) system is not efficient in these tested conditions. Raman analysis was performed after the EIS analysis on the PU-Si(MBT) coating in order to eventually detect traces of MBT in the corrosion product but it was not successful.

This could be because a higher concentration of MBT is needed in order to form a film¹⁴ or because the encapsulated MBT was not able to reach the substrate's surface, either because it remained trapped in the Si NCs and/or PU coating, or because of the too important volume of the cell.

IV.4.2. On AA2024-T3

IV.4.2.1. Reference polyurethane coating (PU)

Impedance results for an $82.1 \pm 2.8 \mu\text{m}$ sprayed PU coating are given in Figure IV. 29 as a reference measurement. As soon as 2.6h after the immersion started, the system does not behave as a pure capacitor, as seen on the modulus diagram showing a horizontal plateau at low frequencies instead of a -1 slope line. The total impedance value of the system is between $5 \cdot 10^7$ and 10^8 ohm.cm^2 . This is a few orders of magnitude lower than what we would expect for an 80 μm -thick PU coating⁴⁷. Another strange phenomenon is that over immersion the total impedance increases. This behavior, observed for the pure polymer, has been reported before for organic coating in immersion and could be due to further cross-linking, possibly due to reactions with oxygen in water⁴⁸. Chemical analysis was not further carried out.

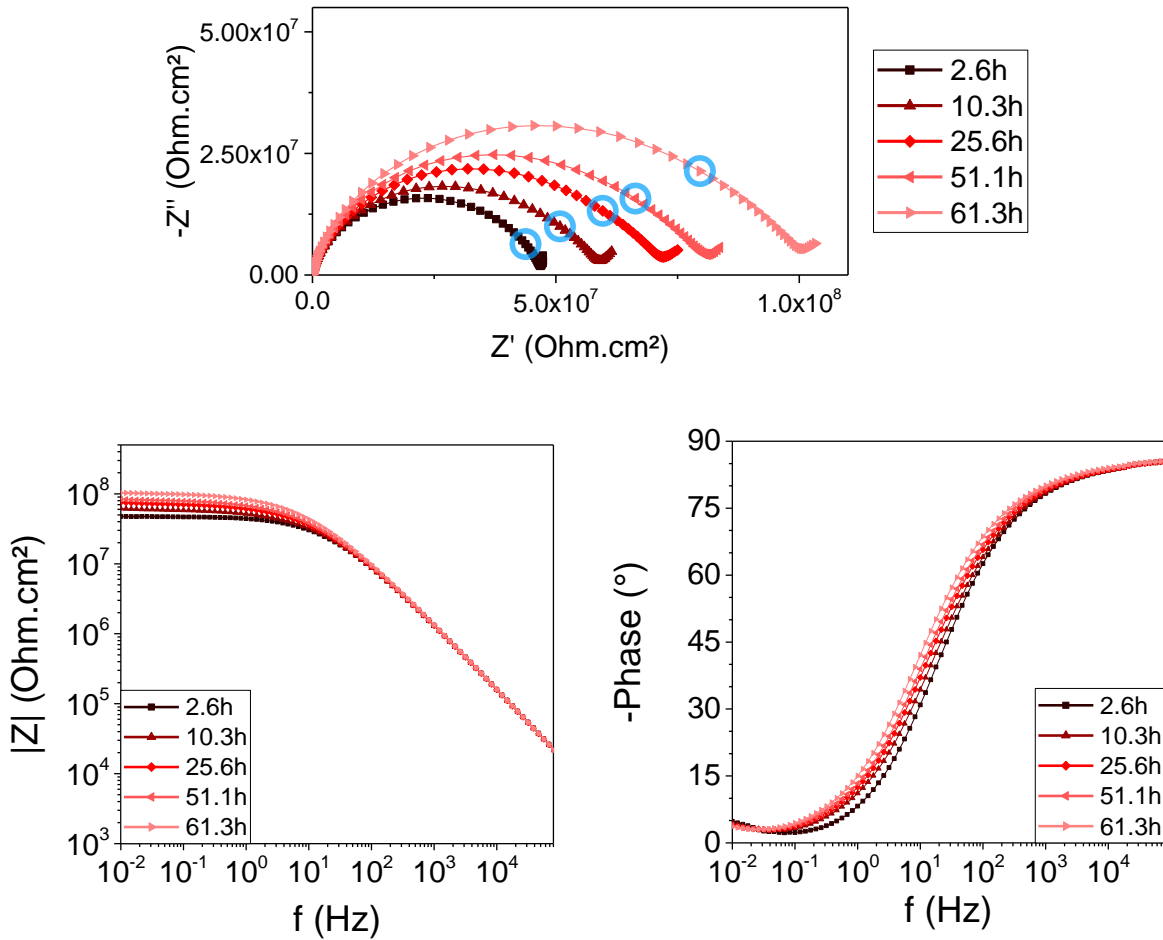


Figure IV. 29: Nyquist and Bode plots for sprayed PU coatings applied on top of AA2024-T3. Spectra have been obtained with 12 pts/decade. The circled value on the Nyquist plot is the 1 Hz measurement

IV.4.2.2. PU coating loaded with “empty” Si NCs (PU-Si)

The evolution of the impedance for a $72 \pm 5.6 \mu\text{m}$ -thick PU-Si coating is given in Figure IV. 30. The first measurement carried out after 2.5h immersion shows a different behavior than the pure polymer with a roughly 10 times lower total impedance. A depressed loop is observed for high and medium frequencies, containing two time constants as seen on the Bode diagram, while an apparent diffusion phenomenon occurs at low frequencies. The main loop can be attributed to both the coating’s response at high frequencies and local corrosion processes under the coating.

Unlike for neat PU, a clear decrease in the system’s impedance is then observed with increasing immersion time, associated with the appearance of two time constants at medium and high frequencies. The time constant observed between 10 and 100 Hz is due to corrosion occurring underneath the polymer layer. This was observed between 1 and 10 Hz for uncoated AA2024-T3 (see section IV.2.2).

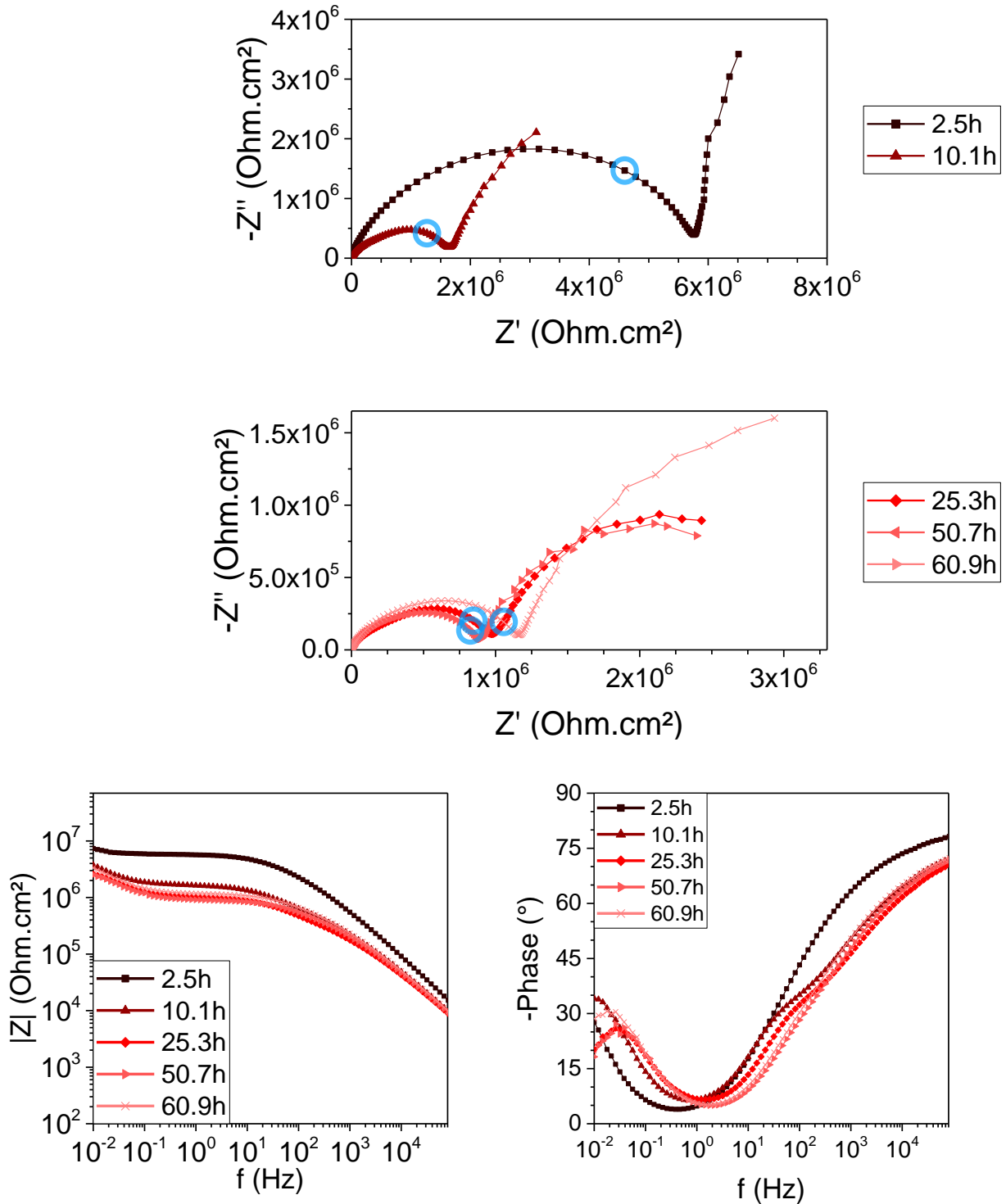


Figure IV. 30: Nyquist and Bode plots for sprayed PU coating loaded with silica nanocapsules, applied on top of AA2024-T3. Spectra have been obtained with 12 pts/decade. The circled value on the Nyquist plot is each time the 10 Hz measurement

The low initial impedance and its quick decrease highlight the negative effect of the incorporation of capsules into the polymer matrix. Clearly, even though the Si NCs are well dispersed, local defects or agglomerates are created, likely due to interfaces between the silica capsules and the surrounding matrix. These defects can be due to the chemical reaction between the capsules' surfaces, mainly through their silanol groups, and diisocyanate monomers as discussed in section III.2.2. This

reaction could then provoke a lack of diisocyanate and *in fine* a non-stoichiometric ratio between the formulation's base and hardener. Another possibility is however that the amount of capsules added is above the polymer's critical pigment volume concentration. Mirmohseni *et al.*⁴⁹ indeed showed an improvement in the barrier properties of a polyurethane matrix filled with up to 1% silica capsules. However, when more capsules were embedded into the coating, this led to the deterioration of the PU's barrier properties. Nonetheless, they used a bimodal dispersion of Si NCs with particles' size exceeding 1 μm , and added as a powder to the waterborne PU, what cannot be compared with our system.

IV.4.2.3. PU coating loaded with MBT-loaded Si NCs (PU-Si(MBT))

After having assessed the impact of the addition of silica containers on the matrix's barrier properties, the same experiments were performed with MBT-loaded Si NCs. The EIS results presented in Figure IV. 31 have been obtained for a $74.6 \pm 3.3 \mu\text{m}$ -thick coating. As one can see, the first measurement shows an impedance similar to that of the PU-Si system. The Nyquist plot allows to identify a depressed capacitive loop while a diffusion phenomenon is seen at low frequencies, as for PU-Si. However a major difference is seen when the inhibitor is present in the solution since no loss of properties is observed. On the contrary, an increase in the total impedance of the system is observed over immersion after 60h.

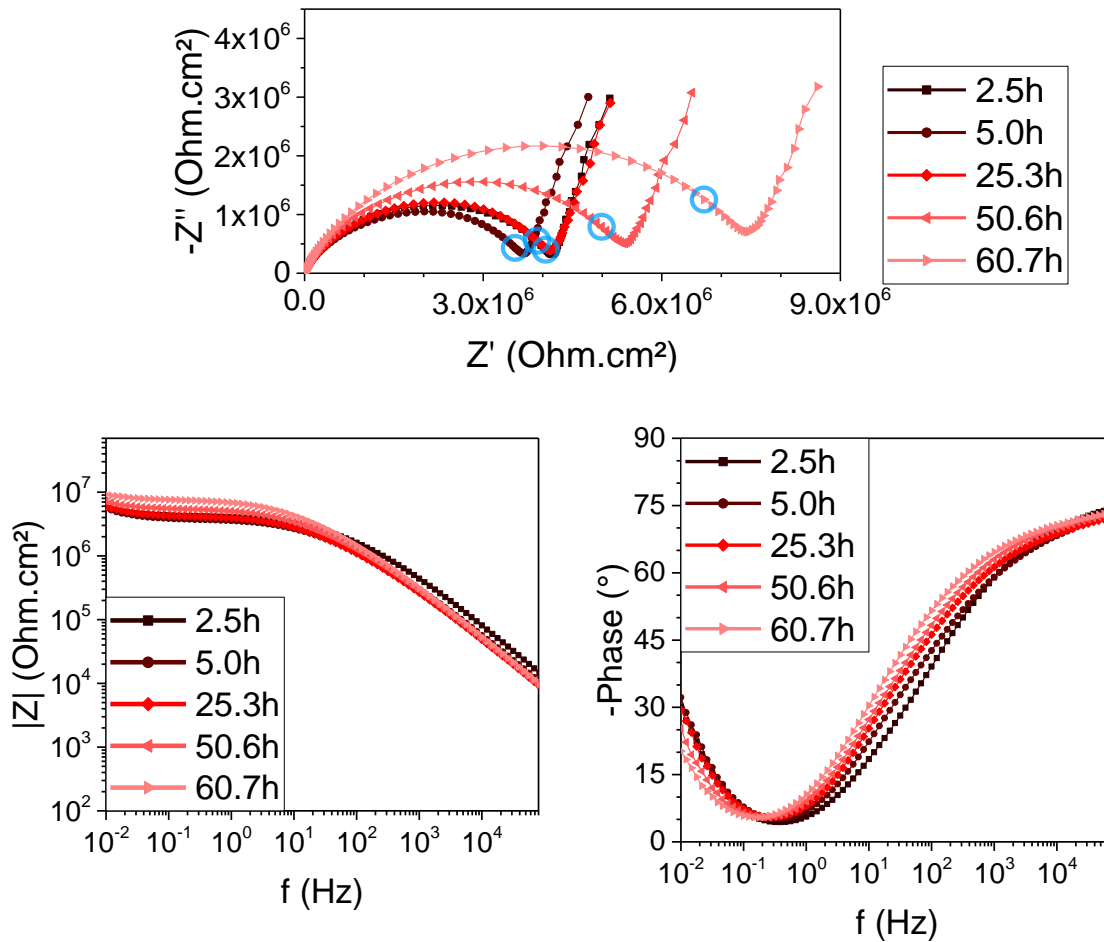


Figure IV. 31: Nyquist and Bode plots for sprayed PU coating loaded with Si(MBT) nanocapsules, applied on top of AA2024-T3. 12 pts/decade were taken. The circled value on the Nyquist plot is each time the 1 Hz measurement

These observations tend to show that MBT can be released from the system. However, this does not compensate for the deterioration engendered by the incorporation of capsules.

IV.4.2.4. Comparison of the performances of the three systems

i. Total resistance of the composite systems

In order to graphically compare the systems' evolution, the depressed semi-circle was fitted to extract the resistive behavior, plotted in Figure IV. 32. As one can see, the system's total resistance is almost divided by ten when the silica capsules are incorporated to the PU matrix. However, only small fluctuations are observed in the case when MBT is encapsulated in the nanocontainers over 60h immersion. On the other hand, a decrease in the coating's resistance clearly occurs in the absence of MBT during the first 30h.

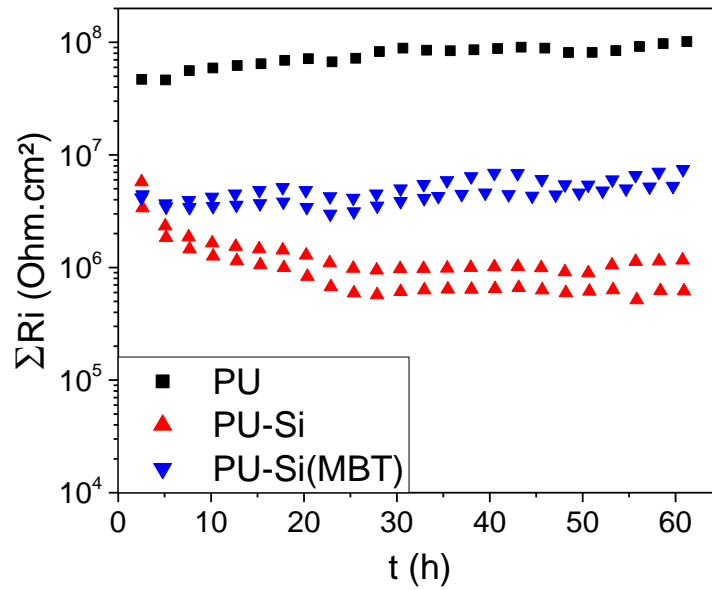


Figure IV. 32: Evolution of the low frequencies modulus for PU, PU-Si and PU-Si(MBT) coatings over immersion in 0.05M NaCl

ii. Attempt of water uptake monitoring

As for bar coated samples, an approximate water uptake has been calculated for sprayed PU systems using Brasher-Kingsbury equation, as plotted in Figure IV. 34. Despite not being performed in acceptable conditions to get a correct water uptake value, it allows to compare the coatings' behavior and corroborates the previous results: the loaded PU coatings show a very important increase in permittivity, which leads to apparent water uptake values above 25% while the pure PU system is around 13%. Interestingly, differences are also observed between the two coatings containing silica nanocontainers. When the MBT-loaded Si NCs suspension is added to the matrix, higher water uptakes are measured and could be due to free MBT molecules that also create preferential water ingress paths.

iii. Coating appearance and properties

After immersion, important differences were observed in the aspect of the samples. The PU samples after immersion did not show any delamination, blistering or corrosion, while both PU-Si and PU-Si(MBT) systems looked bubbly with important blistering, as shown in Figure IV. 33.a. Interestingly, this leads to a loss of adhesion of the PU coating and made possible the removal of the PU layer. Figure IV. 33.b. and c. are pictures of the AA's surface after immersion and removal of the coating. An important degradation and pits are observed on the whole substrate's surface for the PU coating after immersion, while nothing was noticeable after removal of the PU-Si(MBT) layer.

It has to be noticed that bar coated samples never show this kind of blistering, that is then probably dependent on the coating's thickness.

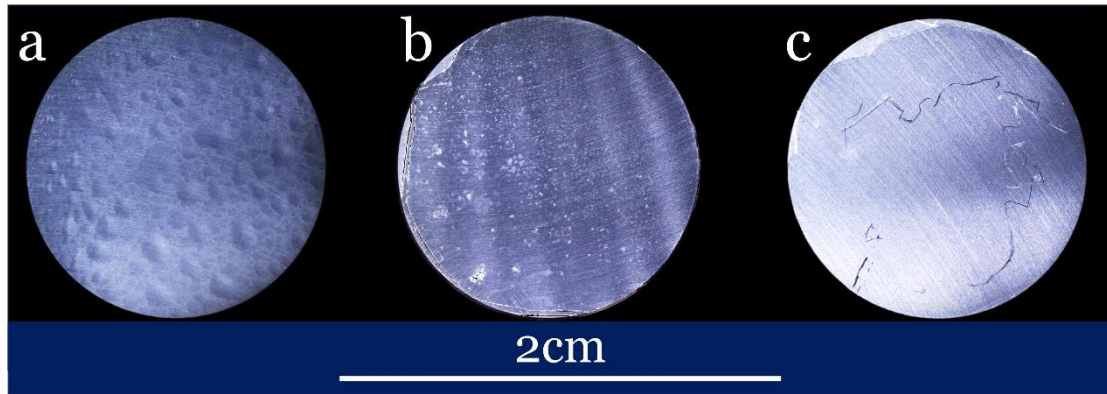


Figure IV. 33: Appearance of (a) Si NCs-loaded PU coating after immersion, and AA's surface after removal of the (b) PU-Si and (c) PU-Si(MBT) coating. Scratches in picture c were made during the coating removal. Contrasts have been enhanced in order to reveal defects

These observations are in good agreement with the EIS analyses: corrosion processes occurring led to the system's resistance decrease, and appearance of a clear time constant in the medium frequencies domain for the PU-Si system. The MBT inhibitor placed in the Si NCs suspension is able to reach the substrate's surface and protect it from corrosion.

As for 20 μm -thick bar-coated coatings on steel substrate, we tried to evaluate an approximate water uptake for sprayed PU systems using Brasher-Kingsbury equation. Results are plotted in Figure IV. 34. The loaded PU coatings show a very important apparent water uptake with values above 25% while the pure PU system one is around 13%. The absorption process is clearly not Fickian and the water uptake value seems not acceptable. Apparently, the Brasher and Kingsbury relation can not be used since some of the initial assumptions from their approach are not full-filled. This is another indication to say that the coating contains too many porosities to be considered as a barrier coating, or that swelling is an important factor that should be considered and measured.

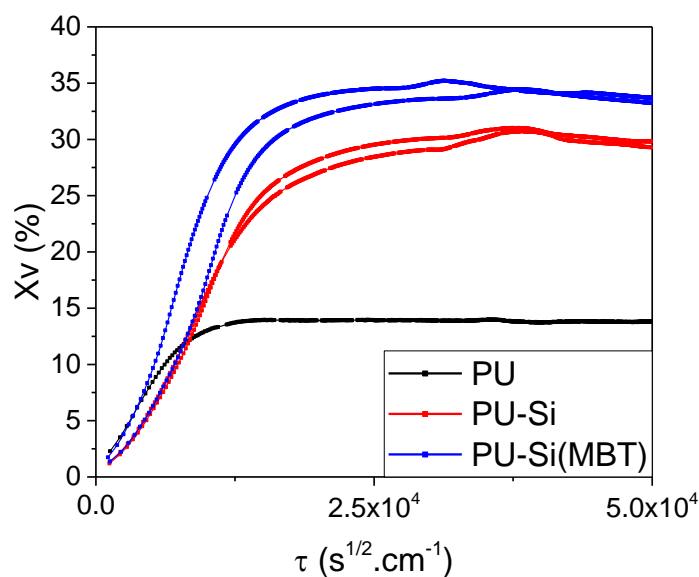


Figure IV. 34: Apparent water uptake calculated using Brasher-Kingsbury equation for PU, PU-Si and PU-Si(MBT) systems

iv. proposed mechanism

From the previous analyses and observations, a degradation mechanism has been proposed and is sketched in Figure IV. 35. Due to the PU coating's intrinsic properties, water quickly progresses through the organic layer.

Incorporation of the nanocontainers leads to the formation of defects that weaken the interface between the silica capsules and the polymer matrix (a & d). These defects constitute preferential pathways for the electrolyte that fasten the degradation of the coating and provoke the swelling of the polymer by increasing the amount of water that penetrates (b & e). This leads to further swelling, creating blisters and allowing the electrolyte to reach the substrate's surface. Corrosion then occurs in the absence of inhibitors (c) whilst when MBT is encapsulated it can be released and partially protect the aluminum alloy (f).

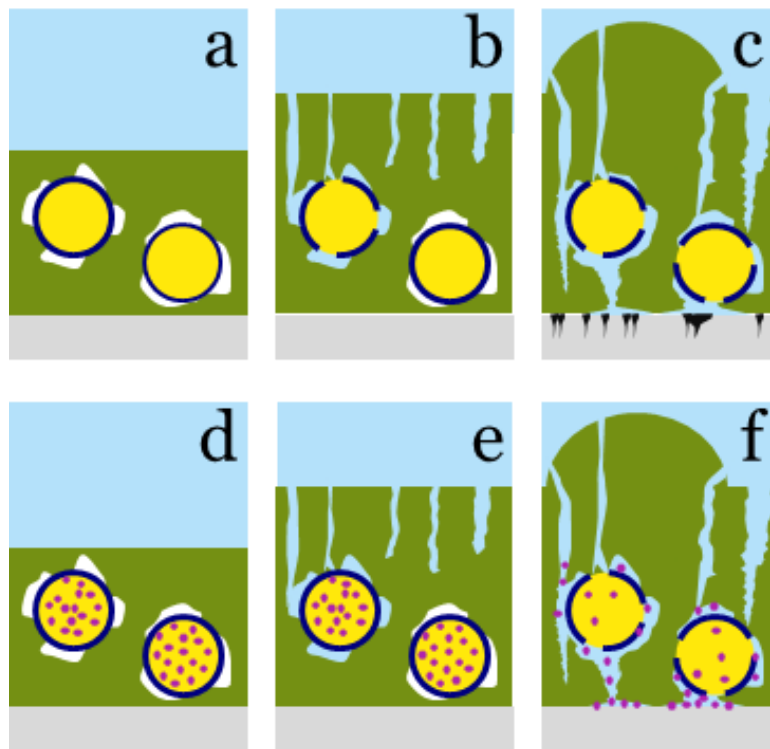


Figure IV. 35: Degradation mechanism of the (a,b,c) PU-Si and (d,e,f) PU-Si(MBT) developed coatings

Despite an ability to release the encapsulated MBT, the designed coating is therefore highly limited by its porosity and must be improved.

IV.5. Conclusion on the system's performances

We have seen in this section that the encapsulated inhibitor (2-mercaptobenzothiazole) is highly effective on AA2024-T3 in a 0.05M NaCl aqueous medium. However, it showed only a short-term effect and low protection when used on steel in the same conditions. Potential alternative inhibitors were then considered: sodium molybdate greatly improved mild steel's resistance in the first times of immersion, while cerium dibutylphosphate was very efficient on AA2024-T3 since no corrosion products were observed after 2 days of immersion.

The performances of the coatings were assessed by EIS, what highlighted a poor barrier property for the pure polyurethane coating, due to its experimental nature. The incorporation of empty silica nanocontainers within the polymer matrix moreover induced defects, what led to an even lower intrinsic resistance of the coating. This is likely due to either a chemical incompatibility between the silica capsules and the polyurethane matrix, to cross-linking defects induced by the addition of silica, or to an amount of Si NCs above the polymer's critical pigment volume concentration. However, the encapsulation of MBT in the silica nanocapsules has a positive effect. Indeed, the coating's barrier properties kept on decreasing upon immersion in the absence of MBT while a stable resistance of the system is observed when the inhibitor is in the coating. This was notably highlighted by the corrosion-free surface of the metallic substrate after immersion only for the MBT-loaded coating.

Despite an apparent smart release of the encapsulated inhibitor, the deterioration of the coating properties observed when the nanocontainers are incorporated makes the built system unusable as it is. Several paths of improvement should therefore be considered. Firstly, no attention was paid to the cross-linking of the polyurethane network. The addition of silica capsules, containing reactive groups such as silanol, likely implies changes in the polymeric network. The ratio between the base, hardener and suspension should therefore be optimized. It would however require to use a high-performance PU. In order to limit the defects created by the incorporation of capsules, the purification of the suspension should also be considered in order to get rid of non-encapsulated MBT and residual surfactants. Moreover, a study concerning the quantity of capsules (and inhibitor) added to the formulation (limited by the dilution induced) should be carried out.

References

1. Scholes, F. H. *et al.* Interaction of Ce(dbp)₃ with surface of aluminium alloy 2024-T3 using macroscopic models of intermetallic phases. *Corrosion Engineering, Science and Technology* **44**, 416–424 (2009).
2. Denissen, P. J. & Garcia, S. J. Cerium-loaded algae exoskeletons for active corrosion protection of coated AA2024-T3. *Corrosion Science* **128**, 164–175 (2017).
3. Brasher, D. M. & Kingsbury, A. H. Electrical measurements in the study of immersed paint coatings on metal. I. Comparison between capacitance and gravimetric methods of estimating water-uptake. *Journal of Applied Chemistry* **4**, 62–72 (1954).
4. Nguyen, V. N., Perrin, F. X. & Vernet, J. L. Water permeability of organic/inorganic hybrid coatings prepared by sol–gel method: a comparison between gravimetric and capacitance measurements and evaluation of non-Fickian sorption models. *Corrosion Science* **47**, 397–412 (2005).
5. Walter, G. W. The application of impedance methods to study the effects of water uptake and chloride ion concentration on the degradation of paint films—II. Free films and attached/free film comparisons. *Corrosion Science* **32**, 1085–1103 (1991).
6. Duval, S., Keddam, M., Sfaira, M., Srhiri, A. & Takenouti, H. Electrochemical Impedance Spectroscopy of Epoxy-Vinyl Coating in Aqueous Medium Analyzed by Dipolar Relaxation of Polymer. *Journal of The Electrochemical Society* **149**, B520 (2002).
7. Castela, A. S. & Simões, A. M. Water sorption in freestanding PVC films by capacitance measurements. *Progress in Organic Coatings* **46**, 130–134 (2003).
8. Nguyen Dang, D. *et al.* Effect of mechanical stresses on epoxy coating ageing approached by Electrochemical Impedance Spectroscopy measurements. *Electrochimica Acta* **124**, 80–89 (2014).
9. Deflorian, F., Fedrizzi, L., Rossi, S. & Bonora, P. L. Organic coating capacitance measurement by EIS: ideal and actual trends. *Electrochimica Acta* **44**, 4243–4249 (1999).
10. Rossi, S., Fedel, M., Petrolli, S. & Deflorian, F. Accelerated weathering and chemical resistance of polyurethane powder coatings. *Journal of Coatings Technology and Research* **13**, 427–437 (2016).
11. Vosgien Lacombe, C., Bouvet, G., Trinh, D., Mallarino, S. & Touzain, S. Water uptake in free films and coatings using the Brasher and Kingsbury equation: a possible explanation of the different values obtained by electrochemical Impedance spectroscopy and gravimetry. *Electrochimica Acta* **231**, 162–170 (2017).
12. Lamaka, S. V., Zheludkevich, M. L., Yasakau, K. A., Montemor, M. F. & Ferreira, M. G. S. High effective organic corrosion inhibitors for 2024 aluminium alloy. *Electrochimica Acta* **52**, 7231–7247 (2007).
13. Goudarzi, N. & Farahani, H. Investigation on 2-mercaptobenzothiazole behavior as corrosion inhibitor for 316-stainless steel in acidic media. *Anti-Corrosion Methods and Materials* **61**, 20–26 (2013).
14. Athar, M., Ali, H. & Quraishi, M. A. Corrosion inhibition of carbon steel in hydrochloric acid by organic compounds containing heteroatoms. *British Corrosion Journal* **37**, 155–158 (2002).
15. Dong, Y., Wang, F. & Zhou, Q. Protective behaviors of 2-mercaptobenzothiazole intercalated Zn–Al-layered double hydroxide coating. *Journal of Coatings Technology and Research* **11**, 793–803 (2014).
16. Wang, G. *et al.* Study of the adsorption of benzimidazole and 2-mercaptobenzothiazole on an iron surface by confocal micro-Raman spectroscopy. *Journal of Raman Spectroscopy* **35**, 1016–1022 (2004).
17. Kakaroglou, A., Domini, M. & De Graeve, I. Encapsulation and incorporation of sodium molybdate in polyurethane coatings and study of its corrosion inhibition on mild steel. *Surface and Coatings Technology* **303**, 330–341 (2016).
18. Vukasovich, M. S. & Farr, J. P. G. Molybdate in corrosion inhibition—A review. *Polyhedron* **5**, 551–559 (1986).
19. Mu, G., Li, X., Qu, Q. & Zhou, J. Molybdate and tungstate as corrosion inhibitors for cold rolling steel in hydrochloric acid solution. *Corrosion Science* **48**, 445–459 (2006).
20. Shams El Din, A. M. & Wang, L. Mechanism of corrosion inhibition by sodium molybdate. *Desalination* **107**, 29–43 (1996).
21. Jay Murray, F., Tyl, R. W., Sullivan, F. M., Tiwary, A. K. & Carey, S. Developmental toxicity study of sodium molybdate dihydrate administered in the diet to Sprague Dawley rats. *Reproductive Toxicology* **49**, 202–208 (2014).

Chapter IV - Corrosion protection and performances of capsules-loaded polyurethane coatings

22. Haynes, W. M., Lide, D. R. & Bruno, T. J. *CRC handbook of chemistry and physics: a ready-reference book of chemical and physical data*. (2017).
23. Boag, A. *et al.* Stable pit formation on AA2024-T3 in a NaCl environment. *Corrosion Science* **52**, 90–103 (2010).
24. Ho, D. *et al.* Cerium Dibutylphosphate as a Corrosion Inhibitor for AA2024-T3 Aluminum Alloys. *Journal of The Electrochemical Society* **153**, B392 (2006).
25. Garcia, S. J., Markley, T. A., Mol, J. M. C. & Hughes, A. E. Unravelling the corrosion inhibition mechanisms of bi-functional inhibitors by EIS and SEM–EDS. *Corrosion Science* **69**, 346–358 (2013).
26. Kokalj, A., Peljhan, S., Finšgar, M. & Milošev, I. What Determines the Inhibition Effectiveness of ATA, BTAH, and BTAOH Corrosion Inhibitors on Copper? *Journal of the American Chemical Society* **132**, 16657–16668 (2010).
27. Balaskas, A. C., Curioni, M. & Thompson, G. E. Effectiveness of 2-mercaptobenzothiazole, 8-hydroxyquinoline and benzotriazole as corrosion inhibitors on AA 2024-T3 assessed by electrochemical methods: Evaluation of inhibitors on AA 2024-T3 by electrochemical methods. *Surface and Interface Analysis* **47**, 1029–1039 (2015).
28. Recloux, I. *et al.* Active and passive protection of AA2024-T3 by a hybrid inhibitor doped mesoporous sol–gel and top coating system. *Surface and Coatings Technology* **303**, 352–361 (2016).
29. Queiroz, F. M., Magnani, M., Costa, I. & de Melo, H. G. Investigation of the corrosion behaviour of AA 2024-T3 in low concentrated chloride media. *Corrosion Science* **50**, 2646–2657 (2008).
30. Conde, A. & De Damborenea, J. An electrochemical impedance study of a natural aged Al-Cu-Mg alloy in NaCl. *Corrosion Science* **39**, 295–303 (1997).
31. Keddad, M., Kuntz, C., Takenouti, H., Schustert, D. & Zuili, D. Exfoliation corrosion of aluminium alloys examined by electrode impedance. *Electrochimica Acta* **42**, 87–97 (1997).
32. Bessone, J. B., Salinas, D. R., Mayer, C. E., Ebert, M. & Lorenz, W. J. An EIS study of aluminium barrier-type oxide films formed in different media. *Electrochimica Acta* **37**, 2283–2290 (1992).
33. Abdollah Zadeh, M., Tedim, J., Zheludkevich, M., van der Zwaag, S. & Garcia, S. J. Synergetic active corrosion protection of AA2024-T3 by 2D- anionic and 3D-cationic nanocontainers loaded with Ce and mercaptobenzothiazole. *Corrosion Science* **135**, 35–45 (2018).
34. Zheludkevich, M. L., Yasakau, K. A., Poznyak, S. K. & Ferreira, M. G. S. Triazole and thiazole derivatives as corrosion inhibitors for AA2024 aluminium alloy. *Corrosion Science* **47**, 3368–3383 (2005).
35. van Soestbergen, M., Erich, S. J. F., Huinink, H. P. & Adan, O. C. G. Dissolution properties of cerium dibutylphosphate corrosion inhibitors. *Corrosion Engineering, Science and Technology* **48**, 234–240 (2013).
36. Aldykewicz, A. J. The Investigation of Cerium as a Cathodic Inhibitor for Aluminum-Copper Alloys. *Journal of The Electrochemical Society* **142**, 3342 (1995).
37. Hassan, H. H., Abdelghani, E. & Amin, M. A. Inhibition of mild steel corrosion in hydrochloric acid solution by triazole derivatives. *Electrochimica Acta* **52**, 6359–6366 (2007).
38. Ferreira, E. S., Giacomelli, C., Giacomelli, F. C. & Spinelli, A. Evaluation of the inhibitor effect of l-ascorbic acid on the corrosion of mild steel. *Materials Chemistry and Physics* **83**, 129–134 (2004).
39. Pokrovski, G. S., Schott, J., Farges, F. & Hazemann, J.-L. Iron (III)-silica interactions in aqueous solution: insights from X-ray absorption fine structure spectroscopy. *Geochimica et Cosmochimica Acta* **67**, 3559–3573 (2003).
40. Birchall, J. D. & Espie, A. W. Biological implications of the interaction (via silanol groups) of silicon with metal ions. in *Silicon biochemistry: Symposium on Silicon Biochemistry, held at the Ciba Foundation, London, 17 - 19 September 1985* (ed. Evered, D.) (Wiley, 1986).
41. Augustyniak, A., Tsavalas, J. & Ming, W. Early Detection of Steel Corrosion via “Turn-On” Fluorescence in Smart Epoxy Coatings. *ACS Applied Materials & Interfaces* **1**, 2618–2623 (2009).
42. Tewari, P. H. & McLean, A. W. Temperature dependence of point of zero charge of alumina and magnetite. *Journal of Colloid and Interface Science* **40**, 267–272 (1972).
43. Frankel, G. S. Pitting Corrosion of Metals. *Journal of The Electrochemical Society* **145**, 2186 (1998).
44. Malouki, M. A., Richard, C. & Zertal, A. Photolysis of 2-mercaptobenzothiazole in aqueous medium. *Journal of Photochemistry and Photobiology A: Chemistry* **167**, 121–126 (2004).

Chapter IV - Corrosion protection and performances of capsules-loaded polyurethane coatings

45. Liang, X. F. & Yang, X. Corrosion Inhibition of 2-Mercaptobenzothiazole for Carbon Steel in Sulfuric Acid Solution. *Advanced Materials Research* **557–559**, 92–95 (2012).
46. Rezaei, F. *et al.* Evaluating water transport through high solid polyurethane coating using the EIS method. *Journal of Coatings Technology and Research* **7**, 209–217 (2010).
47. Lu, F., Song, B., He, P., Wang, Z. & Wang, J. Electrochemical impedance spectroscopy (EIS) study on the degradation of acrylic polyurethane coatings. *RSC Advances* **7**, 13742–13748 (2017).
48. Macedo, M. C. S. S. *et al.* Contribution to a better understanding of different behaviour patterns observed with organic coatings evaluated by electrochemical impedance spectroscopy. *Corrosion Science* **51**, 1322–1327 (2009).
49. Mirmohseni, A., Akbari, M., Najjar, R. & Hosseini, M. Self-healing waterborne polyurethane coating by pH-dependent triggered-release mechanism. *Journal of Applied Polymer Science* **136**, 47082 (2019).

General conclusions

&

Outlook

Conclusions

The present study takes part in the project “New Corrosion Monitoring Material” (NC2M) that aims at developing an innovative protection for steel and aluminum pieces in aerospace structures. The developed technology is based on the encapsulation of active compounds into nanocapsules through a sonication-assisted miniemulsion process. These formed containers are then to be integrated in an aerospace primer in order to provide specific functions to the coating. This work focused on the formation of nanocontainers able to release their payload in a corrosive environment and, for that, pH-sensitive particles were designed. Concerning the coating’s functionalities, corrosion protection associated with a preemptive detection of the corrosion initiation are desired. The anticorrosive properties are brought by the encapsulation of corrosion inhibitors, while the use of colored agents or fluorescing species is considered for the detection of corrosion. This work however focused on corrosion protection, although the system was designed in order to be easily adapted.

Container synthesis

Encapsulation through an emulsion process requires the payload to first be dissolved in the dispersed phase. Therefore, two types of containers have been designed in order to enable the encapsulation of hydrophilic or hydrophobic chemicals.

We reported the synthesis of silica particles, from the interfacial polymerization of tetraethyl orthosilicate (TEOS) as a silica precursor. Silica containers were formed through an oil-in-water miniemulsion. They enabled the encapsulation of molecules that are soluble in organic solvents and with a low solubility in pure water. This was achieved with 2-mercaptobenzothiazole (2-MBT), a corrosion inhibitor. We successfully formed spherical hollow particles with a mean diameter between 180 and 200 nm and a polydispersity index lower than 0.3, evidencing a monomodal size distribution. The stability of the suspension was studied and no evolution of its properties were observed after at least 7 days in acidic and neutral media. However, for alkaline media (pH > 8), it was proved that the suspension was destabilized, and a swelling of the capsules was observed, followed by dissolution of the silica shells. This led to a rapid release of the encapsulated molecules. An optimization of the capsules’ size was tried, by changing the emulsion’s composition or formation parameters and the maximum mean size we obtained was 265 nm, using a different ratio between the two phases’ volumes and adjusting the surfactant concentration. The so-formed silica capsules were therefore suitable for corrosion-triggered effects since local alkalization occurs during corrosion.

For the encapsulation of water-soluble compounds, a process based on previous works and using an oil-in-water emulsion was considered in order to form polyurea particles whose shell can be hydrolyzed in alkaline media. The involved reaction is the interfacial polymerization between toluene 2,4-diisocyanate and diaminobutane, in presence of a surfactant. This surfactant, however

also participates in the reaction. Due to its unavailability, substitution experiments were carried out but could not lead to pH-sensitive capsules. Moreover, the monomers involved in this procedure were used as a first step but present toxicity issues. It was then decided not to further investigate this type of containers.

Incorporation of the capsules and coating formation

In order to form the designed smart-coating, water-based epoxy and polyurethane formulations were considered. These formulations can be diluted in water, what enabled the addition of the capsules suspension as a liquid to the formulation. This reduced the number of steps of the full process, despite limiting the amount of suspension that can be added to the formulation. The formulation was applied on low carbon steel and AA2024-T3, according to ArianeGroup's specifications.

The optimization of the mixing and application procedures led to an apparent dispersion of the silica nanocontainers using an ultra-turrax high-performance disperser combined with a sonication system. However, we could not obtain defect-free epoxy coatings when the silica suspension was added. Further improvements would necessitate either an optimization of the formulation or a purification of the silica suspension in order to remove the residual surfactant molecules. The epoxy system was therefore set aside. On the other hand, polyurethane coatings without any aggregates or observable voids were formed. This was achieved using either bar-coating or spraying that are two industrially applicable techniques. Due to an important evaporation after curing, 25 μm thick coatings were obtained by bar coating while the thickness was increased up to 80 μm when spraying was employed.

The analysis of the formed coatings highlighted a homogeneous dispersion of the silica over the covered area while no significant changes in the polymer structure were observed.

Coatings characterization

Coatings made of pure PU, PU with empty containers and PU with MBT-loaded nanocontainers were analyzed by EIS in a chlorinated medium. Bar-coated steel substrates and spray-coated AA2024-T3 samples have been used. Since the neat PU coating showed very poor properties, no attention was paid to the coating performances.

This work showed that addition of the silica suspension to the polymer matrix induced defects. The total resistance of the system was indeed more than one order of magnitude lower in the case of Si-loaded PU. The presence of MBT in the suspension however showed a little improvement in the charge transfer resistance of the system when applied on steel. Concerning the coated AA2024-T3, a continuous decrease in the coating's total resistance was observed over immersion for the PU in

which empty capsules have been incorporated. However, the initial resistance of the coating remains constant in the presence of MBT.

It was therefore assumed that the incorporation of the designed silica nanocapsules enables a release of the encapsulated agent when the coating is defective and could then enhance its protection. However, the presence of silica capsules in the PU formulation induces the creation of defects. This was attributed to either an impact on the PU cross-linking (probably because of the capsules' reactivity), a wettability issue between the silica shell and the polyurethane matrix or a combination of both.

Alternative inhibitors were also considered, and it was shown that sodium molybdate and cerium dibutylphosphate were efficient inhibitors for the low carbon steel and aluminum alloy that were used respectively.

Conclusion for the NC2M project

The first objective of the NC2M project is to obtain a stable emulsion that could be used for corrosion protection and detection. The synthesis of silica nanocapsules has been achieved and is suitable for this purpose. Organic inhibitors such as MBT and potentially FD1, a fluorescent dye, are amongst the usable compounds.

On the other hand, encapsulation of water-soluble compound was not successful as explained before. An alternative encapsulation protocol therefore has to be developed in order to encapsulate compounds such as inhibitor salts (*e.g.* sodium molybdate) or colored agents for detection (*e.g.* phenolphthalein).

As defined in the NC2M specifications, an efficient process has been developed for the addition of a nanocontainers suspension to a water-based formulation. The homogeneity of the coatings was put forward. Moreover, thanks to the technology used, mixing and application steps can be scaled-up for industrial applications.

The developed coating is able to release the encapsulated molecule upon a water ingress, related to defects and a corrosive environment. Despite a positive effect of the encapsulated molecule, the addition of the nanocapsules however induces an important loss of barrier properties. The NC2M, in its current state, is therefore not applicable. Nonetheless, the possibility to use this system, once improved, has been highlighted for corrosion protection.

Suggestions for improvement

In the present work, we highlighted important breakthroughs towards the building of an efficient smart coating for corrosion protection, that could be adapted to detection. The objective was to develop a complete composite coating. Many steps and techniques were involved and have been

described and, therefore, some parameters were probably not as thoroughly studied as they could be. In our opinion, improvements of the NC2M coatings and outlooks for a more efficient coating concern the containers formation as well as an optimization of the paint formulation.

Development of nanocapsules

Process optimization

The silica nanocapsules suspension presented in this work was directly added to the formulation. This considerably simplifies the process for the coating formation. However, we saw that this limits the coating's final properties. Two main issues were identified and should be overcome.

Firstly, the maximal volume of water that can be added limits the amount of capsules embedded in the polymer matrix. Indeed, the addition of a too important quantity of water destabilizes the paint formulation and leads to a decrease in its viscosity that can be a problem for its application. Since we want to avoid the handling of nanoscale powder, the concentration of the suspension should be considered, controlling the surfactant concentration¹. Ultrafiltration could be a mean to get a slurry of silica capsules that should be redispersible.

Secondly, the suspension being used as-synthesized, the ammonium bromide surfactant is still present in the suspension when it is added to the formulation. This is also true for potential residual alkoxy silane monomers. We suggested that the presence of DTAB could be a reason to explain the difficulty we encountered in order to form a defect-free coating. Therefore, purification of the suspension should be carried out, perhaps using ultrafiltration as well, or dialysis.

Scale-up of the process should also be kept in mind, although it must be considered after optimization of the purification and concentration steps.

Composition of the emulsion

A preemptive detection of corrosion is amongst the main objectives of the NC2M coating. To this end, FD1 has been selected as a fluorescent molecule that could enable the detection of a local acidification due to corrosion. In the case of steel, complexation of FD1 with ferric ions also triggers fluorescence². The encapsulation of FD1 was proven successful using the designed silica nanocapsules and led to a patent in the framework of the project NC2M³. The next step should therefore be the encapsulation of FD1 in order to assess the possibility to detect corrosion at its early stages.

The main issue concerning the miniemulsion process we employed is the toxicity of the dispersed phase. Hexadecane and toluene are indeed toxic and CMR respectively, and should hence be banished from such applications. A change of solvent however would likely imply a change of surfactant as well since its adsorption depends on the solvents' polarity⁴.

General conclusions & Outlook

A change in surfactant could also be of great interest in order to tune the size of the dispersion. As we saw in chapter II, the nature and concentration of the surfactant were the most efficient parameters we considered. A study of the encapsulation efficiency of bigger silica particles could then allow to determine an optimal size of the capsules for the release of a high amount of payload.

A last thing that was not considered in this work but can probably enhance the system's performance is the functionalization of the silica capsules' surface. We evidenced probable problems of cohesion between the capsules' shell and the polymer matrix. Functionalization of the particles' surface could hence be an interesting way to improve the incorporation of the capsules. Grafting could be achieved using the silanol groups that compose the particles' surface. This requires chemistry skills, and could be done depending on the host matrix in order to favor the silica / polymer interactions and enhance the wettability of silica by the paint.

Characterization

Concerning the characterization of the suspension of silica nanocapsules, the presented results could be completed by a study of the capsules' behavior depending on the temperature or under UV. This could indeed be a matter of importance for the final formulation.

Moreover, silica is supposed to be porous, what was however not assessed for our system. Drying is not a priority but could however give more information on the capsules' structure, enabling adsorption measurements for instance,

Encapsulation of water-soluble molecules

As explained in this manuscript, encapsulation of both hydrophilic and hydrophobic molecules is mandatory in order to enable a staggering choice of payloads. Since the synthesis of polyurea particles was not successful and implied toxic chemicals, a new procedure should be developed. As shown in the first chapter, an incredible number of processes and natures of particles can be found. In order to form an emulsion as green as possible, layer-by-layer adsorption and complexation of polyelectrolytes (possibly from natural resources) seem to be the most promising techniques.

Coating enhancement

Since the properties of the polyurethane formulation itself were quite poor, we suggest that it should be changed. Using of a model polymer may be mandatory at first in order to get a better understanding of the suspension's reactivity. Otherwise, the use of a commercial paint instead of a simplified one is required.

In the case that the studied polyurethane matrix is kept, an optimization of the ratio between the base, hardener and suspension should be performed. Indeed, the reactivity of the silica nanocontainers with the formulation's component was only qualitatively assessed and could be

thoroughly examined. The relative quantity of the base and hardener could then be adjusted in order to avoid cross-linking issues.

Changes in the formulation are obviously closely linked to the results obtained for the suspension. Therefore, the next systems to build and analyze would be coatings in which are incorporated suspensions:

- With different sizes;
- With functionalized silica shells;
- After partial evaporation of the aqueous phase;
- Containing FD1.

Moreover, as initially planned, the encapsulation of FD1 within silica nanocapsules would enable the formation of coatings containing both an inhibitor and a sensing molecule. First trials were performed for the NC2M project, monitoring filiform corrosion by fluorescence. The capsules were applied by brush as a suspension directly on top of the metal prior to the application of an organic layer. A deactivation of the filiform corrosion active head was evidenced when the filament reached an inhibitor-containing area (results to be published by Loïc Exbrayat). We can even think of the combination of several inhibitors in order to get a synergistic effect, as sometimes evidenced⁵.

The next steps of the study are naturally ageing studies, starting by ageing in atmospheric conditions, and the study of the system's stability versus UVs or temperature changes since variations can be observed in operational conditions.

In parallel of the proposed improvements, it would be very interesting to try adding the prepared silica suspension to a sol-gel formulation. Since the same chemistry is used for sol-gels and for the prepared capsules, the compatibility should not be troublesome. Moreover, very promising results have been observed for sol-gels, explaining that they are currently investigated⁶⁻⁸.

References

1. Sato, T. & Kohnosu, S. Effect of surfactant concentration on the stability of aqueous titanium dioxide suspensions. *Journal of Colloid and Interface Science* **143**, 434–439 (1991).
2. Augustyniak, A., Tsavalas, J. & Ming, W. Early Detection of Steel Corrosion via “Turn-On” Fluorescence in Smart Epoxy Coatings. *ACS Applied Materials & Interfaces* **1**, 2618–2623 (2009).
3. Rameau, B. *et al.* nanocapsules for early stage corrosion detection. FR 17403538, 20/04/2017 (2017).
4. Nourafkan, E. Evaluation of adsorption of nonionic surfactants blend at water/oil interfaces. *Journal of Dispersion Science and Technology* **39**, 665–675 (2018).
5. Abdolah Zadeh, M., Tedim, J., Zheludkevich, M., van der Zwaag, S. & Garcia, S. J. Synergetic active corrosion protection of AA2024-T3 by 2D- anionic and 3D-cationic nanocontainers loaded with Ce and mercaptobenzothiazole. *Corrosion Science* **135**, 35–45 (2018).
6. Thai, T. T., Druart, M.-E., Paint, Y., Trinh, A. T. & Olivier, M.-G. Influence of the sol-gel mesoporosity on the corrosion protection given by an epoxy primer applied on aluminum alloy 2024 -T3. *Progress in Organic Coatings* **121**, 53–63 (2018).
7. Maia, F. *et al.* Corrosion protection of AA2024 by sol-gel coatings modified with MBT-loaded polyurea microcapsules. *Chemical Engineering Journal* **283**, 1108–1117 (2016).
8. Blohowiak, K. Y., Osborne, J. H. & Seebergh, J. E. Development and Implementation of Sol-Gel Coatings for Aerospace Applications. in (2009). doi:10.4271/2009-01-3208.

Appendices

Appendix 1: UV-vis calibration data for MBT

In order to determine the concentration of MBT for the release study, two calibration curves are plotted, either in neutral or in alkaline (pH = 12) media. For each set, 9 standard solutions from 1 to 35 ppm are prepared. For both conditions, 3 peaks are detected in the UV-vis spectra shown in Figure 1.a & c. Therefore, 3 calibrations curves can be plotted, given in Figure 1.b and d. In order to limit interferences that could be due to the environment, a mean value calculated from the three peaks is used each time. Calibration data are presented in Table 1.

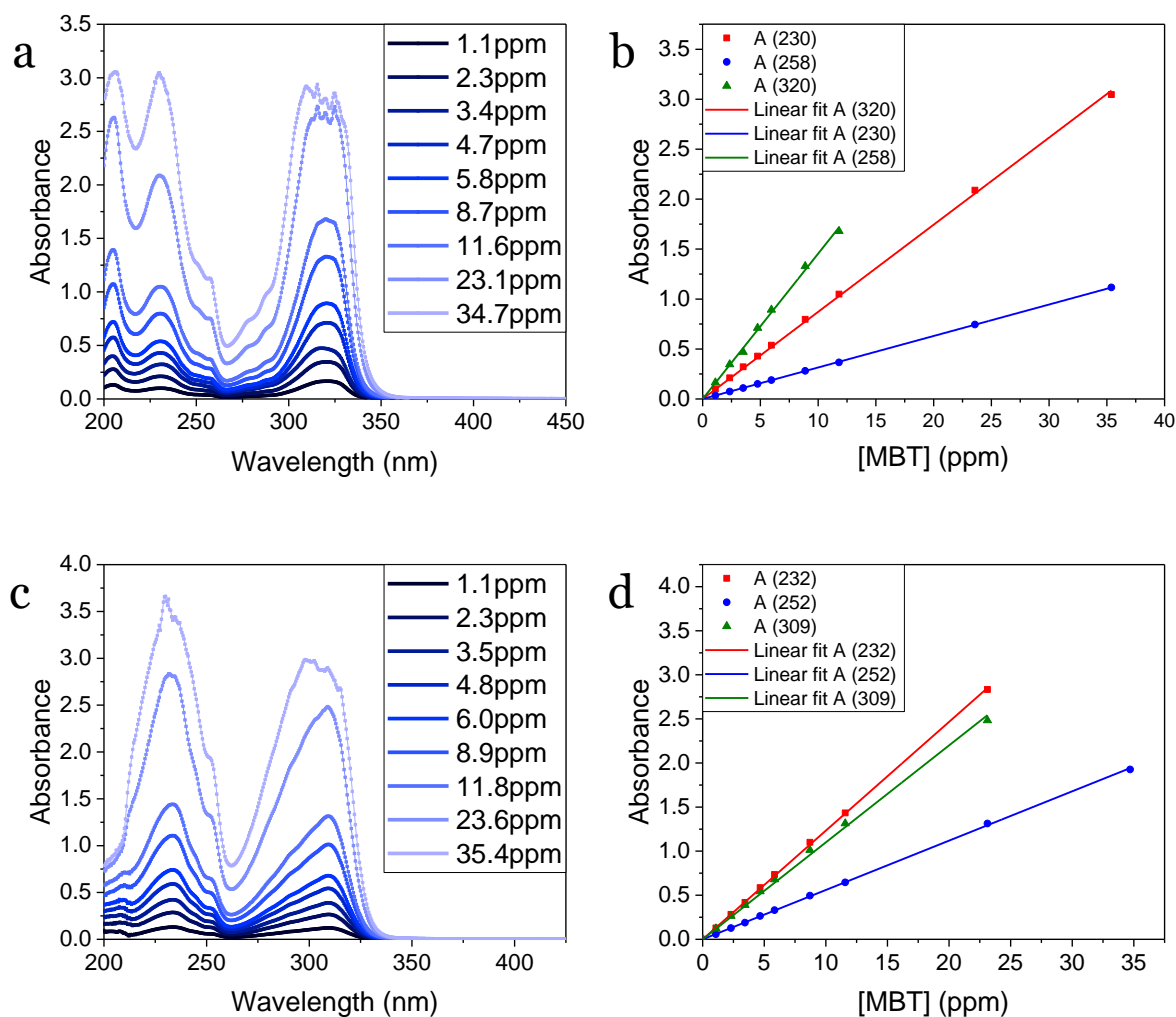


Figure 1: UV-vis spectra of the MBT solutions prepared in (a) pure water and (c) 20 mM NaOH and (b & d) respective calibration curves

Appendices

Table 1: UV-vis calibration data for MBT in the range 0-30 ppm

Medium	Wavelength (nm)	Slope (Abs/[MBT])	Standard deviation	R ²
Neutral	230	0.0872	4.85.10 ⁻⁴	0.99972
	258	0.0315	5.02.10 ⁻⁵	0.99998
	320	0.145	1.62.10 ⁻³	0.99913
Alkaline	232	0.123	4.62.10 ⁻⁴	0.99989
	252	0.0560	1.99.10 ⁻⁴	0.99989
	309	0.110	1.28.10 ⁻³	0.99892

Appendix 2: List of chemicals used

The lists of the chemicals used for the preparation of silica and polyurea capsules are given in Table 2 and

Table 3 respectively. All chemicals have been used as received, taking into account the given purity.

Table 2: List of the chemicals used for the preparation of silica capsules

Name	CAS	Supplier	Purity
Tetraethyl orthosilicate (TEOS)	78-10-4	Acros Organics	98%
Hexadecane (anhydrous)	544-76-3	Sigma-Aldrich	≥99%
Toluene	108-88-3	Carlo-Erba	ACS
Dodecyl trimethylammonium bromide (DTAB)	1119-94-4	Sigma	≥98%
Tetradecyl trimethylammonium bromide (TTAB)	1119-97-7	Sigma-Aldrich	98%
hexadecyl trimethylammonium bromide (HTAB)	57-09-0	Sigma-Aldrich	≥98%
Octadecyl trimethyl ammonium bromide (OTAB)	1120-02-1	Sigma-Aldrich	98%

Table 3: List of the chemicals used for the preparation of PUa microcapsules

Name	CAS number	Supplier	Purity
Cyclohexane	110-82-7	Carlo-Erba	ACS reagent
2,4-toluene diisocyanate (TDI)	584-84-9	Sigma	≥98%
1,4-diaminobutane (DAB)	110-60-1	Aldrich	99%
Ethanol	64-17-5	Carlo-Erba	≥99.9%
Sodium dodecyl sulfate (SDS)	151-21-3	Sigma-Aldrich	≥98.5%
Dialysis tubing membrane 14kDa, 33mm	N/A	Sigma-Aldrich	N/A

Concerning the surfactant, Lubrizol® 5625 and Lubrizol® 5620B were supplied by Lubrizol while Span® 80, Tween® 80 and Span® 85 were produced by Croda. Pure water (18.2 MΩ at 25°C) is used throughout all experiments.

Appendix 3: Summary of the process optimization attempts for silica nanocontainers

Table 4 records the size, polydispersity index and observations made for optimization of the mini-emulsion process presented in Section II.

Appendices

Table 4: Summary of the emulsion process optimization experiments carried out

Checked parameter	Parameter value	Mean size	PDI	Observations
		Average (nm)		
Ref Si	US 60%	188.7 ± 3.6	0.190 ± 0.022	
	DTAB (C ₁₂) 8 mM	164.4 ± 9.9	0.158 ± 0.037	
Ref Si(MBT)	US 60%	187.6 ± 10.7	0.173 ± 0.024	
	DTAB (C ₁₂) 8 mM	190.3 ± 10.7	0.204 ± 0.044	
Sonication	20%	149.3 ± 3.9	0.120 ± 0.027	
	42%	164.4 ± 9.9	0.158 ± 0.037	
	70%	188.7 ± 3.6	0.190 ± 0.022	
	Pulse 5s	184.3 ± 12.4	0.158 ± 0.085	
Mechanical Stirring	3 krpm 5 min		Instable	
	7 krpm 5 min		Instable	
	10 krpm 5 min	398.8 ± 39.7	0.296 ± 0.184	Sedimenting
	10 krpm 5 min less DTAB	435.9 ± 54.8	0.260 ± 0.211	Sedimenting
	15 krpm 5min	364.6 ± 6.5	0.209 ± 0.041	Sedimenting
	15 krpm 5 min less DTAB	343.5 ± 20.6	0.234 ± 0.102	2 clear peaks
	10 krpm 3 min cat HCl	477.6 ± 37.4	0.252 ± 0.052	2 clear peaks
	7 krpm 10 min	327.3 ± 23.7	0.067 ± 0.013	Sedimenting
	7 krpm 10 min large tool	370.5 ± 7.8	0.032 ± 0.004	Sedimenting
	7 krpm 15min		Instable	
Surfactant	8 krpm 5min		Instable	
	C ₁₄	220.7 ± 27.1	0.332 ± 0.113	
	C ₁₆	375.7 ± 44.9	0.192 ± 0.034	
	C ₁₈		Flocculation	
	C ₁₂ 2 mM	210.7 ± 8.5	0.121 ± 0.027	
	C ₁₂ 16 mM	165.3 ± 1.7	0.210 ± 0.028	
Emulsion Composition	C ₁₂ 24 mM	150.7 ± 6.2	0.250 ± 0.070	
	No HD		Instable	
	Less HD	176.1 ± 14.0	0.115 ± 0.048	
	Less TEOS	349.3 ± 23.0	0.304 ± 0.050	
	x2	194.7 ± 9.0	0.136 ± 0.038	
	V _{disp} x2	207.7 ± 2.0	0.093 ± 0.009	
	V _{disp} x4		Gelation	
V _{disp} x2 less DTAB	265.0 ± 7.0	0.079 ± 0.020		